

Electronic Theses and Dissertations, 2020-

2021

Directional Spectral Solar Energy for Building Performance: From Simulation to Cyber-physical Prototype

Joseph Del Rocco
University of Central Florida

 Part of the [Computer Sciences Commons](#), and the [Power and Energy Commons](#)
Find similar works at: <https://stars.library.ucf.edu/etd2020>
University of Central Florida Libraries <http://library.ucf.edu>

This Doctoral Dissertation (Open Access) is brought to you for free and open access by STARS. It has been accepted for inclusion in Electronic Theses and Dissertations, 2020- by an authorized administrator of STARS. For more information, please contact STARS@ucf.edu.

STARS Citation

Del Rocco, Joseph, "Directional Spectral Solar Energy for Building Performance: From Simulation to Cyber-physical Prototype" (2021). *Electronic Theses and Dissertations, 2020-*. 851.
<https://stars.library.ucf.edu/etd2020/851>

DIRECTIONAL SPECTRAL SOLAR ENERGY FOR BUILDING PERFORMANCE:
FROM SIMULATION TO CYBER-PHYSICAL PROTOTYPE

by

JOSEPH A. DEL ROCCO
B.S. University of Central Florida, 2001
M.S. University of Central Florida, 2011

A dissertation submitted in partial fulfilment of the requirements
for the degree of Doctor of Philosophy
in the Department of Computer Science
in the College of Engineering and Computer Science
at the University of Central Florida
Orlando, Florida

Fall Term
2021

Major Professor: Joseph T. Kider, Jr.

© 2021 Joseph A. Del Rocco

ABSTRACT

The original research and development in this dissertation contributes to the field of building performance by actively harnessing a wider spectrum of directional solar radiation for use in buildings. Solar radiation (energy) is often grouped by wavelength measurement into the spectra ultraviolet (UV), visible (light), and short and long-wave infrared (heat) on the electromagnetic spectrum. While some of this energy is directly absorbed or deflected by our atmosphere, most of it passes through, scatters about, and collides with our planet. Modern building performance simulations, tools, and control systems often oversimplify this energy into scalar values for light and heat, when in reality they are interrelated directional spectral quantities of energy that are diffused and attenuated by clouds before colliding with surfaces. In addition to this, live building monitoring and control systems in-the-wild often do not track the location of the sun, separate direct sun energy from scattered sky energy, account for overcast clouds, considering occluded energy, etc. The work in this dissertation provides building energy simulations and control systems with finer-grain control over lighting and heating in order to optimize energy use and improve occupant well-being. We first present a data-driven machine learned sky model for predicting spectral radiance, and show how this technique can be used to produce spectral radiance maps for the entire hemispherical sky. We then integrate these predicted spectral radiance maps and other validated predictions into a custom radiosity engine in order to predict spectral daylighting and heating energy in building interiors. Finally, we present the design and prototyping of a cyber-physical building control system that monitors the sky and occupants in order to harness natural light and heat more effectively. We present ongoing and future work recommendations, such as sky cover projections to help reduce cooling recovery costs, and the use of spectral radiance maps in physically-based rendering engines.

For Dylan and his planet.

ACKNOWLEDGMENTS

First and foremost, I humbly thank and apologize to my wife, son, and parents for supporting and putting up with me throughout this lengthy, stressful academic process. I am in your debt.

I thank my advisor, Dr. Joseph T. Kider Jr., for allowing me to perform this work under him, and for his advice, knowledge, and patience with me. The work in this dissertation is really his, in that, without him and his contributions, it would not even exist. He has a grand vision and the ability to connect disparate yet equally important research projects to push the state of the field he sets his sights on. I also thank my committee members for their time and insight: Dr. Charles E. Hughes (especially, for many things), Dr. R. Paul Wiegand, Dr. Annie S. Wu, and Dr. Hala ElAarag.

To my students, past, present and future, you are the real visible energy at the end of this tunnel.

I would like to acknowledge all of the brilliant people who contributed to this research directly or indirectly in some way, including Dr. Donald P. Greenberg, Dr. Bruce Walter, Kevin Pratt, Dr. Steve Marschner, Hurf Sheldon, Lars Schumann, Daniel Knowlton, Sandy Fang and Ege Sekkin for respective efforts in BPS at Cornell University; C. Brandon Patterson and Dr. Josh Eckroth for machine learning work; Paul Bourke (the world's authority on fisheye lenses); Dr. Arve Kylling; Dr. Stephen M. Fiore; Nathan Moulton and Evans Asuboah; Lauren Doocy, Arash Zarmehr and John Sermarini; Shane Saedie and Jeremiah Eisenmenger for math support; Maik Riechert for raw image advice; and Ethan Frolich, a very helpful independent reviewer.

Finally, I thank Dr. Jeremiah Blanchard for motivating me to pursue a terminal degree; I may not have returned to graduate school without his example and near inexhaustible energy. For additional support, I thank Nick Cunningham, Jason Hinders, Greg Shumaker and Dr. Rob Michlowitz.

TABLE OF CONTENTS

LIST OF FIGURES	ix
LIST OF TABLES	xii
CHAPTER 1: INTRODUCTION	1
CHAPTER 2: BACKGROUND AND RELATED WORK	8
2.1 Sun and Sky Solar Radiation	8
2.1.1 Radiance vs Irradiance	12
2.1.2 Sky Models	17
2.2 Building Performance Simulation	22
2.2.1 Daylighting	25
2.2.2 Building Automation Systems	29
2.3 Background Summary	32
CHAPTER 3: WHOLE SKY SPECTRAL RADIANCE ESTIMATION	33
3.1 Measurements and Data	39
3.1.1 Lens Linearity	39
3.1.2 Sky Color	42
3.1.3 Raw vs. Digital Positive	43
3.1.4 <i>Spectral Sky Viewer</i>	44
3.2 Spectral Shape Estimation	47
3.2.1 High-Dynamic Range Imagery	50
3.2.2 Color Model	51

3.2.3	Spectral Resolution	53
3.2.4	sradmap	54
3.3	Results	55
3.4	Validation	63
3.5	Ongoing Work	66
CHAPTER 4: RADIANT SPECTRAL ENERGY FOR SIMULATION		68
4.1	Methods	69
4.1.1	Radiant Spectral Energy	70
4.1.2	<i>Transition Portal</i> Radiosity Engine	73
4.1.3	Adaptive Smart Spectrally-varying Glazing	75
4.1.4	<i>Rhino 3D 6</i> Plugin	80
4.2	Results	82
CHAPTER 5: SKY AND OCCUPANT AWARE ADAPTIVE FACADE		85
5.1	Facade Concept	87
5.2	Numerical Analysis	91
5.3	Case Study	95
5.4	Facade MPC Model	100
5.5	Facade Physical Prototype	104
CHAPTER 6: CONCLUSIONS		120
6.1	Ongoing and Future Work	122
APPENDIX A: SPECTRAL SKY VIEWER		126
APPENDIX B: SUPPLEMENTARY SKY RESULTS		130
APPENDIX C: SUPPLEMENTARY DAYLIGHTING ANALYSIS		139

APPENDIX D: PUBLISHER PERMISSION LETTERS 143

APPENDIX E: LIST OF RELEVANT PUBLICATIONS BY THE AUTHOR 147

LIST OF REFERENCES 149

LIST OF FIGURES

Figure 2.1: The spectrum of solar radiation	10
Figure 2.2: Global solar radiation is the sum of direct, indirect, and reflected energy . .	11
Figure 2.3: Direct solar (beam) vs indirect diffuse (sky) radiation	12
Figure 2.4: Radiance versus Irradiance	13
Figure 2.5: Incident solar gain on a building surface exterior	16
Figure 2.6: Building energy modeling (BEM) software tools	24
Figure 2.7: Building performance software using <i>RADIANCE</i> and <i>DaySim</i>	28
Figure 2.8: Model-based Predictive Controller (MPC)	31
Figure 3.1: An overview of our spectral radiance estimation work	36
Figure 3.2: Each sky capture was 8 photos and 81 spectral radiance measurements . . .	37
Figure 3.3: Coordinate system for radiant energy measurements	38
Figure 3.4: Lens warp visualized	41
Figure 3.5: Sampling colors from sky imagery	43
Figure 3.6: Camera-processed JPG and minimally-processed (near raw) TIFF	44
Figure 3.7: <i>Spectral Sky Viewer</i> used to identify bad measurements	46
Figure 3.8: Final set of input and output features per sky sample	48
Figure 3.9: Exploratory data analysis feature histograms	49
Figure 3.10: Multiple exposures of the sky for high dynamic range (HDR)	52
Figure 3.11: A spectral radiance measurement plotted at 5 different resolutions	53
Figure 3.12: Model results on each of the four holdout test skies	56
Figure 3.13: Whole sky results with ETR model on 05/27/2013 10:15	57
Figure 3.14: Results of four radiance predictions on 05/27/2013 10:15	58
Figure 3.15: Sky sample color model experiment results	59

Figure 3.16: Spectral resolution of radiance distribution results	60
Figure 3.17: False-colored sradmap of holdout test sky 07/26/2013 13:15	61
Figure 3.18: Spectral radiance maps (sradmaps) of holdout skies	62
Figure 3.19: Validation of radiance with libRadtran	64
Figure 3.20: Validation of radiance for two samples on 05/27/2013 10:15	65
Figure 3.21: Validation of radiance for two samples on 07/26/2013 13:15	65
Figure 3.22: Preliminary results of regression models on all sky data	66
Figure 3.23: Preliminary results for ongoing research with DNN model	67
Figure 4.1: Examples of skies with measured and predicted radiance	71
Figure 4.2: Full skies with spectral radiance used by our plugin	72
Figure 4.3: Sun path and sky patches for radiosity calculations	73
Figure 4.4: Preliminary office result with spectral radiance input	74
Figure 4.5: Glazing options and spectral transmittance	76
Figure 4.6: Ideal year-round glazing solutions	77
Figure 4.7: Model of a spectrally filtering facade like smart-glazing	78
Figure 4.8: Novel fritted smart-film concept	79
Figure 4.9: Screenshot of <i>Rhino 3D 6</i> plugin	81
Figure 4.10: False colored (yellow) spectral renders of a few different bins	82
Figure 4.11: False colored spectral radiosity interior renders	84
Figure 5.1: A cyber-physical building monitoring system design	86
Figure 5.2: Famous adaptive facades found around the world	87
Figure 5.3: Individual adaptive facade units	89
Figure 5.4: Kinetic facade design concept	89
Figure 5.5: Kinetic facade concept actuation	90
Figure 5.6: Facade unit wings being controlled individually	90

Figure 5.7: Daylight analysis of Sierpinski design (1 m working height)	92
Figure 5.8: Daylighting analysis of Sierpinski design (spring equinox)	93
Figure 5.9: Daylighting analysis of Sierpinski design throughout the year	94
Figure 5.10: Site location: Institute for Simulation and Training, UCF	95
Figure 5.11: Daylighting render of case study office 07/01/2017 08:00	96
Figure 5.12: Daylighting and luminance false color render of case study office	97
Figure 5.13: Office site modeled in Rhino 3D	98
Figure 5.14: Rhino Grasshopper script logic for facade creation	99
Figure 5.15: The MPC control system of our cyber-physical prototype	101
Figure 5.16: Early triangular unit physical prototype designs	106
Figure 5.17: Early triangular unit physical prototype opening	106
Figure 5.18: Final triangular unit prototype	106
Figure 5.19: Prototype frame with mounted acrylic	107
Figure 5.20: 3D printing triangular unit rods	109
Figure 5.21: Laser-cutting in progress	110
Figure 5.22: <i>Texas Instruments Innovation Lab</i> , UCF	111
Figure 5.23: Servos and horns used during prototyping	112
Figure 5.24: Assembly of physical prototype	114
Figure 5.25: Wiring of the physical prototype	115
Figure 5.26: Lab testing of the facade physical prototype	117
Figure 5.27: Physical prototype experiment results	118
Figure 5.28: Sky conditions during physical prototype experiment	119

LIST OF TABLES

Table 3.1:	List of observed sky data captures	40
Table 3.2:	The four holdout test skies selected at random and used for final evaluation	51
Table 4.1:	The 4 glazing solutions tested in simulations	80

CHAPTER 1: INTRODUCTION

The research in this dissertation is motivated by one of the greatest challenges of our time: climate change. For decades, researchers and practitioners across a myriad of disciplines have studied contributing factors and proposed solutions to reduce global greenhouse gases (GHG) (mostly carbon). One major contributing factor is the production of electrical energy and its use. Assuming that lower energy use results in less energy production, we focus on the use of energy in buildings. The electricity consumed by buildings and building occupants accounts for more than 40% of GHG in the United States alone (45%+ globally) ([The American Institute of Architects \(AIA\), 2019](#); [Butler, 2008](#)). And unfortunately, a long-term global increase of GHG is expected as more buildings are developed to support the expansion of developing nation infrastructure, world population growth, and city renewal and planning efforts everywhere. This is compounded by digital design trends, smart home technology, healthcare improvements, and the “internet-of-things;” all of which have granted us even longer, energy-consuming lifespans ([Janda, 2011](#)). Urban growth in particular is a problem. By 2050, we expect two thirds of the world’s population to be living in urban areas, a process known as urbanization, which when mismanaged can hinder the local (and even global) climate through the unsustainable consumption and use of energy, heat island effect, and general environmental degradation and pollution between urban and suburban environments ([USDOE Energy Information Administration \(EIA\), 2021](#); [United Nations and Social Affairs, 2018](#); [Sethi and de Oliveira, 2015](#)). In other words, unplanned urbanization in undeveloped countries spells more trouble for climate change. And despite a record drop in GHG emissions due to the COVID-19 pandemic of 2020 and 2021, “...*the world is far from doing enough to put them into decisive decline...low economic growth is not a low-emissions strategy...Only faster structural changes to the way we produce and consume energy can break the emissions trend for good.*” ([Birol et al., 2020](#)).

In the past, electrical energy consumption in buildings was plagued by lighting (Boubekri, 2008). But improvements to lighting technology (advanced light emitting diodes (LEDs), better control software, etc.) and the increase in active harnessing of natural daylight have cut lighting energy usage down to 12% in commercial buildings and 4% in residential buildings in the United States (USDOE Energy Information Administration (EIA), 2021; Capuano et al., 2020). However, thermal comfort (heating, ventilation and air-conditioning (HVAC)) in the US, accounts for roughly 70% of the electrical energy use in buildings (Mazria and Kershner, 2008), or 39% commercial and 30% residential (USDOE Energy Information Administration (EIA), 2021). Even with insulation and material improvements, HVAC remains a challenge. All of this implies that even a small reduction in energy spent on thermal comfort, and to a lesser but still significant extent, lighting, could make a difference in the GHG footprint.

Note there are also economic benefits to utilizing natural daylight for lighting and heating. Cost-benefit analysis and economic impact research dates back to the 1970s (Griffith, 1978; Boyce et al., 2003; Mayhoub and Carter, 2011; Bakshi and Jakubiec, 2011; Sapia, 2013). One recent case-study showed that the implementation of a model-based predictive controller with adaptive blinds for a mid-size 6-story building could save roughly 5000 CHF (\$5000 USD) a year (Sturzenegger et al., 2015).

This dissertation contributes to the initiative of reducing energy use in buildings in the hopes of reducing GHG by refining some of the methods used in building performance simulation (BPS), architectural design tools, and building monitoring control systems, all of which estimate the amount of actual solar energy (both light and heat) on the exterior and interior surfaces of buildings in order to make decisions about energy use. Solar energy can be avoided or passively or actively harvested for the benefit of occupants and our planet, but it is important that software does it accurately to fully realize gains. Note that “building performance” is a very broad field covering factors such as:

energy efficiency, daylighting (the active harnessing of light), occupancy comfort and productivity, material sustainability, water reclamation, acoustics and sound pollution, society and environment, accessibility, etc. ([American Society of Heating, Refrigerating and Air-Conditioning Engineers \(ASHRAE\), 2021](#); [The American Institute of Architects \(AIA\), 2019](#); [Designing Buildings Ltd., 2020](#); [Lechner, 2014](#); [Mallory-Hill et al., 2012](#)) In this dissertation, we narrow our focus to energy efficiency and occupant well-being.

Building energy simulations (BES) / building energy modeling (BEM) simulators often oversimplify solar energy into a limited collection of scalar values when in reality it is composed of infinitesimal directional spectral quantities that are scattered, reflected and occluded before colliding with and entering into buildings. Light versus heat in the solar energy spectrum, the location of the sun, direct / indirect / ground reflected energy, sky conditions, and occlusions from surrounding contributors (e.g. other buildings, large trees, etc.) are all important factors for accurate building energy calculations. Spectral energy (i.e. a spectral breakdown of solar energy) is important because it helps us identify significant quantities of both light and heat separately (as well as ultraviolet). These breakdowns of energy can serve different purposes, yet they overlap on the electromagnetic spectrum and therefore should be preserved intact throughout the BES pipeline for as long as possible. For example, daylighting studies often ignore the effects of heat, while thermal studies often ignore daylighting strategies. The directional aspects of energy (radiance) is even more important for several reasons, including: the fact that solar energy from a 10° circum-solar region of a clear sky is dramatically higher than all of the diffuse energy from the rest of the sky ([Gueymard, 2010](#)); that cloud cover is not uniform, changes constantly, and completely alters the global energy profile by scattering or diffusing large amounts of energy; wavelength-dependent energy scattering aerosols and particulates in the atmosphere can clump into unevenly distributed pockets in the sky distorting expected energy predictions ([Kocifaj, 2015](#)); nearby trees and buildings occlude energy ([Schumann and Greenberg, 2012](#); [Li et al., 2017](#); [Robledo et al., 2021](#)); and

perhaps the most important (though obvious) reason is that the exterior surfaces of buildings face separate directions and thus are subject to completely different amounts of energy. Because of these directional considerations, solar energy must be measured or predicted from the ground versus remote sensing satellites in space, and is expensive to do accurately and continuously. BES programs leverage atmospheric sky models, but often simple analytical ones that oversimplify energy. It is easier and more efficient to process solar energy as a collection of illuminance scalar values versus the many vectors and matrices of values needed to account for directional spectral energy for the entire hemispherical sky. In addition to this, the most commonly used, validated BES programs today are all legacy systems ([Crawley et al., 2008](#)), and few if any are used dynamically for building monitoring and control systems. There is also research that suggests that BES programs themselves are still inaccurate when predicting financial costs associated with utilizing daylight ([Versage et al., 2010](#)).

In this dissertation, we propose a sky and occupant aware building monitoring system that leverages spectral radiant solar energy in order to harness natural light and heat more effectively exterior facing zone. We first present our published research of a validated, data-driven machine learning model for estimating directional spectral energy across entire hemispherical clear skies ([Del Rocco et al., 2020, 2018](#)) and on-going work on scattered skies. We then present our published research on integrating both our generated spectral radiance maps and other validated spectral energy skies into a custom developed radiosity engine and plugin which can be used to estimate the accumulated spectral energy (irradiance) per planar surface (interior and exterior) of a building per spectral bin of interest ([Del Rocco and Kider Jr., 2021](#)), for both early-phase design and in a real-time setting. Finally, we present the design and development of a cyber-physical prototype with adaptive kinetic facade that could be controlled by such a building monitoring system.

Our data-driven machine learning approach for estimating spectral radiance across the entire sky

uses regression models trained on high dynamic range (HDR) imagery and validated spectroradiometer measurements (Del Rocco et al., 2020, 2018; Kider et al., 2014). Our method is more practical and efficient than a hardware-based sky scanning system and much more accurate than a single scalar quantity used in many building performance simulations; it supplies spectral radiance for every point in the hemispherical sky, accounts for seasonal and datetime variation, predicts a wide, useful spectrum of energy (350-1780 nm) at 1 nm resolution, and is validated against libRadtran, a modern atmospheric radiative transfer package (Emde et al., 2016). Although using atmospheric measurements may improve the training and prediction accuracy, we also showed that they were not necessary.

Our spectral irradiance work is an extension of the *Transition Portal* radiosity engine published by Kider et al. (2019). The contributions in this dissertation allow for an early-phase or retrofit building performance engineer to define spectral bins of interest, load solar and sky spectral radiance data from any sky model (ours, libRadtran, etc.), and then run relatively fast simulations to provide spectral irradiance estimations for visual and quantitative analysis (Del Rocco and Kider Jr., 2021). This software is intended to be used by early-phase building designers and architects who are considering different spectral filtering glazing materials as well as other interior layout and design decisions. This modular engine can also be leveraged outside a 3D modeling environment, e.g. by real-time building monitoring systems needing per planar surface estimations.

Our sky and occupant aware adaptive facade cyber-physical prototype is designed to take both daylighting and thermal factors into account (Moulton et al., 2018). Such factors include: directional spectral energy from an appropriate sky model, local atmospheric parameters if required by the sky model, a surrounding environment shadow mask, visual and thermal comfort limits, and occupant overrides per exterior facing zone of interest. It also closes automatically for building occupant privacy outside of daylighting hours. Given external temperature, if independent spectral filter-

ing smart-glazing is available per zone, our building monitor control model can supply additional inputs for actively harnessing or deflecting infrared energy.

Our contributions to the fields of atmospheric science and building performance include:

- ([Del Rocco et al., 2020](#)) A data-driven sky model that takes low resolution input (sky photo and datetime) and predicts spectral energy (350-1780 nm) at 1 nm resolution across the entire skydome for clear skies (and ongoing work with preliminary positive results on scattered skies), which:
 - was trained on the most comprehensive, curated dataset to date of multi-exposure high resolution all-sky photos and spectral energy measurements captured from the ground (and made available to the public ([SENSEable Design Lab \(2016\)](#)))
 - does not require atmospheric measurements to predict spectral energy as opposed to notable prior research ([Kocifaj, 2015](#)) (although atmospheric measurements can easily be provided as training and prediction features if available and desired)
 - accounts for fish-eye lens warp
 - will ultimately require only 1 trained model per sky condition (clear, scattered, over-cast) as opposed to notable prior research requiring many models ([Tohsing et al., 2014](#))
 - is validated against libRadtran ([Emde et al., 2016](#))
- ([Del Rocco and Kider Jr., 2021](#)) A proof-of-concept for the integration of spectral energy into building energy modeling and daylighting software for use in either design or control.
- ([Moulton et al., 2018](#)) A building monitor system design with adaptive facades that uses spectral radiant solar energy in order to harness both natural light and heat.

- An open-source tool (*Spectral Sky Viewer*) for visualizing, curating and exporting datasets of correlating all-sky photos and spectral solar energy ([Section A](#))
- An open-source tool (sradmap) for producing a file with spectral radiance of any resolution given one of our models, a sky photo, and datetime of capture ([Del Rocco et al., 2020](#))
- A novel fritted smart-film idea ([Section 4](#))

The remainder of this dissertation is organized as follows. Some background and prior work relevant to the work in this dissertation is presented in [Section 2](#). Our data-driven method for estimating whole sky spectral radiance and results are detailed in [Section 3](#). Our work integrated spectral energy into a radiosity engine and plugin is presented in [Section 4](#). And our sky and occupant aware adaptive facade cyber-physical prototype is presented in [Section 5](#). Finally we present our conclusions and suggest future work in [Section 6](#). Appendices of our spectral sky data visualization tool (*Spectral Sky Viewer*), supplementary spectral sky predictions, and supplementary daylight analysis are provided as [Appendix A](#), [B](#), and [C](#), respectively. Published works by the author of this dissertation are listed in [Appendix E](#), and any content from these works has been used with permission ([Appendix D](#)).

CHAPTER 2: BACKGROUND AND RELATED WORK

The research presented in this dissertation deals with the prediction and simulation of directional spectral solar energy on the exterior and interior surfaces of buildings. This energy can be avoided or harvested by buildings to reduce energy consumption and improve occupant comfort and well-being. Therefore, some knowledge of atmospheric sky models and building performance simulation is recommended. This background chapter serves to quickly bring the reader up to speed and is divided into two primary sections. [Section 2.1](#) explains the most relevant solar radiation theory, remote sensing radiometry, atmospheric scattering, radiance versus irradiance, and the current state of atmospheric sky models. [Section 2.2](#) provides background on building performance simulation (BPS), building energy modeling (BEM), “daylighting” (the active harnessing of daylight), and the monitoring, control and automation of such efforts by building control systems (BCS).

2.1 Sun and Sky Solar Radiation

Sunlight and skylight have been formally studied for well over two hundred years ([Young et al., 1819](#); [Strutt, 1871](#); [Mie, 1908](#)). Electromagnetic energy, black body radiation, and radiant flux have also been studied for quite some time ([Faraday, 1832](#); [Stefan, 1891](#); [Wien, 1894](#); [Boltzmann, 1898](#); [Planck, 1901](#)). Within the last century, we have refined our understanding of how sunlight becomes skylight and then collides with our planet. Note the terms radiation and energy are often used interchangeably. Electromagnetic radiation from our sun (solar energy / sunlight), traveling in a straight line from our sun to our planet, is denoted as extraterrestrial solar radiation before it enters our planet’s atmosphere, and terrestrial solar radiation thereafter. On a clear day, a large percentage of this terrestrial solar radiation passes directly through our planet’s atmosphere and is therefore referred to as direct solar (or beam) radiation. During this process, atmospheric conditions determine how much of this terrestrial solar radiation is absorbed, scattered and reflected

by atmospheric molecules, clouds, aerosols (particulates suspended in gasses), etc. to produce the attenuated solar energy we call indirect diffuse (or sky, or atmospheric) solar radiation (aka skylight). The exact amount of this direct solar energy (sunlight) that becomes indirect diffuse energy (skylight) varies based on atmospheric conditions, which can attenuate direct energy by as little as 10% on clear, dry days, to as much as 100% on completely overcast days (U.S. DoE EERE, 2013). The difference between direct and indirect solar radiation is shown in [Figure 2.3](#).

For the purposes of modeling and harnessing solar energy, it is important to note that a non-insignificant amount of this energy is also reflected from the ground before colliding with surfaces of interest; this is called albedo (or ground reflected) solar radiation. There are of course an infinitesimal amount of additional reflections that occur between surface objects before colliding with a surface of interest, but in most cases that energy is dwarfed by the main three contributions. We call the total sum of this direct beam, indirect diffuse, and albedo solar energy that reaches a surface of interest, global solar radiation (GSR) ([Iqbal, 1983](#)). The term "solar resource" refers to the amount of potential GSR that can be harnessed by humans or buildings of interest ([Stoffel et al., 2010](#)). All of these subsets of solar radiation can be measured over wavelengths of the electromagnetic spectrum and are thus often simply referred to as, spectral energy. [Figure 2.1](#) depicts the difference between extraterrestrial and terrestrial spectral energy after it has been attenuated by molecules in our atmosphere. [Figure 2.2](#) shows the energy that contributes to GSR on a surface of interest and [Equation 2.2](#) shows the actual calculation from EnergyPlus, the standard, validated energy modeling software from the United States Department of Energy ([Crawley et al., 2001](#)).

Spectrum of Solar Radiation (Earth)

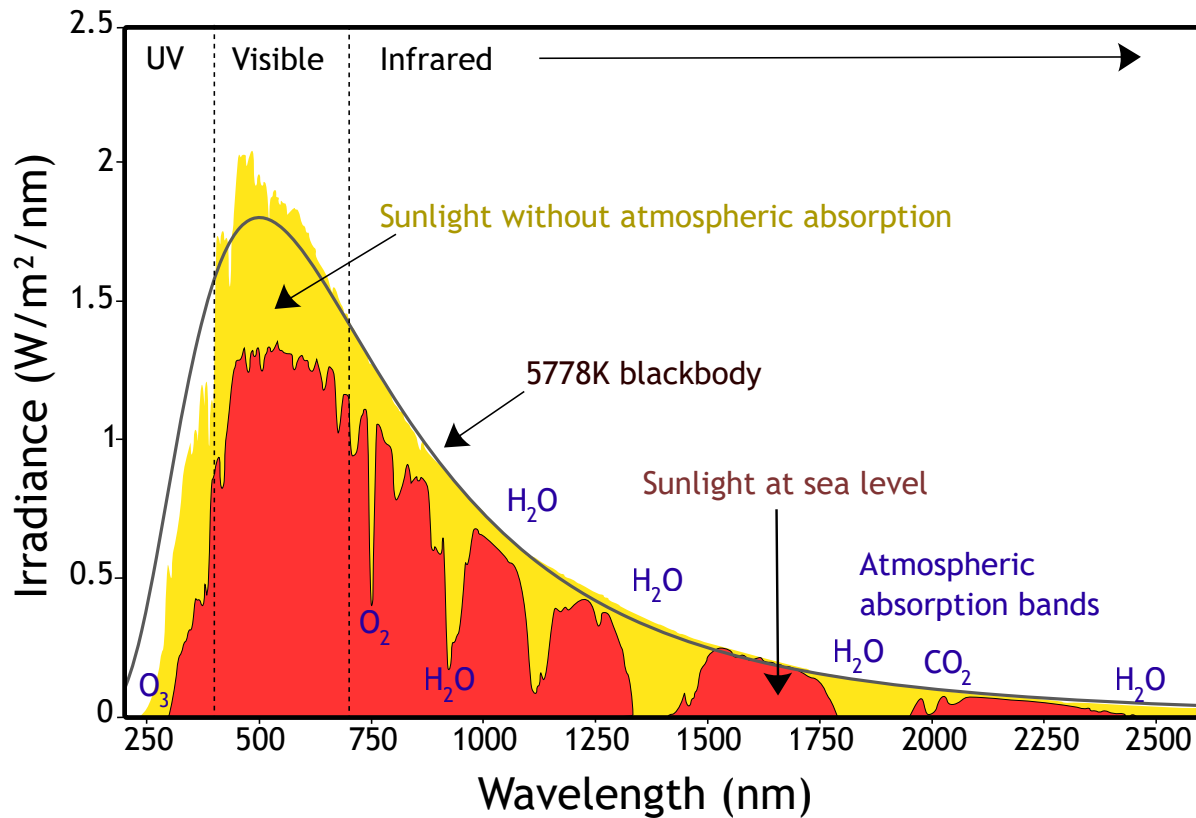


Figure 2.1: Extraterrestrial and terrestrial solar radiation plotted by [Anthony Beck \(2013\)](#) with data from the American Society for Testing and Materials (ASTM) Terrestrial Reference Spectra. This measurement includes direct and all indirect solar energy for a single sky. The red data is spectral energy of interest to building performance simulations. The H₂O and CO₂ labels indicate the molecular absorption of solar energy at the corresponding wavelengths. Note that these measurements are being replaced by work by [Gueymard \(2018\)](#).

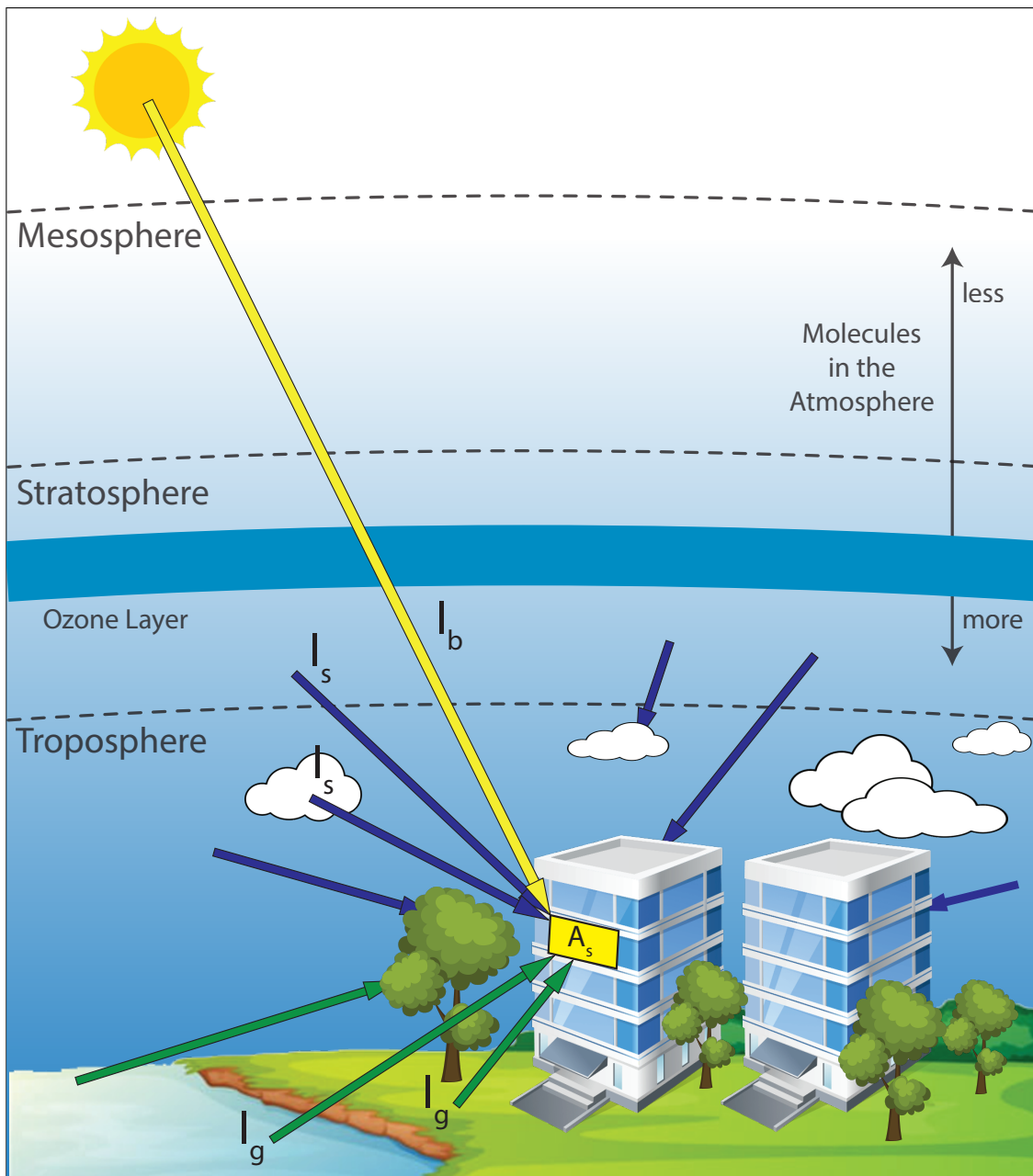


Figure 2.2: This figure depicts global solar radiation (GSR), which is the sum of direct (beam) radiation, indirect diffuse (sky) radiation, and reflected albedo (ground) radiation on a terrestrial surface of interest (A_s) Equation 2.2. Direct beam solar radiation (I_b) is shown in yellow, indirect sky (I_s) in blue, and ground reflected (I_g) in green. Note that energy can be absorbed, scattered, or occluded by molecules, clouds, trees, buildings, billboards, etc.

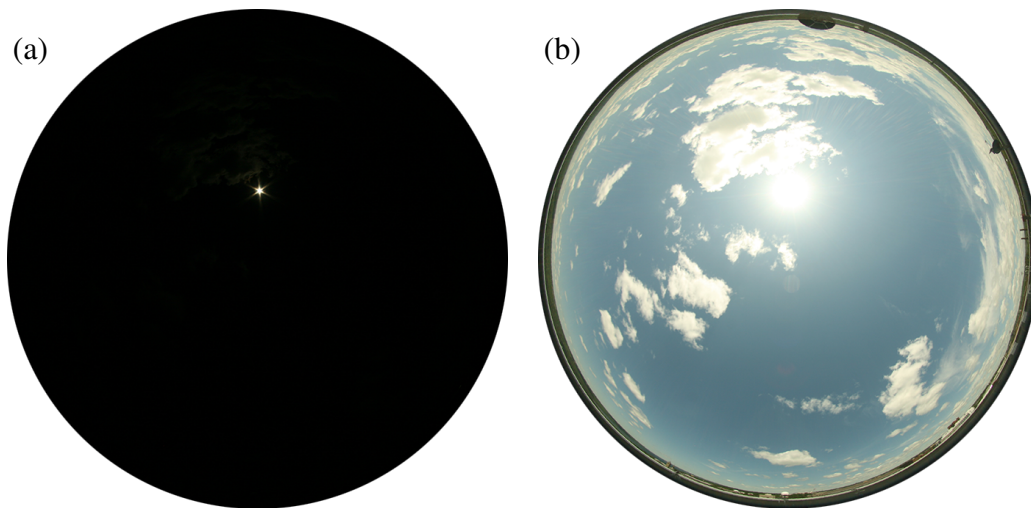


Figure 2.3: This figure shows what direct solar (beam) radiation looks like before (a) and after it has scattered about the atmosphere (b). These sky photos were captured with a commercially available digital camera with a fish-eye lens within just a few seconds of each other (Kider et al., 2014). (a) is a 1/15 second exposure and (b) is a 1 second exposure.

2.1.1 Radiance vs Irradiance

The study of light sources and their measurement is known as photometry and its scientific history begins in the 18th century alongside the invention and industry of wide area gas lighting. Experiments, treatises, essays, and formal scientific publications by Bouguer (1729), Lambert (1760), Dibdin (1889) and others led to the standardization of early lighting measurement techniques, equations, and units (Bertenshaw, 2020). With respect to sunlight, both direct and indirect terrestrial solar radiation are quantities of directional energy moving through atmospheric mediums (e.g. water vapor, oxygen, nitrogen oxides, carbon oxides, hydrocarbons, halocarbons, etc.) (Iqbal, 1983; Solomon et al., 1999; Kocifaj, 2009). This directional energy is called radiance (aka luminance, radiant energy, specific intensity). Once this energy reaches a surface of interest, indeed as all such directional energy quantities reach this same surface, the produced light on the surface is known as irradiance (aka illuminance, radiant incidence). As depicted in Figure 2.4, radiance is computed as the energy measured within a 3D conal angle (steradian) parallel to the direction

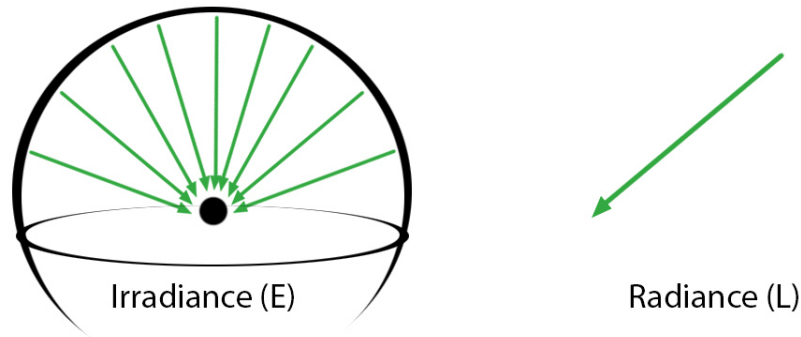


Figure 2.4: The solar energy quantities radiance and irradiance depicted by [Marasov \(2019\)](#). Radiance (L) is a directional quantity outgoing from some point to the surface of interest, while irradiance (E) is the summation of all such radiance quantities converging on a surface. Both can be scalar or spectral quantities.

of that energy, while irradiance is the sum of all such radiance vectors (covering all corresponding steradians) converging on some surface area of interest. Units can vary, and historically have corresponded to the amount of light given off by a “standard candle” (thus, candela), but today spectral radiance is typically measured in watts per meter squared per nanometer per steradian ($W/m^2/nm/sr$) and spectral irradiance as ($W/m^2/nm$). Therefore, irradiance on the surface of a building can be modeled as the integration of incident radiance vectors coming from all directions ([Pharr et al., 2016](#)). It is important to note that until recently, even accurate, single scalar irradiance computations in BES software were often considered inefficient and unusable due to the complexity of interior building geometry and the surrounding built environment of urban areas ([Kider et al., 2019](#); [Jones et al., 2012](#); [Schumann and Greenberg, 2012](#)).

The radiant transfer equation (RTE) below, originally formulated by [Chandrasekhar \(1960\)](#) and propagated by [Iqbal \(1983\)](#) among many others, is still in use today and models how radiant energy moves through a medium and is altered by three interactions: emission, absorption, and scattering. Solar radiation moves through the atmosphere and is either absorbed, scattered or ignored by different atmospheric molecules as well as particulate matter from dust, pollutants, forest fire ash, etc.

The RTE formula isolates these interactions and computes the expected change in radiant energy. For the purposes of solar radiation, emissive terms are purposely excluded as they do not apply.

Incoming spectral radiance $I_\lambda(\mathbf{x} \leftarrow \vec{\omega})$ arriving at point \mathbf{x} from the direction $\vec{\omega}$, is defined as:

$$I_\lambda(\mathbf{x} \leftarrow \vec{\omega}) = \overbrace{T(\mathbf{x}, \mathbf{x}_s) I_\lambda(\mathbf{x}_s \rightarrow \vec{\omega})}^{\text{reduced transmitted radiance}} + \overbrace{\int_0^s T(\mathbf{x}, \mathbf{x}_t) \sigma_s(\mathbf{x}_t) I_{i\lambda}(\mathbf{x}_t \rightarrow \vec{\omega}) dt}^{\text{accumulated in-scattered radiance}}, \quad (2.1)$$

where $T(\mathbf{x}, \mathbf{x}_s)$ is the transmittance between two points, \mathbf{x} and \mathbf{x}_s , σ_s represents the scattering coefficients, and emission is ignored. Equation 2.1 is used for both direct and indirect radiance propagation.

As previously mentioned, global solar radiation (GSR) is the total sum of direct (beam) radiation, indirect diffuse (sky / atmospheric) radiation, and reflected ground (albedo) radiation that eventually reaches a surface of interest. Traditional BES software, such as EnergyPlus, typically uses irradiance for the sake of efficiency. In this dissertation, however, we argue that radiance quantities should be made available and propagated as far down the pipeline as possible and then combined to compute irradiance when necessary. Ultimately, irradiance is a function of directional radiance, which can be occluded and scattered due to building geometry, surface materials, and large objects in the surrounding environment.

Incident solar gain is the total sum of energy absorbed by an exterior surface of interest. This calculation takes into account surface material properties and insulation. Here we show the computation of incident solar gain from EnergyPlus. It begins with the calculation of GSR. Note that the indirect diffuse sky intensity (I_s) can be supplied as either a radiance or irradiance quantity, and indeed is often still supplied as irradiance in most energy simulations today.

$$GSR = (I_b \cdot \cos \theta \cdot \frac{A_s}{A} + I_s \cdot F_{ss} + I_g \cdot F_{sg}), \quad (2.2)$$

where,

θ = the angle of incidence (based on sun location)

A_s = the sunlit area of the surface

A = the total area of the surface

I_b = the intensity of direct solar (beam) radiation

I_s = the intensity of indirect diffuse (sky) radiation

I_g = the intensity of albedo (ground) radiation

F_{ss} = the angle factor between surface normal and sky

F_{sg} = the angle factor between surface normal and ground ,

and the intensity values I_b and I_s are computed via [Equation 2.1](#). Along with I_g , these values can be radiance or irradiance quantities.

The incident solar radiation calculation is then coupled with building surface material properties to compute the absorbed solar energy, or gain on a building wall (depicted in [Figure 2.5](#)). First we compute the short wave radiant flux absorbed at the surface of the surface insulation QSM :

$$QSM = \alpha_{INS} \cdot GSR , \quad (2.3)$$

where α_{INS} is the solar absorption factor of the insulation. There are many types of insulation, and these vary per climate locale.

To compute the radiant flux at the surface of the wall, we need two components, the amount of energy transmitted through the insulation (TS), and the amount of energy aggregated / reflected

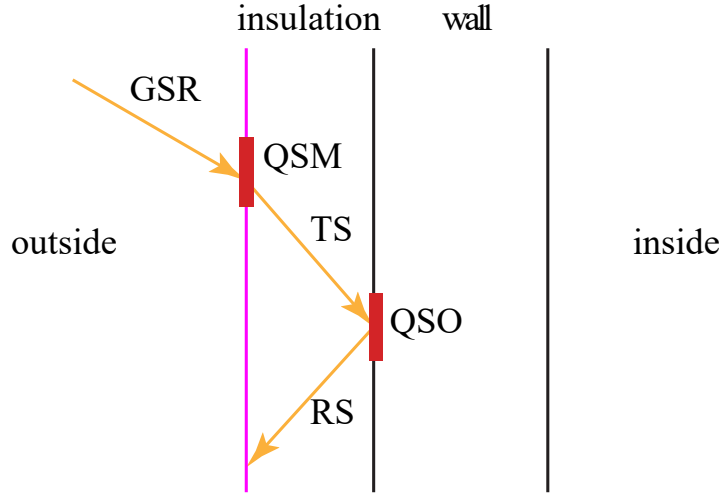


Figure 2.5: Incident solar gain on a building surface exterior wall, as defined by EnergyPlus (Crawley et al., 2001). GSR refers to global solar radiation reaching the surface of interest and is computed by Equation 2.2. TS and RS are the energy transmitted and reflected through the insulating material, respectively. QSM and QSO are the short wave radiant fluxes absorbed at the surface of the exterior wall insulation and wall itself, respectively.

within the insulation (RS):

$$TS = (\tau_{INS} \cdot GSR) \cdot (\alpha_{WALL}) , \quad (2.4)$$

$$RS = (\tau_{INS} \cdot GSR) \cdot (1 - \alpha_{WALL}) \cdot \alpha_{INS} \quad (2.5)$$

Thus, QSO is equal to:

$$\begin{aligned} QSO &= (\tau_{INS} \cdot GSR) \cdot \{ \alpha_{WALL} + (1 - \alpha_{WALL}) \cdot \alpha_{INS} \} \\ &= \left\{ \frac{\tau_{INS} \cdot QSM}{\alpha_{INS}} \right\} \cdot \{ \alpha_{WALL} + (1 - \alpha_{WALL}) \cdot \alpha_{INS} \} \\ &= (\tau_{INS} \cdot QSM) \cdot \{ \alpha_{WALL} + (1 - \alpha_{WALL}) \} \end{aligned} \quad (2.6)$$

where,

- Q_{SM} = short wave radiant flux absorbed at the surface of the INS
- Q_{SO} = short wave radiant flux absorbed at the surface of the WALL
- τ_{INS} = transmittance of INS
- τ_{WALL} = transmittance of WALL
- α_{INS} = absorbance of INS
- α_{WALL} = absorbance of WALL

Q_{SO} is therefore the incident solar gain, or amount of solar radiation that reaches the surface of an exterior wall of a building. This value should be computed per exterior surface of interest for accurate building energy simulations. In [Section 4](#) of this dissertation, we argue that these equations in EnergyPlus should be modified with spectral variants to allow for dynamic spectral filtering of UV and infrared energy based on various scenarios.

2.1.2 Sky Models

In order to compute with these aforementioned solar energy radiances and irradiances, hemispherical sky measurements or accurate predictions are needed. It is extremely difficult and expensive (both computationally and financially) to constantly measure solar and sky radiance coming in from every unoccluded direction and then computing the downstream irradiance on every surface of interest. Thus, throughout the past century, researchers of varying backgrounds have proffered atmospheric (sky) models to estimate this energy. Sky models typically fall into one of three categories: analytical, physically-based, and data-driven. Early work often simplified solar and sky models by simulating luminance distributions and salient color characteristics with simple analytical equations. Later, the atmospheric science and computer graphics communities proposed brute-force physically-based simulations of energy or light transport throughout the atmosphere using various techniques including ray-tracing, Monte Carlo stochastic sampling, and radiative transfer. More recently, researchers have attempted to model skylight with data-driven approaches that

measure, process, and quantify large sets of data and search for correlations and trends. Reviews of varying sky models have been compiled by [Badescu et al. \(2012\)](#); [Li et al. \(2014\)](#); [Bruneton \(2016\)](#); [Antonanzas-Torres et al. \(2019\)](#).

Analytical skylight models fit parametric functions to observations of the sky, such as work by [Pokrowski \(1929\)](#); [Steven and Unsworth \(1977\)](#); [Kittler \(1994\)](#). Such models were standardized by the International Commission on Illumination (CIE) to calculate the spatial distribution of skylight, and are based on measurements of luminance, indirect sky irradiance, and direct solar radiance. Early analytical approaches include the BRE average sky by [Littlefair \(1981\)](#), and the Intermediate Sky by [Nakamura et al. \(1985\)](#). One of the most popular analytical models is the all-weather model by [Perez et al. \(1993\)](#), which formulated a mathematical equation with five coefficients to model sky luminance. This model was extended by [Preetham et al. \(1999\)](#) to calculate sky color values by fitting equations to a brute-force physically-based simulation. [Hosek and Wilkie \(2012a\)](#) made several improvements including ground albedo, more realistic turbidity, and the handling of spectral components independently. Turbidity contributions also came from [Rosen \(1992\)](#); [Brunger and Hooper \(1993\)](#); [Igawa et al. \(2004\)](#); [Kocifaj and Kómar \(2016\)](#) and others. [Yao et al. \(2015\)](#) also improved the Perez all-sky model. Recent sky view radiance work has been done by [Ivanova and Gueymard \(2019\)](#). [Lee Jr \(2008\)](#) studied overcast skies to find meridional consistencies. [Cordero et al. \(2013\)](#) studied albedo effect on radiance distributions. CIE skies have been used in many building performance simulation pipelines. The more recent of these analytical models can be used to produce realistic looking graphics renderings of the sky and outdoor scenes, but often suffer from inaccuracies ([Zotti et al., 2007](#); [Kider et al., 2014](#); [Bruneton, 2016](#)). Such models were used to validate a branch of *RADIANCE* ([Subsection 2.2.1](#)) for building performance research and is known as *DaySim* ([Daysim, 2019](#)).

Physically-based sky models produce the highest quality results in terms of simulated energy and

downstream renderings. These models directly compute the transfer of solar radiation in the atmosphere through the radiative transfer equation (RTE) (2.1) (Chandrasekhar, 1960; Iqbal, 1983). They also directly calculate the composition of the atmosphere through Rayleigh and Mie scattering and polarization. The atmospheric research community developed programs such as 6SV (Vermote et al., 2006), SMARTS (Gueymard et al., 1995; Gueymard, 2019), MODTRAN (Berk et al., 2014), and SBDART (Ricchiuzzi et al., 1998), which seem to produce accurate predictions, but focus on irradiance rather than radiance throughout the sky dome and often require accurate atmospheric measurements which can increase computational cost and may be unavailable for standard commercial and residential buildings. As for real-time efficiency, SMARTS actually uses parameterizations instead of rigorous RTE to obtain diffuse irradiance values. libRadtran (Mayer and Kylling, 2005; Emde et al., 2016) seems to be one of the most comprehensive, configurable, and validated software packages used by researchers today. It offers a variety of well-known RTE solvers and configuration settings and can estimate direct and indirect radiance and irradiance energy to any wavelength and resolution of the electromagnetic spectrum. It can be configured with many parameters, including datetime, site location data, atmospheric measurements such as aerosol optical depth (AOD), regional and global climate data, etc. to enhance the accuracy of results (Hess et al., 1998; Holben et al., 1998). We use it to validate our own data driven approach discussed in Section 3. Advanced multi-scattering equations have been solved and demonstrated by Kocijaj (2009, 2012, 2015). The computer graphics community has also developed numerous Monte Carlo-based stochastic approaches (Nishita et al., 1993, 1996; Haber et al., 2005; Jarosz, 2008) to solve radiative transfer with the rendering equation (Kajiya, 1986). These methods produce pleasing visual renderings of skies and often approximate the complicated scattering calculations with phase substitutions by Henyey and Greenstein (1941) or Cornette and Shanks (1992).

Data-driven sky model approaches systematically gather measurements of the sky and then search for a relationship to model and simulate. This is motivated by the fact that modern atmospheric

measuring stations installed at labs around the world are powerful and accurate, but often expensive, slow, and not ubiquitous enough to provide the local atmospheric measurements needed for building performance simulations / solutions at arbitrary locations. For example, the sky scanning results of the new Mantis spectropolarimeter at the Navy Research Laboratory measures a limited range of 400 - 1000 nm for only 72° of the sky, takes 10 minutes to complete, and no publicly-available dataset was published (Foster et al., 2020). In Section 3 of this dissertation, we present a data-driven machine learning solution using regression models trained on the dataset captured by a custom sky scanning framework described in Kider et al. (2014) and depicted in Figure 3.1.

The closest work to our own is the work by Tohsing et al. (2014), who used 1143 separate machine learned regression models (one per color component (RGB) per wavelength of the visible spectrum (380-760 nm)) to estimate whole sky radiance. The authors used only 113 samples from a single clear sky day, with all skies being captured within a 12 day period. Whole sky scans took 12 minutes to complete and therefore a synthetic image was used for color sampling. Another older data-driven solution included high-dynamic range (HDR) imagery and image-based lighting to produce luminance values for the sky directly from captured photographs (Stumpf et al., 2004). Saito et al. (2016) improved upon the work of Sigernes et al. (2008) to estimate sky radiance specifically “without any training sets,” by using an equation of total ozone column and raw sky image RGB counts. They focused on the zenith of the sky (i.e. a single point in the sky) and estimated spectral radiance for a subset of visible wavelengths (430-680 nm). A notable contribution is the color matching functions, which took into account camera lens wavelength dependence, vignetting, and CMOS noise, and were used for cloud detection in Saito and Iwabuchi (2016). Artificial neural networks (ANN), genetic algorithms, and pseudoinverse linear regression models were used in various projects by López-Álvarez et al. (2008); Cazorla et al. (2008a,b) often using spot measurements or a custom sky scanner. Their models focused on visible spectra with a final dataset of only 40 samples. More recently, Priya and Iqbal (2015) and Satylmÿs et al. (2016) used

ANNs to model certain aspects of solar radiation. [Chauvin et al. \(2015\)](#) used a custom sky imaging framework for irradiance and cloud detection for the purposes of concentrating solar plant technology. A noted contribution was their observation of the importance of the circumsolar region (likely due to influence from [Gueymard \(2010\)](#)), which is in opposition of many sky models that seems to avoid it, and their use of the central angle between sun position and sky point of interest (denoted SPA). Their research was used for intrahour forecasting to improve solar resource acquisition ([Nou et al., 2018](#)).

Regardless of the sky model chosen, it is our intention that it provide spectral radiance predictions for the entire hemispherical sky so that vectors of spectral energy can be occluded and scattered properly during building daylighting and energy simulations. The interdisciplinary nature of this research between sky model research and building performance led to interesting insight:

“... in Figs. 19-21 you compare measured and modelled spectral radiances. Such comparisons are rare as most comparisons/validations of radiative transfer models have been done for irradiances. It is thus interesting to see that libRadtran captures most of the overall variability.”

Dr. Arve Kylling, co-author of libRadtran ([Mayer and Kylling, 2005](#)),
in email discussions on using libRadtran as input and validation for our research.

2.2 Building Performance Simulation

Building performance simulation (BPS) is an active area of research involving the modeling and simulation of buildings and their many possible performance evaluations, including: life cycle energy and water consumption and costs, daylighting ([Subsection 2.2.1](#)), occupant comfort, occupancy load and queuing, air flow, visual and thermal comfort, heating, ventilation and air conditioning (HVAC) loads and performance, hydronic loads (e.g. boilers, chillers), net-zero water reclamation, estimate carbon impact, evaluating equipment, building materials and designs, elevator scheduling, and many more. Most building simulations are unfortunately run only during retrofit projects or code compliance certifications, but BPS software can also be run during the early-phase design of buildings, well before the layout, materials and equipment have been finalized.

Building energy modeling (BEM) is the physically-based energy analysis of buildings. BEM software takes building information models (BIM) which describe building measurements, materials, lighting, HVAC, water heating and refrigeration, control systems, etc., along with occupant schedules and equipment use behaviors, climate and local site data, and they compute thermal loads, energy usage and costs, system impacts, condensation buildup, occupant comfort, etc. ([U.S. DoE EERE, 2016a](#)). There have been a handful of influential BEM software packages from as early as the 1970s, including the DOE, DOE-2, PowerDOE and eQUEST line by ([James J. Hirsch & Associates \(JH\), 1999](#)), BLAST, ESP-r and TRNSYS ([Beckman et al., 1994](#); [Beausoleil-Morrison et al., 2014](#)), and most notably, *EnergyPlus* ([Crawley et al., 2001](#)), the industry standard in the United States. *EnergyPlus* open-source (on GitHub) and promoted and funded by the US Department of Energy and the European Union. It has a long, rich history of development and is composed of various sub-engines and plugin modules provided other years by many contributors. Many other tools and frameworks work in concert with *EnergyPlus* to provide powerful building

performance modeling and simulation, some more accurate and stable than others (Figure 2.6). Some of these include the *EnergyPlus* wrapping software development kit (SDK), *OpenStudio* by U.S. DoE EERE (2016b), which makes it easier for other BPS software to integrate with *EnergyPlus*, Simergy, the *SUSTAIN* ecosystem by Greenberg et al. (2013), BEopt by Christensen et al. (2006) at the National Renewable Energy Laboratory (NREL), Insight360, etc. Ladybug and Honeybee by Roudsari et al. (2013) are also publicly-funded wrapping software (plugins) that enable integration with BEM software, such as DaySim (Daysim, 2019), a branch of RADIANCE (Ward, 1994) that was validated with daylight coefficients by Reinhart and Walkenhorst (2001). BEM software is actively and widely-used but is of course not perfect. Some of these tools have been developed independently in a vacuum without regular updates. For example, the DaySim repository hasn't been updated for over 3 years and has been used by the MIT Sustainable Design Lab more than by anyone else. Even the authors of *EnergyPlus* have declared that the BEM software packages with the most extensive validation and capabilities are all legacy products (Crawley et al., 2008). Finally, BEM software functions only as well as its inputs. Garbage in leads to garbage out, which can lull clients into accepting false analysis. It is important for a user of BEM and BPS software to fully understand and vouch for the inputs and configurations provided.

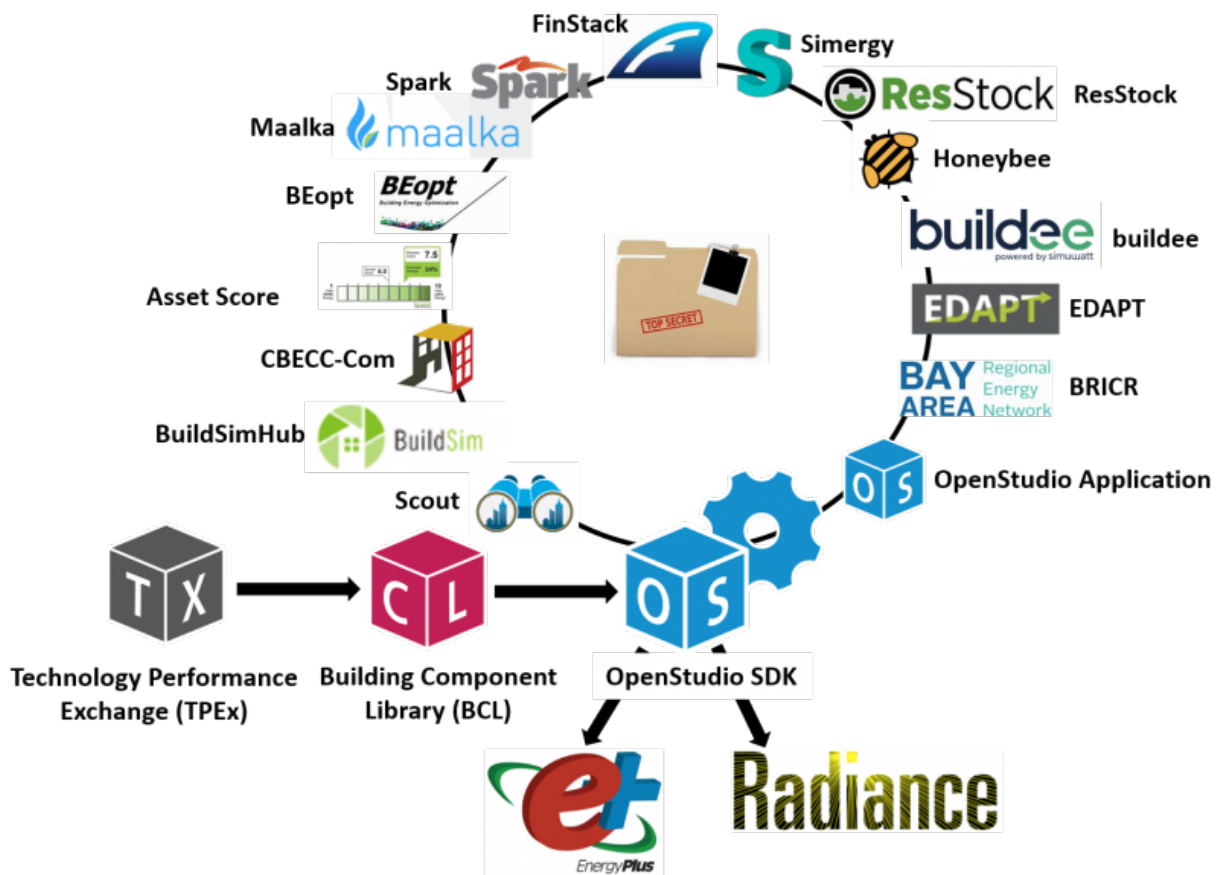


Figure 2.6: Notable building energy modeling (BEM) software packages acknowledged by the U.S. DoE EERE (2016a), some of which were used in this dissertation.

2.2.1 Daylighting

Daylighting is the passive or active harnessing of daylight in buildings to simultaneously reduce energy consumption and improve occupant quality of life. Some examples include additional and clerestory windows, skylights and tubes, light shelves, glass bricks, etc. ([Treado et al., 1984](#)). Prior to simulation, architects and engineers used protractors, a handful of sun locations for reference, and building window percentage to sketch crude predictions of where light patterns would fall. These days, daylighting simulations are increasingly becoming part of the early-phase design process of buildings and are used to provide all interested parties with visual and numeric analysis about natural light entering interior building spaces. Architects, builders, interior designers and building performance experts are educated about daylighting and its benefits. There is even a prestigious architecture award dedicated solely to daylighting ([Velux Foundations, 2019](#)).

During the day when weather allows, natural daylight is a free illuminate that can be utilized because it has been shown to:

- reduce energy spent on artificial lighting ([Ihm et al., 2009](#))
- reduce heating loads (for climates that need heat), especially if short-wave and long-wave infrared is harvested ([Bainbridge and Haggard, 2011](#))
- reduce distracting sounds (e.g. buzzing) from artificial lighting bulbs and ballasts
- reduce costs, manufacture and waste associated with light bulbs
- reduce time spent operating, adjusting, controlling artificial lighting
- improve physical and mental health ([Potočnik et al., 2019](#); [Ulrich, 1979](#))
- promote circadian rhythms ([Konis, 2019](#); [Rea et al., 2002](#))

- lead to more interesting building architecture, facades, fenestration, and materials (Baker et al., 2013)

There is a wealth of research about the benefits of harnessing daylight in general (Tzempelikos and Athienitis, 2007; Olbina and Hu, 2012; Kim and Todorovic, 2013; Favoino et al., 2014; Hoffmann et al., 2016; Reinhart and Davila, 2016), and a wealth of physiological and human factors research that seems to indicate that daylight and natural landscapes are beneficial to physical and mental health (Ulrich, 1979; Berman et al., 2008; Kaplan and Kaplan, 1989; Kaplan, 1995).

The simulation of daylighting has grown over the last few decades in large part because of the highly influential rendering software package known as *RADIANCE* by Ward (1994); Larson and Shakespeare (1998). *RADIANCE* has been (and still is) behind the scenes of major building designs, modeling and simulation tool-chains (Figure 2.7), and has been funded by the US Department of Energy since 1985 (and at one point the Swiss government). *RADIANCE* is a physically-based approach to rendering, provides luminance calculations, and supports the rendering of complicated internal geometry, fenestration, natural and artificial electric lighting, light bulb IES profiles, etc. (Larson and Shakespeare, 1998; Bourgeois et al., 2008; Saxena et al., 2010; Ward et al., 2011) It was later branched, modified and validated against daylighting coefficients from Perez et al. (1993) by the MIT Sustainable Design Lab group to provide better justification and daylight metrics for the illumination it provides (Reinhart and Walkenhorst, 2001; Daysim, 2019; Jakubiec and Reinhart, 2011).

RADIANCE provides relatively accurate illuminance renderings and analysis with a recursive ray-tracing algorithm that casts rays into the scene from the camera, takes into account surface material radiance scattering functions, and implements the standard rendering equation by Kajiya (1986).

Here is the core rendering equation of *RADIANCE* by Ward (1994):

$$L_r(\theta_r, \phi_r) = L_e(\theta_r, \phi_r) + \int_0^{2\pi} \int_0^\pi L_i(\theta_i, \phi_i) \rho_{bd}(\theta_i, \phi_i; \theta_r, \phi_r) |\cos \theta_i| \sin \theta_i d\theta_i d\phi_i \quad (2.7)$$

where all light rays are in (polar, azimuth) angles from surface normal, and reflected radiance L_r is equal to emitted radiance of the surface L_e plus the integration of all incoming radiance rays over the surface hemisphere. Each incoming incident radiance L_i is multiplied by the cosine of its angle with the normal of the surface and the bidirectional reflectance-transmittance distribution (BRTD) function of the surface material, ρ .

The efficient implementation of *RADIANCE* made it very feasible (and very popular) to use. Various optimizations include: hierarchical spatial partition of geometry, user directed pre-processing of additional light sources, pre-processing of light volumes, adaptive sampling of light sources, caching in various places, utilization of parallel processing for various algorithms, animation pre-optimizations, etc. The *RADIANCE* pipeline consists of over a 100 separate programs that perform various separate focused jobs, much like a UNIX operating system. One interesting historical aside is that *RADIANCE* was first created to model artificial electrical lighting specifically (not daylighting). Over the years, daylighting was integrated to support difficult-to-render scenes, such as atria, large windowed areas, complex fenestration, and combinations of natural and electric lighting. In [Subsection 3.2.4](#), we suggest integrating our *sradmap* tool into the *RADIANCE* pipeline.

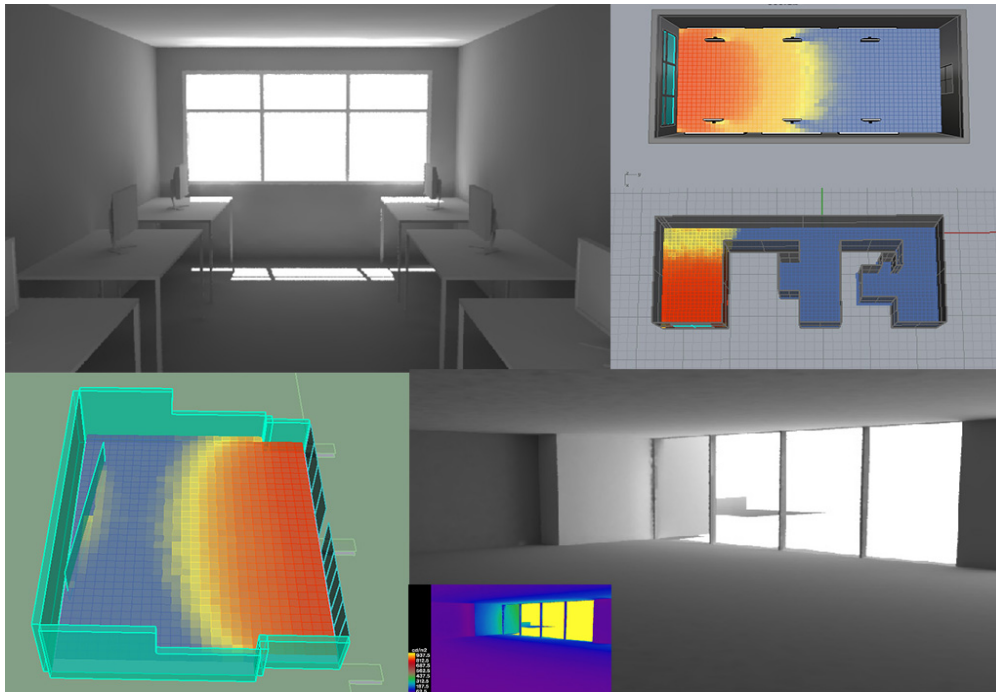


Figure 2.7: (Top) Examples of using *RADIANCE* (Ward, 1994) and *DaySim* (Reinhart and Walkenhorst, 2001) for daylight simulation. (Bottom) Building performance software packages that interface with *RADIANCE*, some of which were used in this dissertation (U.S. DoE EERE, 2014).

2.2.2 Building Automation Systems

Automation (control) systems for industrial and mechanical processes have been studied for roughly a century, though increasingly so in recent decades. The standard proportional–integral–derivative (PID) controller was developed in the 1920s and is still in use today. It is typically a single-input single-output feedback controller (think thermostat with temperature setpoint and single temperature sensor) and is widely used in a variety of industries (Bennett, 1993). More complex PID controllers do exist with nested feedback loops, in parallel or in series with one another, or even coupled with additional behaviors to handle multivariable problems, though such cases tend to be the exception rather than the rule. Some limitations with PID controllers include difficulty with non-linear references (moving setpoints), difficulty with slow or intermittent process updates, and their tendency to overshoot and oscillate until convergence.

Rule-based control (RBC) strategies have also been used in research and industry, are still in use today, and often heralded for their “simplicity” compared to more complex controllers, particularly in commercial building HVAC systems (Nesler, 1986; Schein et al., 2005; Salpakari and Lund, 2016; Hu et al., 2021). Rule-based strategies have also been adopted to mimic decision making experts (termed “expert systems”) (Feigenbaum et al., 1970; Shortliffe et al., 1975; Campbell et al., 2002; Liao, 2005; Thompson et al., 2015). RBC systems employ a software engine that processes rules manually written or generated by engineers in either a backward chaining or forward chaining (“production system”) processing method until completion. Somewhat alongside and intertwined with rule-based systems is fuzzy logic (Zadeh, 1973), a method for non-Boolean (many valued) logic reasoning intended to be used for “poorly-defined processes.”

Complex multi-variable dynamical systems are now often controlled with model-based predictive controllers (MPC or even “MPC controller”). MPC controllers, sometimes called dynamic matrix controllers (DMC), are continuous, iterative finite-horizon optimization programs that utilize

a model of a system to predict future behavior over some short time horizon in real-time and determine which control action(s) to take to meet desired reference target setpoints (Figure 2.8). The benefits of MPC mainly include: multi-input multi-output variables which allow for fast linear algebra solvers and account for complex relationships between variables, “look-ahead” / predictive behavior (similar to feedforward control), and constraints on inputs to prevent unrealistic input drivers (Rawlings, 2000; Qin and Badgwell, 2003; Rossiter, 2017). They are therefore sometimes referred to as “feedforward-feedback controllers with constraints.” MPC controllers derive from optimal control theory by Kalman et al. (1960); Kalman (1960) (particular their linear quadratic Gaussian (LQG) controller), culminating in two separate papers in the late 1970s by authors Richalet et al. (1978) (MPC) and Cutler and Ramaker (1980) (DMC). They have been used in research and industry across a myriad of fields, including building performance, all sorts of industrial plants, metallurgy, power generation and distribution, food processing, automated vehicles, aerospace, and even secure contracts with BitCoin. (Bruijn and Verbruggen, 1984; Harrold and Lush, 1988; Bemporad and Morari, 1999; Tzempelikos and Athienitis, 2007; Kennel et al., 2012; Camacho and Bordons, 2015; Gutjahr et al., 2016; Aste et al., 2017; Guo et al., 2018; Jahanbin and Haghghi, 2021). There is even research on optimizing MPC controllers themselves, particularly those employed by building HVAC systems (Ferreira et al., 2012; Kusiak et al., 2014; Asadi et al., 2014; Garnier et al., 2015; Huang et al., 2015; Zhao et al., 2015; Kim et al., 2016; Sturzenegger et al., 2015; Afram et al., 2017; Carrascal-Lekunberri et al., 2017).

Two drawbacks to real-time MPC controllers compared to more traditional PID and rule-based controllers, are their complexity and intensive computational load. A computer with a fast CPU and abundant RAM is often required to run the models (or sometimes entire simulations executed stochastically) and optimization functions being solved at each timestep. It is possible to run MPC controllers on embedded systems and micro-controllers, but real-time processing constraints often limit performance (Forgione et al., 2020). Despite these limitations, we believe the adaptive facade

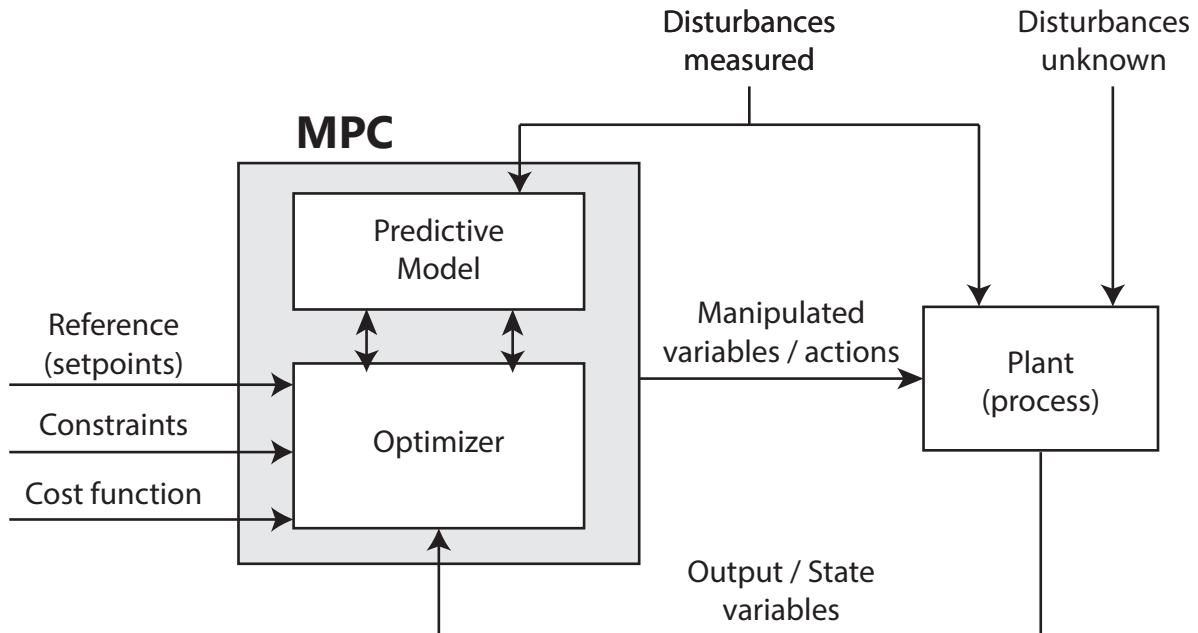


Figure 2.8: A high-level diagram of a typical model-based predictive controller (MPC).

cyber-physical building monitor prototype we propose in [Section 5](#) should utilize a MPC controller running on a performant PC, as the cost savings realized by daylighting and thermal improvements should outweigh the cost of a single high-end computer. Also, the timestep duration would likely be in the minutes as opposed to more demanding systems like automated vehicle systems which need to make decisions within millisecond windows.

Of additional interest to the work in this dissertation is the automated control of daylighting blinds. Although automation of artificial electrical lighting systems have been around for decades, [Reinhardt \(2004\)](#) and later the MIT Sustainability Lab were one of the first to publish on the topic of automating daylighting with blinds. Much downstream work has followed this line of research as well, including work by [Olbina and Hu \(2012\)](#), [van den Wymelenberg \(2012\)](#), [Mettanant and Chaiwiwatworakul \(2014\)](#), [Eltaweel and Su \(2017\)](#), and [Gunay et al. \(2017\)](#). And there is recent

research with building occupant comfort in mind, as well as occupancy schedules, behaviors, and preferences surrounding building automation systems in general, for example work by [Yan et al. \(2015\)](#), [Ahmadi-Karvigh et al. \(2017\)](#), [Stazi et al. \(2017\)](#), and [Sun and Hong \(2017\)](#). Note many of these methods do not detail their control systems so much as their models, which seem to be rule-based and/or probabilistic, and thus suggest a PID or rule-based controller.

2.3 Background Summary

In short, this dissertation focuses on building performance simulation (BPS) only as far as building energy modeling (BEM) and occupant comfort is concerned, and it does so by proposing changes to existing BPS and control pipelines in order to produce more accurate results that take into account radiant spectral energy. Use of a modern radiant energy predicting sky model is necessary to ensure BEM software accounts for occluded and cloud-refracted energy (radiance rather than irradiance), while spectral energy gives simulations and control systems a single “wide” input with both light and heat, which in turn allows for dynamic harnessing and filtering of both, provides for a simplified, unified daylighting and thermal modeling pipeline. In the following three chapters we detail our work on: (1) a data-driven radiant, spectral energy sky model, (2) a radiant, spectral energy bin simulator for early-phase building design, and (3) a cyber-physical prototype of an adaptive facade concept that considers radiant, spectral energy for visual and thermal comfort, season, time of day, and occupant overrides.

CHAPTER 3: WHOLE SKY SPECTRAL RADIANCE ESTIMATION

Much of the research in this chapter appears in the following publications:

- Del Rocco, J., Bourke, P. D., Patterson, C. B., and Kider, J. T. (2020). Real-time spectral radiance estimation of hemispherical clear skies with machine learned regression models. *Solar Energy*, 204:48–63. <https://doi.org/10.1016/j.solener.2020.04.006>
- Del Rocco, J., Patterson, C. B., Dhrif, H., and Kider, J. T. (2018). Learning and estimating whole sky visible, VNIR, SWIR radiance distributions from a commercial camera. In *Optics and Photonics for Information Processing XII*, volume 10751, page 107510F. SPIE. <https://doi.org/10.1117/12.2321295>

Full sky atmospheric spectral radiance distributions (UV, IR and visible spectra) are complicated to model and difficult or expensive to measure in real-time because spectral radiance is directional and must be calculated throughout the skydome at some resolution. This complexity often results in these distributions being simplified into a single downwelling irradiance measurement. Yet simulation accuracy is greatly affected by such directional measurements, so an optimal means of calculating these distributions is needed for real-time applications of building performance (Hensen and Lamberts, 2012; Jakica, 2017), environmental science (López-Álvarez et al., 2008), PV alignment (Smith et al., 2016), and physically based rendering (Nimier-David et al., 2019; Hosek and Wilkie, 2012a; Satylmÿs et al., 2016).

Here we present our data-driven, machine learning approach to estimate spectral radiance for any point in a clear sky to within acceptable tolerances for simulations and real-time controls. The primary contribution of our research is the reconstruction of high-dimensional atmospheric spec-

tral radiance for the entire sky, including non-visible spectra, UV and near IR, given only a low-dimensional RGB photograph of the sky and its capture time. The overall process is depicted in [Figure 3.1](#) and we give an overview here. Step I: prior to our work, multiple skies were measured over an entire year with a digital camera and spectroradiometer measurements at discrete points in the sky ([Figure 3.2](#)) ([Kider et al., 2014](#)). Step II: we then took this resulting data (used for various research projects) and cleaned, correlated, visualized and exported known good quality measurements to be used for training our sky models. Step III: exploratory data analysis, feature selection, and many machine learning models were investigated, resulting in 4 final models that could be used for experiments and eventually trained on capture date and time, look of sky, and corresponding spectral energy (350-1780 nm). The predictions by these models on holdout skies were then validated by our own measurements and later against libRadtran ([Emde et al., 2016](#)). Step IV: all 4 models (although only the best performing is needed) were used to predict spectral energy for every single pixel of 4 holdout test skies to produce spectral radiance “maps” (files of spectral radiance predictions per point in the sky).

Prior data-driven skylight models include work by [Tohsing et al. \(2014\)](#), [Saito et al. \(2016\)](#), and [López-Álvarez et al. \(2008\)](#); [Cazorla et al. \(2008a,b\)](#). Tohsing et. al leveraged ground-based sky radiance photographs and a non-linear regression model per wavelength to reconstruct the visible spectrum. Saito et. al used total ozone column readings, camera color matching functions, and a linear algebra approach. Cazorla et al. used neural networks, genetic algorithms, and regression models. Our proposed approach considers and estimates a much wider spectral range, and does so for the entire sky. In contrast to more traditional atmospheric science models, we purposely omit aerosol particulate and trace gas measurements to test viability of our method for real-time applications (e.g. commodity building monitoring systems, residential solar installations, rendering pipelines, etc.), which may not have access to such data to compute a physically-based approach. Also, we note that [Steven and Unsworth \(1977\)](#) found “*departures due to variation in atmospheric*

turbidity [...] to be small,” and that [Willers \(2013\)](#) states that “*aerosol attenuation in the atmosphere has a relatively weak spectral variation.*”

Note the work presented here focuses on clear skies specifically. Some prior work ([Del Rocco et al., 2018](#)), and ongoing work, include preliminary predictions of cloudy skies. Work by [Chauvin et al. \(2015\)](#); [Nou et al. \(2018\)](#) and others show that it is possible to separate clouds from clear skies and handle the areas separately when estimating radiance or irradiance. Four separate regression models are developed with a machine learning approach by feeding a combination of measured and engineered features from correlated sky imagery and spectral radiance. A series of experiments are performed to test model effectiveness and efficiency with regards to changes in exposure, sky sample color model, and spectrum resolution. A tool is developed using a model to predict spectral radiance distributions for the entire sky, at 1 nm resolution, to within 7.5% RMSD overall. Results are validated against libRadtran ([Emde et al., 2016](#)).

Throughout this work, hemispherical coordinates are used for both sun and sky samples, and are specified as (azimuth, altitude), where azimuth is an angle Eastward from North, and altitude is ($90^\circ - \text{zenith}$). Zenith is perpendicular to ground normal. Note that sky imagery is vertically flipped due to capture orientation [Figure 3.3](#).

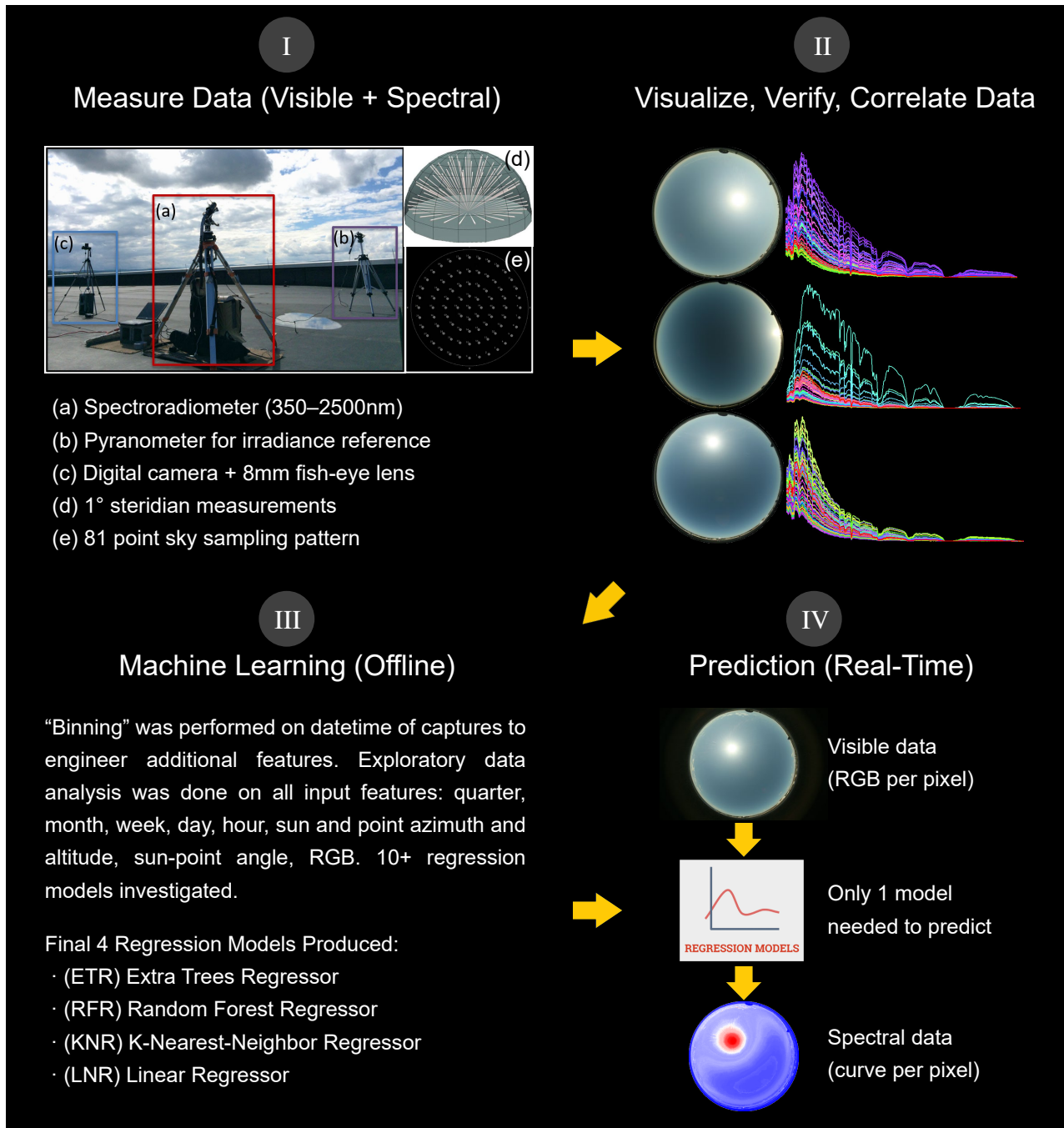


Figure 3.1: This figure serves as an overview of our whole sky spectral radiance estimation work. (I) sky data is measured by [Kider et al. \(2014\)](#); (II) sky data is curated, correlated, visualized, and exported via *Spectral Sky Viewer* ([Section A](#)); (III) EDA and machine learning methods applied to create models [Section 3](#); (IV) models are used to produce spectral radiance maps ([Figure 3.18](#)).

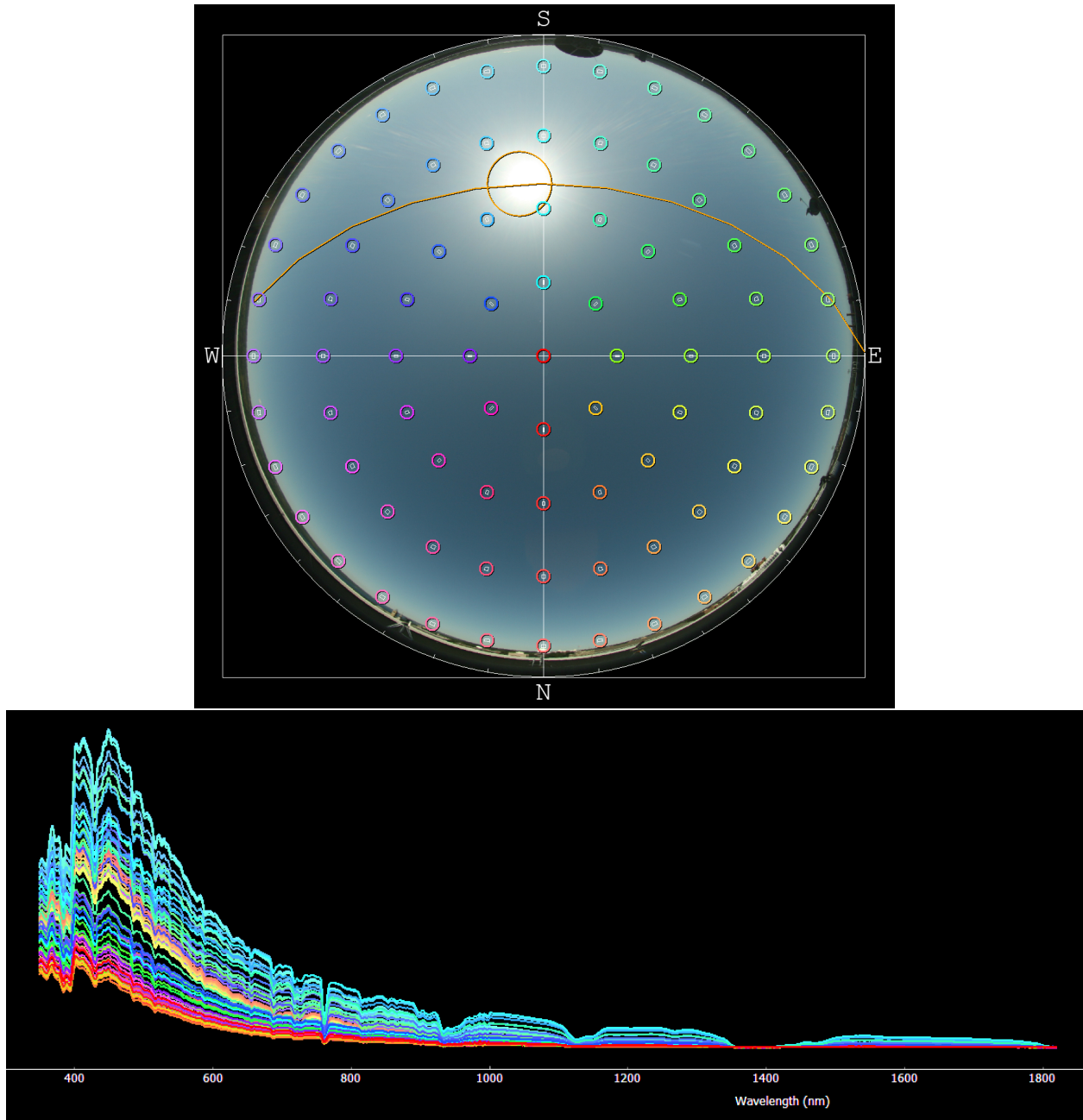


Figure 3.2: A single sky capture consisted of 8 photos (8 exposures to account for HDR) and 81 spectral radiance measurements between 350-2500 nm (350-1780 nm used in this work). This figure shows a single 1 s exposure of a sky along with the correlating spectral radiance measurements plotted in *Spectral Sky Viewer* (Section A). The colors here merely correlate radiance measurement with sky location. Sun location and path have been computed and overlaid (Reda and Andreas, 2004).

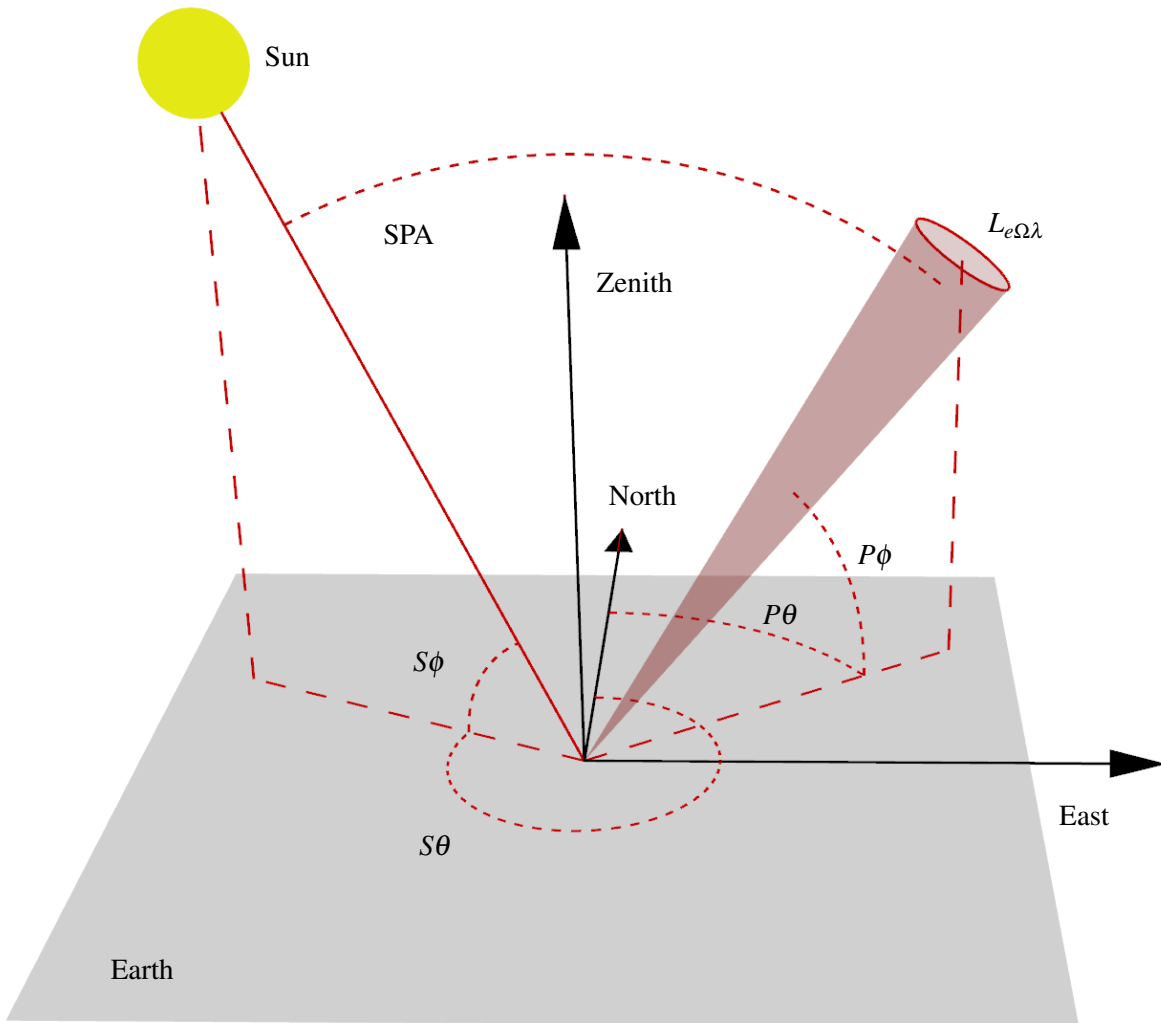


Figure 3.3: This figure depicts a typical radiometry coordinate system when measuring solar radiation from the ground. A single (direct or indirect) spectral radiance measurement ($L_{e\Omega\lambda}$) is measured at sky coordinates $(P\theta, P\phi)$ (azimuth, altitude). The sun is located at coordinates $(S\theta, S\phi)$, and the central angle between sun and sky point of interest is denoted as SPA (Chauvin et al., 2015). Zenith is perpendicular the ground normal.

3.1 Measurements and Data

Measurements in this work come from the sky scanner discussed in detail by [Kider et al. \(2014\)](#). This framework captured high-resolution HDR imagery of the sky (8 exposures), along with atmospheric spectral radiance distributions (350-2500 nm) from 81 sample points in concentric circle patterns across the sky ([Figure 3.2](#)). Measurements were taken from the ground. The spectral radiance distributions were measured in $W / m^2 / nm$ with an ASD FieldSpec Pro spectroradiometer through a 1° solid angle fore-optic ([Malthus and MacLellan, 2010](#)), and were validated against NASA data sets ([Kider et al., 2014](#)). The multiple exposure photographs of the sky were captured in both CR2 (raw) and JPG formats consecutively at 4368 x 2912 pixels with a commodity Canon 5D digital single-lens reflex (DSLR) full-frame camera, with Sigma 8 mm f/3.5 EX DG circular fisheye lens, and Kodak Wratten neutral density filter. JPG quality level was set to 100. We automated the process with libgphoto2, which took approximately 40 s to capture all exposures and formats of photographs of the sky. Irradiance was also measured, but is ignored for this work.

All measurements were taken at a single site location, (42.44344, -76.48163) decimal degrees, rooftop of Frank Rhodes Hall, Cornell University, Ithaca, New York, USA. 453 total captures were taken over 16 days between 2012-2013, covering all four seasons, dawn to dusk, and various sky covers. About 25% of those captures consisted of full clear skies (0 octas), from which 6006 individual clear sky samples were used for this work. Scattered and overcast skies were ignored for this work. A complete table listing of all usable captures is shown in [Table 3.1](#). The final curated dataset is available to the public through our lab website [SENSEable Design Lab \(2016\)](#).

3.1.1 Lens Linearity

Because our work involved mapping hemispherical sky coordinates to 2D pixel coordinates, and vice versa, it was important to accurately model the behavior of the fisheye lens employed. In

Table 3.1: List of observed sky data captures, which include correlated HDR imagery and spectral radiance distributions. There are 81 such radiance measurements per capture. A sky “sample” is a radiance measurement coupled with the color of the sky at that location.

Date	Time	Captures	Samples	Sky Cover(s)
11/06/2012	12:26 - 16:21	41	3321	SCT
11/15/2012	11:15 - 16:26	56	4536	CLR, SCT
04/13/2013	09:55 - 10:01	2	162	OVC
04/14/2013	10:42 - 18:36	46	3726	SCT, OVC
04/15/2013	07:38 - 08:03	8	648	SCT, OVC
05/12/2013	10:30 - 13:45	14	1134	SCT, OVC
05/26/2013	10:30 - 17:30	29	2349	CLR, SCT
05/27/2013	09:30 - 18:30	37	2997	CLR, SCT
05/30/2013	09:30 - 12:45	14	1134	SCT
05/31/2013	09:00 - 15:00	25	2025	SCT
06/15/2013	07:45 - 18:30	44	3564	CLR, SCT
07/26/2013	11:00 - 14:45	16	1296	CLR, SCT
07/29/2013	09:00 - 14:00	21	1701	SCT, OVC
08/30/2013	09:15 - 14:00	18	1458	SCT, OVC
09/24/2013	06:49 - 18:09	38	3078	CLR
09/26/2013	08:30 - 15:40	44	3564	SCT
16 Days		453	36693	

a perfect circular fisheye lens, often called a "tru-theta" lens, equal increments in radius on the fisheye image correspond to equal angle increments of the respective field rays. Actual fisheye lenses typically exhibit some form of non-linearity, even those lenses designed to be linear (Bourke, 2016). Although more important with variegated skies (scattered, overcast, etc.), a measurement difference of even a single degree can result in sampling pixels in or out of the sun’s corona. The standard ideal lens equation for mapping hemispherical sky coordinates to 2D center offset

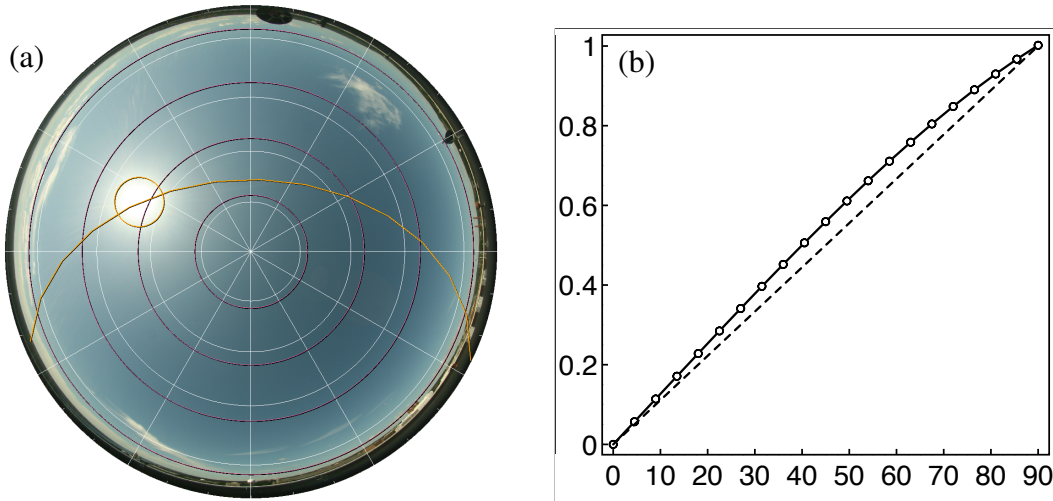


Figure 3.4: (a) shows the visual difference in linearity of actual lens (pink) vs ideal lens (white). Sun path and position after lens correction is overlaid (orange). (b) shows the actual lens sample points (solid) vs ideal (dashed), used to fit [Equation 3.2](#).

coordinates can be written as:

$$(x, y) = \frac{2 \cdot \text{zenith}}{\text{fisheyefov}} \cdot (\cos(\text{azimuth}), \sin(\text{azimuth})). \quad (3.1)$$

The following procedure measured the relationship between field angle and position in images:

1. A close and distant vertical feature in the fisheye image was chosen. The zero parallax position of the lens is the position along the lens axis where those features stay aligned despite rotations perpendicular to the lens axis.
2. A narrow object in the image was aligned as reference with the center of fisheye image.
3. The lens is rotated in 5° steps from 0 to 90° , and a photograph taken.
4. For each photograph, the distance of the reference point from the center was measured.

For our Sigma 8 mm f/3.5 fisheye lens, this resulted in the following non-linear curve (plotted in [Figure 3.4](#)), which was then used to alter zenith of sky coordinates ($r = \text{zenith}$):

$$r' = 0.7230r + 0.0252r^2 - 0.0499r^3 - 0.0004325r^4. \quad (3.2)$$

3.1.2 Sky Color

Color at a particular location in the sky is a fairly subjective measure. What our eyes detect, what instruments measure, and how that data is processed, differs dramatically. Nevertheless, our research investigates the relationship between sky color and energy distribution, and thus a metric must be used.

To obtain sky color at specific points in the sky, we projected the bounds of a 1° solid angle (same as fore-optic we used when measuring radiance) onto the 2D sky images captured with our digital camera (multiple images for the HDR experiment), and then sampled the pixels with a square convolution of similar width to the radius ([Figure 3.5](#)). In image processing, a convolution is an algorithm that involves sliding a matrix of weights or values (the kernel) over a set of pixels, and performing some calculation in order to produce a new set of pixels ([Parker, 2010](#)). Such convolutions are used to implement a wide variety of image filters like blurring, edge highlighting, etc. We used a Gaussian convolution, in particular, to blend the pixel colors together, weighting pixels closer to the center higher than pixels near the edges of the projected bounds. We are aware that a square convolution does not account for all pixels in a projected circular area exactly (in fact the projected circle becomes an increasingly oblong ellipse as altitude decreases). A rectangular convolution kernel would likely provide better coverage of the pixels in the projected bounds. Our kernel was chosen for real-time efficiency and overlap with existing image processing techniques and libraries, most of which use a square kernel. The weights of our Gaussian kernels were

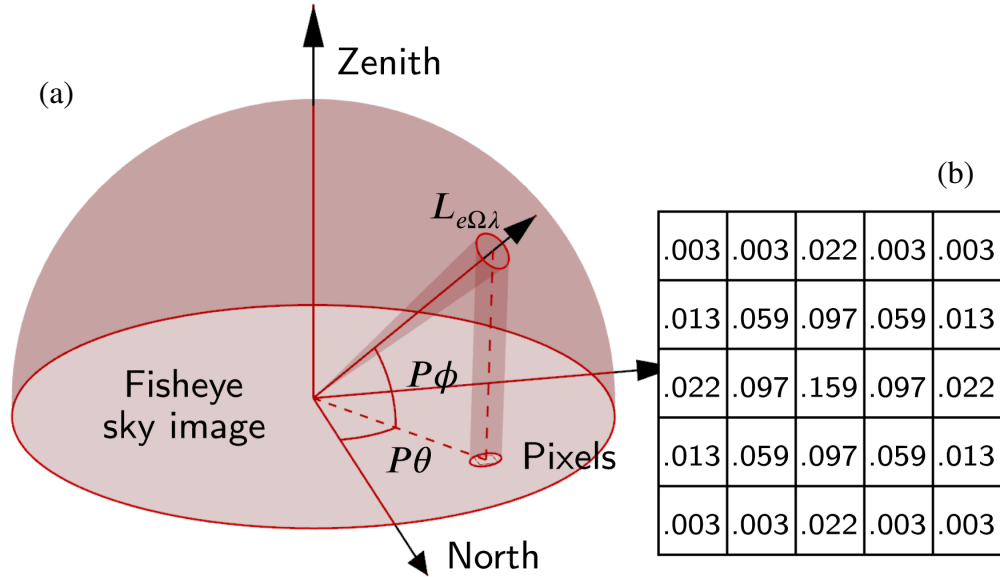


Figure 3.5: (a) illustrates a steridian capture area projected onto a sky image, the bounds of which contain the sky color pixels of interest. (b) shows the weights of a 5x5 Gaussian convolution matrix applied to the pixels in those bounds.

generated with the following equation (Fisher et al., 1996):

$$kernel(x, y) = \frac{1}{2\pi\sigma^2} \cdot e^{-\frac{x^2+y^2}{2\sigma^2}}, \quad (3.3)$$

with kernel dimensions relative to the bounds of the convolution, and a standard deviation (σ) of half the radius.

3.1.3 Raw vs. Digital Positive

As mentioned, we captured photographs in two formats, Canon CR2 (raw) and a traditional camera-processed compressed JPG format. Raw images contain much more capture information in a pre-interpolated format, before debayering, noise filtering, color space conversions, gamma correction, etc. In our previous work, we worked with the compressed JPG captures, which were smaller and faster to process (Del Rocco et al., 2018). For this work, we strove for accuracy of recorded color

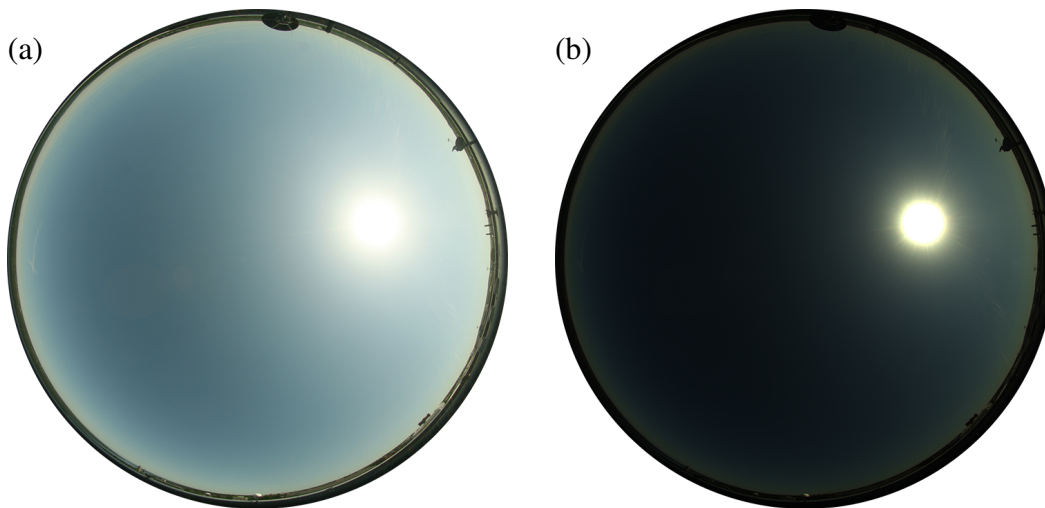


Figure 3.6: 05/27/2013 09:00 1s exposure of sky as a more traditional, camera processed, compressed JPG (a), and as a minimally processed, uncompressed TIFF (b). (a) is closer to what humans see when looking at the sky; (b) is a more accurate representation of what the sensor detects.

values and interpolated the raw photographs as uncompressed TIFFs, using camera white balance, but no other post-processing options that digital cameras use to produce images closer to what humans see (e.g. gamma correction, additive brightness, exposure shift, etc.). We used rawpy to read and process the raw images (Riechert, 2018; LibRaw, 2018). Figure 3.6 shows the difference. Our previous work already showed that it is possible to infer a relationship between look of sky and spectral radiance using compressed imagery. The consistency of raw photograph interpolation may be more crucial than the specific parameters used.

3.1.4 *Spectral Sky Viewer*

Measurements culled from our final datasets are due to careful examination of the data. We developed an open-source, cross-platform application called *Spectral Sky Viewer* to load, visualize, curate, and export our measurements (Figure 3.7). The application was written in Python with the use of modules PyQT, PIL, colormath, etc. Although it was developed on Windows 10, PyQT

is a cross-platform graphical user interface API, and no OS specific routines were used. Some functionality includes: ability to view NREL SPA computed sun location and hourly path, a rich exporter for constructing various datasets, EXIF image meta-data viewer, user-specified sampling patterns and lens linearity curves, and persistent system and user settings. Although using this tool to curate our data was a supervised process, it allowed us to navigate the abundance of data and identify dropped, locked, missing, occluded, and over-saturated measurements.

We also used *Spectral Sky Viewer* to separate clear, scattered, and overcast skies for various research projects. Although procedural assessment is certainly possible ([Yamashita et al., 2004](#); [Li et al., 2011](#); [Tohsing et al., 2014](#); [Saito and Iwabuchi, 2016](#)), we manually assessed our data to ensure accuracy. Efficient algorithms can and should be used to automatically assess sky cover during real-time application of this work. Like [Lee Jr \(2008\)](#), we used the standard categorization of sky conditions provided by the US National Oceanic and Atmospheric Administration (NOAA) ([Office Of The Federal Coordinator For Meteorological Services And Supporting Research, 2017](#)). We used the following three distinctions: clear (CLR), scattered (SCT), and overcast (OVC), where CLR and OVC represent 0 and 8 oktas of cloud cover, respectively. SCT was used to describe skies with any cloud coverage between 1-7 oktas. We ignored the distinction of few (FEW) and broken (BKN) skies. As mentioned, this research focused only on clear sky datasets. In theory, our models can be trained on skies of any condition, and in practice, both clear and cloudy models are often used in concert ([Xie et al., 2016](#)).

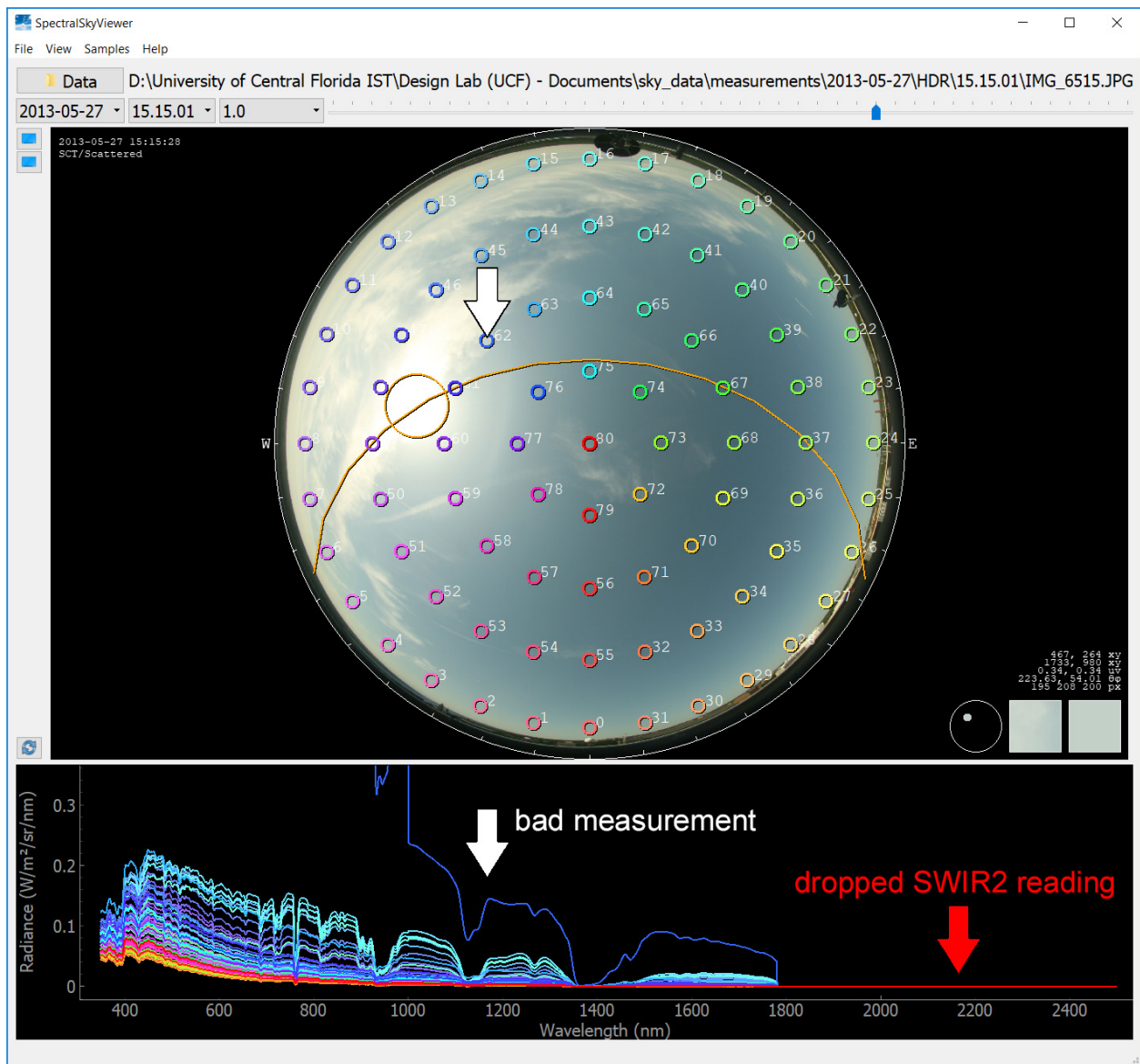


Figure 3.7: Capturing data in the wild is a challenging process. Inconsistent processes and environmental conditions often contribute to measuring error. And errors in data may vastly affect machine learning algorithms. *Spectral Sky Viewer* was written to help us visualize sky data and identify anomalies, including dropped, locked, missing, occluded, and over-saturated measurements. More screenshots and description of *Spectral Sky Viewer* can be found in [Section A](#).

3.2 Spectral Shape Estimation

The research question for this part of our work asks whether it is possible (or not) to estimate the atmospheric radiance distribution of a clear sky given only a picture of the sky and its capture timestamp. In other words, is there a relationship between the time of day, what a commodity camera sees in the sky, and its underlying spectral energy, despite the fact that we know solar radiation is absorbed and scattered by atmospheric particles at certain wavelengths? We used machine learning to help us search for such a relationship, but given the sheer magnitude of machine learning approaches (statistical models, artificial neural networks, support vector machines, etc.), we limited the scope of this research to regression models. Predicting a curve is more of a regression rather than a classification or clustering problem. More than 10 separate regression models were trained and tested, including: linear, Ridge ([Hoerl and Kennard, 1970](#)), Lasso ([Tibshirani, 1996](#)), ElasticNet ([Zou and Hastie, 2005](#)), Lars, KNN, RandomForest ([Kocev et al., 2013](#)), ExtraTrees ([Geurts et al., 2006](#)), etc. WEKA toolkit ([Hall et al., 2009](#)) was used to discover possible candidate models, but ultimately all machine learning models were configured and processed with scikit-learn in Python ([Pedregosa et al., 2011](#)).

Imperative to all machine learning algorithms is the quality and organization of training and testing data. Our data was distilled down to 6006 sky samples, each representing a single point in a clear sky along with corresponding spectral radiance measurement and capture timestamp. Our collection of sky samples was randomized and divided into an 80:20 train:test ratio. 10-fold cross-validation was used during training to dampen the effects of outliers ([Picard and Cook, 1984](#); [Kohavi et al., 1995](#)). The samples from four arbitrary skies, selected at random, served as absolute hold-outs ([Table 3.2](#)); i.e., no samples from these skies were ever used for training or preliminary testing. These techniques are often employed to help minimize overfitting through data leakage.

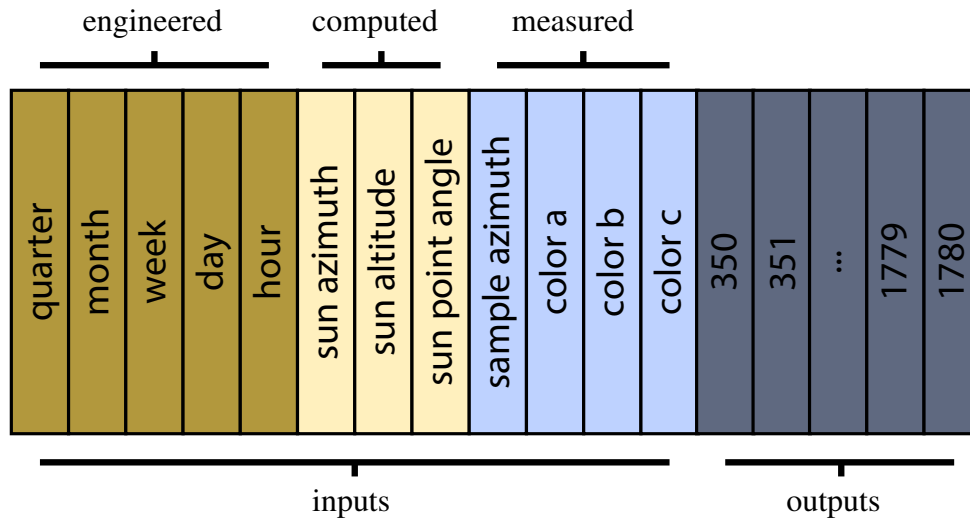


Figure 3.8: A single sky sample consists of 12 input features and 1430 output features (350-1780 nm radiance). Capture timestamp is binned for seasonal and daily variation. Sun coordinates are computed with NREL SPA. Sample azimuth and altitude are inherent to sky scanning logic yet insignificant according to EDA.

“Easily the most important factor [for success or failure of machine learning] is the features used.” (Domingos, 2012)

Each sky sample was engineered into an array of input and output features. Assuming a relationship between time of day, sky color, and radiance distribution, one of our goals was to discover the minimum set of features needed to show that relationship. From the raw measurements of capture timestamp, sample azimuth and altitude, sky color, and corresponding spectral radiance measurement, we engineered the additional features: sun azimuth and altitude, sun-point-angle (SPA), quarter, month, week, day and hour. The capture timestamp was “binned” into these discrete groupings to help the models internally correlate data throughout the year, as opposed to treating the timestamp as a single number or string (Macskassy and Hirsh, 2003). Sun position was computed with the solar position algorithm provided by NREL (Reda and Andreas, 2004).

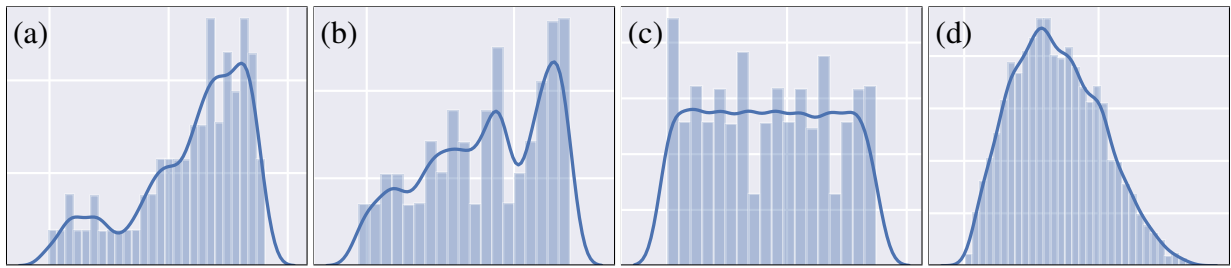


Figure 3.9: Histograms of input features: sun azimuth (a), sun altitude (b), sample azimuth (c), and SPA (d). (d) was much more significant than (c), likely because it combined the positions of both sun and sample points into a single feature.

SPA comes from the insights of [Chauvin et al. \(2015\)](#), in contrast to our initial approach of culling all samples within a 20° circumsolar region ([Del Rocco et al., 2018](#)), like authors [Saito et al. \(2016\)](#) and [Tohsing et al. \(2014\)](#). The final input and output features of each sky sample are shown in [Figure 3.8](#).

Various exploratory data analysis (EDA) techniques were employed to gauge the significance of each possible input feature, including: histograms, correlation matrix, feature importance, etc. ([Yu, 1977](#)). While sky colors were found to be the most significant features, sample azimuth was found to be the least. As [Figure 3.9](#) shows, 81 samples per capture evenly distributed across the sky resulted in a nearly flat distribution of sample azimuth values. The SPA feature was a combination of both sun and sample locations in a single feature, and was much more significant.

Preliminary results encouraged us to focus on the following regression models: linear regression (LNR) (provided only as a baseline), k-nearest-neighbors (KNN), random forest (RFR), and extra-trees (ETR). Although the performance of RFR and ETR are often comparable, in prior experiments we found that RFR performed significantly better on scattered cloudy skies ([Del Rocco et al., 2018](#)). RFR and ETR are ensemble (decision tree) regression models, which implement a set of “if-then-else” rules internally for both training and prediction. This is why the model file

sizes are so large. For all four of our models, tuning was done automatically with scikit-learn’s GridSearch algorithm, though some hyperparameters were tuned manually, including the number of trees and maximum tree depth of ensemble models.

Four separate error metrics were used to evaluate performance, including: coefficient of determination score (R^2), mean bias deviation (MBD), root mean squared deviation (RMSD), and ratio of measured and predicted radiance curves. MBD and RMSD come from [Iqbal \(1983\)](#). Prior authors used MBD for single wavelength results ([Tohsing et al., 2014](#); [Cazorla et al., 2008a](#)), but we found RMSD to be more appropriate for a spectrum of wavelengths. The R^2 metric from scikit-learn is calculated as follows:

$$R^2(t, p) = 1 - \frac{\sum_{i=1}^N (t_i - p_i)^2}{\sum_{i=1}^N (t_i - \bar{t})^2} , \quad (3.4)$$

where (t, p) is a (truth, prediction) pair, N is the number of radiance distributions, and $\bar{t} = \frac{1}{N} \sum_{i=1}^N t_i$. Note that this metric can be negative, despite the name R^2 .

Along with a useful tool for viewing and exporting correlated sky data with many options, we developed a framework of Python scripts to send datasets through our machine learning pipeline of training, testing and plotting. The main script takes parameters such as: model type, dataset of sky samples, pseudo-random number seed, number of cpu cores to use, cross-validation amount, and model specific hyperparameters like polynomial expansion, maximum tree depth, etc. All of our code is 100% cross-platform, open-source and freely available to the public through our lab website [SENSEable Design Lab \(2016\)](#).

3.2.1 High-Dynamic Range Imagery

Simultaneously capturing the sun and sky with photography is difficult due to the range of illumination and intensity of the sun vs. sky, as well as the temporal changes that occur. Our dataset

Table 3.2: The four holdout test skies selected at random and used for final evaluation. These skies were selected randomly with no prior knowledge about them, and were excluded from all training and testing until final evaluation of the machine learned models.

Date	Time	Part of Day	Season	Sky Cover
05/26/2013	15:15	Afternoon	Spring	CLR
05/27/2013	10:15	Morning	Spring	CLR
07/26/2013	13:15	Midday	Summer	CLR
09/24/2013	15:39	Afternoon	Fall	CLR

of sky imagery followed the capture approach proposed by [Stumpfel et al. \(2004\)](#). We took eight to nine photographs (depending on the time of day) to capture ~ 17 stops of dynamic range. [Figure 3.10](#) shows the difference in exposures captured. The top row (f/16 f-stop) accounts for the solar region and intensity of the sun. The bottom row (f/4 f-stop) captures the indirect skylight.

This experiment was designed to test the differences and effectiveness of using HDR imagery vs. a single exposure. For each sky sample’s color feature, we used the RGB color values from exposures 5-8 (f/4 f-stop) as input features for model training and prediction. Exposures 1-4 were ignored for this experiment. Although there are algorithms to merge multiple exposures into a single image for sampling, we simply sampled each exposure separately and used each sampled color as a separate input feature.

3.2.2 Color Model

Colors are qualia for combinations of electromagnetic energy within the range of wavelengths visible to humans (the visible spectrum). The human eye detects energy with the use of retinal rods and cones and the brain merges the results into what we call a color ([Kinney, 1958](#)). Modeling the values of these colors is a field of research in and of itself ([Koenderink, 2010](#)). And yet, we are attempting to estimate spectral radiance using color values as a primary feature. This begs

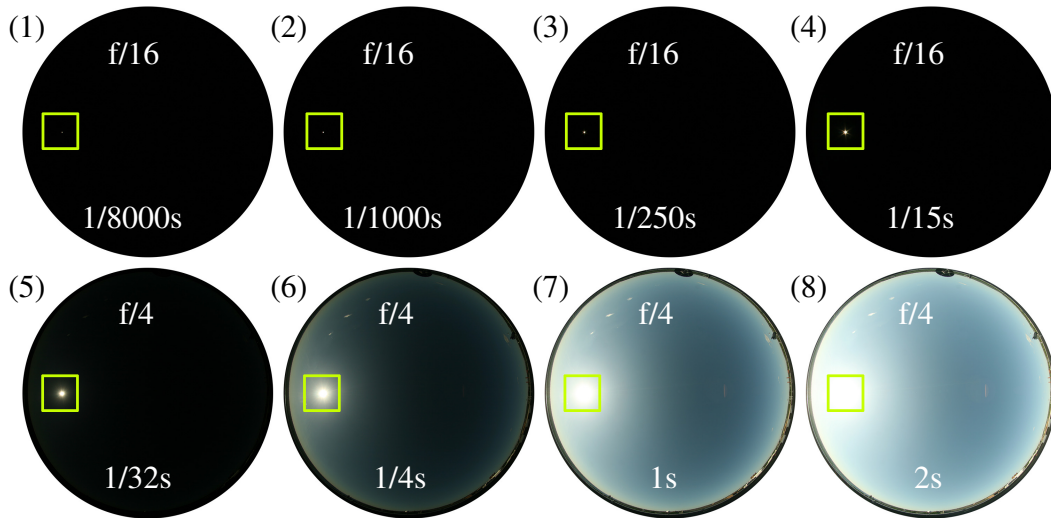


Figure 3.10: 8 exposures were taken to account for high dynamic range of sun + sky photography. F-stop $f/4$ captures (5-8) were used for this work, where as $f/16$ captures were used for prior work by [Kider et al. \(2014\)](#). The 1 s exposures (7) specifically were used for non-HDR experiments during this work. Yellow squares highlight sun location.

the research question: which color model best represents the underlying energy? Digital all-sky cameras typically store measurements with trichromatic RGB color models (e.g. sRGB, Adobe RGB, ProPhotoRGB, etc.), but do so mostly for historical reasons relating to technology. There are a variety of other tristimulus color models that attempt to capture more of the color space detectable by the average human ([Poynton, 1995](#); [Stone, 2015](#)), many of which derive from the CIE 1931 RGB and XYZ color space definitions ([Wright, 1929](#)). However, it is unclear which model is most beneficial for machine learning algorithms processing sky images.

For this experiment, we compared the overall training and predictive effectiveness of our models while only changing the color model used for each sky sample's color feature. Four separate color models were tested: sRGB ([Stokes et al., 1996](#)) (the default), HSV ([Smith, 1978](#)), HSL ([Joblove and Greenberg, 1978](#)), and LAB ([Robertson et al., 1977](#)). All other features were fixed. Because our commercial digital camera captured skies in an sRGB format, we then converted to the other

color models using algorithms provided by the Python colormath module. The resulting datasets were fed through our machine learning pipeline separately.

3.2.3 Spectral Resolution

This work is intended to be used in a real-time setting, both simulated and cyber-physical, therefore model size and processing speed is important. For applications that predict a general quantity of energy in certain parts of the spectrum, it may be reasonable to limit the resolution of spectral data used during model training and prediction. Certainly the visual difference and area under the curve (amount of energy) between a 1 nm and 10 nm resolution curve is not significant. A spectral resolution experiment was designed to find the smallest model and dataset that still predicted with acceptable accuracy, by training and testing models using spectral resolutions of 1, 5, 10, 15 and

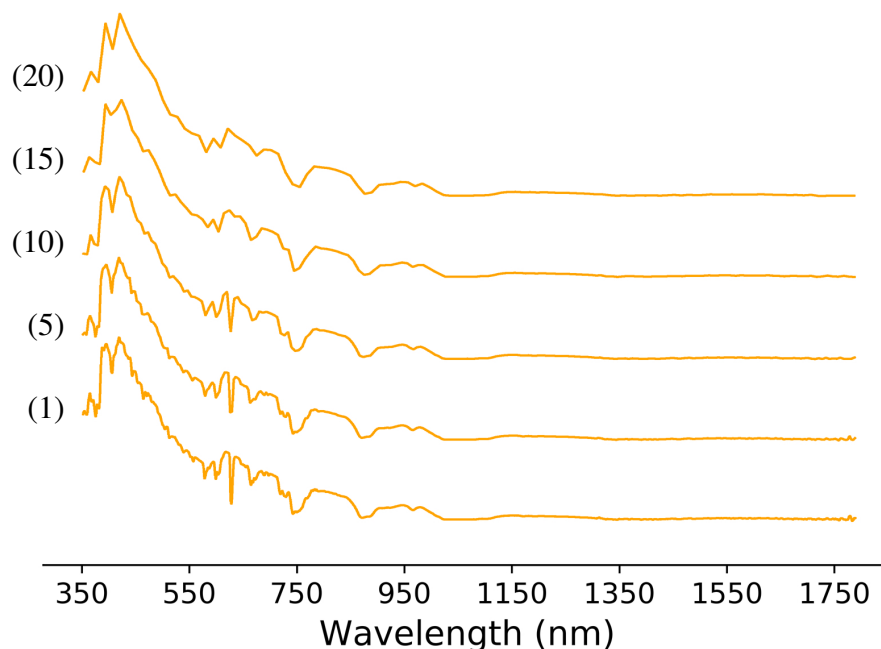


Figure 3.11: 05/26/2013 15:15 sample 24 (90° azimuth, 12.12° altitude) plotted at 5 different resolutions, 1, 5, 10, 15 and 20 nm, labeled accordingly. Note that the general shape of the spectral curve is retained even at lower resolutions.

20 nm. Note that some pure spectral colors exist entirely within a 15 nm range, and therefore resolution should not be diminished too much if color information is important. [Figure 3.11](#) shows the visual difference of the five resolutions for a single measured radiance distribution. Depending on the downstream application, there is still plenty of useful information at lower resolutions.

This experiment was run on a Dell XPS 8920 PC with Intel 4 Core i7-7700K 4.20 GHz CPU and 16 GB of RAM. The operating system was x64-bit Microsoft Windows 10 Enterprise. All manually executable applications (i.e. ignoring OS services) were closed at the time of the experiment. Five runs were executed per resolution size and the timings averaged.

3.2.4 sradmap

Ideally our models should be able to generalize across the space between the sky samples used for machine learning. The same input features shown in [Figure 3.8](#) can be collected for any pixel of a sky image, and then fed through our models to produce a lookup file (map) with spectral radiance predictions per pixel. We call the resulting file of this process a spectral radiance map (sradmap). Although the primary purpose is to provide spectral radiation predictions per pixel location, they can also be summed, normalized, and plotted against a false-color map to help visualize the predicted energy for the whole hemispherical sky.

The name sradmap is an homage to radmap by [Anselmo and Lauritano \(2003\)](#), a supplementary tool for the daylight simulator RADIANCE ([Ward, 1994](#)). In the building performance space, our sradmap generator can be integrated into daylight simulators, energy modelers, and parametric design tools like RADIANCE, EnergyPlus ([Crawley et al., 2001](#)), SUSTAIN ([Greenberg et al., 2013](#)), and Ladybug Tools ([Roudsari et al., 2013](#)). In the rendering space, sradmaps can be sampled from renderers like Mitsuba ([Nimier-David et al., 2019](#)) and Hyperion ([Burley et al., 2018](#)), for use in scenes with natural daylight.

3.3 Results

Three of the four final regression models (ETR, RFR, KNR) resulted in very high R^2 scores and acceptably low RMSD error on all holdout test skies listed in [Table 3.2](#). As expected, the baseline LNR model resulted in relatively poor predictions across all test skies, with an overall error of 14-24% RMSD. By contrast, ETR resulted in 4-7.5% RMSD. For test sky 07/26/2013 13:15, three of the four models predicted within 4% RMSD. In general, the tree-based models (ETR and RFR) perform better than the nearest-neighbor model (KNN). RMSD results for all models on each test sky are shown in [Figure 3.12](#).

[Figure 3.13](#) shows a comparison of all 81 measured and ETR predicted radiance distributions, their standard deviations, and overall averaged ratio between measured and predicted on test sky 05/27/2013 10:15. The standard deviations of measured and predicted are nearly identical, and the averaged ratio is nearly 1.0. Note the noisy error in the ratio graph resides within an H_2O and CO_2 absorption band, where atmospheric radiance is extremely small ([Lacis and Hansen, 1974](#)), and measurements are susceptible to noise.

For the same holdout test sky (05/27/2013 10:15), [Figure 3.14](#) shows ETR prediction error across the entire hemispherical sky, and highlights the two worst spectral radiance predictions (23.63% and 21% RMSD). Two other predictions selected at random are shown for comparison. A vast majority of the 81 samples are predicted to within 1% RMSD. Note that even with “high” error, predicted curves align with ground truth measurements in terms of shape. The models therefore have learned the wavelength relative intensities of the sky in accordance with capture time, sun location, etc. This is consistent with nearly all predicted results; while the magnitudes per wavelength sometimes deviate, the general shapes each predicted curve is accurate.

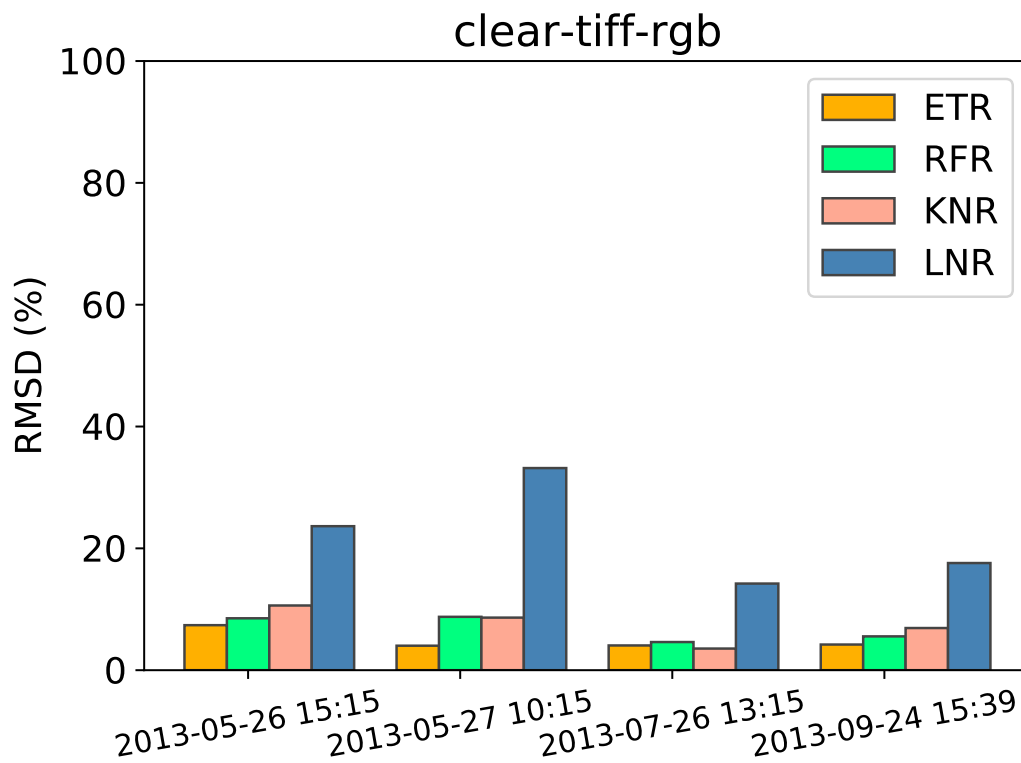


Figure 3.12: Model results on each of the four holdout test skies listed in Table 3.2. ETR performed the best, with an error of 4-7.5% RMSD. LNR was by far the worst performing.

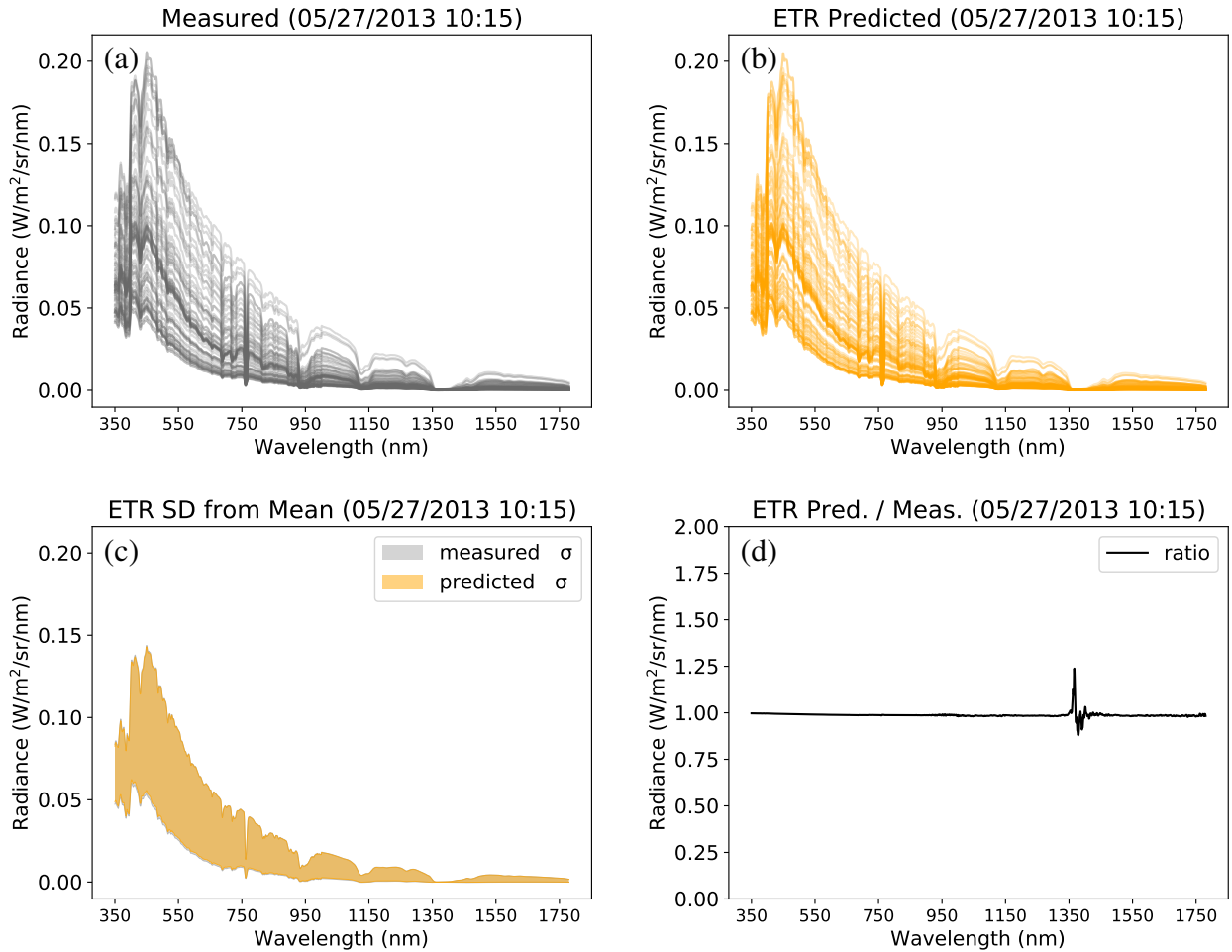


Figure 3.13: Whole sky results for holdout sky 05/27/2013 10:15 with ETR model; no ground truth sky samples from this capture were used for training. (a) and (b) show the measured and predicted spectral radiance distributions; (c) shows the standard deviation from mean for both measured and predicted distributions; and (d) is the overall ratio between the two. Note the error in the ratio is within the absorption band near 1350 nm, where radiance is extremely small.

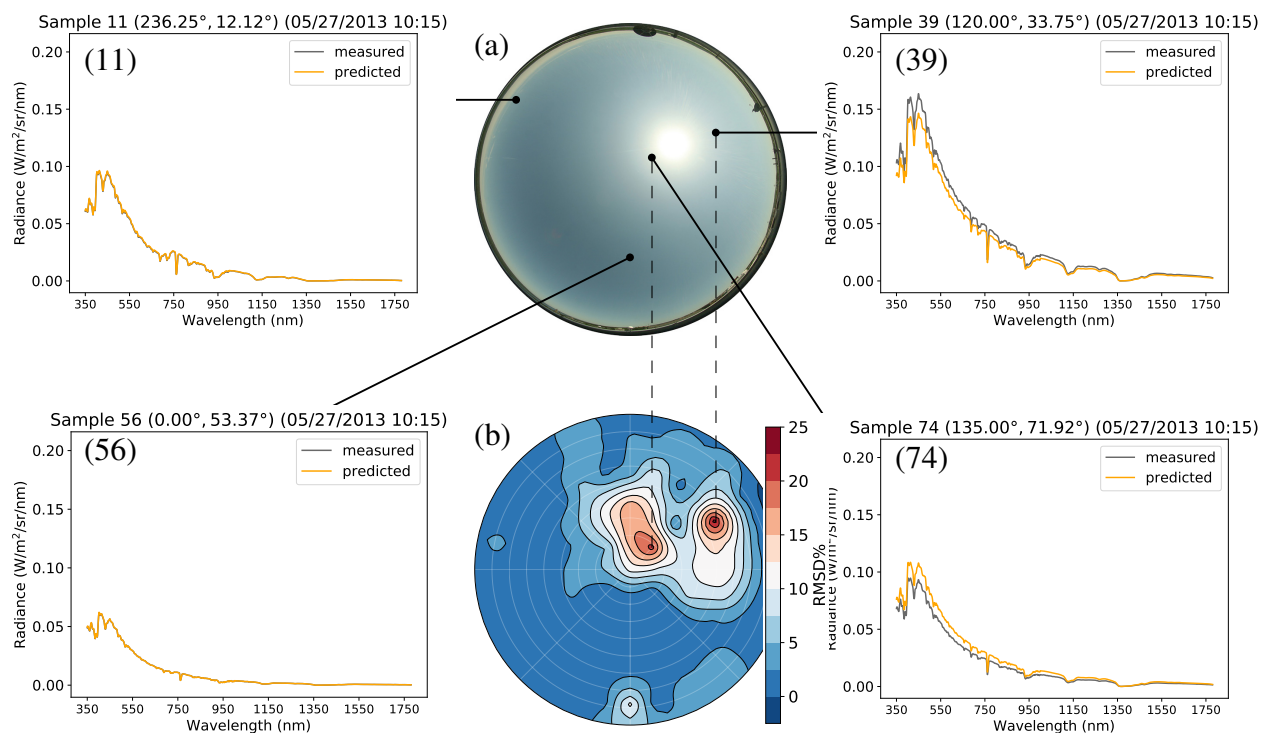


Figure 3.14: ETR results of four radiance predictions on holdout test sky 05/27/2013 10:15. (a) shows the camera processed JPG sky capture for convenience (the model was trained on TIFF data). (b) shows RMSD error across the entire sky. Radiance for samples (11), (56), (39) and (74) are pinpointed at their location in the sky. Samples (39) and (74) were the two worst predictions, with RMSD errors of 23.63% and 21% respectively.

Although we were expecting some insight from providing multiple exposures of sky images, results seem to indicate that HDR data, at least for clear skies, does not improve model prediction. All HDR runs resulted in similar error to non-HDR runs. This may be because clear sky color changes are so “uniform” throughout the day, that multiple exposures lack significance. In other words, all provided exposures may have had the same color change trends. We suspect that HDR data will be more significant in predicting scattered and overcast skies, as the color variations of clouds are less uniform across exposures.

Results of our color experiment (Figure 3.15) seem to indicate that color model is irrelevant to

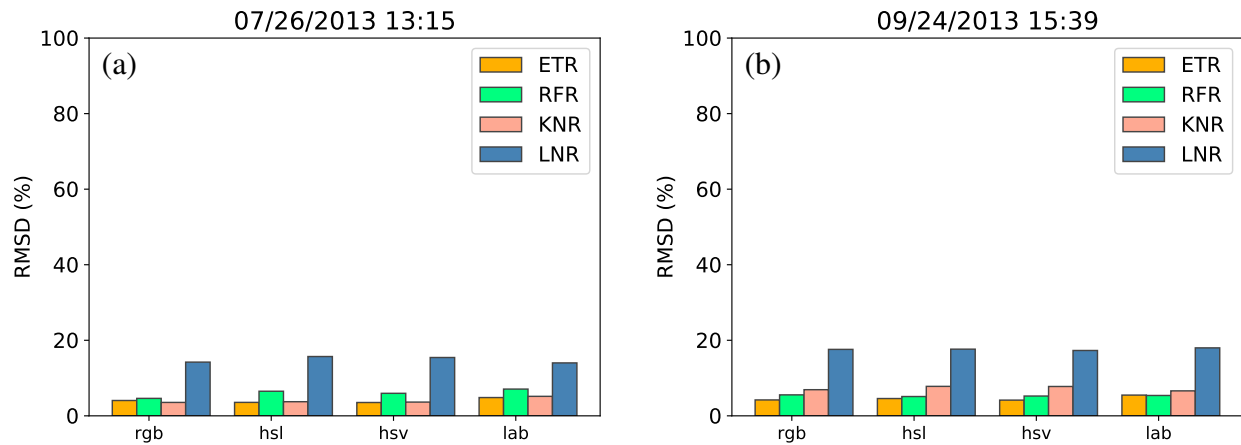


Figure 3.15: Sky sample color model made little to no difference in training and prediction results. (a) and (b) show RMSD results on 07/26/2013 13:15 and 09/24/2013 13:15 respectively.

our method. This implies that our method can be used with any representation of color, as the trends in color across the sky are similar regardless of format. It is unclear if using color data initially captured in an sRGB format somehow restricted the range of the other color models after conversion. In other words, would initially capturing the sky in a color model that maps to a larger color space be better?

The results of the spectral resolution experiment (Figure 3.16) show the benefits of decreasing spectral resolution from 1 to 5 nm. Not only does prediction accuracy improve, but model sizes (particularly the large ensemble models), as well as model training and prediction times, decrease significantly. The improvements in prediction accuracy are likely due to several factors: less noise in the spectral radiance distribution, and an overall simpler prediction problem (fewer outputs to predict). Dataset size also decreases with reduced resolution, but is eclipsed by the largest model sizes. Beyond 5 nm resolution, further reductions result in diminishing returns. This is an important find for real-time applications, which may operate on limited embedded hardware.

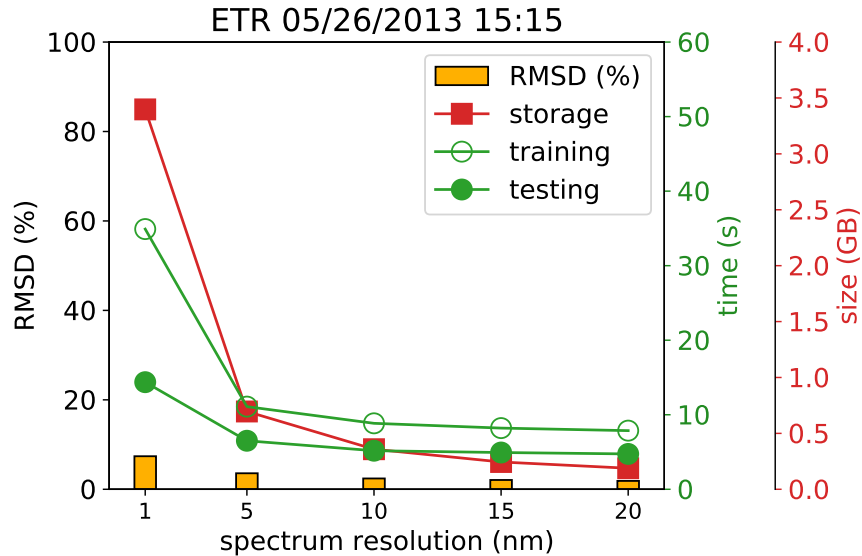


Figure 3.16: Limiting resolution to 5 nm drastically decreases model size, improves computation speed, and even increases prediction success, likely because the radiance curve is less noisy. Further reductions yield diminishing returns.

We note here that results between the minimally processed, uncompressed TIFF sky images and traditional, camera processed, compressed JPG sky images, were roughly the same. TIFF color data resulted in slightly better results ($\sim 1\%$) on some skies, though this may be within the standard deviation of prediction error and machine learning random fluctuation. Since the TIFF images (~ 35 MB) are at least 1000% larger than the JPG images (~ 2.5 MB) compressed with quality level 100, and the results are similar, we recommend the use of JPG images in real-time applications of our method.

Spectral radiance files (sradmaps) are the culminating output of our method. They are generated by extracting and engineering features per pixel of test skies (Table 3.2) and feeding them through one of our models. Linear scale false-color visualizations of ETR model predicted sradmaps are shown in Figure 3.18 and Figure 3.17. Test sky images were first scaled down to a resolution

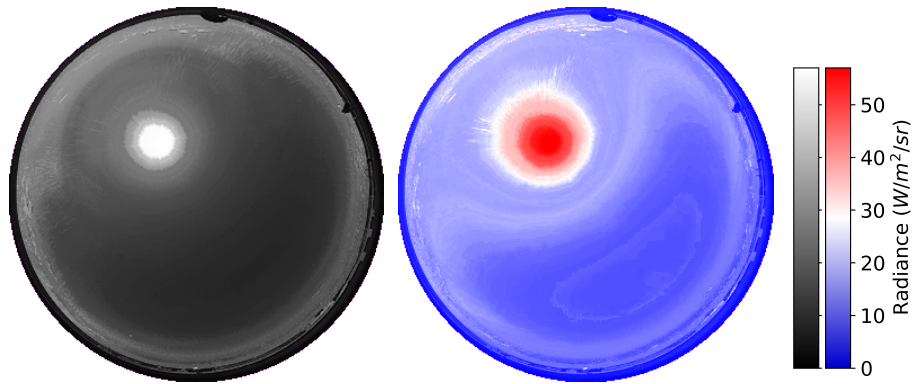


Figure 3.17: False-colored sradmap visualizations for holdout test sky 07/26/2013 13:15. Each pixel plotted is a summation of an entire spectral radiance distribution (350-1780 nm).

of 333x333 pixels, to anticipate real-time processing speeds. sradmap generation, visualization, and logged output took ~ 20 s to complete on the same machine specified in [Subsection 3.2.3](#); embedded hardware would likely take longer, though various optimizations can be made to the process. The sradmaps demonstrate that our models have the ability to generalize across the entire hemisphere (i.e. predict spectral radiance for every point in the sky) even when trained on a mere skeleton of samples (81 concentric 1° steradians). Note that most of the sky is unaccounted for by the skeleton, including points beyond the variance of sun and sky coordinates. sradmaps contain predictions for the entire sky.

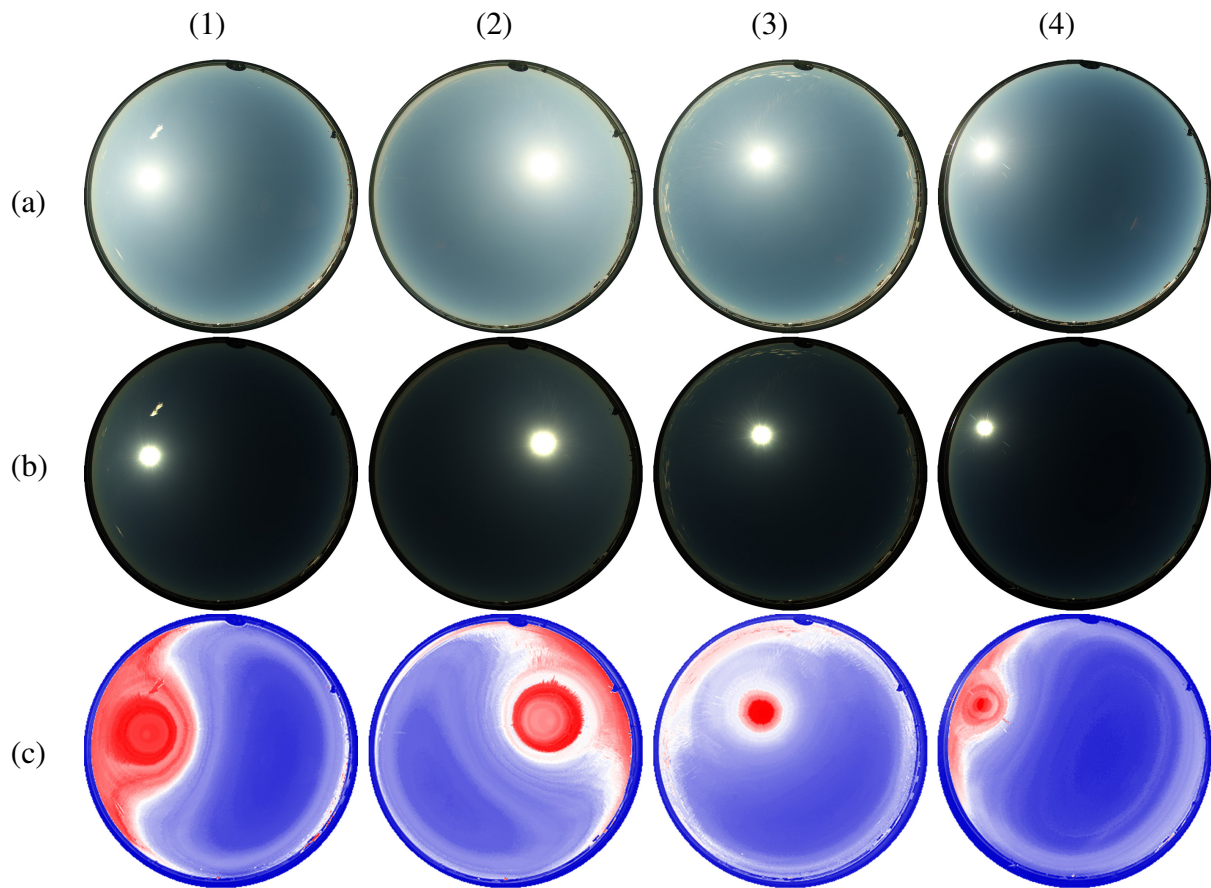


Figure 3.18: Columns (1-4) are the holdout test skies in [Table 3.2](#), in respective order. Rows (a) and (b) show traditional, camera processed JPG and minimally processed TIFF captures, respectively. Row (c) shows the sradmaps generated for skies in row (b); we predict spectral radiance (350-1780 nm) for each pixel of each image, sum the distribution, and visualize with false-color map.

3.4 Validation

Our results are validated 2 separate ways: (1) by holdout measurements unseen by our models, and (2) by libRadtran, a validated, atmospheric radiative transfer software package.

Our holdout test sky measurements (Table 3.2) were chosen at random and kept from training or preliminary testing of any model. Machine learning projects often use this method to validate a model's ability to generalize over unforeseen data. The results presented in Figure 3.12, Figure 3.13, and Figure 3.14 show the results of comparing predictions against these holdout measurements for the 81 sky samples per sky. The results of our additional experiments show that our method is robust against implementation details such as image compression, exposure, and color model.

Finally, we compare our ETR model predictions with ground truth measurements and the atmospheric spectral radiance distributions computed by libRadtran (Emde et al., 2016). libRadtran was configured the same for all four holdout test skies. In other words, no sky-specific data (atmospheric measurements, parameters, or ranges) were specified per test sky (Hess et al., 1998; Holben et al., 1998). For example, the O₂ band around 750 nm is represented in our results but not by the libRadtran predictions because we did not include the REPTRAN absorption parameters. Because of the framework we were using, only visible wavelength energy was available from libRadtran. Nevertheless, Figure 3.19 and Figure 3.20 show that visible spectral radiance from libRadtran for three of our four holdout test skies were in alignment with both ETR model predictions and ground truth measurements. However, for test sky 07/26/2013 13:15, libRadtran deviates from both ETR predictions and ground truth measurements (Figure 3.21). All tested samples for this sky show similar deviations in magnitude, but not curve shape. As mentioned, libRadtran requires accurate atmospheric data for its calculations. Because such data was not configured, and because our predictions are closer to ground truth measurements, it is possible that our ETR model learned the sky

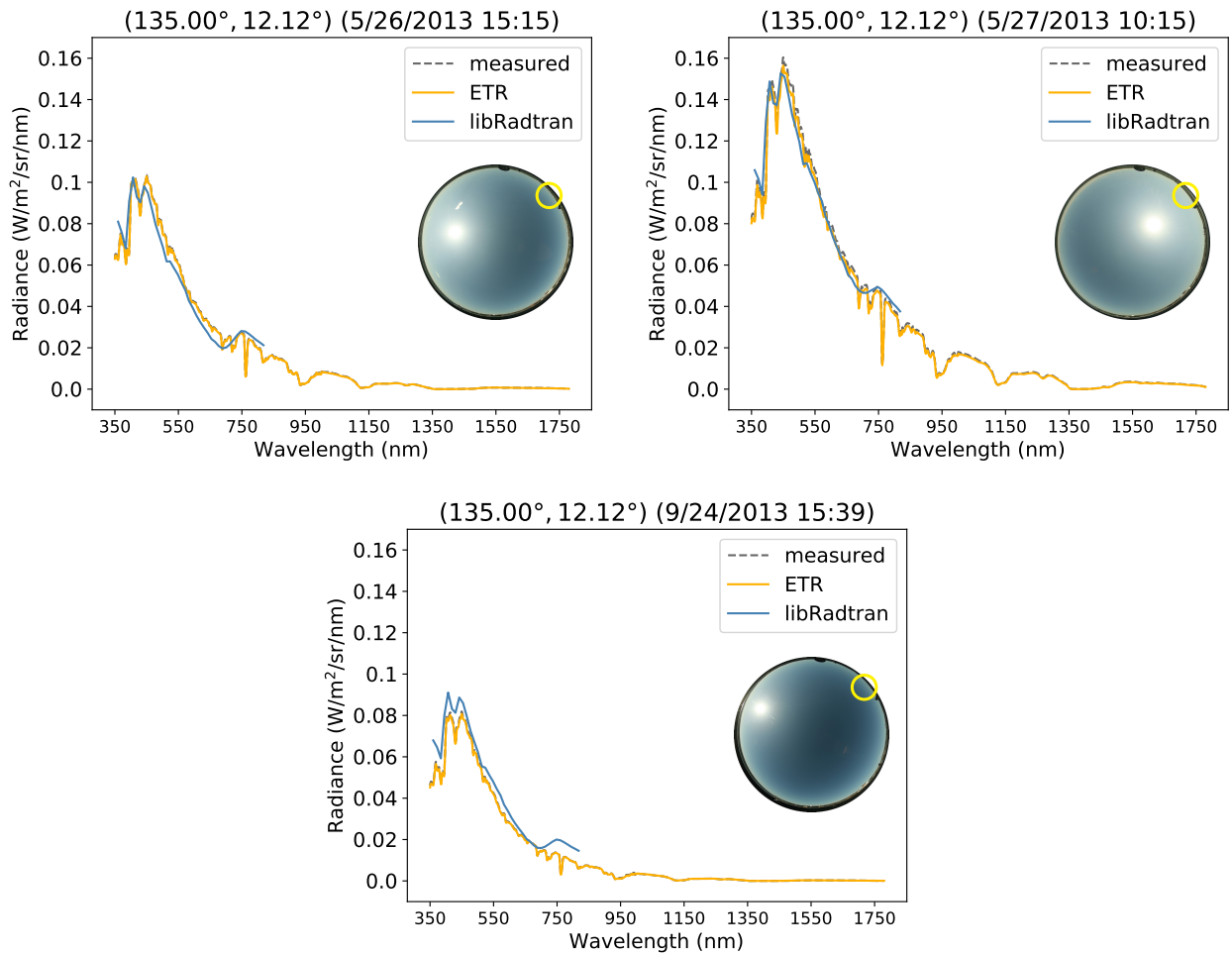


Figure 3.19: Spectral radiance at (33.75° azimuth, 12.12° altitude), circled, for two of the holdout test skies in Table 3.2. Spectroradiometer measurement, ETR model prediction, and libRadtran estimation plotted.

specific atmospheric conditions libRadtran needed in order to compute accurately. In particular, we note the high-level cirrus clouds along the horizon, which might indicate ice crystals in the atmosphere, and account for deviations between data-driven predictions and physically-based model calculations.

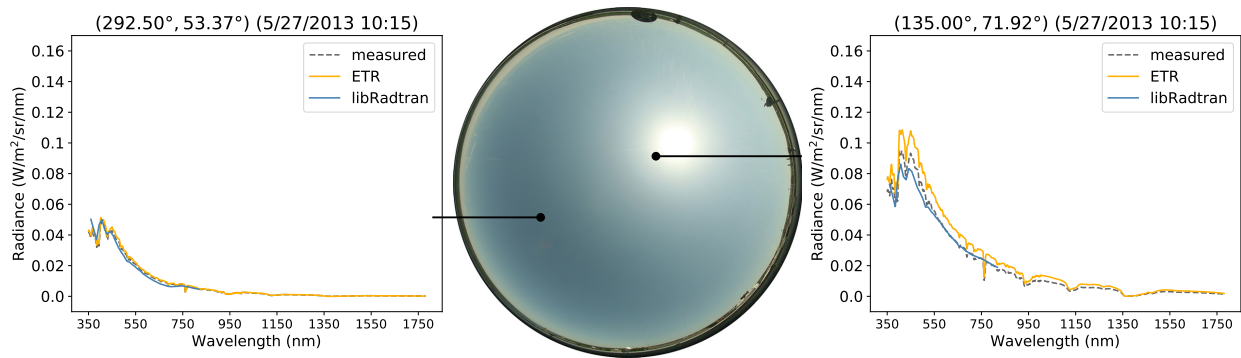


Figure 3.20: Spectral radiance for two sky samples of holdout test sky 05/27/2013 10:15. Spectroradiometer measurement, ETR model prediction, and libRadtran estimation plotted.

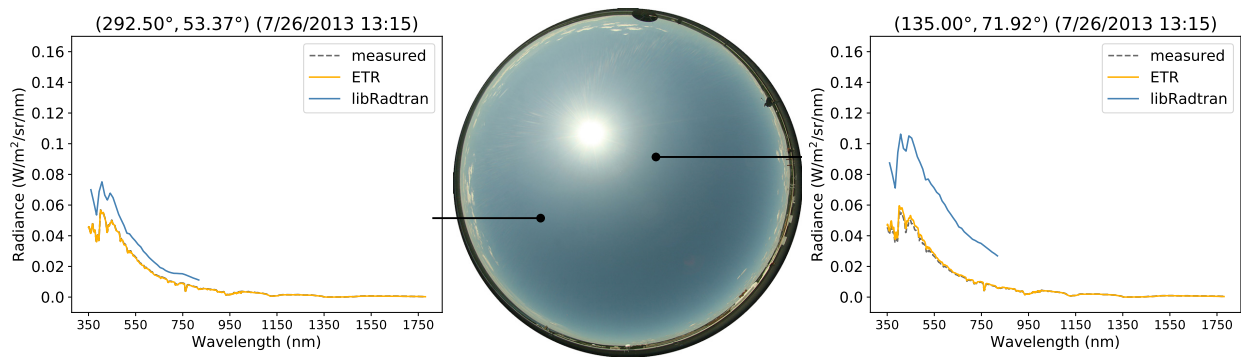


Figure 3.21: Spectral radiance for two sky samples of holdout test sky 07/26/2013 13:15. Spectroradiometer measurement, ETR model prediction, and libRadtran estimation plotted. libRadtran computed radiance deviates from both ETR predictions and measured ground truth data, likely because of the lack of needed atmospheric configuration data.

3.5 Ongoing Work

Early in our sky model research, we tested models on all sky covers: clear, scattered and overcast (Table 3.1, Del Rocco et al. (2018)). However, preliminary results indicated that the regression models could not learn enough from unclear skies (Figure 3.22). We have recently trained and tested on scattered sky data with a deep-neural-network (DNN), and the results seem to be comparable or even slightly better than our regression models on clear sky data Figure 3.23. The DNN model is currently configured with 3 layers, 300 x 800 x 500 neurons, and trained for 400 epochs before convergence. We trained on 10000 sky samples, tested with 3000, and left an additional 3000 holdout samples for further testing. Whole sky error results on one of our test skies is 3.63% RMSD (slightly better than our ETR regression model on clear sky data (Figure 3.12)). We are further tuning the DNN model and experimenting with using entire pixel subsets of skies instead of a single Gaussian weighted color per sky sample. We will also test our model on mixed and separate sky cover datasets in attempts to train a unified model.

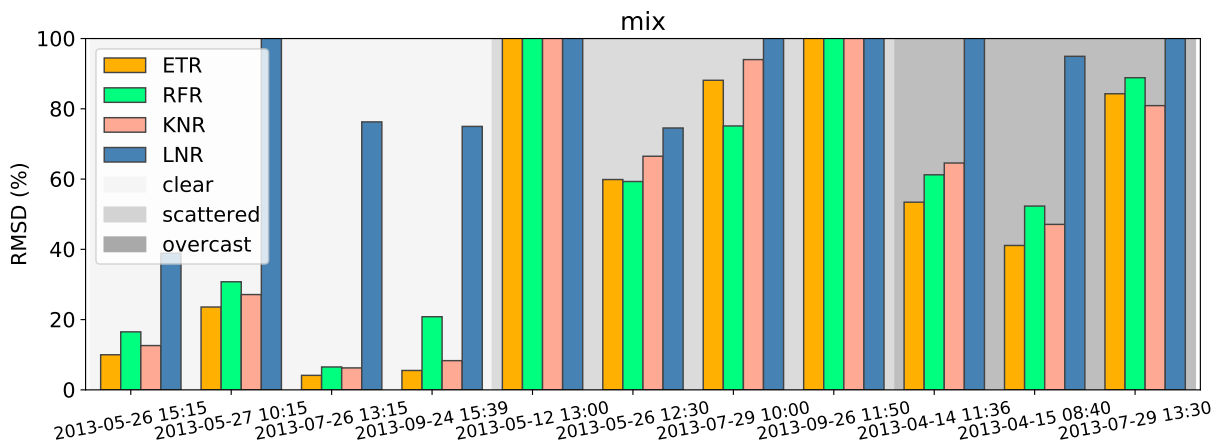


Figure 3.22: This figure shows the early results of our regression models on all sky covers.

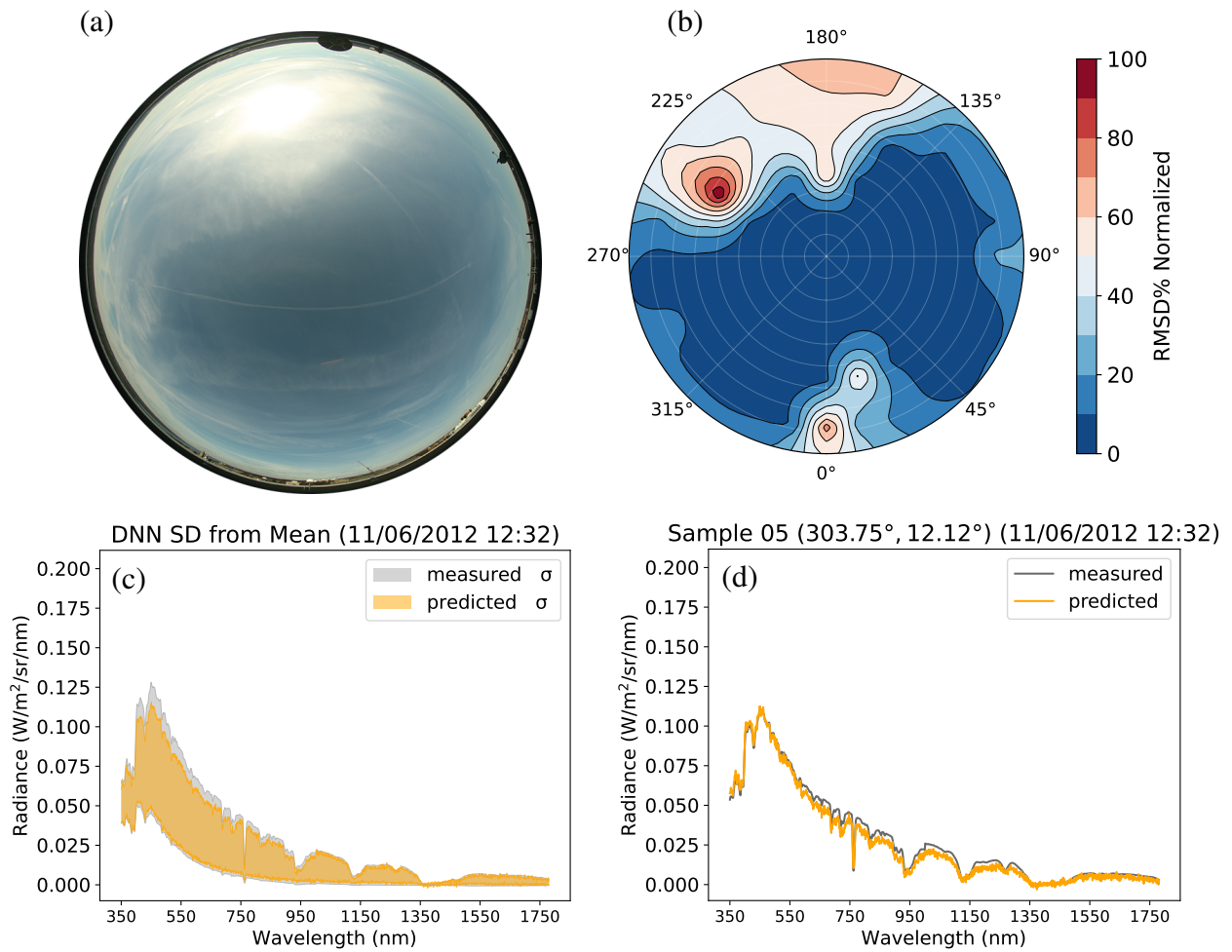


Figure 3.23: This figure shows preliminary whole sky results on test sky 11/06/2012 12:32 with a deep-neural-network (DNN) model. (a) shows a 1 s exposure of the sky, (b) shows the whole sky RMSD normalized, (c) shows the standard deviation range of measured and predicted spectral radiance across the whole sky, and (d) shows the results of a single sky sample.

CHAPTER 4: RADIANT SPECTRAL ENERGY FOR SIMULATION

Much of the research in this chapter appears in the following published paper:

Del Rocco, J. and Kider Jr., J. T. (2021). Radiant spectral energy for simulation in the built environment. In *Proceedings, Building Simulation 2021: 17th Conference of IBPSA*. IBPSA

Modern building performance simulations (BPS) have largely ignored spectral energy for a variety of reasons. One reason is that BPS algorithms have been developed and validated incrementally over decades (Crawley et al., 2008). In that time, the models and algorithms have relied mostly on irradiance approximations to simplify daylighting and energy calculations already in need of optimization, especially for increasingly complex building geometry and surrounding environments (Kider et al., 2019; Nguyen et al., 2014; Jones et al., 2012). In addition to this, most sky model research is limited to subsets of the visible range (Kocifaj, 2015; Tohsing et al., 2014). The push for BPS in early-stage design also demands real-time solutions. It is only natural to assume that spectral data (input, output, or both) might further slow down the simulation pipeline (Hong et al., 2008). The data needs to be transformed and marshaled through a variety of legacy and modern software systems: plugins for architectural modeling packages e.g. *Rhino 3D* (Robert McNeel & Associates, 1980), critical energy analysis engines and interfaces e.g. EnergyPlus (Crawley et al., 2000) and OpenStudio (Guglielmetti et al., 2011), fenestration software, automation tools (e.g. Ladybug Tools (Roudsari et al., 2013)), Radiance (Ward, 1994), not to mention the coordination effort involved between tool providers.

Yet real-time BPS pipelines must eventually use full-spectrum energy to provide the most accurate results for daylighting and energy analysis, and a “spectral revolution” is already underway. Spectral ray-tracing renderers have recently been developed (Nimier-David et al., 2019; Balakrishnan

and Jakubiec, 2019). The spectral composition of artificial and natural light sources in the built environment is increasingly being studied to support circadian rhythms and melatonin production in building occupants (Potočnik et al., 2019; Konis, 2019; Hraška et al., 2014), even using recently developed specialty BPS tools (Solemma, 2019; Inanici and ZGF Architects, 2015).

It is our belief that a single spectral input for BPS will simplify the pipeline of specialized file formats and processes, as both daylighting and thermal analysis are possible from the same spectrum of energy. We have anticipated this and worked towards a solution for BPS to use both light and heat from the same spectral inputs. Here, we present a plugin for *Rhino 3D* which accepts whole sky spectral energy sources and interfaces with the *Transition Portal* radiosity engine (Kider et al., 2019) to visualize any number and size of spectral bins of interest. To demonstrate our system under varied times of day and sky conditions, we use both measured and predicted spectral energy. The measured energy comes from the Kider et al. (2014) dataset, and the validated predicted energy comes from both real-world skydome photographs passed through a machine-learned model by Del Rocco et al. (2020), as well as predictions from libRadtran (Emde et al., 2016). We propose and simulate an adaptive smart spectrally-varying glazing solution that filters heat during warm climates but allows it during cool climates to maximize energy performance with natural heating.

4.1 Methods

This work presents a novel interactive method for early-phase design and retrofitting BPS that takes advantage of radiant spectral energy to visualize natural daylighting and thermal potential. We have modified our *Transition Portal* radiosity engine to compute a full-global illumination solution across user-defined spectral bins of interest. We summarize the process in three steps: (1) spectral solar and sky radiance energy is computed given an appropriately configured sky model and required input, (2) facade and glazing *Transition Portals* modulate user-defined bins of spectral energy that can enter the building, and (3) the radiosity-based rendering engine accelerates the

global illumination solution. Overall this approach provides real-time daylighting and thermal potential feedback for any site location and time of year provided a model can produce the spectral energy.

4.1.1 Radiant Spectral Energy

Terrestrial (atmosphere-attenuated) solar radiation typically measures between 350 to 2500 nm with a spectrometer ([Figure 2.1](#)), although this can vary. This includes the spectral ranges ultraviolet (UV) (350-400 nm in this case), visible / light (VIS) (350-780 nm), and most near-infrared energy (NIR) (780-2500 nm), although the literature reveals that spectral ranges are loosely defined. The traditional term for visible-near-infrared (VNIR) refers to VIS and NIR spectra combined ([Meseguer et al., 2012](#)). NIR is often split into two separate ranges called VNIR (780-1000 nm) and SWIR (1000-2500 nm), although we don't differentiate in this work. Note that some humans (and many animals) can detect visible energy as low as the 310 nm wavelength ([Yokoyama et al., 2014](#)), and that plants can utilize UV energy as low as 280 nm, although some of this is naturally filtered by the ozone layer ([Stapleton, 1992](#)).

Any number or range of spectra (disparate or overlapping) can be visualized with our method. Throughout this paper, we refer to 3 spectral bins of interest, VNIR (“full-spectrum” for our dataset, 350-1780), VIS (350-780 nm), and IR* (780-1780 nm). [Figure 4.1](#) shows measured and model-predicted spectral curves plotted with ranges of interest, VIS and IR*. These measurements and predictions come from [Del Rocco et al. \(2020\)](#) and [Kider et al. \(2014\)](#). These full-sky spectral radiance predictions as well as predictions from libRadtran ([Emde et al., 2016](#)) were used in this work.

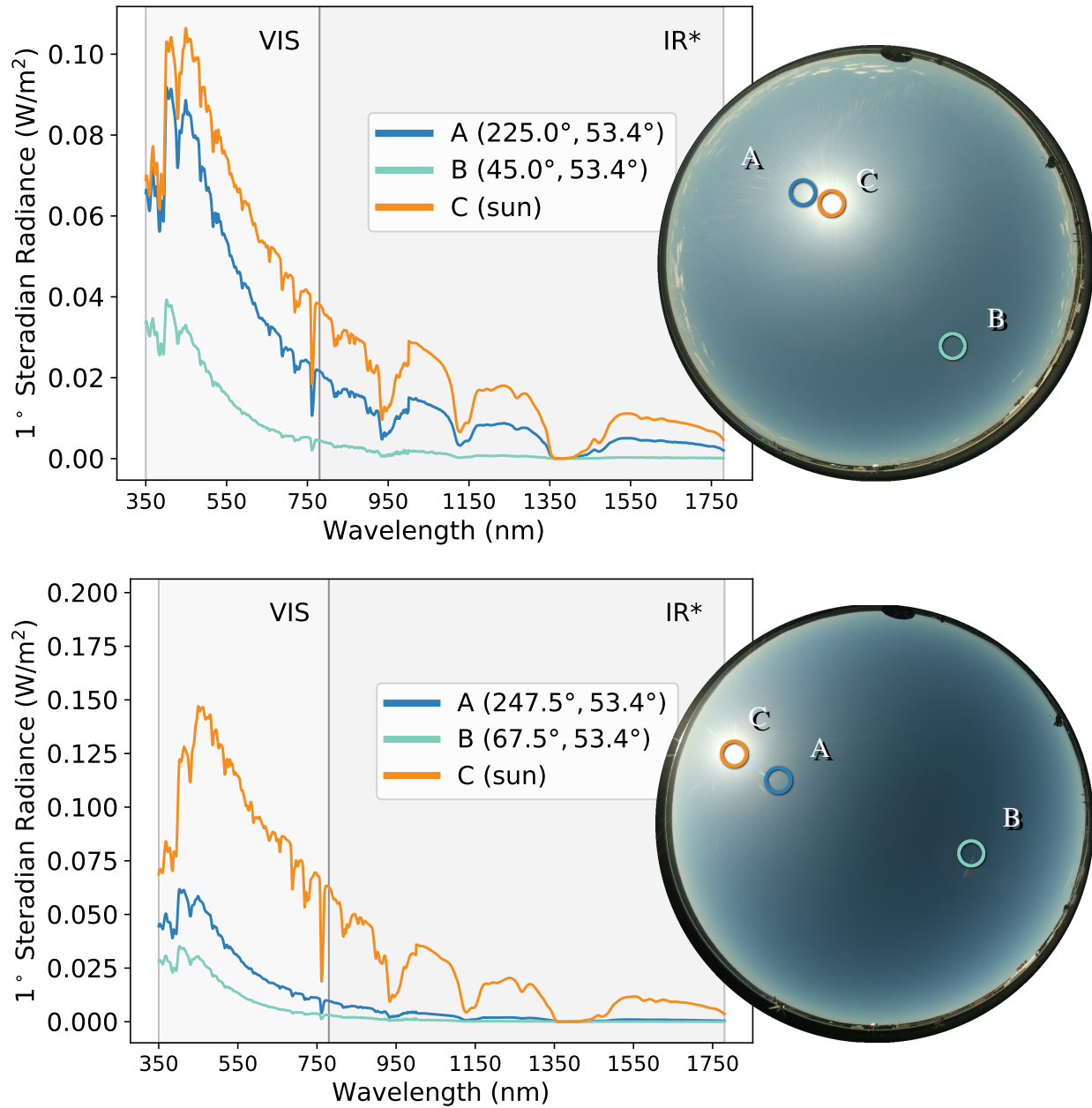


Figure 4.1: Sky captures 7/26/2013 13:15 EST (top) and 9/24/2013 15:39 EST (bottom) from dataset by Kider et al. (2014). Points (A) (B) and (C) each represent the spectral radiance from a 1° steradian. (A) and (B) were measured, while (C) was predicted.

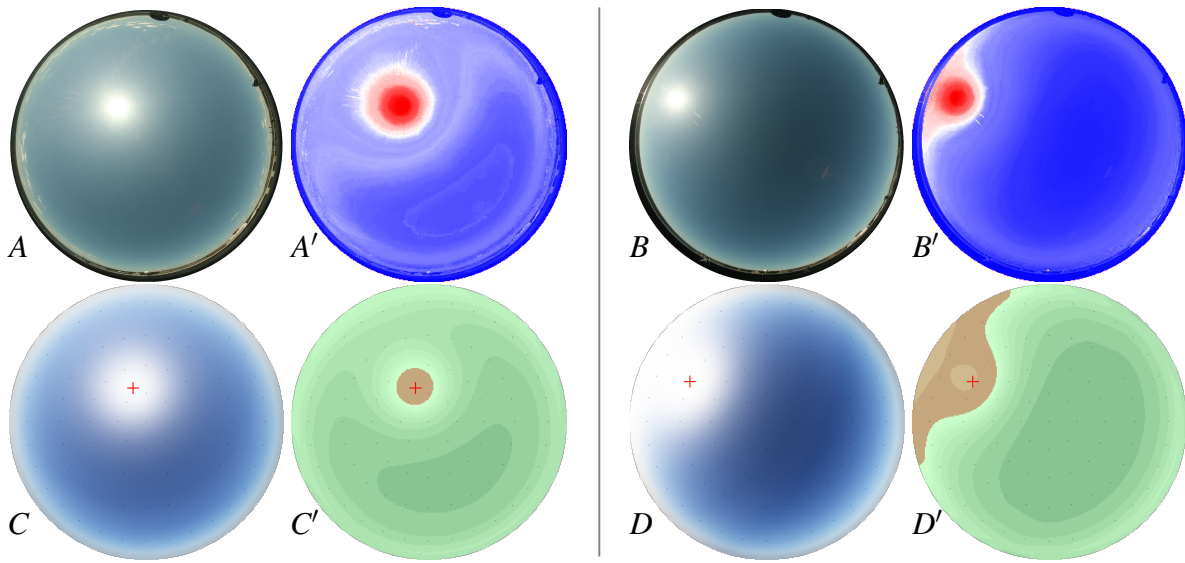


Figure 4.2: Skies 7/26/2013 13:15 EST and 9/24/2013 15:39 EST (A , B) from all-sky captures by [Kider et al. \(2014\)](#) and machine-learned model predicted radiant spectral energy (A' , B') from [Del Rocco et al. \(2020\)](#). Skies at the same location and datetime were generated with physically-based radiative transfer software package libRadtran (C , D) along with luminance and spectral energy (C' , D'). Radiant spectral energy from skies such as these were used during simulations.

Spectral radiance across the skydome may come from any appropriate, properly configured sky model. There has been a wealth of research into sky models over the past few decades, roughly grouped into three categories: analytical, physically-based, and data-driven. Analytical models use sky observations to derive parametric functions ([Hosek and Wilkie, 2012b](#); [Preetham et al., 1999](#)). Physically-based models are the most accurate as they utilize the radiative transfer equation (RTE) to compute the transfer of solar radiation and composition of the atmosphere resulting from *Rayleigh* and *Mie* scattering and polarization ([Emde et al., 2016](#); [Kocifaj, 2015](#)). Data-driven models take advantage of massive training datasets and machine learning methods to find parallels between sky features and spectral energy ([Del Rocco et al., 2020](#); [Chauvin et al., 2015](#); [Tohsing et al., 2014](#)). Although most skylight models calculate radiance and irradiance, many produce only a single combined irradiance value, RGB color, or limited visible spectrum range. While

these models are indeed useful for BPS, spectral energy is needed for spectral-varying glazing and materials to differentiate light from heat. Our approach requires a skylight model that provides a wide range of spectral energy.

Note that spectral radiance from discretized points across the skydome (versus global irradiance) is what allows BPS to account for occlusion from nearby buildings and trees as well as cloud diffusion which produce complex energy scattering scenarios that absolutely affect global illumination, daylighting, and thermal analysis (Schumann and Greenberg, 2012).

4.1.2 Transition Portal Radiosity Engine

The first step of our pipeline computes solar and sky energy for the input forcing function of our radiosity engine (Figure 4.1). Figure 4.3 shows an example of a sun path and sky patches that contribute spectral energy to our simulations. The sky patches and their form factors are pre-calculated only once. And only when sky condition input changes (due to a date/time change) is the appropriate spectral energy recollected and radiosity recomputed.

We use a finite elements radiosity based approach (Goral et al., 1984) to determine the illuminance

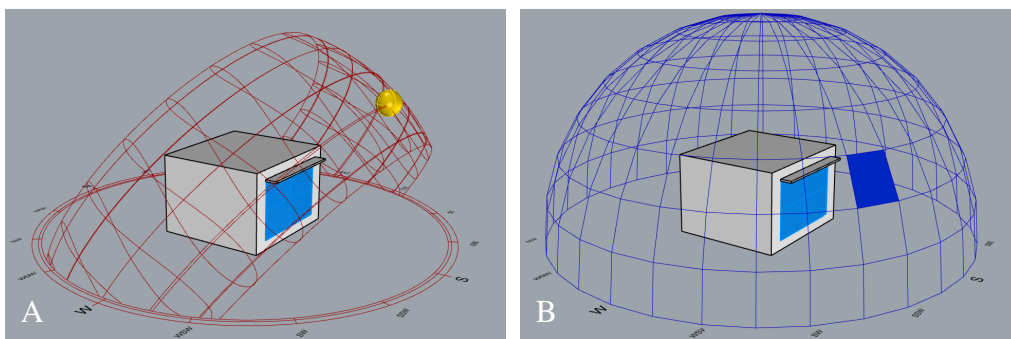


Figure 4.3: Spectral energy is gathered for the (A) solar sun path and the (B) sky patch locations given input sky capture or site location and sky conditions.

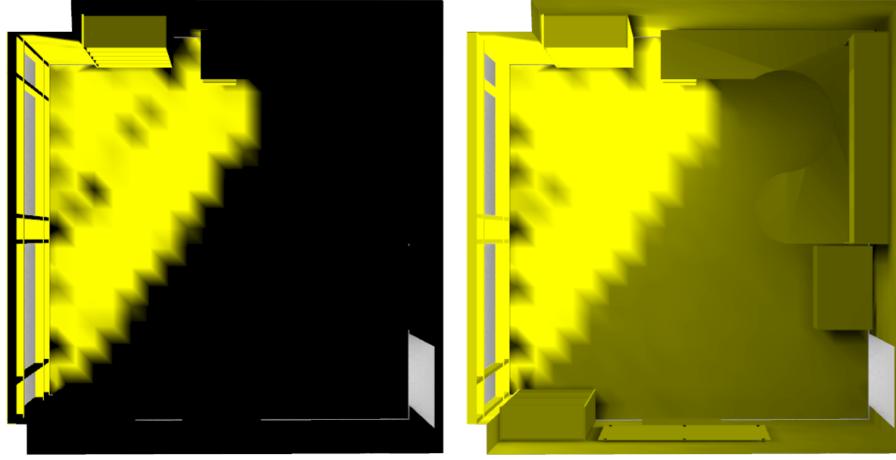


Figure 4.4: Preliminary result of an office showing direct incident solar emission and sky patch indirect contributions discussed in [Figure 4.3](#).

E in the building ([Greenberg et al., 1986](#)). This computes the full global illuminations lighting solution in the space. First, the space is discretized into a set of discrete patches to calculate this illuminance. The direct light from the sun, sky, and additional light sources (D) and the indirect light being reflected (ρ) is added to compute the final global illuminance E_i on a patch i mathematically as:

$$E_i = D_i + \sum_j F_{ij} \rho_j E_j \quad (4.1)$$

The form factor F_{ij} expresses the quantity of light that moves between patch j to fall on patch i . This is expressed by a double integral equation between the two patches as follows:

$$F_{ij} = R \int_{A_i} \int_{A_j} \frac{(\hat{n}(\mathbf{x}_i) \cdot \hat{\omega}_{ij})^+ (\hat{n}(\mathbf{x}_j) \cdot \hat{\omega}_{ji})^+}{\|\mathbf{x}_i - \mathbf{x}_j\|^2} V(\mathbf{x}_i, \mathbf{x}_j) d\mathbf{x}_j d\mathbf{x}_i \quad (4.2)$$

where,

$$\hat{\omega}_{ij} = \frac{\mathbf{x}_j - \mathbf{x}_i}{\|\mathbf{x}_j - \mathbf{x}_i\|} \quad \text{and} \quad R = \frac{1}{\pi A_i} \quad (4.3)$$

We use a Monte Carlo ray casting method to calculate the form factors similar to [Jones et al. \(2013\)](#)

to approximate the integral.

To calculate the final building illuminance we express this term in a simple matrix equation:

$$\mathbf{A}_\lambda E_\lambda = D_\lambda \quad \text{where} \quad \mathbf{A}_\lambda = \mathbf{I} - \mathbf{F}\mathbf{P}_\lambda \quad (4.4)$$

where \mathbf{F} is the form factor matrix, D is a vector of the forcing function from the sun/sky illuminances from the transition portal, \mathbf{P} is a diagonal matrix containing the patch reflectivities, the identity matrix \mathbf{I} and E is the unknown vector of total illuminances which we solve for. λ represents the number of wavelength bins we solve for. \mathbf{F} remains constant across the different λ bins. There are numerous ways to solve this radiosity equation. We utilize an LU factorization approach similar to [Kider et al. \(2019\)](#).

The spectral *Transition Portal* engine accelerates the calculation of different facades and shading devices by accounting for these in the radiosity forcing function calculation. This can be modulated differently for the different spectral wavelength bins (λ) allowing complex spectral facades, glazing, and shading devices to be accurately simulated. This direct illuminance can be calculated by pixel counting ([Jones et al., 2012](#)) or ray tracing ([Kider et al., 2019](#)). Both methods estimate the fraction that each patch is unoccluded by shading devices or attenuated by glazing. Both the solar shading materials and attenuation glazing transmission can operate differently between visible and infrared wavelength having different effects on daylighting and thermal properties.

4.1.3 Adaptive Smart Spectrally-varying Glazing

In addition to more traditional static or kinetic shading devices, smart (switchable) glazing solutions (marketed as “smart glass,” “e-glass,” / “smart film,” “e-film”) have already been proposed for building performance ([Ardakan et al., 2017](#); [Wong and Chan, 2014](#)) and are commercially available ([Market Research Explore, 2019](#)). These glazing solutions are generally produced in one of

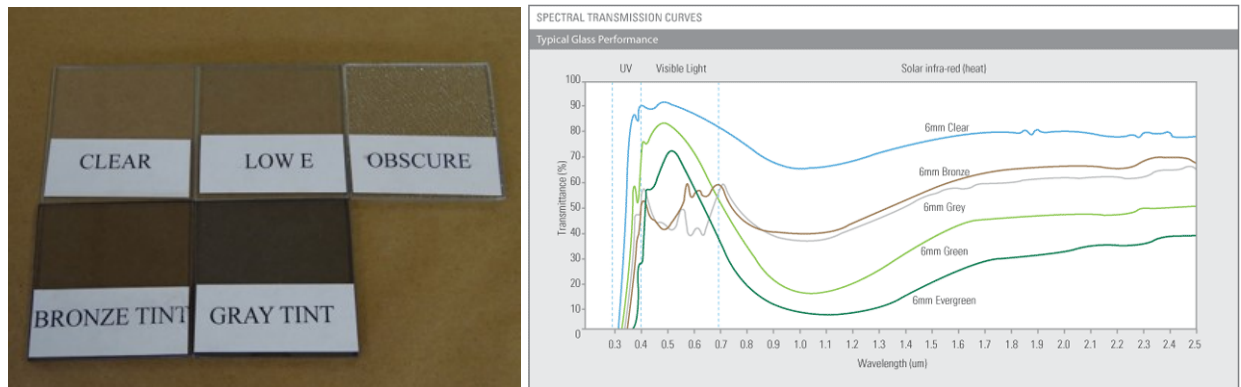


Figure 4.5: This figure shows some older, standard glazing options (LEFT) and spectral transmittance of specific products offered by [Metro Performance Glass Ltd. \(2021\)](#) (RIGHT).

three ways: electrochromic substrate, liquid or gel suspended particle, or polymer-dispersed liquid crystal (PDLC), which are manufactured quite differently but function in a very similar manner. All of these solutions can toggle (transmit or reflect) or even dim visible spectrum energy given a low voltage charge. One rather important difference is that electrochromic solutions are transparent when no voltage is applied, unlike suspended particles or PDLC which require a charge to maintain transparency. Building usage and occupancy factors into the performance of smart glazed buildings ([Ghosh and Mallick, 2018](#)).

Two older, non-smart, non-adaptive, yet very prevalent technologies often applied to glazing as an alternative (or in addition to) other shading solutions are tinting and low emissivity (*Low-E*) coatings. Both of these well-known, abundant solutions are ideally transparent to visible spectrum energy and reflective to non-visible spectrum energy, although most literature shows this is not yet the case ([Wang and Shi, 2017](#)). Most existing products also ignore long-wave infrared radiation for the most part ([Zhao et al., 2018](#)). Tinting involves mixing materials into the glass itself whereas *Low-E* coatings are applied to glazing surfaces, inside or outside, and to any number of panes. Unlike *Low-E* glass, tinted glass often changes color with glass thickness. These solutions often partially occlude visible spectrum energy ([Yuste et al., 2011](#)). Tinting often reduces visibility more

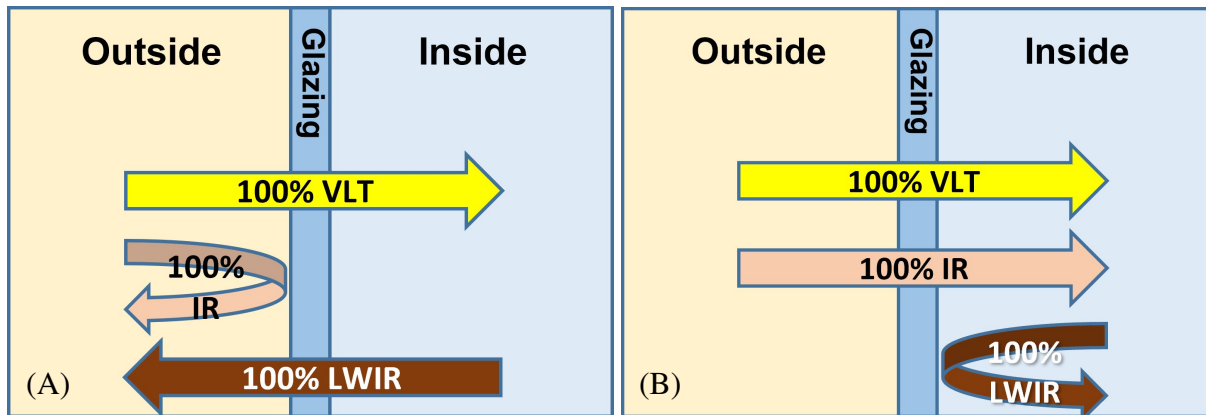


Figure 4.6: This figure depicts the “ideal” (if simplified) glazing scenarios for summer months (A) and winter months (B). VLT stands for visible light transmittance. IR and LWIR are infrared and long-wave infrared, respectively. Typically, buildings want to reject (and dissipate) heat energy during summer months and allow (and retain) heat during winter months.

than the heat gain coefficient, and multiple *Low-E* coatings (*Low-E2*, *Low-E3*) incrementally affect parts of the visible spectrum. Tinted or *Low-E* glazing commonly has a visible transmittance (τ_{vis}) of only 50-90% (Yuste et al., 2011). Some of these solutions are depicted in Figure 4.5.

Adaptive smart spectrally-varying visibly-transparent glazing solutions can improve natural daylighting, heating and cooling automatically by responding to environmental conditions. Often building daylighting scenarios are configured to shade direct (beam) energy but allow indirect (sky) energy as it does not produce glare scenarios (Boubekri, 2008). Assuming this configuration, we would then allow all visible energy to maximize the amount of light in the interior space (although slight reductions could be made to reduce some of the heat if desired). Adaptive smart glazing could then automatically allow non-visible spectral energy for natural heating during winter months versus summer months instead of requiring climate specific glazing products (Figure 4.6). In summer months, building glazing could then spectrally filter infrared energy from entering while simultaneously allowing long-wave infrared that builds up to escape. Doing so would reduce the amount of recovery cooling required, and therefore the associated energy use and costs. In winter

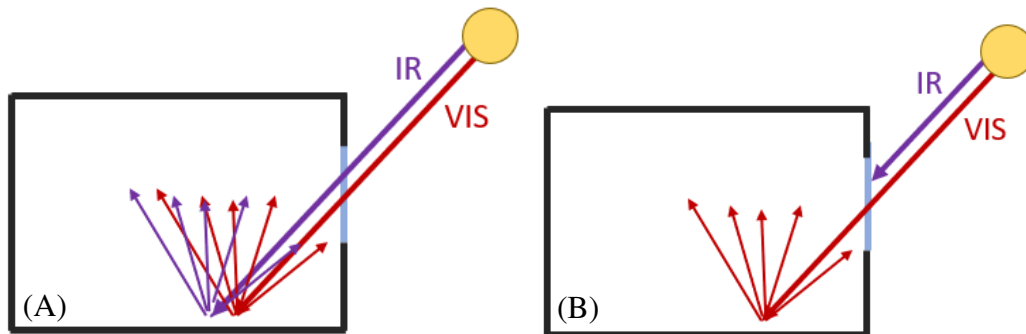


Figure 4.7: The *Transition Portal* spectral radiosity engine supports facades which filter or allow certain wavelengths during global irradiance calculations.

months, however, we want the opposite to help reduce energy and costs associated with heating, especially in temperate and sub-polar climate regions. The more free heat we can actively capture, the better.

Note that visible energy filtering of *Low-E* coatings and tint can affect building occupants (Potočník et al., 2019). Light shelves or indoor greenhouse spaces could selectively allow small amounts of UV-A or UV-B spectrum energy for plants (Turnbull et al., 2013) and indoor birds, while still being energy efficient. Finally, given the chemical substrate voltage propagation of smart glazing, it should be possible to displace discretized patches or patterns throughout the glazing to produce non-smart “fritted” areas that are unaffected by the voltage. Since most smart glazing is charged from the sides, these fritted patterns would provide the inverse shading of traditional patterns. A few mechanically-adaptive fritted glazing solutions have also been proposed (Drozdowski and Gupta, 2009), but we believe our non-mechanical fritted smart glazing proposal is novel (Figure 4.8).

With our spectrally-aware *Transition Portal* radiosity engine we simulate the direct solar emissivity and radiosity of a local office space built to scale with 4 different glazing solutions applied:

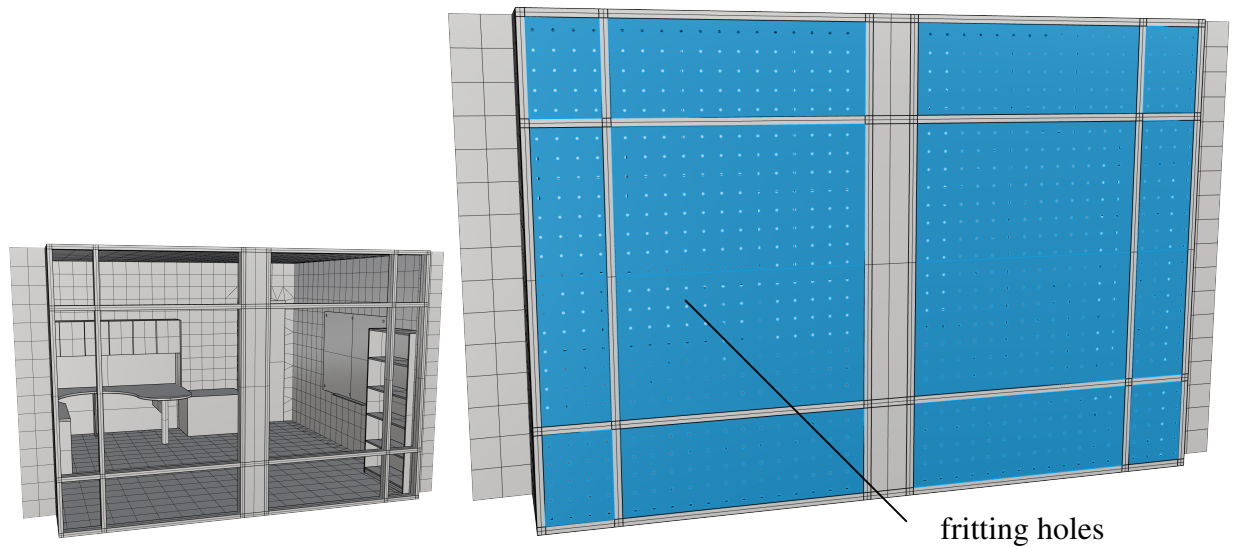


Figure 4.8: This figure shows our novel fritted smart-film concept, which removes uniform segments (holes) at any resolution from any smart-film, and allows for all energy to pass through unfiltered at the hole locations. The smart-film is depicted in blue only to distinguish between fritted and non-fritted areas.

traditional non-shaded glazing, commercially available *Low-E* coated, spectrally-varying smart glazing, and our fritted smart glazing proposal (Table 4.1). The baseline non-shaded glazing has 100% transmittance across all wavelengths VIS and IR* (VNIR); the *Low-E* coated glazing has 85% visible transmittance ($\tau_{vis} = 85\%$) (VIS spectra) and completely reflects IR* wavelengths (Yuste et al., 2011); the smart glazing has $\tau_{vis} = 100\%$ and also completely reflects IR*; the fritted smart glazing has a $\tau_{vis} = 100\%$ but allows roughly 30% IR* spectra. Since the last two glazing solutions are switchable, they can be toggled on and off (and theoretically dimmed) for parts of the year when computing daylighting and energy summaries. Ultimately these transmittance and filter properties can be configured for simulation (Figure 4.7).

Table 4.1: The 4 glazing solutions tested in simulations. The transmittance (τ) filters for VIS and IR* spectra are denoted, whether or not the glazing is powered, and whether or not it is commercially available.

Type	τ_{vis}	τ_{IR^*}	Powered	Available
non-shaded	100%	100%	no	yes
Low-E	85%	0%	no	yes
Smart	100%	0%	yes	yes
Smart Fritted	100%	30%	yes	no

4.1.4 *Rhino 3D 6* Plugin

Our previously published *Transition Portal* radiosity engine code is written and optimized for the GPU in C++ using standard graphics libraries (Kider et al., 2019). This work modified the engine to support spectral radiance values so that separate bins of spectra could be visualized separately for various purposes. We also wrapped the radiosity engine with a 64-bit *Rhino 3D 6* plugin written in C# with an interfacing managed-C++ layer. The plugin supports: (1) defining layers of geometry and glazing with material properties for transmittance, (2) defining spectral bins and false-colors for visualization, and (3) loading files with direct sun and indirect sky spectral radiance vectors. The number of sky patches is configurable so that any granularity can be defined. This gives downstream or future work contributions the ability to occlude diffuse radiation as necessary from neighboring objects. Although our plugin is intended for early phase building designers / architects, some of the functionality is currently still executed through *Rhino* commands, not the GUI interface. A screenshot of the plugin being used in *Rhino 6* is shown in [Figure 4.9](#).

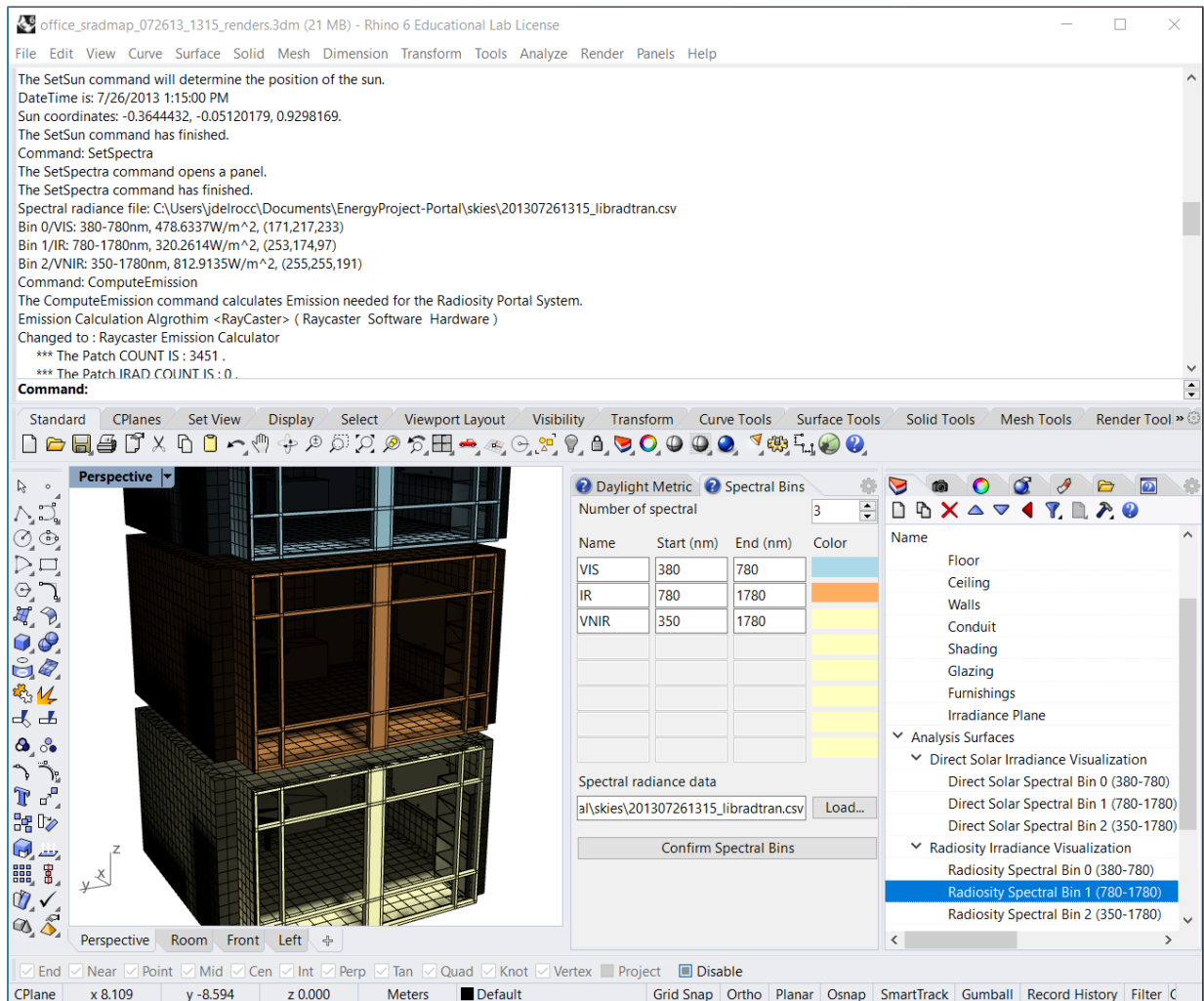


Figure 4.9: A screenshot of the *Transition Portal* radiosity engine running in our 64-bit plugin in *Rhino 3D 6*, visualizing spectral energy bins VIS, IR*, and VNIR. Note the panel for specifying the names, wavelengths and colors of the spectral bins of interest.

4.2 Results

We ran different spectral visualization studies with typical office space model geometry in the Southeastern United States, although the spectral radiance sky data comes from the dataset measured, validated, and modeled by (Kider et al., 2014; Del Rocco et al., 2020). The purpose of the study was to demonstrate how different bins of wavelengths of the solar radiation spectrum could be visualized individually and as combinations to produce illuminance and irradiance metrics. Our office was constructed with a patch size of 6" and a total of 3451 patches. Simulations were run from our *Rhino 3D* plugin interfacing with the *Transition Portal* spectral radiosity engine on a *Windows 10* PC with *Intel Core i7-7700K CPU 4.2GHz*. Direct incident solar emission was computed for visible energy (VIS), near-infrared (IR*) and the “full-spectrum” (VNIR) in ~ 2 minutes, form factors in ~ 30 seconds, and final spectral radiosity in ~ 1 minute, with a complete simulation time of roughly 3.5 minutes. If only the final radiosity visualizations are desired, the direct solar emission visualizations can be omitted to improve processing performance.

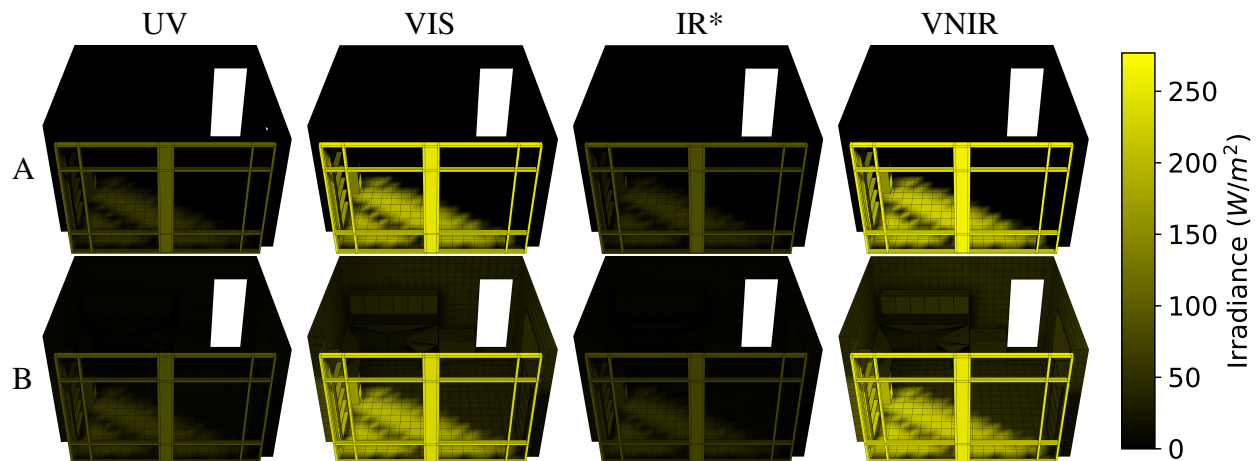


Figure 4.10: False colored (yellow) spectral renders for various bins separated into direct incident solar emission (A) and radiosity (B). The colorbar correlates with the radiant spectral energy input from sky capture 9/24/2013 15:39 EST (Figure 4.1). Any number of spectral bins (down to 1nm resolution) can be visualized in any color.

Figure 4.11 shows one of the main target use cases for our *Transition Portal* spectral radiosity engine - the ability to simulate spectrally. We demonstrate the baseline office with typical 100% transmittance glazing and support mullions for our three spectral simulation bins (VIS, IR*, and VNIR) Figure 4.11(A). We then vary the facade type to simulate a low-e coated spectral glazing, spectral-filtering smart glazing, and fritting. These results have similar global illumination illuminance in the VIS bin with the baseline office simulation. The spectral-varying facade materials affect the IR* bin. The *Transition Portal* spectral radiosity engine allows architects to test a wider class of facade options and breaks out the simulation so they can visualize the effects of a facade on daylighting and thermal outputs. This provides insight and balance between design requirements and constraints.

Figure 4.10 shows the breakdown between direct incident solar radiation versus indirect illumination as both are computed and visualized. Figure 4.10 also demonstrates that any spectral bin of interest can be visualized, including per wavelength. This method can be further refined and optimized to produce spectral outputs for building-control algorithms which can then be utilized by the RCS of state-of-the-art building monitoring systems that take into account spectrally-varying parameters. It is still infeasible to equip buildings with radiance (not irradiance) measuring equipment to produce full skydome radiant spectral energy for such a system. And modern atmospheric models have become increasingly complex requiring many local measurements including aerosol optical depth (AOD), cloud fraction, reflectance, altitude, ground albedo, scale height, gamma, etc. (Kocifaj, 2015). Thus we propose the use of a commercially available all-sky camera to monitor the sky along with other cheap, readily available sensor data and regularly pass them to a modern skylight model that can produce approximate radiant spectral energy with low-resolution inputs. Such a system is feasible and affordable now and has the ability to drive RCS of spectrally-aware building monitor systems. Such a system will have finer-grain control.

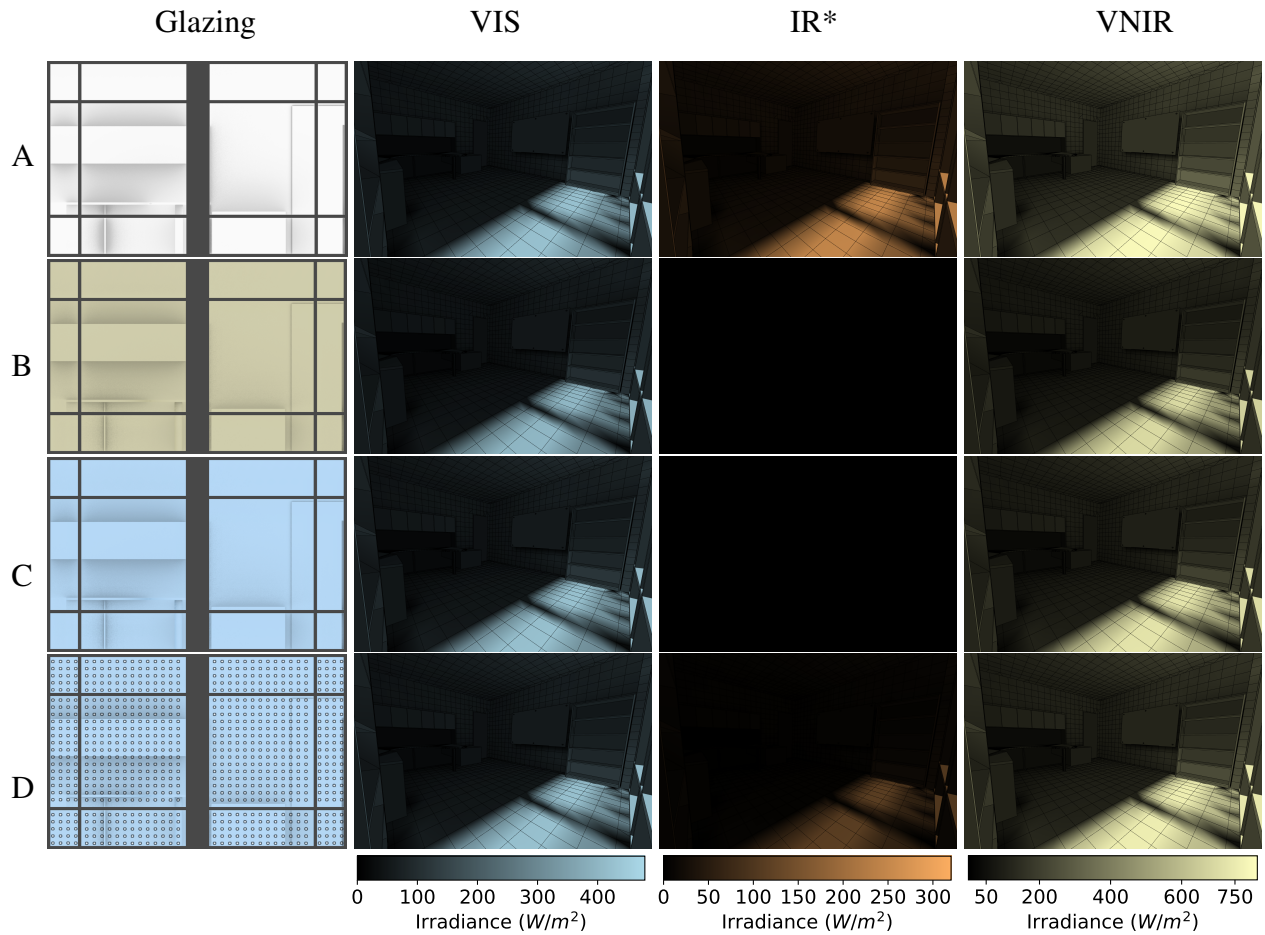


Figure 4.11: False colored spectral radiosity renders with radiant spectral energy for visible spectrum (VIS) (350-780nm), near-infrared (IR*) (780-1780nm), and combined visible and near-infrared (VNIR) energy with simulated spectral energy from libRadtran on sky 7/26/2013 13:15 EST with [Table 4.1](#) glazing solutions. IR* wavelengths are filtered out completely by (B) and (C) glazing solutions while fritted glazing (D) allows ~30% IR* transmittance. Note the higher intensity of smart glazing (C) in VIS spectrum over *Low-E* (B).

CHAPTER 5: SKY AND OCCUPANT AWARE ADAPTIVE FACADE

Some of the research in this chapter appears in the following publication:

Moulton, N., Del Rocco, J., Kider Jr, J. T., and Fiore, S. M. (2018). An affective kinetic building façade system: Mood Swing. In *Proceedings, 13th Conference on Advanced Building Skins*, pages 417–426. Advanced Building Skins GmbH. ISBN: 978-3-9524883-4-8. <https://abs.green/files/pdf/content-2018.pdf>

Although many downstream applications of our research are possible, one immediately viable option is a building monitoring system equipped with all-sky camera that automates kinetic facades and/or smart-glazing in response to spectral radiant energy predictions. Such a system could automatically harness (or attenuate) light and heat with more fine-grain control and accuracy than one that operates on a single downwelling measurement, and is much more affordable and efficient than a live sky scanning system. Ideally it would also provide support for spectrally filtering smart-glazing to filter short and long-wave infrared energy during certain scenarios, and should allow for occupant overrides. In this chapter we discuss existing designs and then present an adaptive building facade prototype system of our own, from concept, design, and simulated case study analysis, to constructed cyber-physical prototype.

[Figure 5.1](#) gives a high-level overview of a sky and occupant aware cyber-physical building monitoring system that could be leveraged by buildings today. We explain the steps denoted with numbers in the figure. First (1), an all-sky camera is mounted to the top of the building to capture the sky at some desired interval (e.g. every 1 - 10 minutes) and feed those images, along with any available atmospheric readings from regional measuring stations, to a modern sky model (2) which produces a spectral radiance map (sradmap) of the sky ([Del Rocco et al., 2020](#)). The surrounding

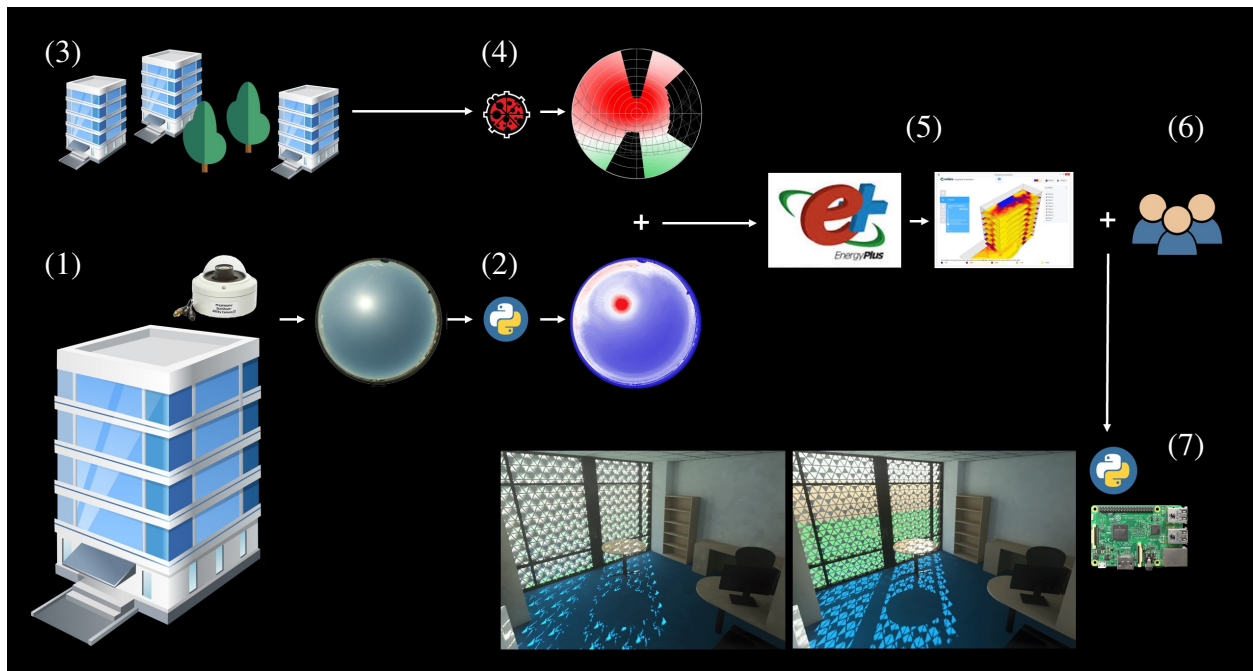


Figure 5.1: A cyber-physical building monitoring concept with adaptive facades. Steps (1) through (7) are detailed in the paragraph text and involve: (1) monitoring the sky, (2) predicting spectral radiance, (3) surveying the surrounding environment, (4) occluding the energy that doesn't reach the building, (5) building energy modeling, (6) occupant overrides, and (7) driving kinetic facades.

environment is surveyed occasionally (3) (i.e. once per year or as needed) with fed into shadow mask software (Roudsari et al., 2013) (4) to produce a skydome mask which is then applied to the sradmap to find the remaining spectral radiance energy that actually reaches the building. The remaining spectral radiance vectors are fed into any desired (but real-time capable) BEM software with spectral radiance support (5) to predict final light and heat in zones with glazing. These predictions are then combined with occupant schedules, overrides, and any other desired factors (6) and fed into a model-based predictive controller (MPC) that drives the hardware which automates the kinetic facades and/or smart-glazing (7).

5.1 Facade Concept

Adaptive building facades employ sensor-based automation systems to respond to external environmental conditions. This allows buildings to react to exterior environmental conditions in order to: implement daylighting (the active harnessing of natural daylight), reduce energy spent on artificial lighting, encourage occupant well-being with circadian lighting and natural vistas, attenuate or capture short-wavelength infrared energy for heat, etc. Daylight is important for physical and mental health, from the sunlight's ability to increase vitamin D, to the alleviation of Seasonal Affective Disorder (SAD). Research has shown that daylighting and nature may have positive impacts on well-being (Ulrich, 1979); benefit cognitive processes (Berman et al., 2008); and renew attention (Kaplan, 1995). Adaptive facades are also growing in popularity due to parametric design tools to quickly design, simulate and mechanically control them (Velasco et al., 2015). One notable design even incorporates photovoltaic panels as facade units (Nagy et al., 2016). Figure 5.2 illustrates various famous adaptive building facades that have the ability to adapt to their environment.

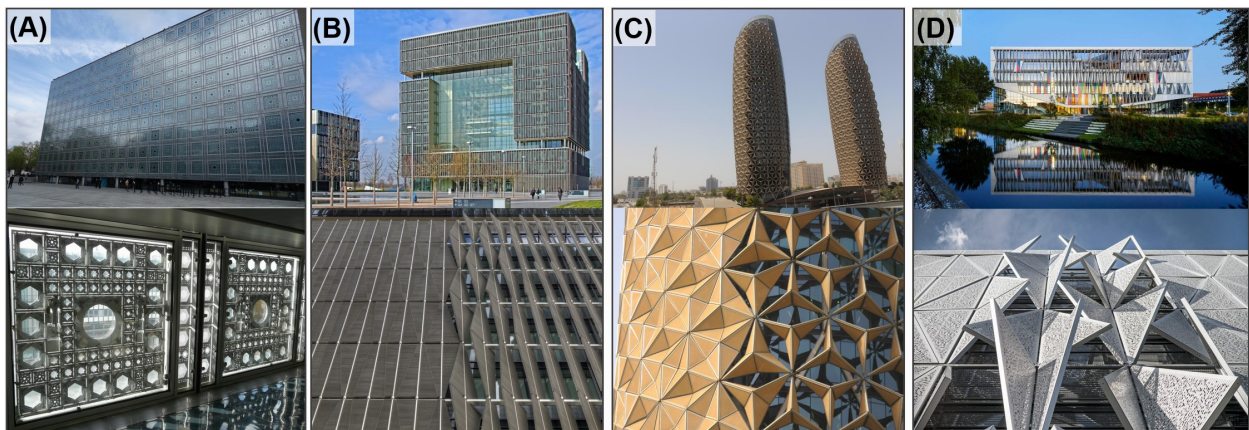


Figure 5.2: Famous adaptive facades found around the world: (A) Musée de L'Institut du Monde Arabe (Jean Nouvel, Architecture-Studio, Pierre Soria and Gilbert Lezenes, 1987); (B) SDU Campus Kolding (Henning Larsen Architects, 2014); (C) Q1 Building, ThyssenKrupp Quarter (SWD Architekten + Chaix & Morel et Associés, 2010); (D) Al Bahar Towers (Aedas Architects, 2012).

Our kinetic facade design consists of an interlocking array of equilateral triangular units supported by framing hardware, and is intended to be mounted over any exterior facing glazing surface. Each triangular unit is subdivided by an inner equilateral triangle, denoting its center and primary shading surface, and the remaining space resulting from the subdivision of the outer and center triangles is then filled by three triangular, adjustable shading surfaces we call “wings.” Each wing is controlled by a servo motor, either directly or in drive train, that rotates it toward the center of its unit. The units can be controlled both globally and independently of each other. This allows the facade to respond to a variety of situations. This facade concept also provides architects with an interesting exterior building “skin” design. [Figure 5.3](#) depicts various configurations of a unit, while [Figure 5.4](#) illustrates the facade concept as a whole with multiple units side-by-side.

To give building designers more options, the center equilateral shading triangle of each facade unit can be configured to any ratio of its outer triangle bounds, provided all facade units maintain the same ratio. This allows for numerous interesting design and natural lighting configurations. Consider a center shading triangle that bisects its outer bounds by half on each side. We call this the Sierpinski design because it mimics the famous fractal by [Sierpinski \(1988\)](#). We call the design where the center shading triangle bisects its bounds at a ratio of $\frac{1}{\phi}$, the Golden design, for the golden ratio. This architectural concept allows for a variety of different dynamic configurations for daylighting. For individual unit control, two options are possible: (1) a single servo with drive train that lifts all three “wings” uniformly at the same rate and limits, and (2) a servo per wing, which allows for a much greater range of configurations, including more traditional shading devices, light shelves, and non-uniform patterns. These tiled triangular units are not confined to any predetermined number or size, and many complex shading and daylighting patterns are possible. We can design this building facade concept to respond to various external environmental conditions and interior occupancy scenarios. [Figure 5.5](#) and [Figure 5.6](#) illustrate the facade under global and individual unit control at various angles.

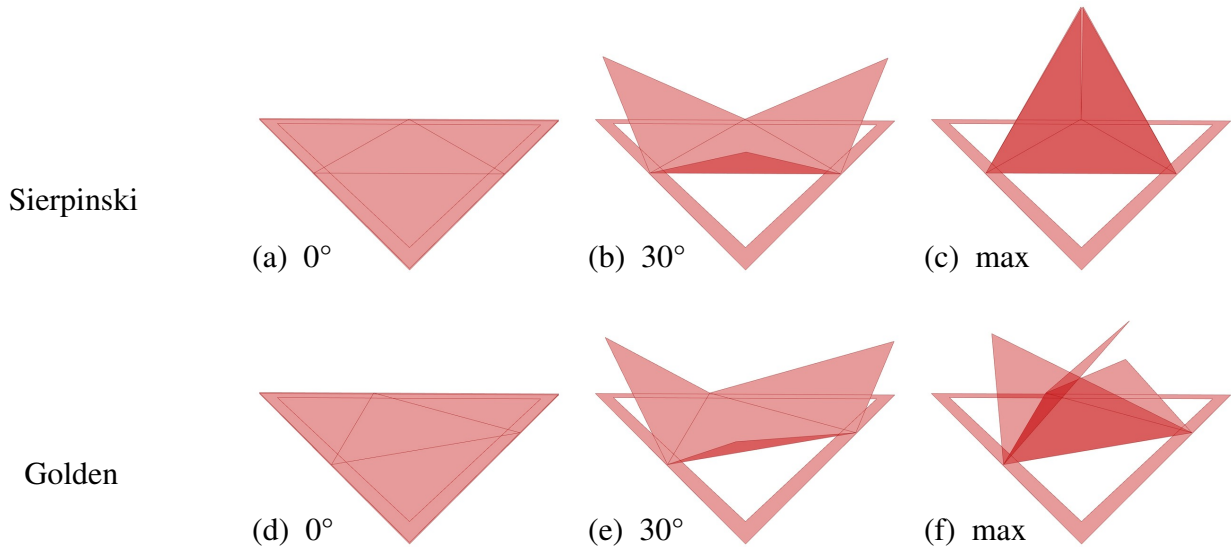


Figure 5.3: Individual facade units of Sierpinski and Golden configuration with wings opened and closed. (a), (b), and (c) are of Sierpinski design open at angles 0°, 30°, and maximum, respectively, while (d), (e), and (f) are of Golden design at the same angles.

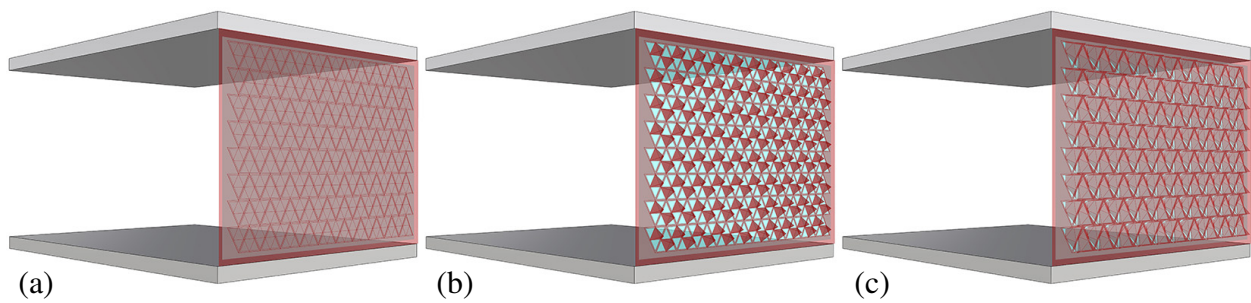


Figure 5.4: Our adaptive facade design concept. (a) and (b) show the Sierpinski configuration fully closed and opened, respectively. (c) shows a 30° open Golden configuration.

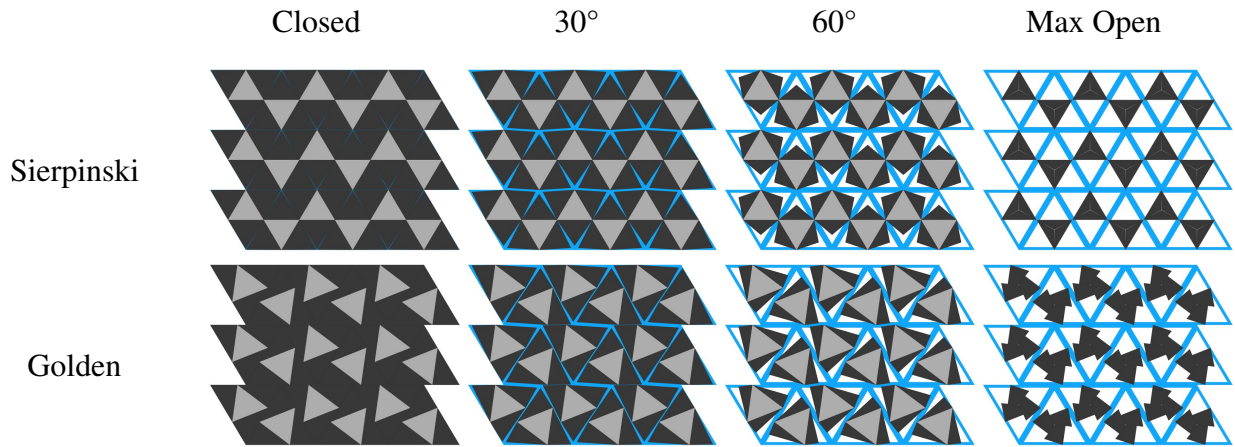


Figure 5.5: Our adaptive facade concept at various global control actuation. The center shading triangular surface is depicted in light gray, while the kinetic “wings” are dark gray. Each of the facade unit bounds / frame is depicted in blue.

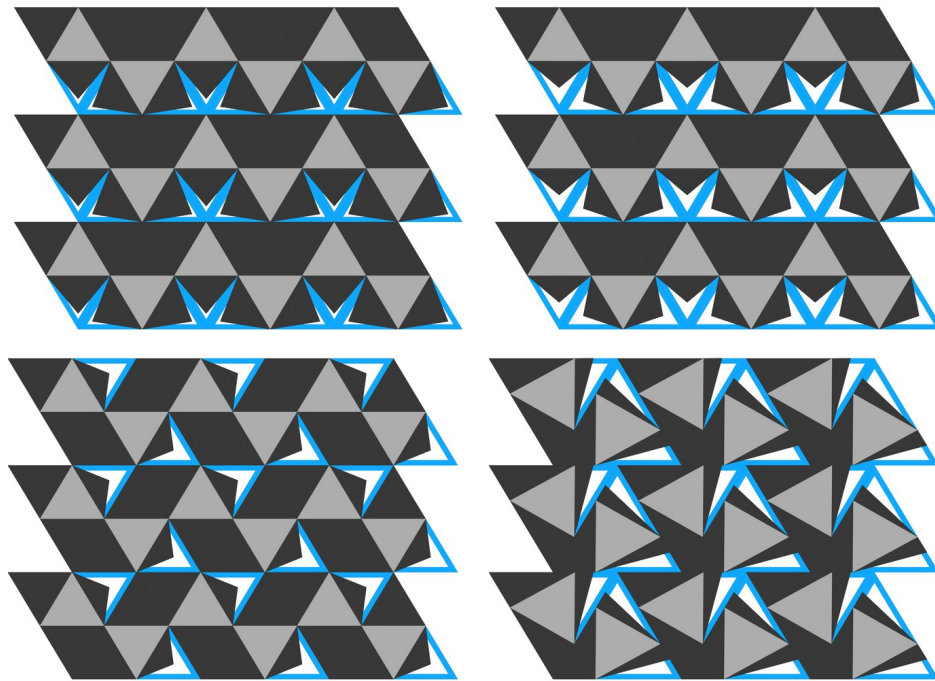


Figure 5.6: Theoretically, each facade unit could be controlled individually. Each wing of each facade unit could have its own servo or similar mechanism. Such a design would allow for a much greater range of open configurations, including those similar to more traditional shading devices, light shelves, and non-uniform patterns.

5.2 Numerical Analysis

Recent developments in computational modeling and simulation tools bridge the gap between architecture and engineering. Energy modeling software EnergyPlus (Crawley et al., 2001), combined with daylighting and automation tools like RADIANCE (Ward, 1994), DIVA-for-Rhino, and Ladybug Tools (Roudsari et al., 2013) provide ways to test and analyze a wide variety of parametric designs and configurations. In this work, we utilize Ladybug Tools which computes with DaySim, a branched validated version of Radiance (Daysim, 2019; Ward, 1994), to numerically simulate and measure the actively harnessed daylight from our facade concept. We first looked at the range of lighting levels that our design produced under different configurations (Figure 5.4, Figure 5.5, Figure 5.6), and as expected, the level of light varied depending upon the configuration. Figure 5.7 depicts the daylighting analysis for the Sierpinski design at a 1 m working height in the built space during Spring Equinox at 09:00. We then ran this simulation on a few different important days and times throughout the year (Figure 5.8). Figure 5.9 shows a yearly temporal map we generated to get a better feel for the lighting in the space year round. Averaged temporal maps (Reinhart and Wienold, 2011) have now become common in daylighting studies.

Although simulations were run with both Sierpinski and Golden designs, we focus on the Sierpinski design for the remainder of this dissertation. Figure 5.9 visualizes three design configurations, Sierpinski 30°, 60°, and maximum angle of opening, and their effect on daylighting throughout the year. The importance of this analysis is to account for an average year of weather data for the site location, which is available through local monitoring stations and the National Center for Environmental Information (NCEI, 2019).

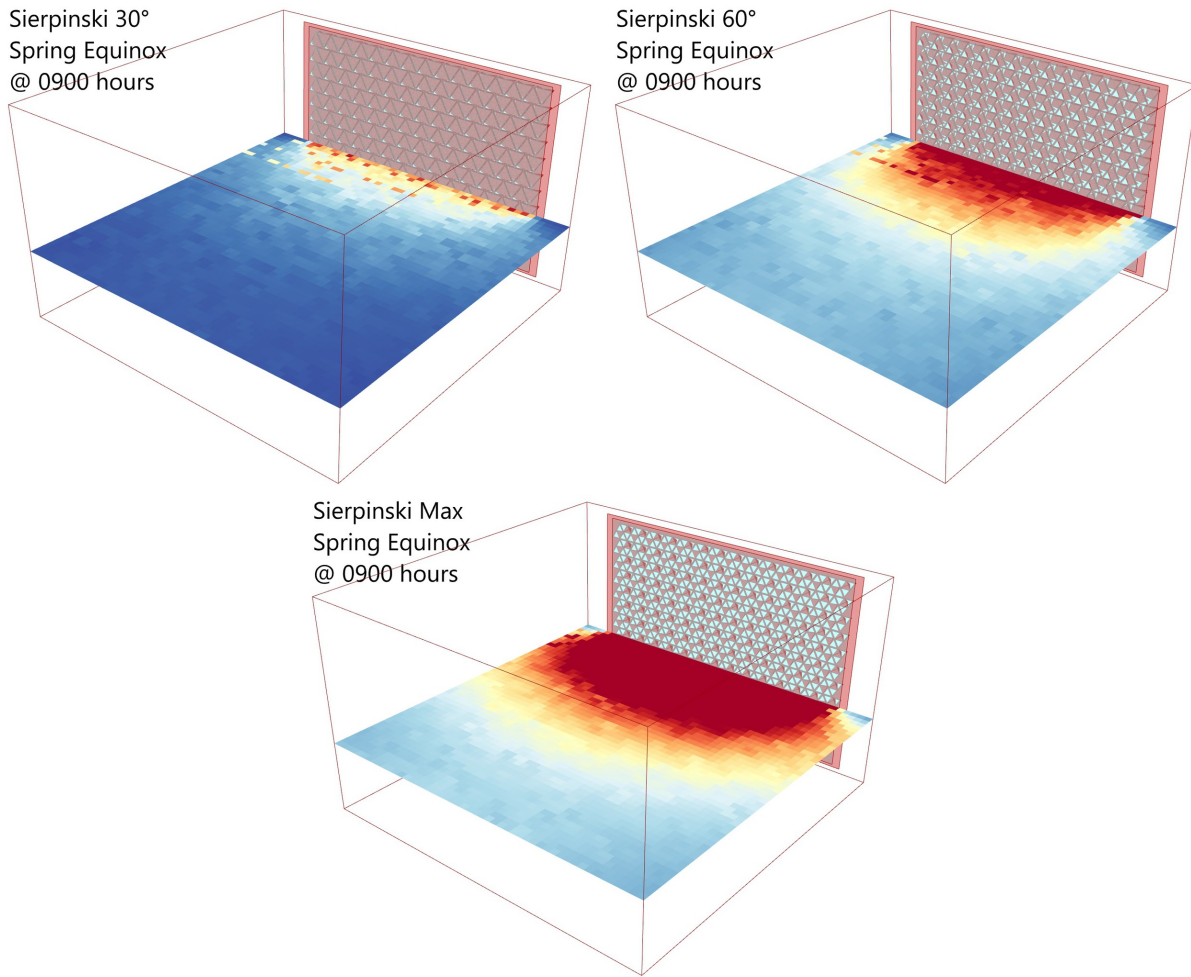


Figure 5.7: Daylight analysis of Sierpinski design, 30°, 60°, and max actuation during Spring Equinox at 09:00. The irradiance planes are situated at the standard working height of 1 m (i.e. the height of a desk surface).

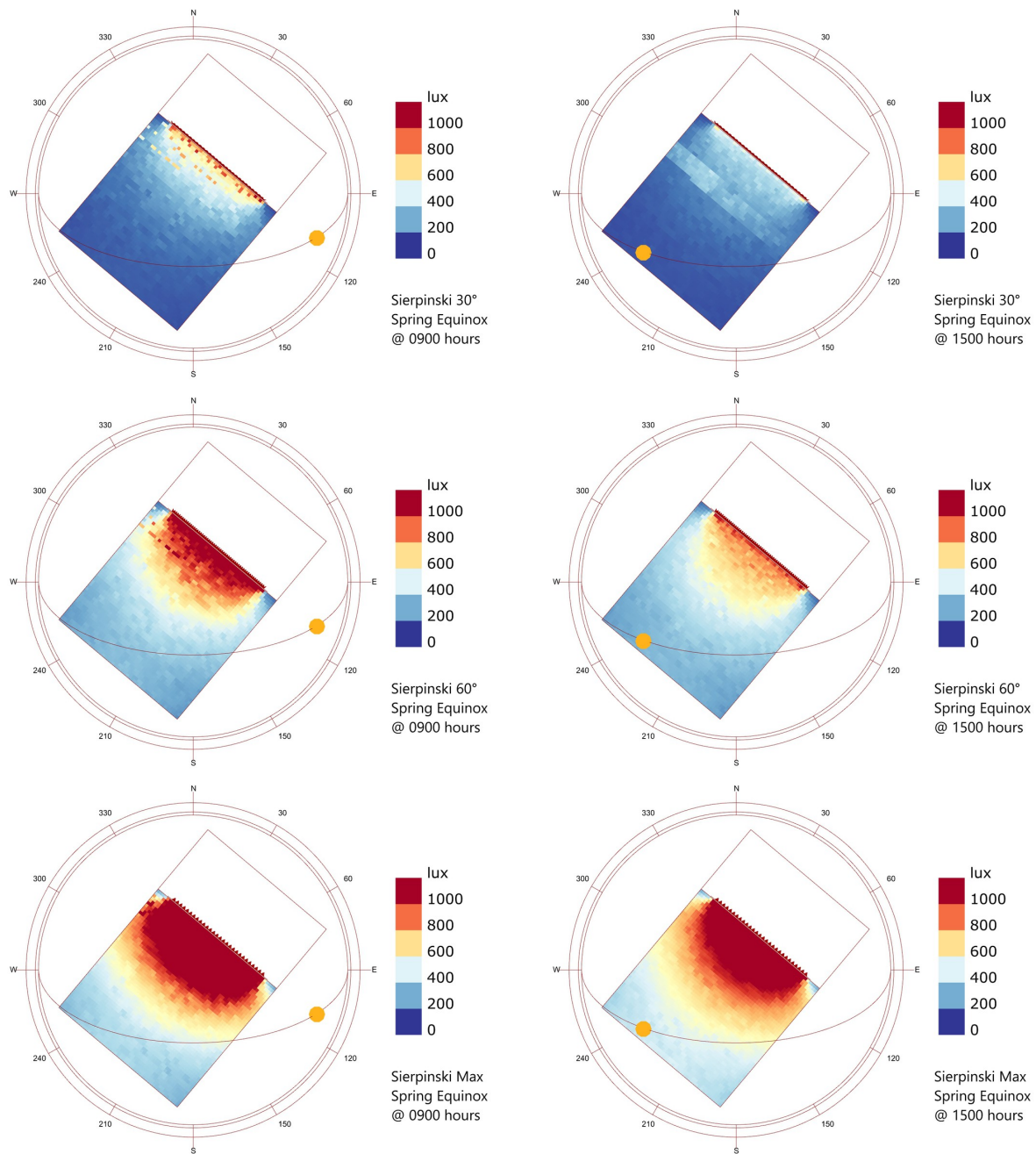


Figure 5.8: Daylighting analysis of Sierpinski design, 30°, 60°, and max actuation, during the spring equinox at 09:00 and 15:00. More daylighting analysis can be found in [Section C](#).

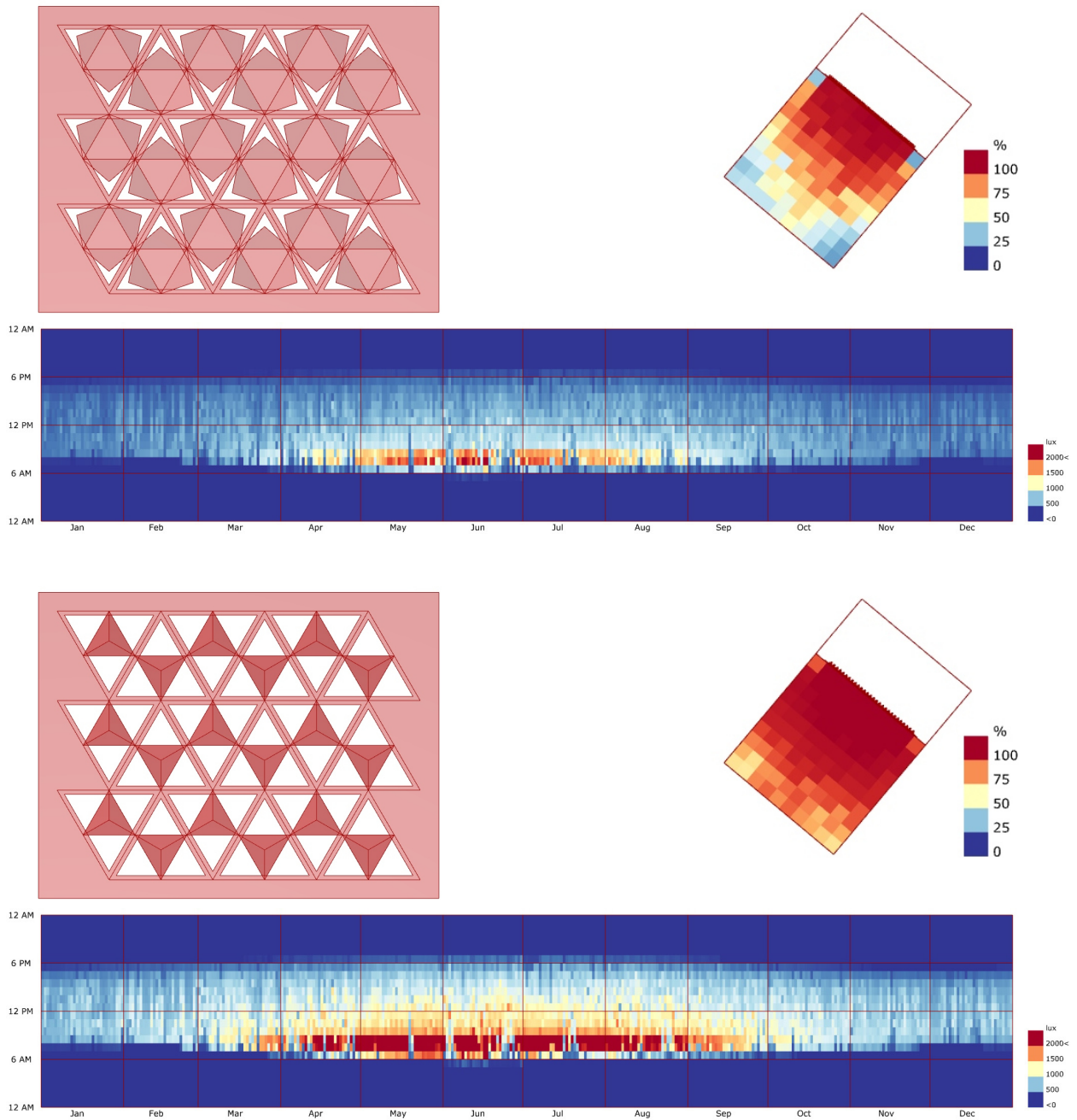


Figure 5.9: Daylighting temporal map analysis of Sierpinski design, 60° and max actuation, throughout the year, accounting for average annual weather, plotted hourly for all days of the year. Mini-plots of the space show continuous daylight autonomy (CDA) ≥ 200 lux. CDA is useful to gauge how well lit the space is over time (Reinhart and Wienold, 2011).

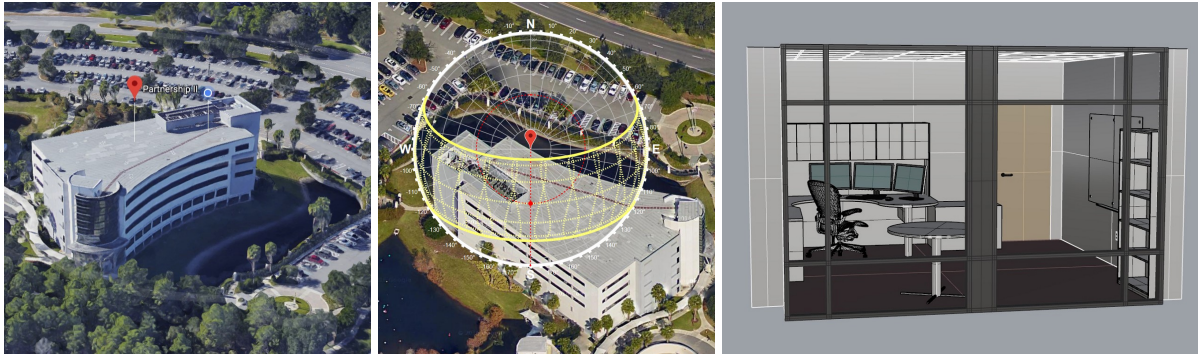


Figure 5.10: The site location for this case study is a typical office space at the Institute for Simulation and Training (IST) at the University of Central Florida (UCF) in Orlando, Florida, United States. The office faces northeast. We model and simulate our kinetic facade over the exterior window frame.

5.3 Case Study

The purpose of our case study is to evaluate the facade design for a single room before building and deploying a prototype. Our case study site location is Institute for Simulation and Training, Partnership II, located near the University of Central Florida, in Orlando, Florida, United States, DMS coordinates ($28^{\circ} 35'09.8''N$, $81^{\circ} 11'57.6''W$). This building is representative of typical office working environments in North America. [Figure 5.10](#) shows the building, solar path, and office we modeled and simulated with our adaptive facade concept. The case study site was approximately 18 ft x 16 ft, with roughly one-fourth of the space being floor to ceiling glazing where the facade was tested. The reflectivity of the different materials in the office was measured and set to simulate realistic conditions at the site. [Figure 5.11](#) and [Figure 5.12](#) demonstrate what the room will look like at 08:00 near the summer solstice. [Figure 5.13](#) and [Figure 5.14](#) show the case study office space modeled in Rhino 3D 6 and parts of the Grasshopper script logic used to create and drive the kinetic facade, respectively.

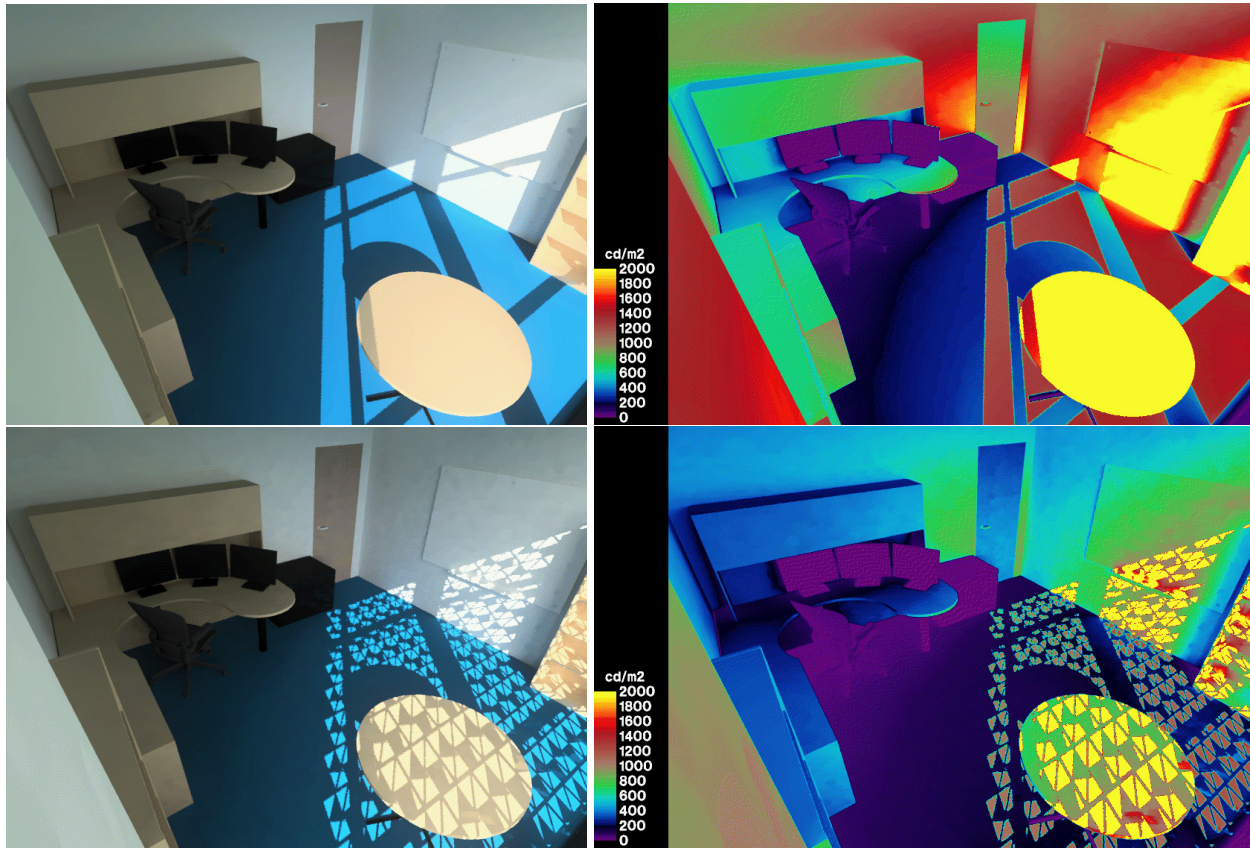


Figure 5.11: Daylighting render of our case study office at site location on 07/01/2017 at 08:00 with and without facade.

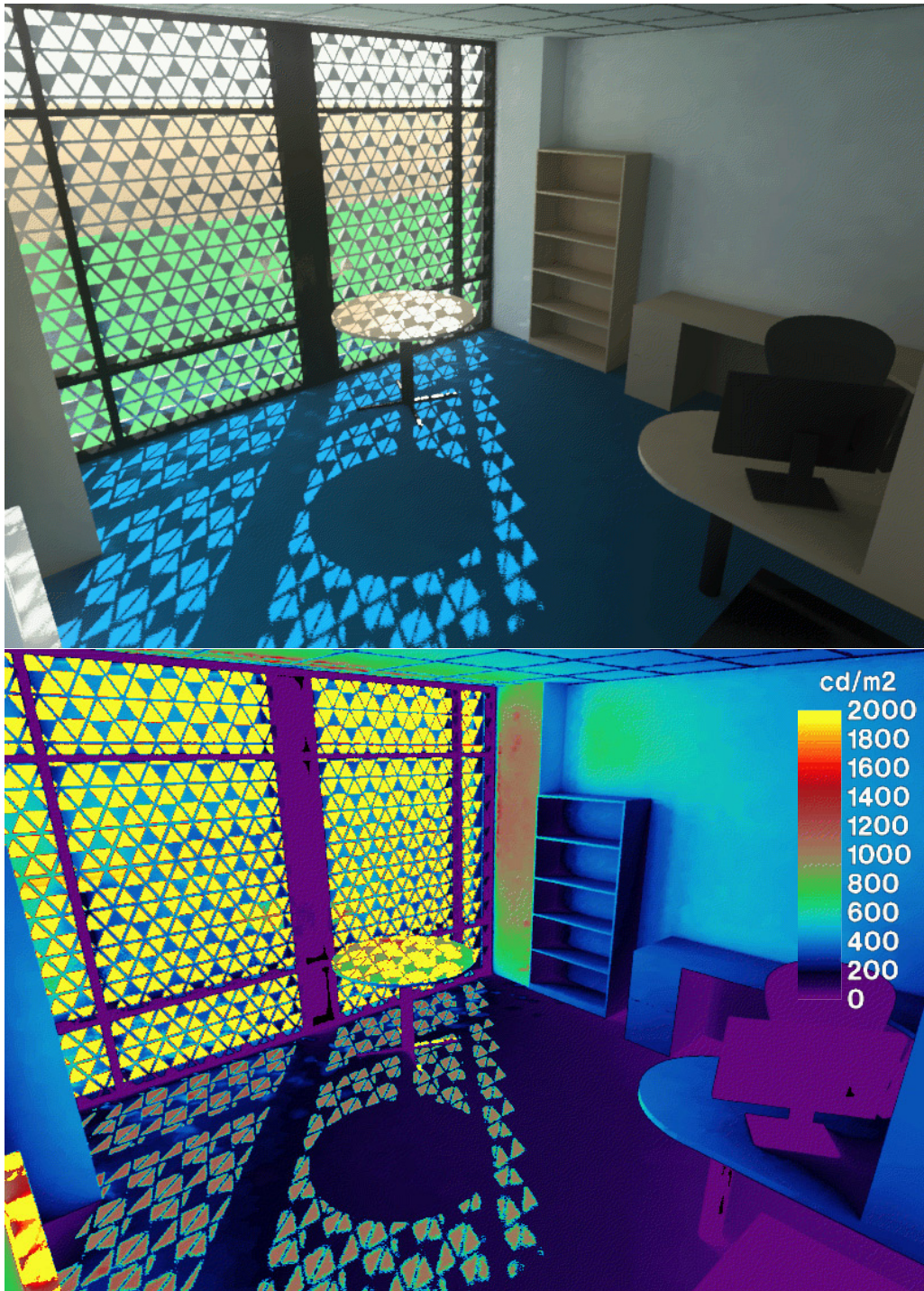


Figure 5.12: Daylighting and lux false color render of our case study office at site location on 07/01/2017 at 08:00 with facade units set to max open.

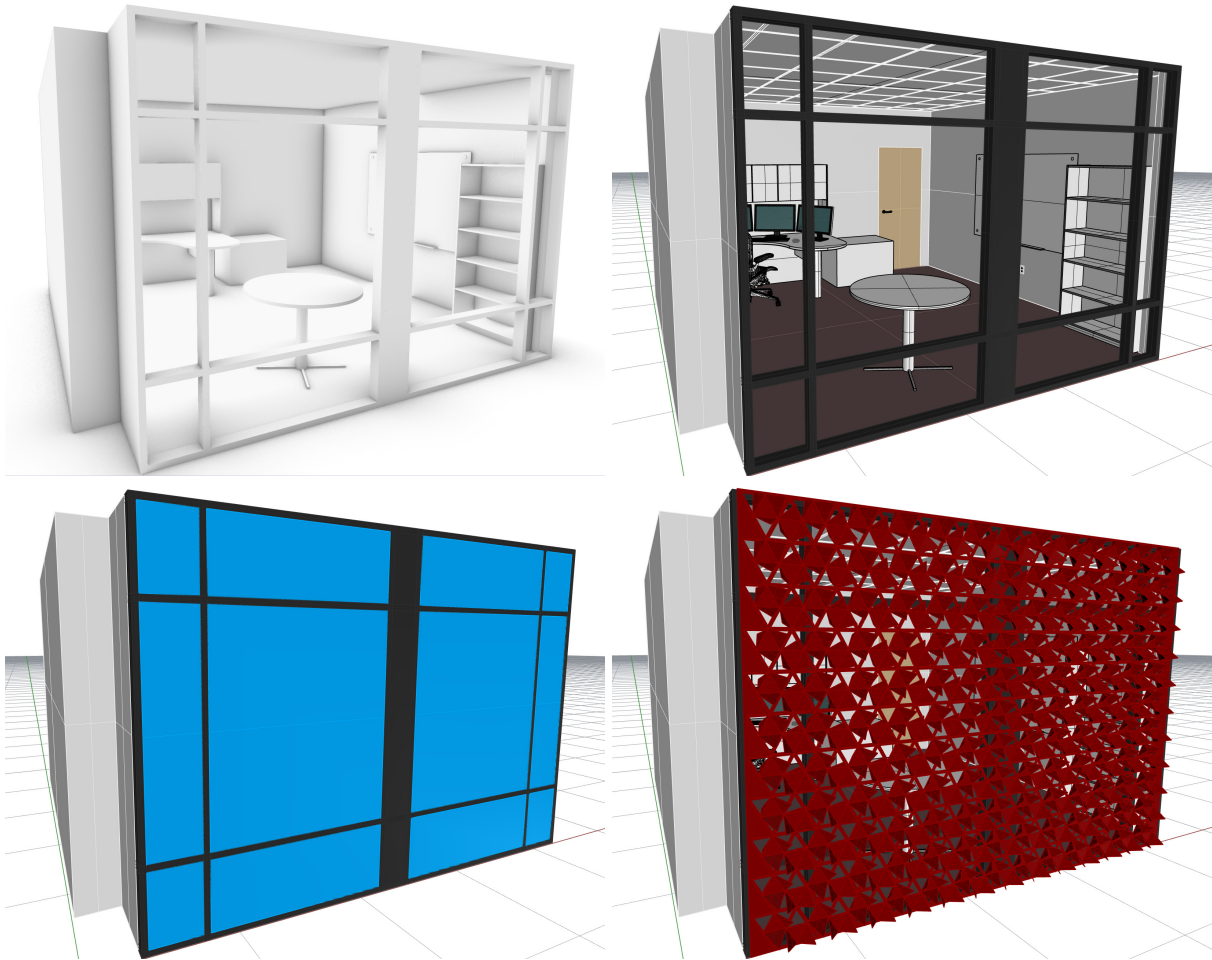


Figure 5.13: This figure shows various views of the office geometry modeled in Rhino 3D 6. The facade geometry was built and manipulated with Grasshopper logic scripting. The surface materials of the inside geometry and mullions were configured with realistic material properties for the purposes of reflection. The color of the glazing and facade do not effect lighting simulations.

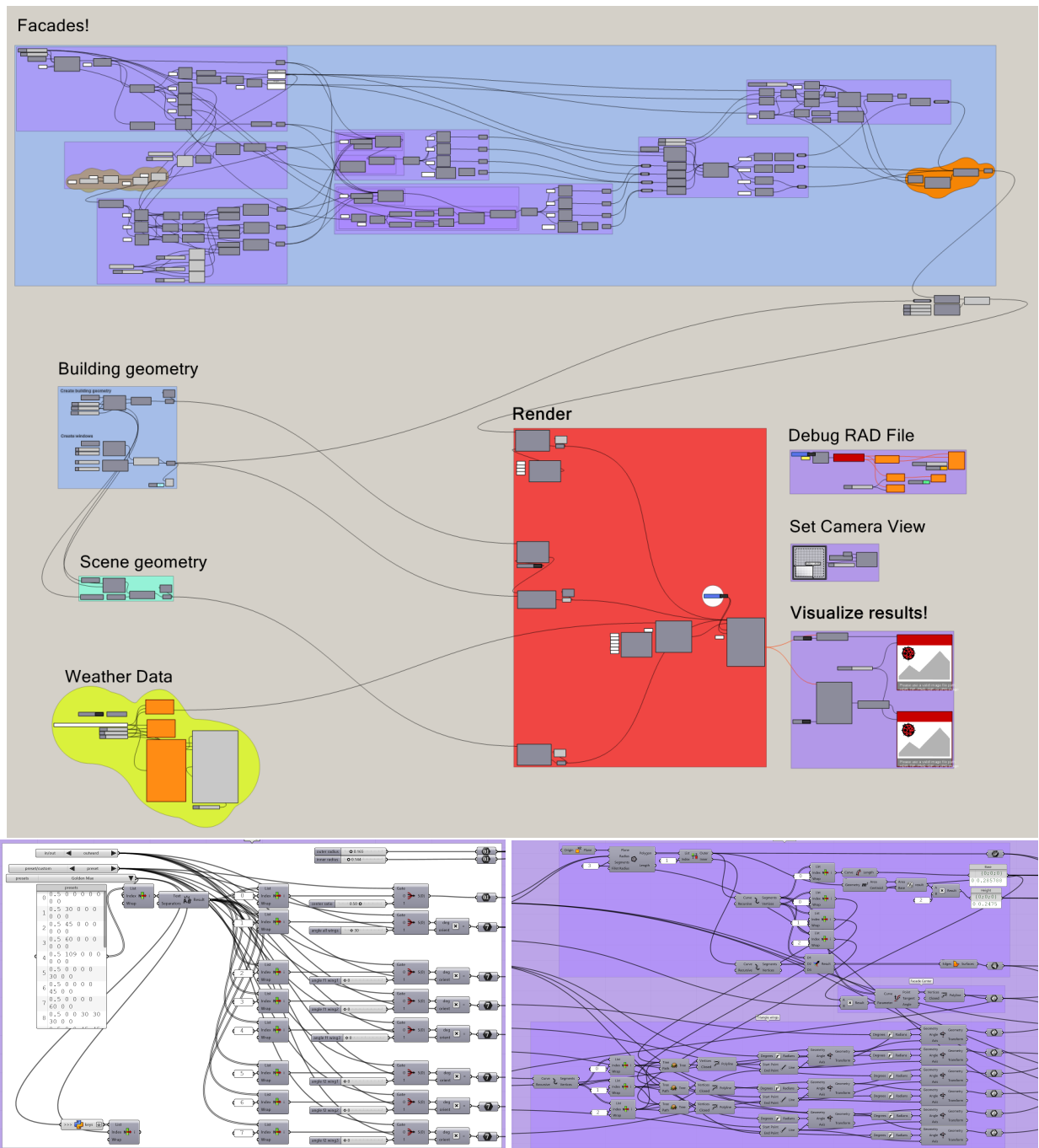


Figure 5.14: This figure shows parts of the Grasshopper script logic used to create the facade. Everything is configurable, from the dimensions of the facade units, to the number of units tiled horizontally and vertically, to the surrounding frame details. Constraints were applied so the facade units couldn't be opened beyond realistic angles.

5.4 Facade MPC Model

The sky and occupant aware building monitoring system proposed in [Figure 5.1](#) calls for a model-based predictive controller (MPC). One benefit of an MPC control system is the support for multiple input and output control variables between the controller and the controlled system ([Rawlings, 2000](#); [Qin and Badgwell, 2003](#)). Our design requires separate control inputs for kinetic facade units (for light) and smart-glazing (for heat). Another benefit is smoother control by providing constraints / limits on control variables to prevent unrealistic movement which can be too fast and potentially dangerous to system hardware and/or occupants ([Rossiter, 2017](#)). But the biggest distinctive advantage MPC provides over other control systems is the ability to model the physical system as a whole, which allows the controller to keep up with complex relationships between system variables. For example, increasing the amount of daylight into a space also heats the space.

[Figure 5.15](#) provides more details into the required pieces of an MPC controller for our sky and occupant aware building monitoring system. The “real-time” timestep is configurable but recommended between 1-5 minutes to adapt to cloud movement. Each timestep, an all-sky camera provides a photo of the sky which is passed (along with any required atmospheric measurements) to a sky model capable of providing spectral energy across the whole sky ([Del Rocco et al., 2020](#)). The resulting spectral energy is then filtered (occluded) by a pre-computed shadow map ([Roudsari et al., 2013](#)) and passed (along with a pre-configured building information model (BIM)) to BEM software capable of computing spectral irradiance per room at any desired patch resolution, although a single spectral metric may be sufficient ([Del Rocco and Kider Jr., 2021](#)). Finally, control logic with access to setpoints, occupant overrides, datetime, and schedules makes control decisions per room / zone equipped with kinetic facade and smart-glazing, e.g. whether or not (and how much) to actuate the facade to allow for the most amount of indirect light but also block direct beam light shining into a space which might cause visually discomforting glare.

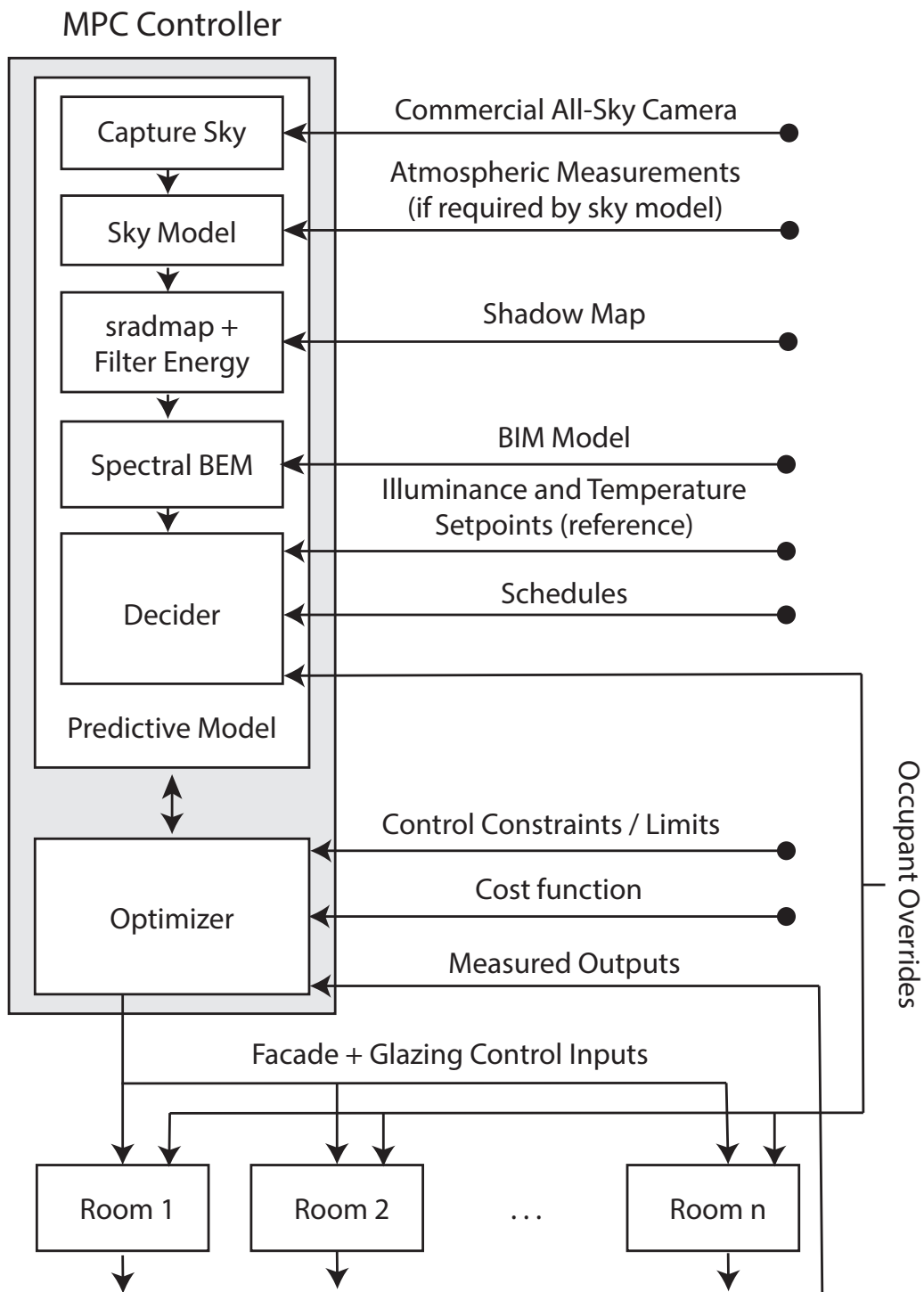


Figure 5.15: This figure highlights the design and inputs of our MPC control system.

Here we present a list of the high-level factors that the system MPC controller's predictive model should take into account. Some of these factors could be figured / computed once for the entire building, while others require control variables and outputs per zone. For example, given a spectral radiance sky model that provides energy across the skydome, daylighting and energy modeling could be computed just once for the entire building (each timestep) providing illuminance and visual and thermal comfort metrics for all zones with glazing. But then the MPC optimizer should solve for control variables per zone individually and transmit them accordingly. Some of these factors can be precomputed sparingly, but most of them should be considered per timestep of the controller. Note the controller real-time constrained timestep could be as slow as 3 to 10 minutes if desired, as building daylighting and energy simulations are still time consuming (as discussed in previous chapters) and intra-minute predictions are unnecessary for a building monitoring system that adapts to changes in the sky.

The following factors should be computed offline once (or at most once a year) and used as input into the model:

- Shadow masks of the hemispherical sky should be computed occasionally to account for neighboring buildings, billboards, trees, large permanent shrubbery, etc. These masks should be captured / computed from the center top of the building and provided as input to the model so that it can apply them to (filter) the spectral radiant energy provided by the sky model.
- Sunrise and sunset times should be provided as inputs for each day of the year so that daylight hours are known in advance. Tables of such data are easy to obtain and/or compute with the NREL SPA algorithm ([Reda and Andreas, 2004](#)) for years in advance. The building facade system MPC model should ensure that control timestep updates occur only during daylight hours, and simply close all wings to prevent seeing building occupants from the outside of the building.

- Default visual comfort limits should be predetermined offline, either loaded from standard recommendations or configured and done so for daylight hours only. This includes both minimum and maximum levels which the model will use to harness more daylight or deflect incoming beam radiation to reduce glare as necessary per zone.
- Actuation angular limits and movement speed constraints should be predetermined offline and loaded as constraints into the optimizing solver to limit angular movement and prevent fast movements by the facade units, which could be visually jarring and/or damage the units themselves and/or passers-by.
- Site location, elevation, albedo, climate zone, and general (non-sky specific) atmospheric parameters should be acquired to improve the accuracy of any sky model.

The following factors should be computed once per MPC controller timestep for the entire building:

- Daylighting and building energy modeling simulations capable of processing spectral radiance throughout the sky at some configurable resolution should be run per timestep to provide accurate spectral irradiance vectors with both light and heat for each zone. Zone compute grid resolution could be pre-configured or defaulted to a single irradiance vector per zone.
- If local atmospheric parameters are required by the sky model, and they are available from a public database of local measuring station through an API, acquire them. Local atmospheric parameters could include: outdoor temperature, humidity, barometric pressure, active precipitation including ground snow (changes albedo), wind speed and direction, aerosol optical depth (AOD), cloud height, cloud cover octas or percentage, types of clouds, ash, pollutants, etc.

The following factors should be considered per MPC controller timestep for each zone:

- Visual comfort setpoints should be used by the model to provide both an optimal level of illumination of visible energy per zone, and reduce excessive illumination as the result of direct beam solar radiation. Given metrics provided by the daylighting simulation per timestep, the MPC will control within these setpoints. In general, per zone, we should see facades fully open when only indirect sky radiation is available, and they should fluctuate slowly between partially closed to fully open as clouds move in front of the sun. On a clear day with direct beam solar hitting the zone and no occluders nearby, the facades should block a majority of incoming radiation to prevent visual discomfort (glare).
- Occupants can override (set) the facade angles to any desired (possible) configuration if they desire to do so regardless if the decision results in visual and/or thermal discomfort. Occupants have the right to increase or decrease natural daylight as they see fit, and to view the outside for piece of mind, safety, and curiosity.
- Thermal comfort limits and external temperature could be used by the model to control for infrared filtering with smart-glazing. If external temperature is below the minimum limit the controller can allow incoming infrared energy; if above the maximum limit, it can filter infrared. This behavior will generally follow the seasons, but updates per timestep allow for temperature fluctuations throughout the day, such as days that start off cold and warm up or vice versa.

5.5 Facade Physical Prototype

Here we detail the process and materials used to construct the physical portion of our facade prototype. Translation from design to physical prototype in this case was conceptually simple, at first involving nothing more than a servo and some pliable material for the unit center and

wings, but became physically challenging due to gravity pulling on the “wings” of the units. In other words, a “top-down” prototype on a horizontal plane was much easier to build than one mounted to a vertical plane. Various designs were considered, from a complex drive train of gears and pulleys, to a “string and spring” concept that pulled the wings with a continuous servo against tension from springs. Eventually we settled on a central “pulley” disc that lifted the wings with static rods. Various triangular unit prototype versions are shown in [Figure 5.16](#) and [Figure 5.17](#). The final triangular unit prototype is shown in [Figure 5.18](#).

Early on in the process, an outer frame composed of 2 in x 4 in wood was built to the dimensions of the window frame we would be using during testing (originally the same office simulated in [Figure 5.10](#)). A “cart” with casters was added to make it easier to move around, and bolts for easy mounting and removal. As the triangular units are equilateral by design, only simple calculations were needed to find the best array layout (rows and columns) of units sized appropriately to fill the space. A final count of 6 rows of 7 units, each with triangular sides of 6.5 inches in length, would fill most of the space. Various ideas were proposed for mounting the triangular units to this frame, including mounting rods and tracks, but in the end we decided to have a large piece of clear acrylic cut to the frame size that we would attach the triangular units directly to. This decision was made to remove the complications of mounting and to keep the incoming light patterns as similar to the simulation results as possible. It also allows us to reuse this structure as new facade designs are tested in the future. The large, heavy, clear piece of acrylic was both epoxied and screwed to the frame to distribute the weight as evenly as possible and ensure it did not crack or split due to gravity pressure. As for screwing the acrylic to the frame, a special drill bit was needed to drill through the acrylic without cracking it, and for each screw, both a neoprene and metal washer were used to dampen pressure, while flexible silicone was filled into the remaining space around each screw. Thus if the epoxy weakened due to gravity and movement over time, this would relieve some of the eventual pressure on the acrylic. See [Figure 5.19](#).

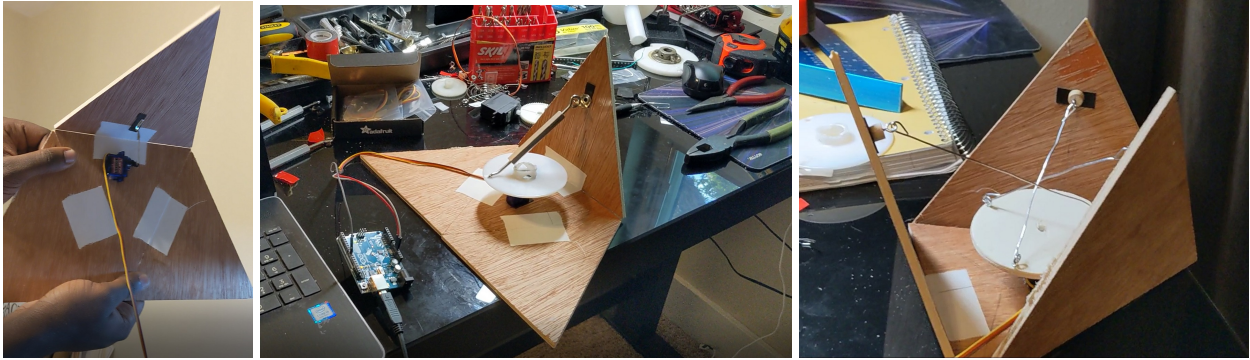


Figure 5.16: This figure shows various early triangular unit prototype designs, including a servo per wing, turnbuckle bolts and galvanized wire rods. Other more complex (non working) prototypes are not shown.

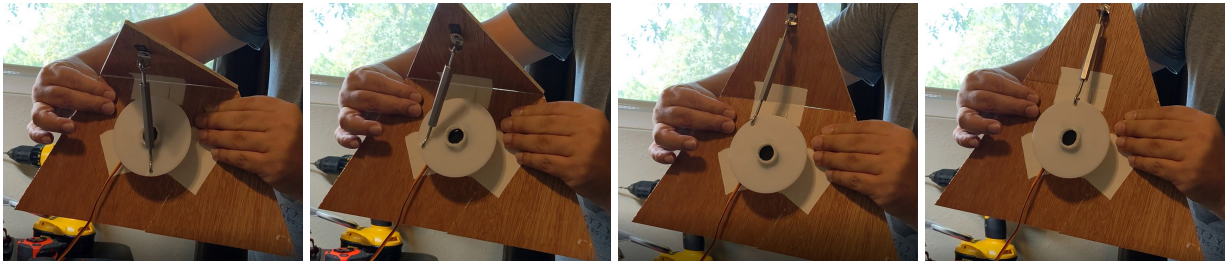


Figure 5.17: This figure demonstrates the second prototype in Figure 5.16 opening against gravity.

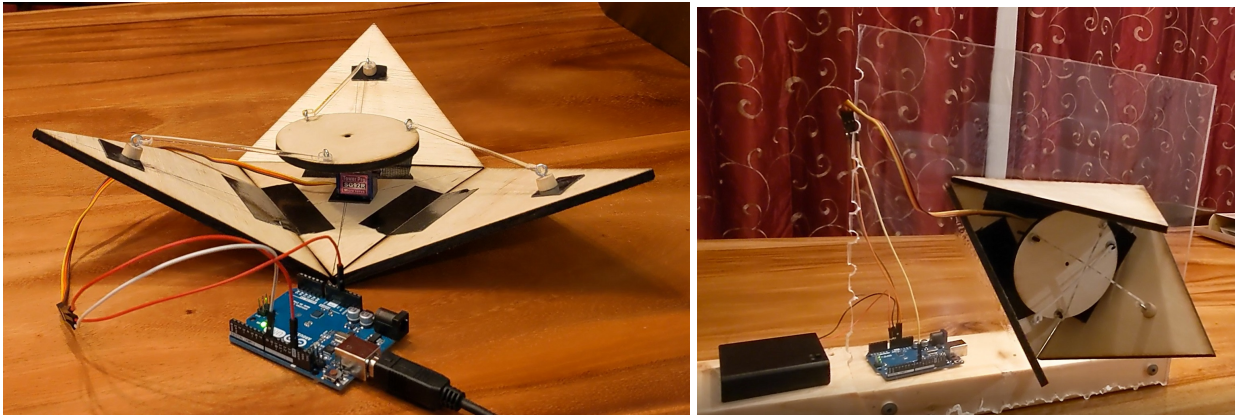


Figure 5.18: The final triangular unit prototype working horizontally and vertically against gravity. The vertical test is mounted with the same material as the final intended facade prototype.



Figure 5.19: Here we show the 2 x 4 frame with mounted acrylic. The acrylic was both epoxied and screwed with star-drive deck screws pulling against neoprene and metal washers.

Throughout the prototyping process, various lightweight materials were tested for the unit center and “wings,” including: cardboard, acrylic, balsa wood, and lauan plywood. These were taped together with strips of non-reflective Gaffer tape for a smooth, bendable, yet strong binding that could eventually be removed. The center pulley disc also moved from plastic to wood. The connecting rods were the most diverse, constructed from galvanized wire, wood, 3D printed plastic, and acrylic. We also needed to consider how the rods would be mounted to the pulley disc and triangular wings. This design evolved the most because of the angular movement that occurs between rod and mounting point. Most of these materials were purchased from local hardware

or surplus shops like [Skycraft Surplus Ltd. \(1974\)](#). We were constantly considering the weight, stress, and angular movement of rods and joints while looking for and trying pieces. Sometimes what worked well horizontally, didn't work as well vertically, or vice versa. And if building a single well-designed and durable triangular unit wasn't challenging enough, we then needed to consider how all of the units would be produced as uniformly as possible. For example, galvanized wire for the rods, while strong and cheap, were difficult to cut and bend (and ultimately reproduce) to the exact lengths and hooks needed. 3D designed and printed rods, while lightweight, perfectly rounded unlike laser-cut materials, and flexible for snapping into place, were too expensive to produce en masse because of the cost of the ink required ([Figure 5.20](#)). Sometimes what we found locally, couldn't be found (affordably) over the Internet to complete our project, while other times we needed to wait for materials to come in, simply to try them and realize they wouldn't work as originally thought. The final triangular unit prototype is shown in [Figure 5.18](#).

We utilized the *Texas Instruments Innovation Lab* on campus at the University of Central Florida ([Figure 5.22](#)), which offers a 75-watt laser-cutter with 2 ft x 4 ft bed, metal shop and various high quality 3D printers. Finally, we settled on laser-cutting all triangular unit wings, backings, and pulley discs out of lauan plywood and laser-cutting the rods out of acrylic. The materials at connection points between rods, discs and wings would be leveraged from local hardware stores. We designed all of the wood and acrylic pieces for laser-cutting in *Rhino 3D 6* and exported flat vector graphics files (PDFs) for the software to work with. Sometimes this involved setting certain "layers" of curves to different colors so the laser could switch between marking and cutting ([Figure 5.21](#)). Despite all of our planning, several trips were needed to the Innovation Lab over a period of a few months.

To actuate the kinetic triangular units, we originally started with Longrunner LKY62 continuous servos, but because the current required to spin the servos was dependant upon the lift weight (a



Figure 5.20: Here we show the 3D printing of triangular unit rods, which were perfect for the prototype because of their round shape and flexibility, but were too expensive to produce en masse.

changing variable during prototyping), and because there was no feedback sensor to determine how far the servos had moved, we abandoned these servos for TowerPro SG92R micro servos with a standard range of 0-180°(Figure 5.23). These micro servos are only 23 x 11 x 29 mm and weigh only 9 grams, yet have 2.5 kg-cm of torque and can turn their full range of motion in just 0.3 seconds. We purchased them through [Adafruit Industries](#) (2005). We initially mounted one of these servos per wing, but for cost reasons simplified the design to a single servo per unit. This decision removed the ability to control unit wings individually, a desirable but expensive feature



Figure 5.21: Here we show various photos of the laser-cutter at work on sheets of lauan plywood and acrylic. All triangular unit centers, backs, “wings,” discs, and connecting rods were cut with a Universal Laser Systems ILS12.150D laser-cutter. Our Rhino designs provided holes in the discs and centering markings per wing to save us time during assembly.



Figure 5.22: We utilized the *Texas Instruments Innovation Lab* in the Engineering II building on UCF campus for all laser-cutting and 3D printing. The lab offers a “maker space” complete with 75 watt laser-cutter, a wide variety of 3D printers, workbenches, electronic lab bench, soldering stations, general tools, etc.



Figure 5.23: Here we show the Longrunner LKY62 continuous servo and the TowerPro SG92R standard servo experimented with, both of which came from [Adafruit Industries \(2005\)](#). The TowerPro servos were ultimately used for this work. The rightmost image shows available horns that were used to connect the servos to the triangular unit facade discs.

during prototyping. We considered screwing or gluing the servos to the units, but decided on using strong Scotch Mount 3M double sided tape in case servos had to be replaced or eventually reused. This also allows us to reuse the facade frame acrylic in the future.

Assembly, mounting, wiring, and row-by-row testing of all triangular units alone took months (part-time). Each unit required: wings to be taped, backing to be glued, rod connecting point tabs to be pre-drilled with eye hooks screwed in, cotter pins and washers to be installed on the discs along with servo horns to be screwed on, rods to be hooked into place, servos to be mounted, wires to be cut and stripped soldered and heat-shrink wrapped, etc. Sometimes the glue curing would limit what else could be done or altogether put a stop to assembly for that day. Only some of the rods could be hooked into place as wiring and soldering required movement of the wings to access the wires. Therefore the process was interleaved with some of the assembly occurring before wiring and mounting and some after. During this assembly, mounting and wiring phase, the entire facade frame was brought up and down as needed to access all of the units and their wires ([Figure 5.24](#)). The final step involved taping any remaining areas of the facade that were not covered by the triangular units. We did this with Gaffer tape so that it could be easily removed in

the future if additional rows or designs were desired. Throughout the process of constructing the physical facade prototype, we strove to preserve the acrylic frame for use in future projects.

We used an Arduino MEGA2560 for the micro-controller because it can control up to 54 separate digital I/O lines along with 16 analog inputs. Our design would have either 42 or 49 triangular units (6 or 7 rows) and feature a potentiometer for manual control. The required amperage needed to power so many triangular units was discussed and computed along with the required gauge of wire (this included a discussion about solid versus stranded wire). The Arduino itself would not be able to power so many servos because of the required current, so a Letour 5 volt 30 ampere AC to DC external power supply converter was used to provide the power. The decision was made to run the wires from the units to the end of each row, joining the power and ground lines because only the control wires needed to be unique, and then run the wires down the frame to the micro-controller and external power supply. We used 3 component 22 AWG stranded wire for the servos with control sent directly to the Arduino and joined the power and ground with a power distribution block per row. Each row of power and ground was run to the external power supply via 2 component 14 AWG stranded wire. All 6 rows of power and ground were then joined to 10 AWG wire which was then connected to the external power supply. To complete the circuit a ground wire was run from the Arduino to the external power supply as well ([Figure 5.25](#)).

To connect each servo to the Arduino, the wires would have to run alongside the triangular units somehow without interfering with the incoming light or preventing the wings from fully opening. Among many other things, this was not considered during design and simulation, and therefore had to be figured out during prototyping. We arranged the triangular units various ways and discussed how the wires could best be hidden while still maintaining the original orientation and light pattern results of the our simulations for best comparisons. We eventually decided upon adding a backing piece to each unit which when mounted creates a channel between the triangular units and the

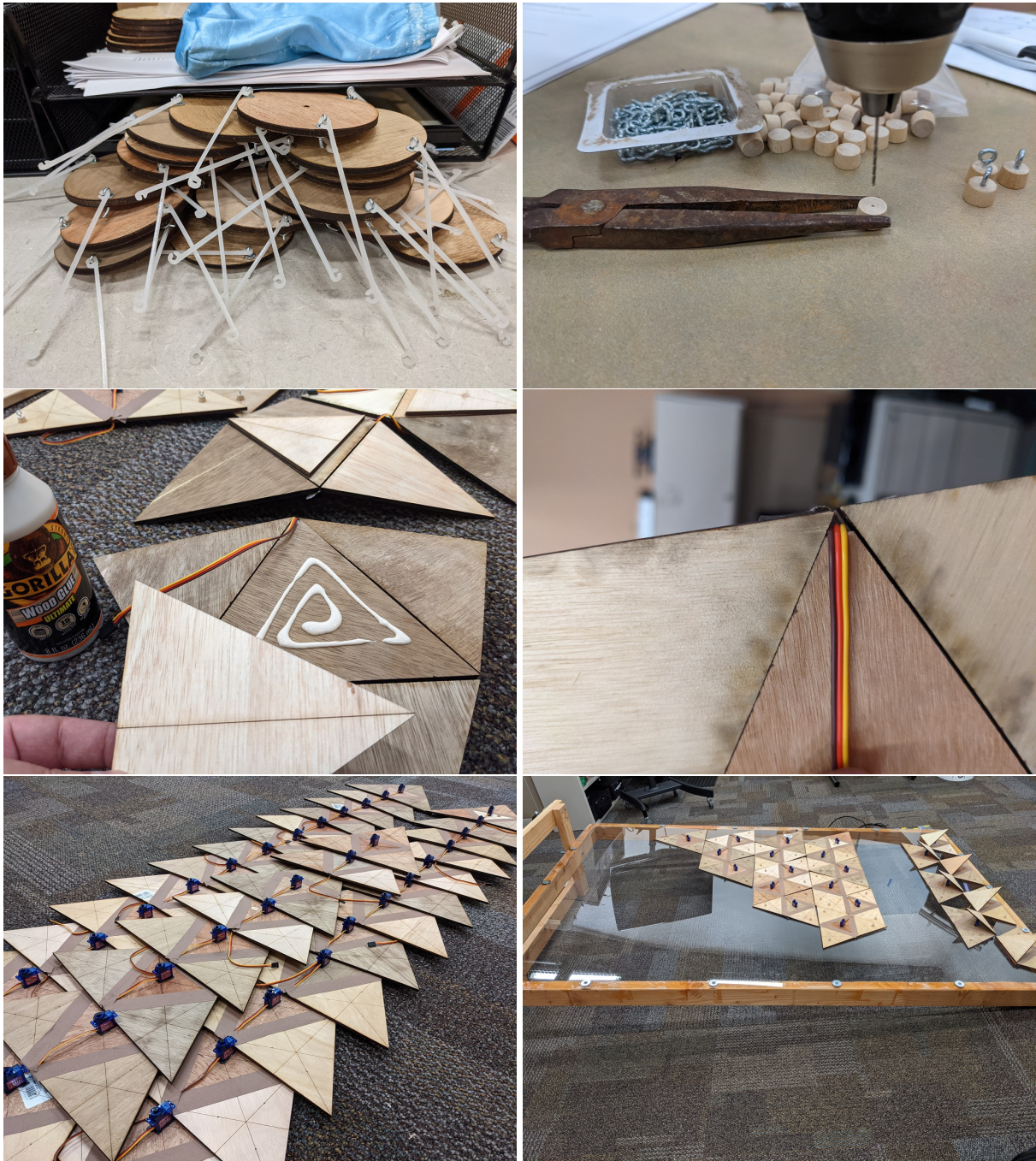


Figure 5.24: This figure shows several snapshots during assembly. In truth, assembly and wiring stages were somewhat interleaved.



Figure 5.25: This figure shows several snapshots during wiring. In truth, assembly and wiring stages were somewhat interleaved.

acrylic backing to run the wires without interfering with the light or the unit wings. These backing pieces were cut at the lab relatively late in the prototyping process. Once mounted, we soldered each of the 3 wires per servo of 42 triangular units for a total of 126 soldering points. Each stranded wire connection was made with a “lineman’s” (or “Western Union’s”) splice and wrapped with heat-shrink tubing. The control wires were also numbered to make it easier to track down servos if they failed. Because we used stranded wire, which is more flexible and malleable, we also had to solder stiff tips to each control wire so that they could be properly inserted into the Arduino digital input ports, as stranded wire would often bend when inserted.

The facade physical prototype was tested row by row of triangular units as it was wired and assembled (Figure 5.26). Once a row was working, it was easier to add additional rows to the programming. The default program was to simply “sweep” the servos, or in this case, actuate the triangular facade units from fully closed to fully open and back gently. It also brings the units back to a closed position if started in an already open position.

Finally, a proof of concept experiment (field test) (Figure 5.27) was performed in a conference room within the same site location, identical window size and glazing as was used in our simulations (Figure 5.10). The experiment was performed on Saturday, 10/09/2021 between 13:15 and 13:30 EST. As the site location faces Northeast, all incoming energy was indirect diffuse sky and ground reflected energy (i.e. no direct beam sunlight reached our facade in this particular field test). Our facade was designed to be mounted on the outside of a building, and so testing must comply, but to avoid actually mounting the facade to the exterior of the building at that time, it was simply held in place and powered by a nearby exterior power receptacle. There were other windows in the conference room which had to be covered to not interfere with the incoming light harnessed by our facade. Thankfully, a light blocking phantom screen covered most of the windows, while the remaining window were covered with curtains. Interior lighting was disabled for

the experiment. Photos were taken of the facade while it was manually controlled (occupant override) to various angles: 30°, 60°, and 90°. A photo of the sky and surrounding environment are shown in [Figure 5.28](#).



Figure 5.26: This figure demonstrates testing of the physical prototype in a lab space, which was accomplished one row at a time. Because the frame is larger than a typical doorway, it requires multiple people to move it to an actual experiment.

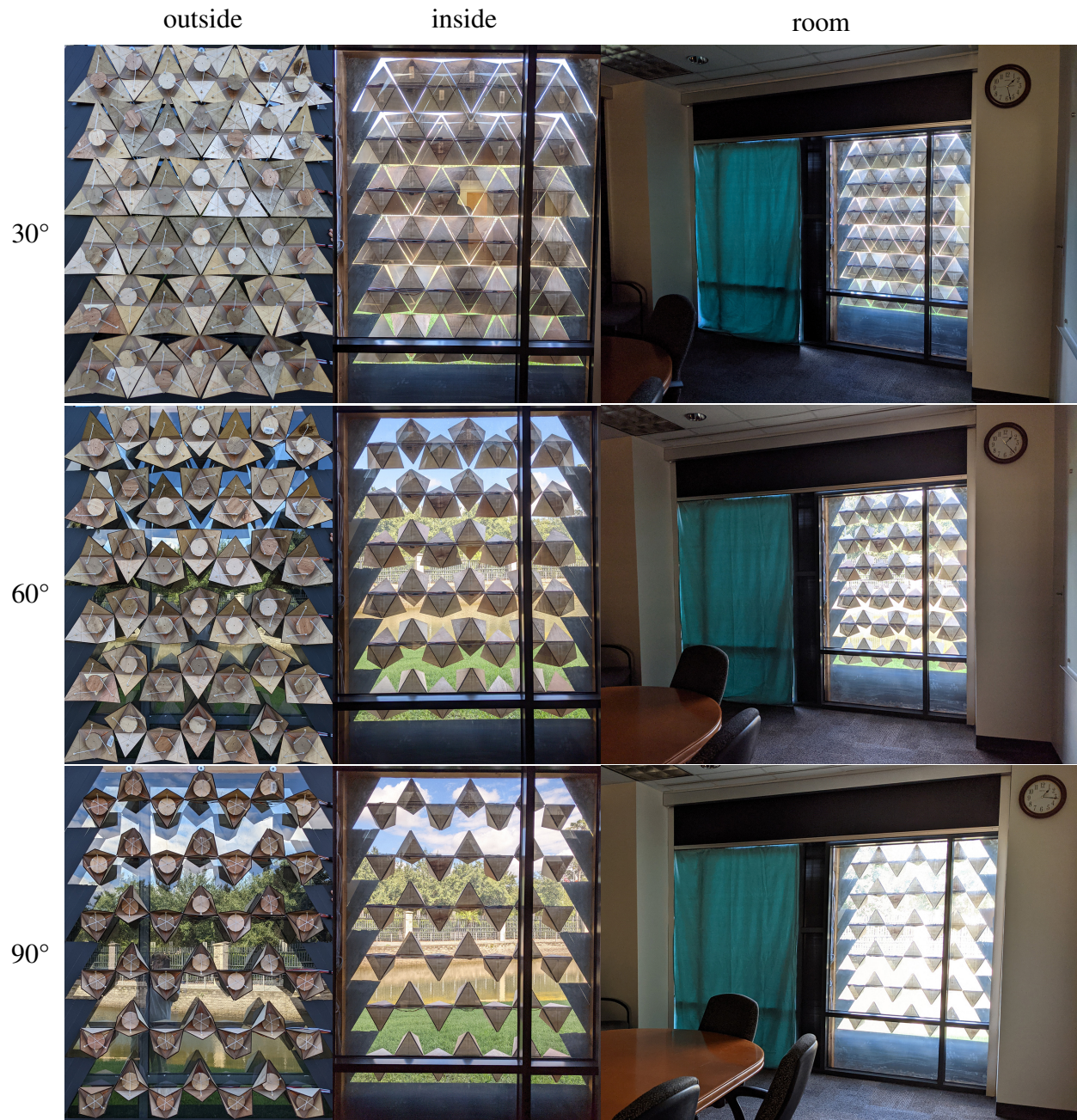


Figure 5.27: This figure shows the results of testing our kinetic facade physical prototype over a window in a conference room at the same site location as our simulations in [Figure 5.10](#). Three degrees of opening were tested, 30°, 60°, and 90°(max open for this design). Although environmental conditions were not perfectly controlled, we can still see the increase and decrease in harnessed light in the space.



Figure 5.28: A photo of the sky on Saturday, 10/09/2021 at 13:15 EST when the physical facade prototype was tested in a real setting. Note the shadow of the building and lack of direct beam solar because the site location faces Northeast.

CHAPTER 6: CONCLUSIONS

Buildings contribute to climate change and the global greenhouse gas (GHG) footprint indirectly through the use and thus production of electrical energy. Heating, ventilation, air-conditioning (HVAC) and artificial lighting contribute significantly toward building energy use and therefore reductions can help curb GHG emissions. This dissertation contributes by refining some of the methods used in building performance simulation (BPS), architectural design tools, and building monitoring control systems, all of which can leverage solar energy (both light and heat) to reduce artificial lighting and HVAC energy use. Building energy modeling (BEM) and daylighting studies often oversimplify the actual solar energy resulting from the sky and the surrounding environment as well as ignore the fact that it contains both light and heat. This radiant spectral solar energy can be avoided or passively or actively harvested, but it is important that simulations and buildings do it accurately to maximize gains.

Whole sky spectral radiance distributions are needed for accurate computations in a variety of applications. Real-time capable models are needed to estimate them to within acceptable tolerances. We presented a solution for this that: (1) collated and processed photographs of the entire hemispherical sky along with radiance measurements throughout the sky, (2) used those measurements and modern machine learning methods to train regression models, and (3) used the downstream models to predict atmospheric spectral radiance (350-1780 nm) at 1 nm resolution for entire skies, given a photo of a clear sky and its capture timestamp. The whole sky RMSD error of our predicted results for all four holdout test skies, none of which were used for training, was below 7.5% RMSD, and most of the predicted spectral radiance distributions were in line with libRadtran's. Our data-driven sky model results show that image compression, color model, and exposure of clear sky imagery have little to no effect on our method. This implies that our solution is robust

and less likely to be affected by implementation details. We also showed that our regression models have the ability to generalize across the hemispherical space between measured sky samples, allowing for atmospheric spectral radiance predictions for every point in a sky image. Our regression models can be used, as-is, with similarly exposed and oriented sky photos, and our methods can be reproduced to train models using new datasets. Various sky scanning systems exist which can be employed to provide more training data for this approach.

We developed and presented a spectral energy solution for early design BPS and real-time control systems in the built environment by modifying a custom radiosity engine for radiant spectral energy and providing a plugin interface from a modeling software package often used by architects. With this process, we ran spectral energy simulations through four separate glazing options on a realistic, sufficiently complex model of an existing office. We demonstrated that our proposed adaptive smart glazing solutions could filter or allow visible and/or thermal energy, or indeed any spectral range of interest, and in general be used for natural daylighting and heating solutions. Our results imply that such a spectral energy modeling system is fast enough to be used in early-phase design by building designers utilizing parametric design for interiors, shading devices, materials, etc. Also, a more refined and modular version of this system could be packaged and used by building monitoring systems to drive real-time control systems.

Finally, we designed, modeled, simulated, and constructed most of an adaptive facade cyber-physical prototype building monitoring system, which has the potential to monitor the sky and occupants and then drive kinetic facades and smart glazing appropriately. A more refined version of this system could be constructed and made available for buildings with high HVAC and/or interior lighting costs to help actively harness light and heat more efficiently. Such a system is not limited to the exterior facade we designed and built; any kinetic facade could be controlled by such a system and could be coupled with, de-coupled, or replaced by smart glazing solutions for

independent spectral modulation.

The work we have done contributes to the fields of atmospheric science, building performance, and smart architecture by detailing a new data-driven sky model, proposing changes to daylighting and energy modeling and simulation pipelines, and by cyber-physical experimentation, respectively. Much of the research presented in this dissertation has been published in relevant, peer-reviewed conferences and journals. We are confident that our contributions are valuable to the building performance community because some of our work has already been cited in recent literature. We hope we have motivated the community to improve upon our methods to further realize more fine-grain, sky and occupant aware building control systems. Such systems need to account for radiant energy to properly handle occlusion, as well as for energy that is diffused in specific cloud formations. A spectral energy pipeline would ultimately simplify lighting and heating simulations, give building monitor control systems the ability to filter or allow infrared (given the glazing technology), and give early-phase building designers the ability to simulate and compare glazing options. Accounting for these factors will improve the accuracy of building performance simulations and strengthen real-time building control, which in turn can reduce energy needs, greenhouse gas emissions, and save money.

6.1 Ongoing and Future Work

Work on predicting spectral radiance from scattered and overcast skies using our dataset is currently underway. We have already seen promising results ([Figure 3.23](#)). Scattered skies account for the bulk of our training data as well as the more interesting energy scattering scenarios. More modern machine learning techniques (e.g. deep-learning with *Google TensorFlow*) are already being leveraged. Once scattered sky research is complete, we will attempt to train a single unified model that handles skies of all conditions: clear, scattered and overcast. Ideally, two separate models per sky condition should be trained, one that includes regional atmospheric measurements, and

one that does not, to account for situations where atmospheric measurements are not available.

We believe it to be worthwhile to produce a single (or multiple) merged dataset(s) of existing ground-to-sky measurements, normalized, from different locations around the world. Existing correlated sky imagery and spectral radiance datasets from around the world can be used by all data-driven approaches. We imagine an open, standardised, searchable dataset for skies measured from the ground. The greatest challenge would be normalization (rotation, file formats, lens linearity, camera calibration, etc.), which could be done during an upload process or more likely as a separate pre-process before being uploaded. Once normalized, such comprehensive datasets could lead to even more robust machine-learned models (e.g. more variations of skies, turbidity, pollution, etc.), especially if coupled with atmospheric input features from triangulated atmospheric measuring station data. Site location coordinates and/or elevation could also be investigated as input features themselves when using multi-site data to help the machine learning algorithms learn location-specific variations. Even if all datasets cannot be merged into a single dataset, merging a few at a time can still help prevent machine learning algorithms from over-fitting region-specific nuances.

It is possible to combine our proposed whole sky aware building monitor prototype with projections of upcoming skies. Cloud formations can be predicted in upcoming skies to within intrahour estimates (Nou et al., 2018; Chacon-Murguia and Ramirez-Alonso, 2015; Chen and Mied, 2013; Song and Ra, 2000; Skowronski, 1999). If such skies were fed to a whole sky aware building monitoring system, preemptive changes could be made per zone to account for expected increases and decreases in solar radiation. Doing so could help reduce HVAC recovery time and operating cost. Abrupt increases in direct beam solar radiation, for example as clouds block and reveal the sun, can cause zones to heat up quickly beyond set point and require an HVAC system to spend more time (and cost) in recovery. Intrahour sky predictions could drive preemptive control modifications

to HVAC cold deck temperature and flow set points in order to reduce this recovery time. Such feedforward control of HVAC systems is already done for anticipated occupant loads and outside temperatures, but could also be done for expected increases in direct beam solar radiation through cloudy sky predictions.

The renderings produced by the *Transition Portal* radiosity engine by [Kider et al. \(2019\)](#) as well as our spectral bin renderings ([Del Rocco and Kider Jr., 2021](#)) should be validated with measurements. Spectral pyrometers should be used to measure spectral irradiance on surfaces after it passes through various glazing configurations and then compared with simulation results. Doing so will either validate our engine or give us a direction for improvement. We believe our fritted smart-film concept to be novel and recommend that it be explored. We are not experts in material science or glazing development, so we leave it to the appropriate communities to explore this idea further. We do believe that fritted smart-film is a viable solution to attenuating spectral energy without compromising visible light transmission.

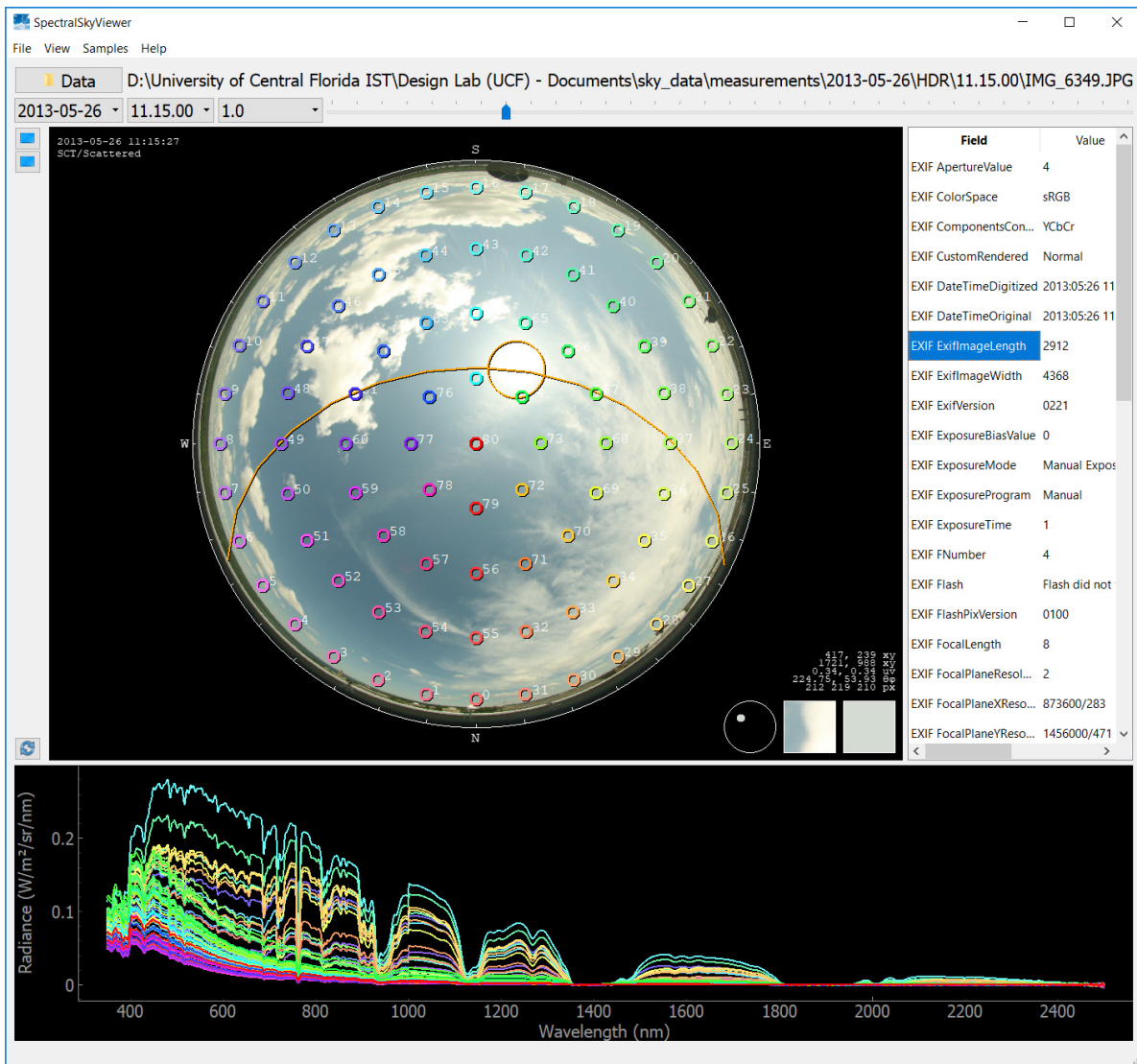
During the construction of our physical prototype, we mounted the triangular units directly to an acrylic support “window” merely to simplify the work needed to test our facade. However, this approach inspired the idea of a new configuration of shading devices that attach directly to glazing and are powered by a low-voltage charge given off or inducted through the glazing itself (e.g. PDLC). Such shading devices could be: (1) easily applied in all manner of ad-hoc or predetermined patterns, (2) controlled wirelessly, either manually or by a building control system, and (3) could remove the hurdles associated with mounting, wiring and retrofitting a building with an adaptive facade system. Monitoring and control programming could be downloaded and run locally by zones that have them installed even if a building monitoring system is not in place. If cheap and made commercially available, such units could be applied to the interior of glazing of buildings by residents that want smart facades in their rooms despite the state of their building, essentially

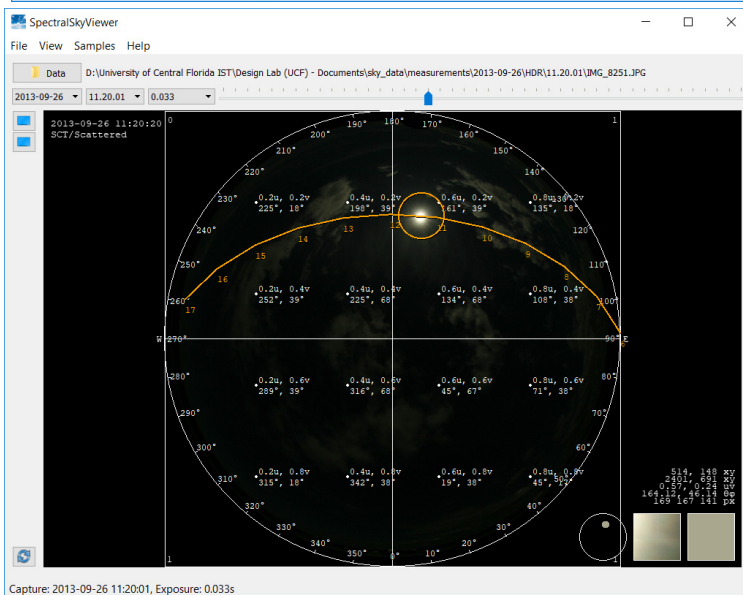
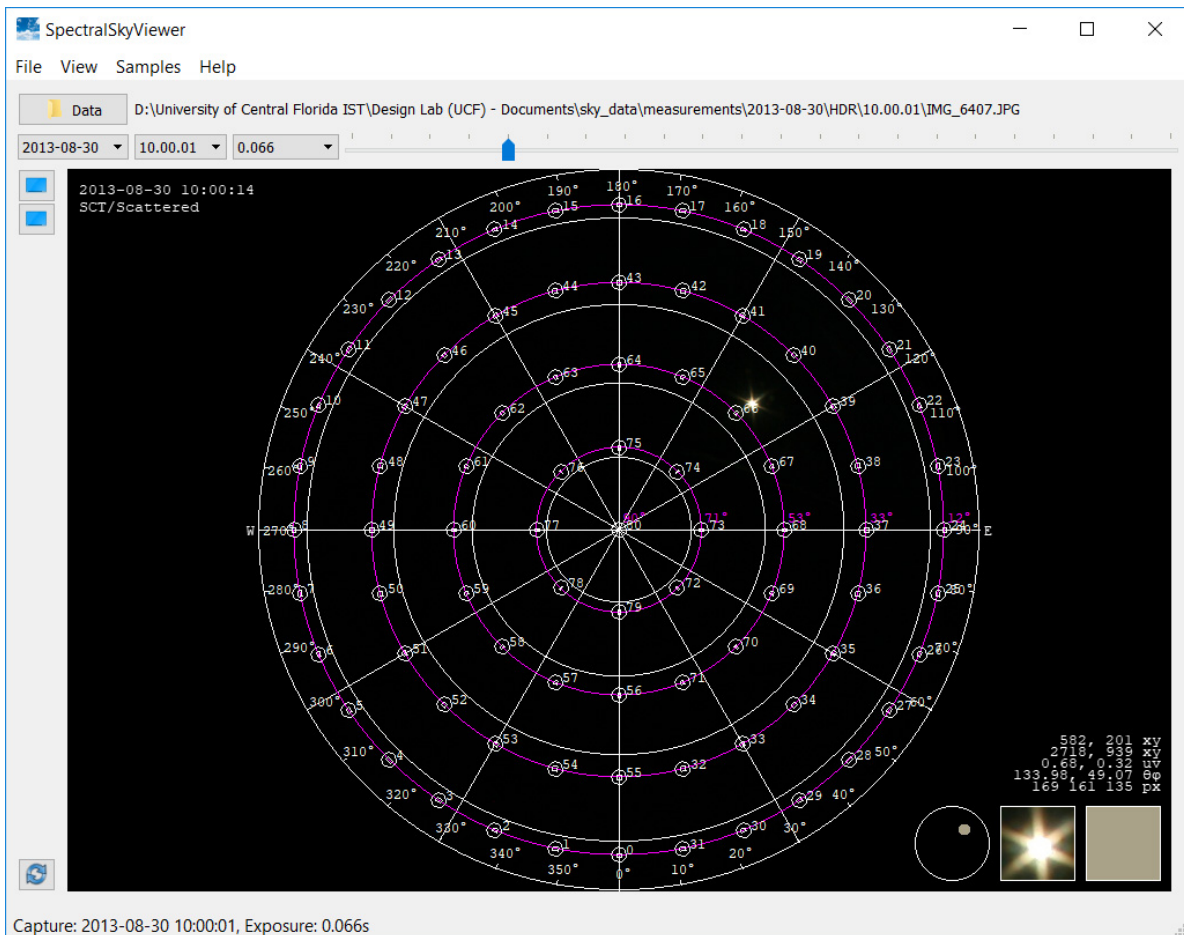
crowd-sourcing adaptive daylighting and heating in residential buildings.

Finally, it is our hope that our spectral radiance maps (sradmaps) contribute to not only the BPS community but also the modern computer graphics community. The rendering of naturally-lit indoor scenes can be improved with accurate spectral radiance whole sky models that give rendering engines the ability to occlude energy and utilize spectral input. Spectral rendering pipelines already exist, and though still new to the graphics community, they will eventually be at the forefront in the not-so-distant future. We believe that accurate spectral energy predictions are pertinent to accurate daylight rendering.

APPENDIX A: SPECTRAL SKY VIEWER

Spectral Sky Viewer can be used to: easily browse multiple exposure sky photography alongside correlating spectral radiance measurements, view NREL solar positioning algorithm (SPA) sun path and location, inspect EXIF meta-data of digital photographs, customize and visualize sky sampling patterns, use any custom fisheye lens linearity equation for transforming sky coordinates to image coordinates (and vice versa), and export any collection of sky samples with any correlating set of features. It was developed in Python and is open-source, cross-platform, and freely available from the [UCF SENSEable Design Lab](#).





Export Options

Export Samples To: C:/Users/ydelrocc/Desktop/clear.csv

Sample Features:

- Date of Capture
- Time of Capture
- Coordinate System
- Sun Azimuth
- Sun Altitude
- Sky Cover Assessment
- Sample Pattern Index
- Sample Azimuth
- Sample Altitude
- Sun Point Angle (SPA)
- Sample Pixel Region/Kernel (n x n)
- Sample Pixel Weighting Algorithm
- Sample Pixel Color Model
- Photo Exposure Time (s)
- Sample Pixel Color Components
- Sample Radiance (W/m²/sr/nm)

HDR Source: TIFF Color: RGB Pixel Region: compute 1 fixed Pixel Weighting: Gaussian

Coordinates: Polar Spectral Range: 350 to 1780 (nm) Spectral Resolution: 1 (nm)

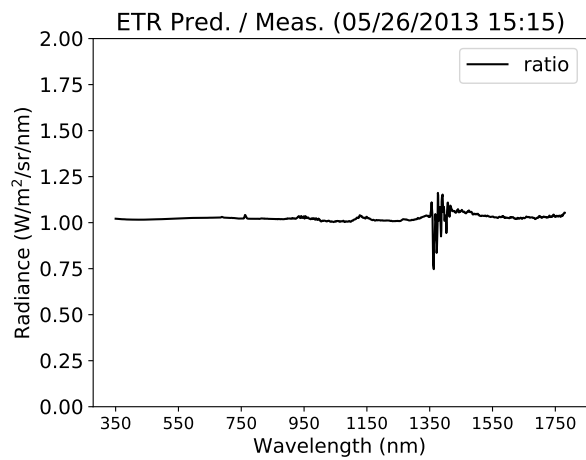
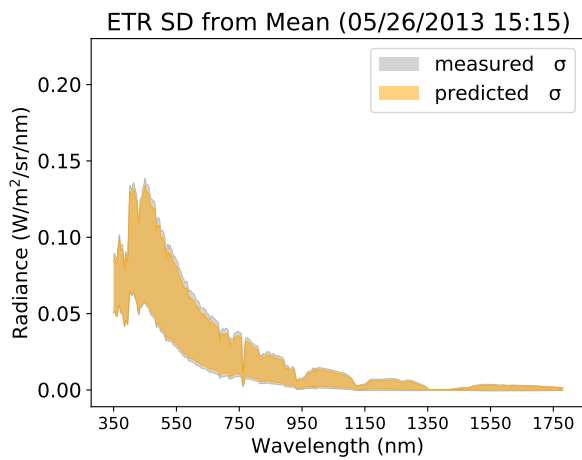
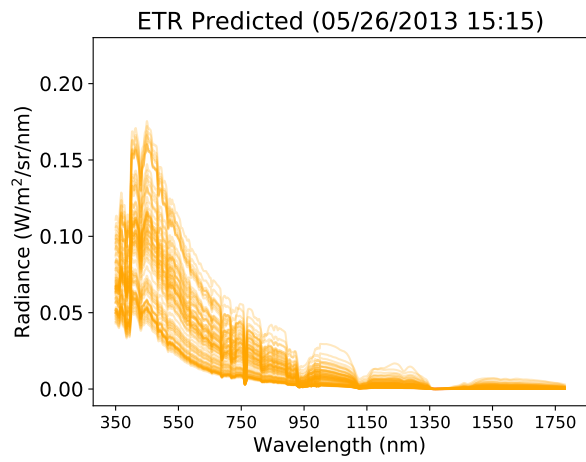
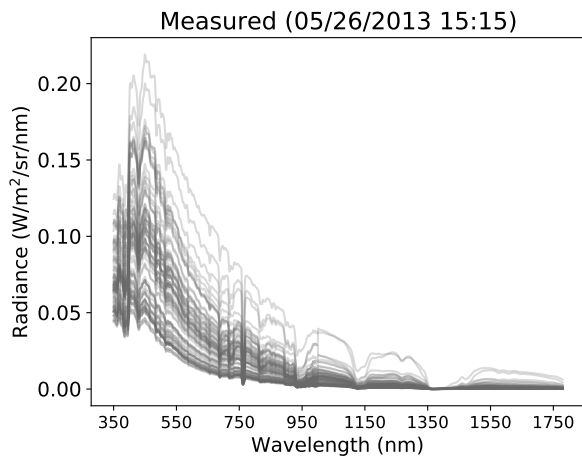
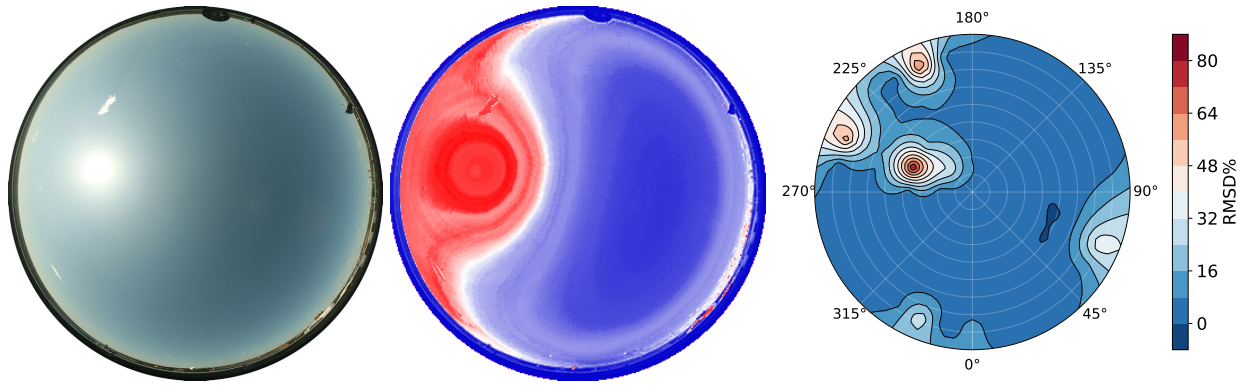
Save Cancel

The exporter extracts Gaussian weighted pixel colors from multiple exposures of any provided image format for any sampling pattern locations, along with any subset and resolution of correlating spectral radiance measurements. Coordinates can be exported in various spaces, colors in various color models, weighting from various algorithms, etc. The export functionality take the parsing work out of spectral sky data and are useful for machine learning training datasets and other scientific analysis. Such exported datasets were requested and used by a handful of international scientists not involved with this dissertation.

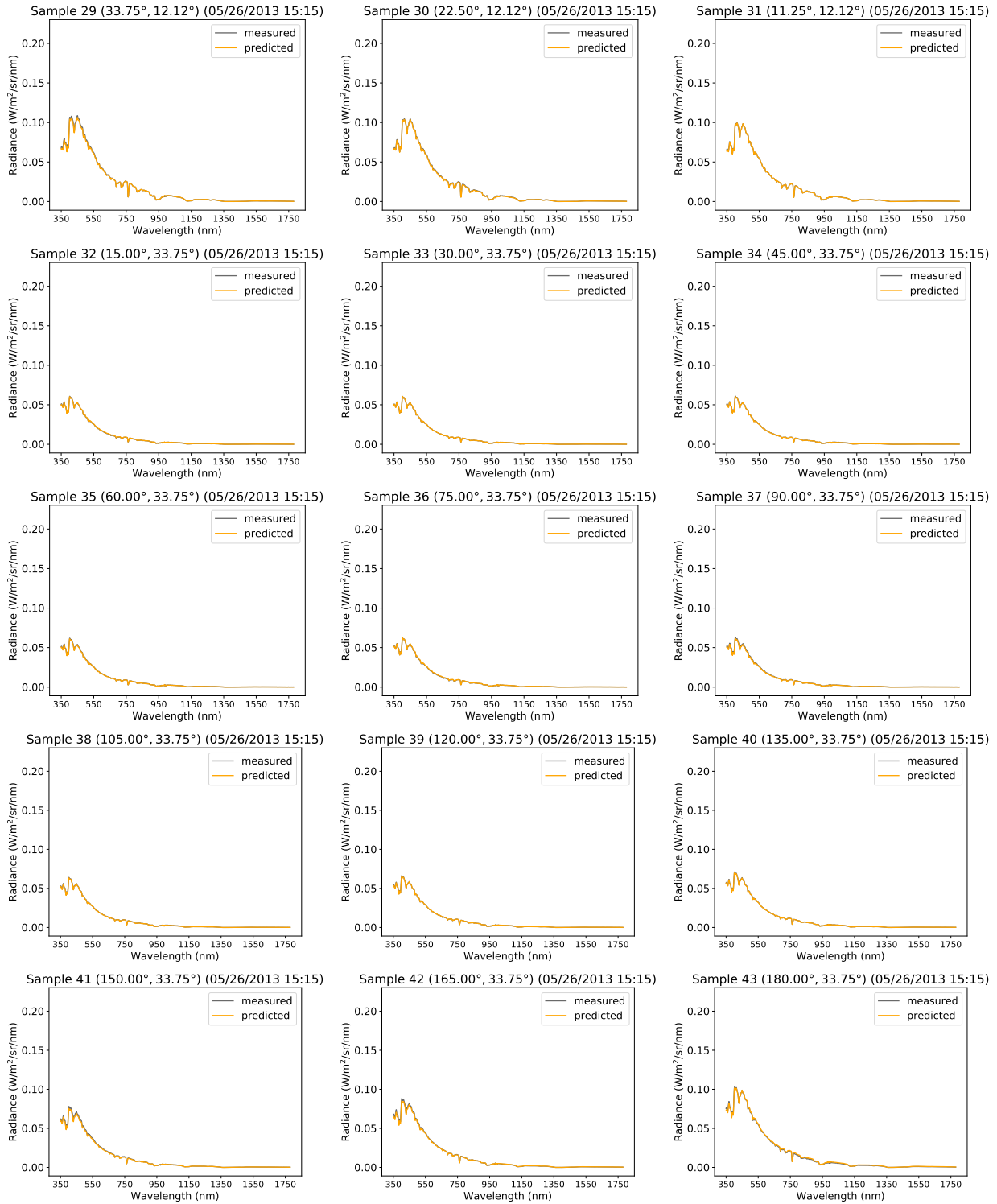
	A	B	C	D	E	F	G	H	I	J	K	L	M	N	O	P	Q	R
1	Date	Time	Spact	SunAzimut	SunAltitude	SkyCo	Sampl	SampleAzir	SampleAlti	SunPointAr	ColorA	ColorB	ColorC	350	351	352		
2	5/26/2013	14:00:00	1	238.298	57.6439	2	0	0	12.1151	95.606	1	167	175	153	0.060797	0.061759	0.061882	0.061
3	5/26/2013	14:00:00	1	238.298	57.6439	2	1	348.75	12.1151	90.318	1	188	187	160	0.065762	0.067039	0.067321	0.067
4	5/26/2013	14:00:00	1	238.298	57.6439	2	2	337.5	12.1151	84.628	1	147	172	159	0.066114	0.067312	0.067494	0.067
5	5/26/2013	14:00:00	1	238.298	57.6439	2	3	326.25	12.1151	78.697	1	143	167	161	0.06612	0.067158	0.067414	0.067
6	5/26/2013	14:00:00	1	238.298	57.6439	2	4	315	12.1151	72.684	1	147	170	163	0.066389	0.067607	0.06784	0.067
7	5/26/2013	14:00:00	1	238.298	57.6439	2	5	303.75	12.1151	66.754	1	154	175	168	0.067788	0.068889	0.069088	0.069
8	5/26/2013	14:00:00	1	238.298	57.6439	2	6	292.5	12.1151	61.095	1	159	182	174	0.069582	0.070777	0.071004	0.070
9	5/26/2013	14:00:00	1	238.298	57.6439	2	7	281.25	12.1151	55.925	1	166	188	179	0.072264	0.073543	0.073836	0.073
10	5/26/2013	14:00:00	1	238.298	57.6439	2	8	270	12.1151	51.503	1	173	194	185	0.075645	0.076912	0.077718	0.077
11	5/26/2013	14:00:00	1	238.298	57.6439	2	9	258.75	12.1151	48.12	1	178	199	190	0.079184	0.080515	0.080881	0.080
12	5/26/2013	14:00:00	1	238.298	57.6439	2	10	247.5	12.1151	46.067	1	179	201	193	0.082261	0.083688	0.084169	0.084
13	5/26/2013	14:00:00	1	238.298	57.6439	2	11	236.25	12.1151	45.556	1	180	202	195	0.085172	0.086838	0.087183	0.087
14	5/26/2013	14:00:00	1	238.298	57.6439	2	12	225	12.1151	46.645	1	178	200	193	0.087084	0.088805	0.089281	0.089
15	5/26/2013	14:00:00	1	238.298	57.6439	2	13	213.75	12.1151	49.213	1	172	196	189	0.087771	0.08954	0.089977	0.090
16	5/26/2013	14:00:00	1	238.298	57.6439	2	14	202.5	12.1151	53.008	1	219	220	195	0.087752	0.089481	0.089938	0.089
17	5/26/2013	14:00:00	1	238.298	57.6439	2	15	191.25	12.1151	57.735	1	177	188	182	0.086294	0.088099	0.088571	0.088
18	5/26/2013	14:00:00	1	238.298	57.6439	2	16	180	12.1151	63.111	1	152	178	169	0.08386	0.08553	0.086065	0.086
19	5/26/2013	14:00:00	1	238.298	57.6439	2	17	168.75	12.1151	68.892	1	139	165	161	0.081247	0.082922	0.083334	0.083
20	5/26/2013	14:00:00	1	238.298	57.6439	2	18	157.5	12.1151	74.873	1	130	159	158	0.076772	0.078269	0.078775	0.078
21	5/26/2013	14:00:00	1	238.298	57.6439	2	19	146.25	12.1151	80.875	1	127	155	155	0.074408	0.075851	0.0762	0.076
22	5/26/2013	14:00:00	1	238.298	57.6439	2	20	135	12.1151	86.736	1	123	155	153	0.071576	0.072992	0.073486	0.07
23	5/26/2013	14:00:00	1	238.298	57.6439	2	21	123.75	12.1151	92.298	1	126	156	153	0.07175	0.073142	0.073655	0.073
24	5/26/2013	14:00:00	1	238.298	57.6439	2	22	112.5	12.1151	97.399	1	168	172	154	0.068615	0.069837	0.07028	0.070
25	5/26/2013	14:00:00	1	238.298	57.6439	2	23	101.25	12.1151	101.87	1	139	165	161	0.068703	0.070161	0.070609	0.070
26	5/26/2013	14:00:00	1	238.298	57.6439	2	24	90	12.1151	105.539	1	155	167	154	0.067046	0.068459	0.068801	0.068
27	5/26/2013	14:00:00	1	238.298	57.6439	2	25	78.75	12.1151	108.239	1	160	171	154	0.070878	0.072408	0.072841	0.072
28	5/26/2013	14:00:00	1	238.298	57.6439	2	26	67.5	12.1151	109.83	1	159	179	164	0.067659	0.069115	0.069594	0.069
29	5/26/2013	14:00:00	1	238.298	57.6439	2	27	56.25	12.1151	110.221	1	165	177	158	0.068689	0.070256	0.070636	0.070
30	5/26/2013	14:00:00	1	238.298	57.6439	2	28	45	12.1151	109.386	1	182	191	169	0.06393	0.065315	0.065791	0.06
31	5/26/2013	14:00:00	1	238.298	57.6439	2	29	33.75	12.1151	107.378	1	169	176	155	0.068803	0.070131	0.070423	0.070
32	5/26/2013	14:00:00	1	238.298	57.6439	2	30	22.5	12.1151	104.307	1	164	171	152	0.067621	0.06888	0.069286	0.069
33	5/26/2013	14:00:00	1	238.298	57.6439	2	31	11.25	12.1151	100.326	1	141	165	156	0.068753	0.070076	0.070417	0.07
34	5/26/2013	14:00:00	1	238.298	57.6439	2	32	15	33.749	81.637	1	82	116	127	0.053631	0.054507	0.054493	0.054
35	5/26/2013	14:00:00	1	238.298	57.6439	2	33	30	33.749	85.556	1	80	115	127	0.054196	0.054881	0.054951	0.054
36	5/26/2013	14:00:00	1	238.298	57.6439	2	34	45	33.749	87.922	1	80	114	126	0.05558	0.055587	0.055866	0.055

APPENDIX B: SUPPLEMENTARY SKY RESULTS

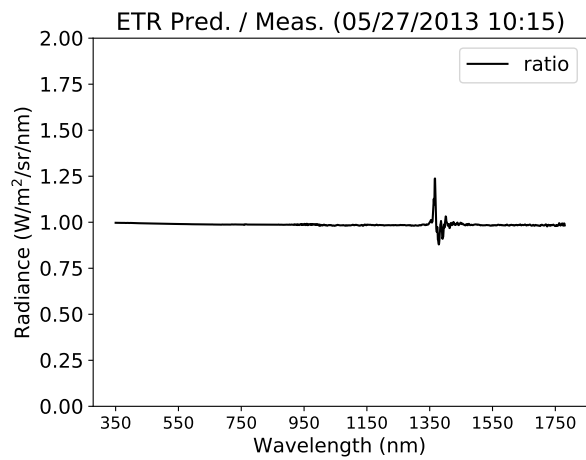
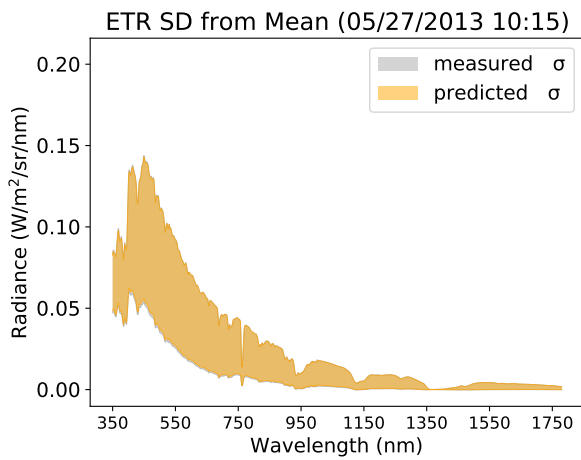
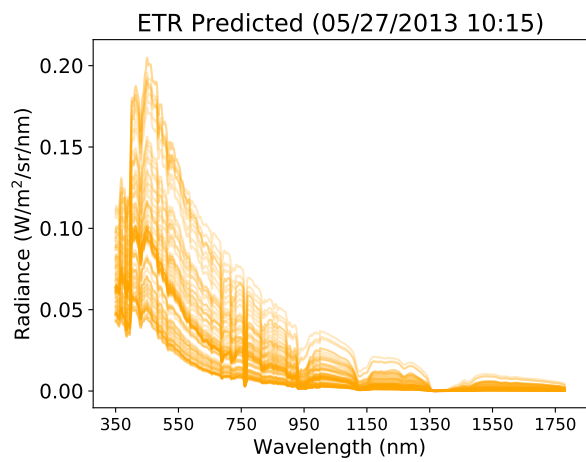
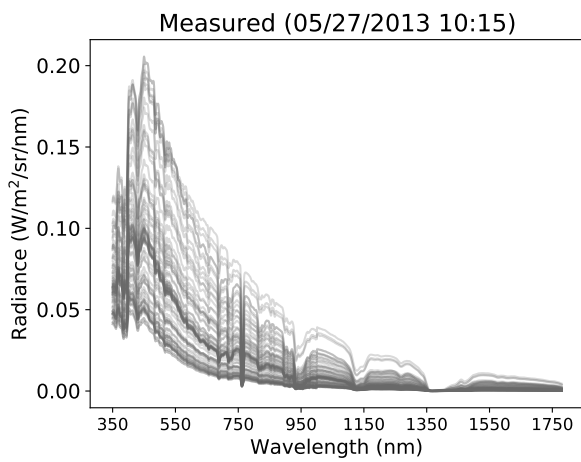
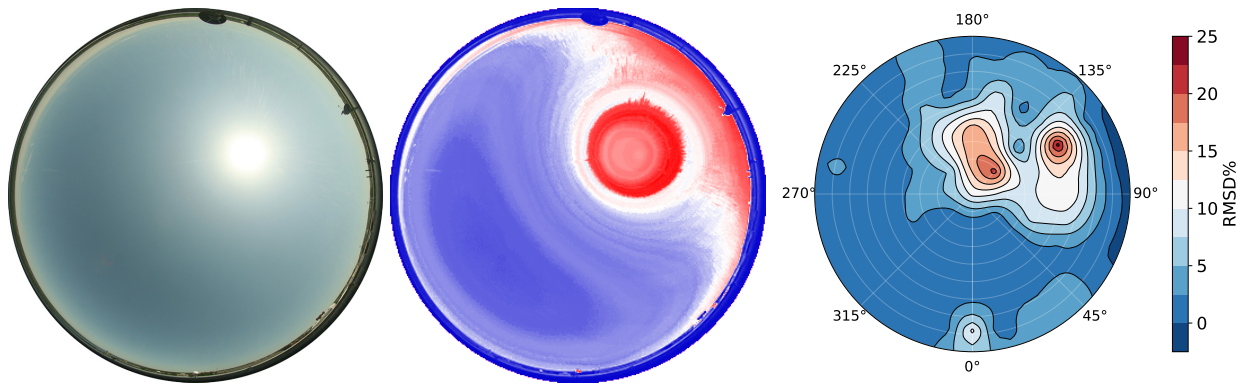
Whole sky ETR model predicted atmospheric spectral radiance distributions for holdout test sky 05/26/2013 15:15, discussed in [Section 3](#).



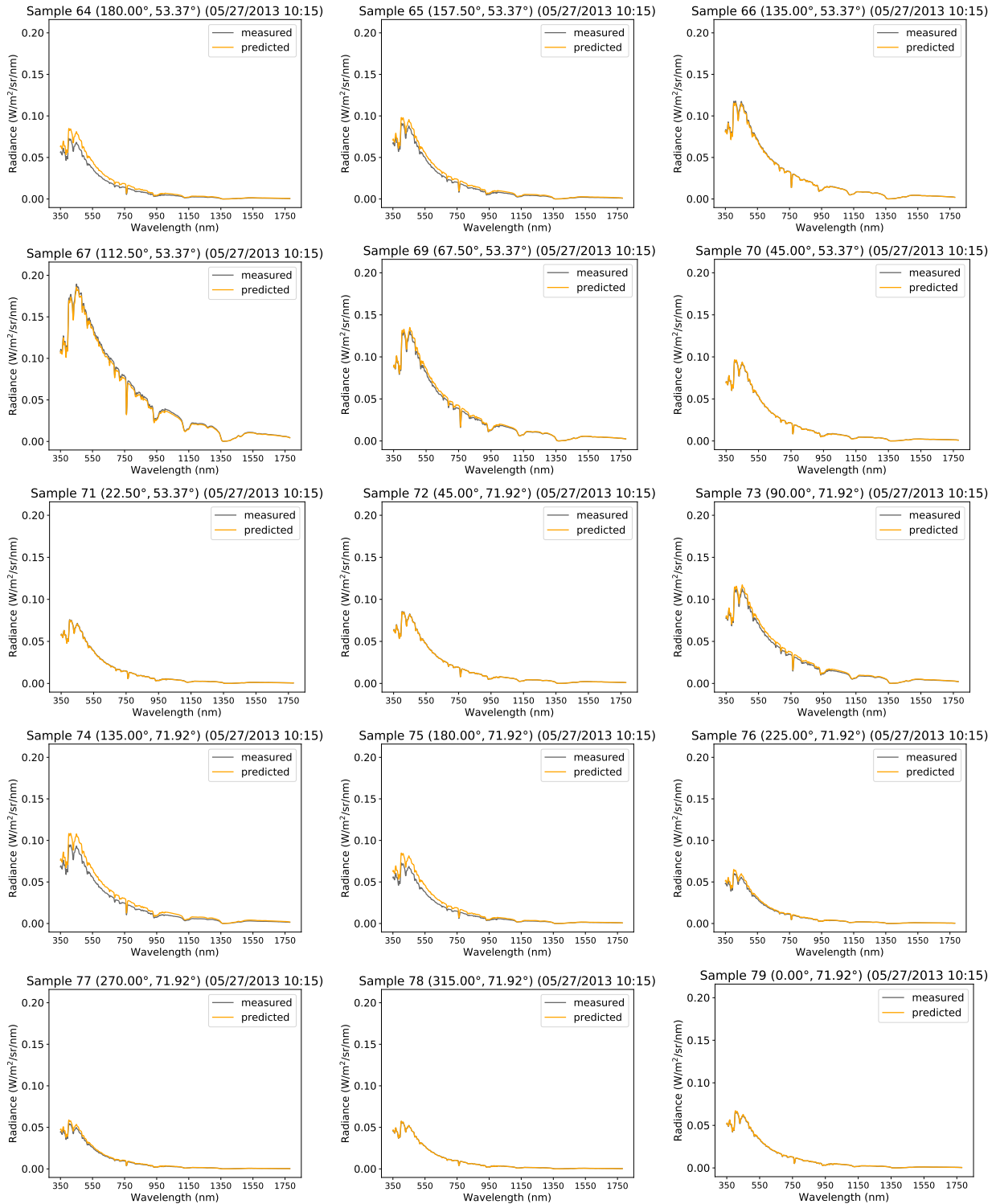
15 of 81 consecutive ETR spectral radiance predictions for holdout test sky 05/26/2013 15:15.



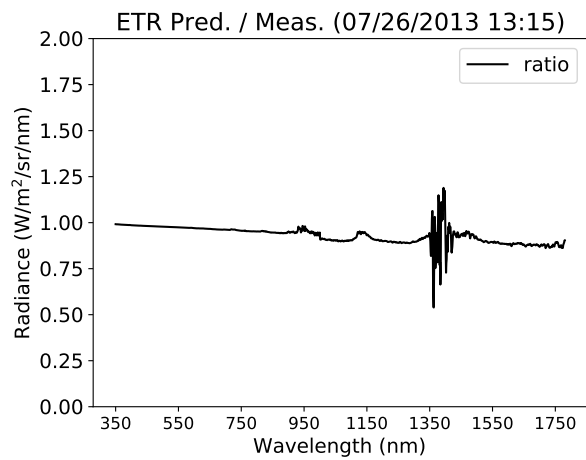
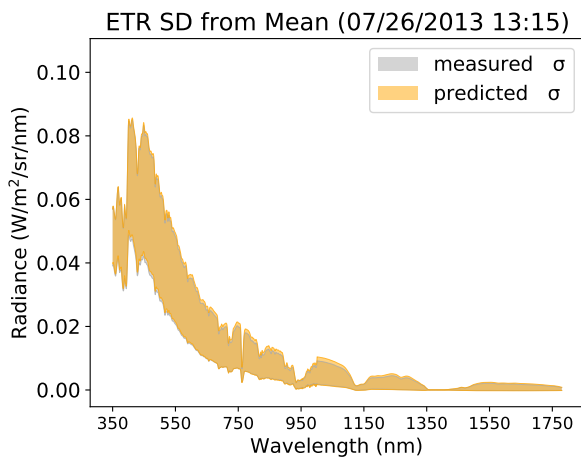
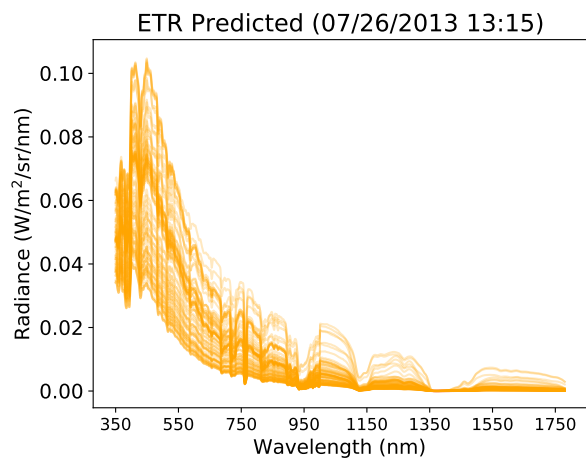
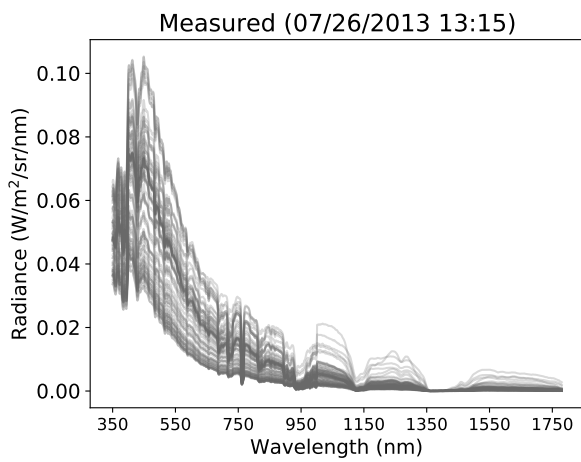
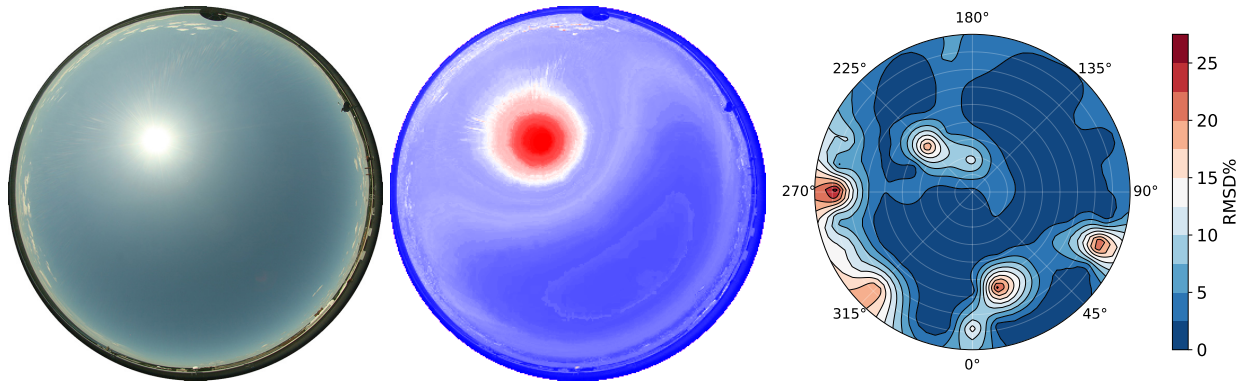
Whole sky ETR model predicted atmospheric spectral radiance distributions for holdout test sky 05/27/2013 10:15, discussed in [Section 3](#).



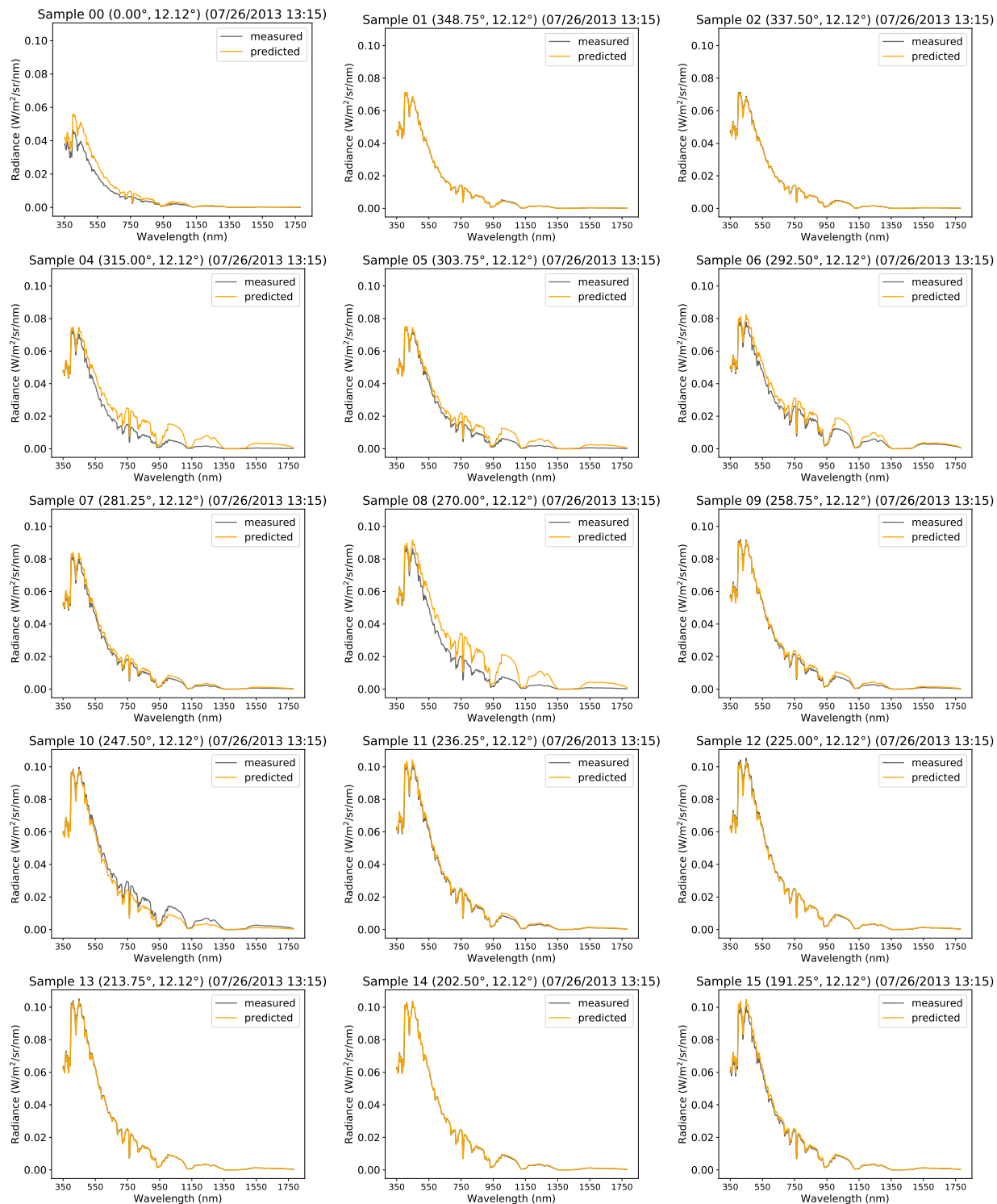
15 of 81 consecutive ETR spectral radiance predictions for holdout test sky 05/27/2013 10:15.



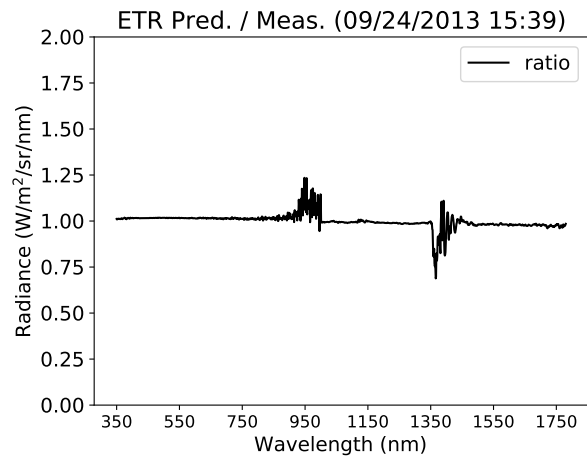
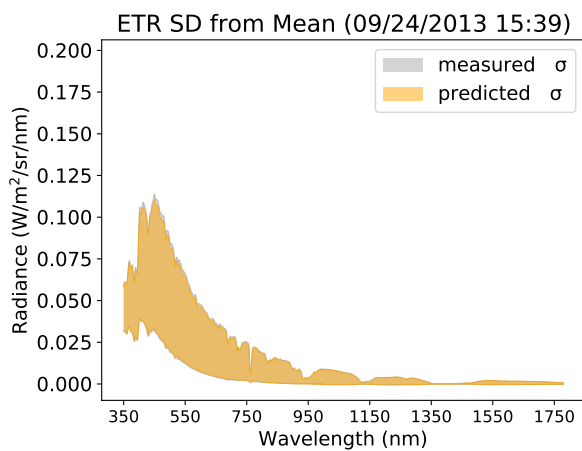
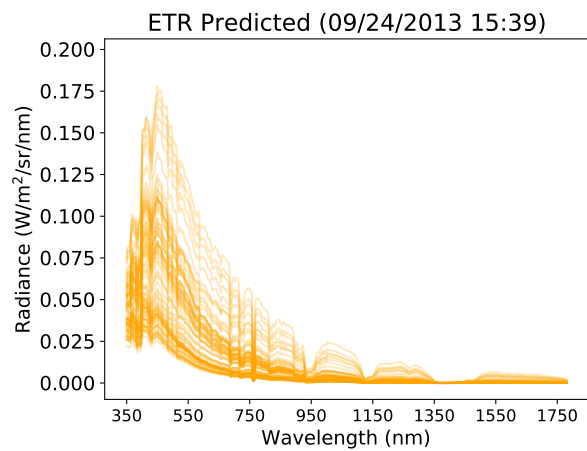
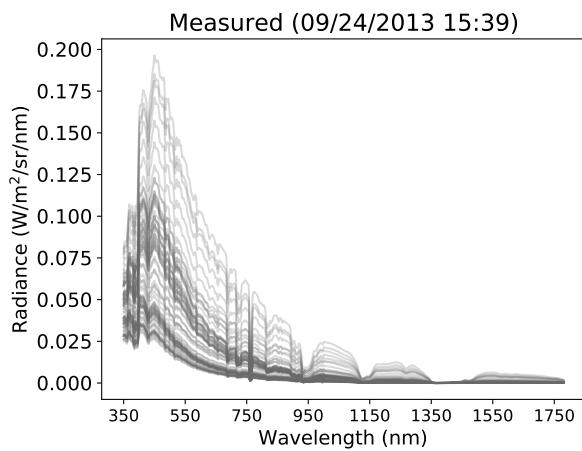
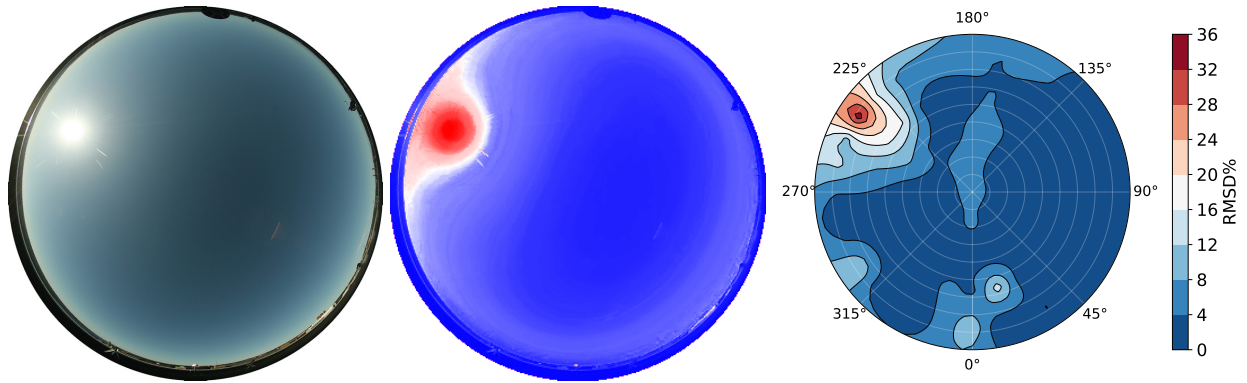
Whole sky ETR model predicted atmospheric spectral radiance distributions for holdout test sky 07/26/2013 13:15, discussed in [Section 3](#).



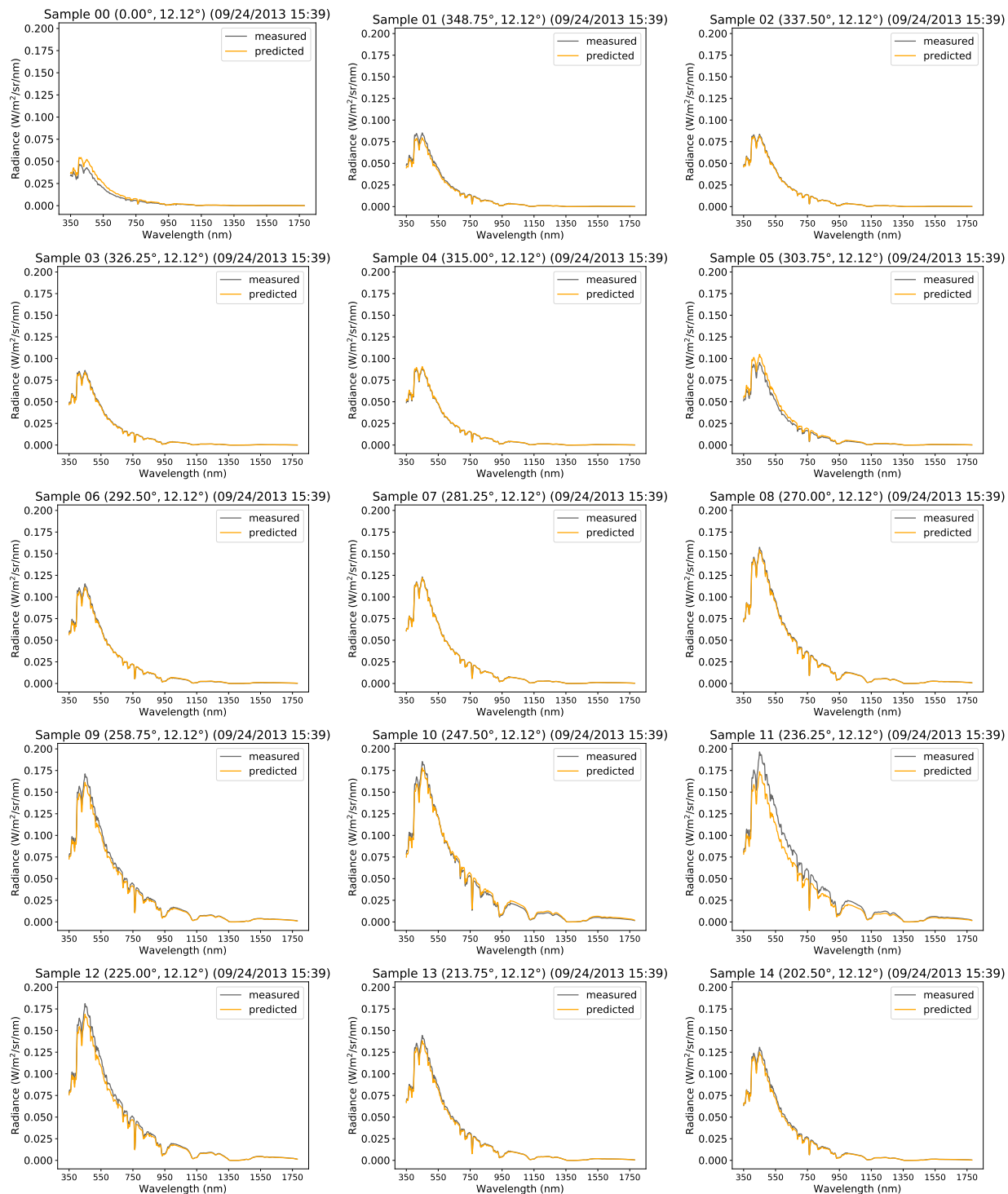
15 of 81 consecutive ETR spectral radiance predictions for holdout test sky 07/26/2013 13:15.



Whole sky ETR model predicted atmospheric spectral radiance distributions for holdout test sky 09/24/2013 15:39, discussed in [Section 3](#).

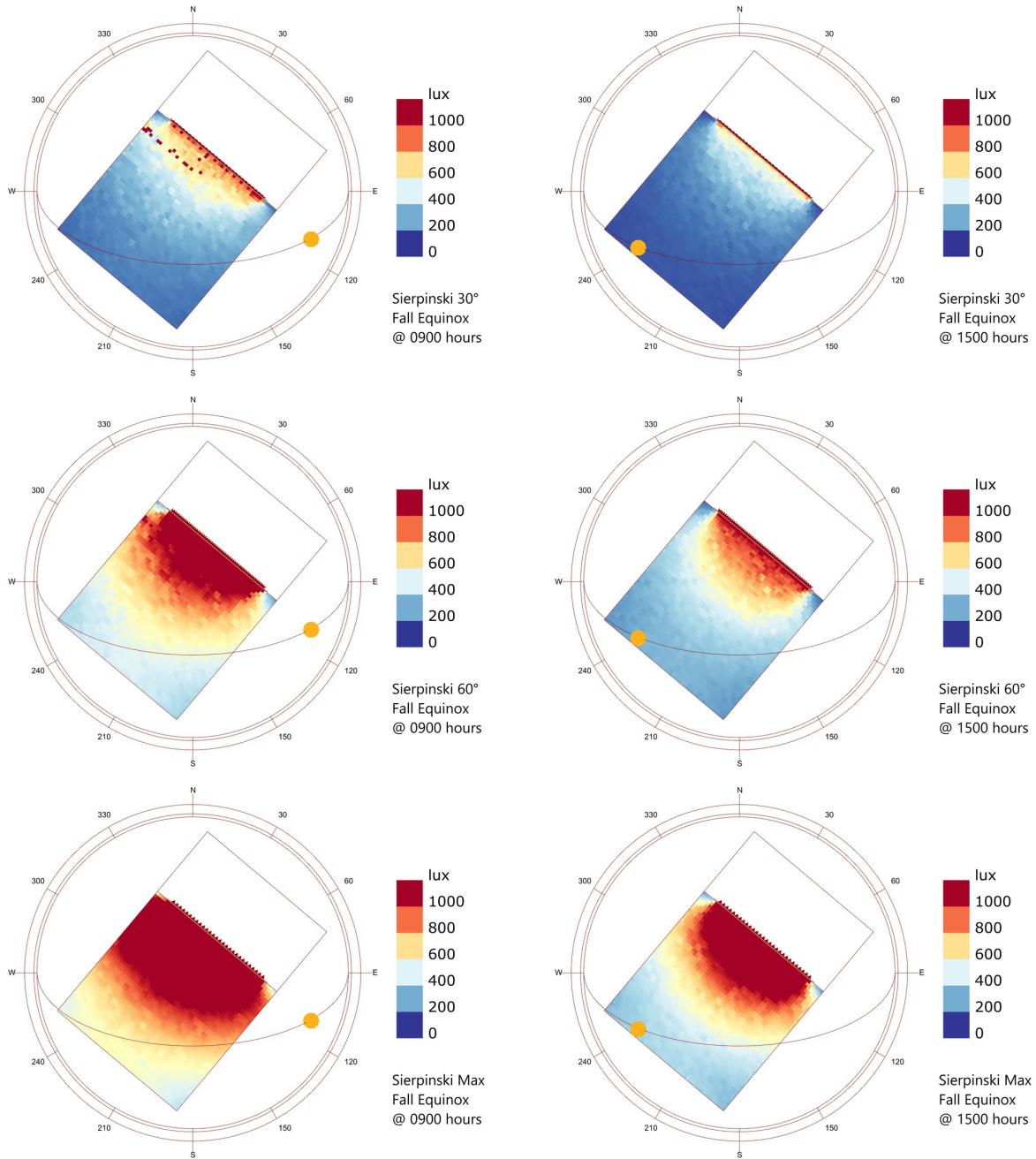


15 of 81 consecutive ETR spectral radiance predictions for holdout test sky 09/24/2013 15:39.

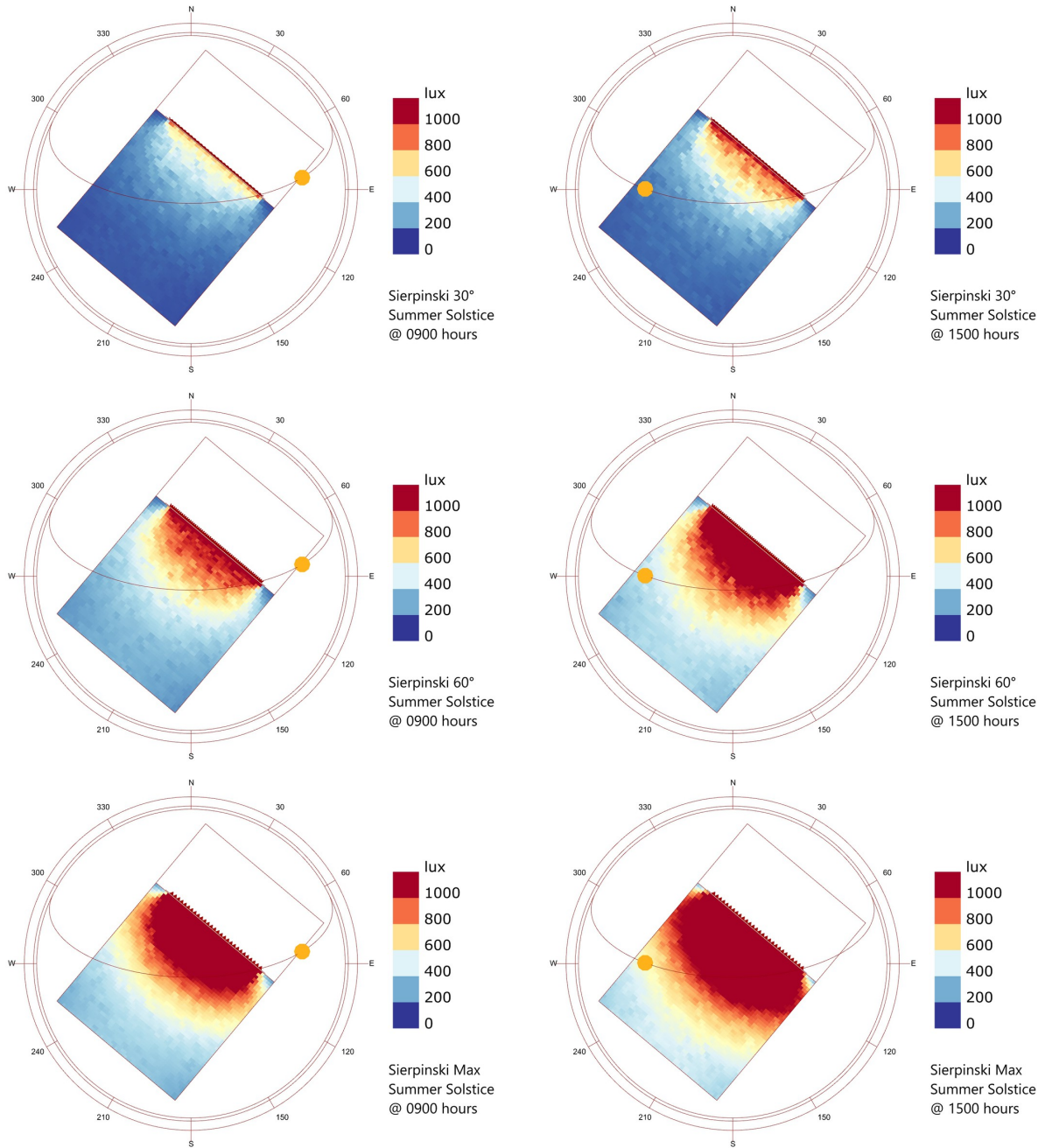


APPENDIX C: SUPPLEMENTARY DAYLIGHTING ANALYSIS

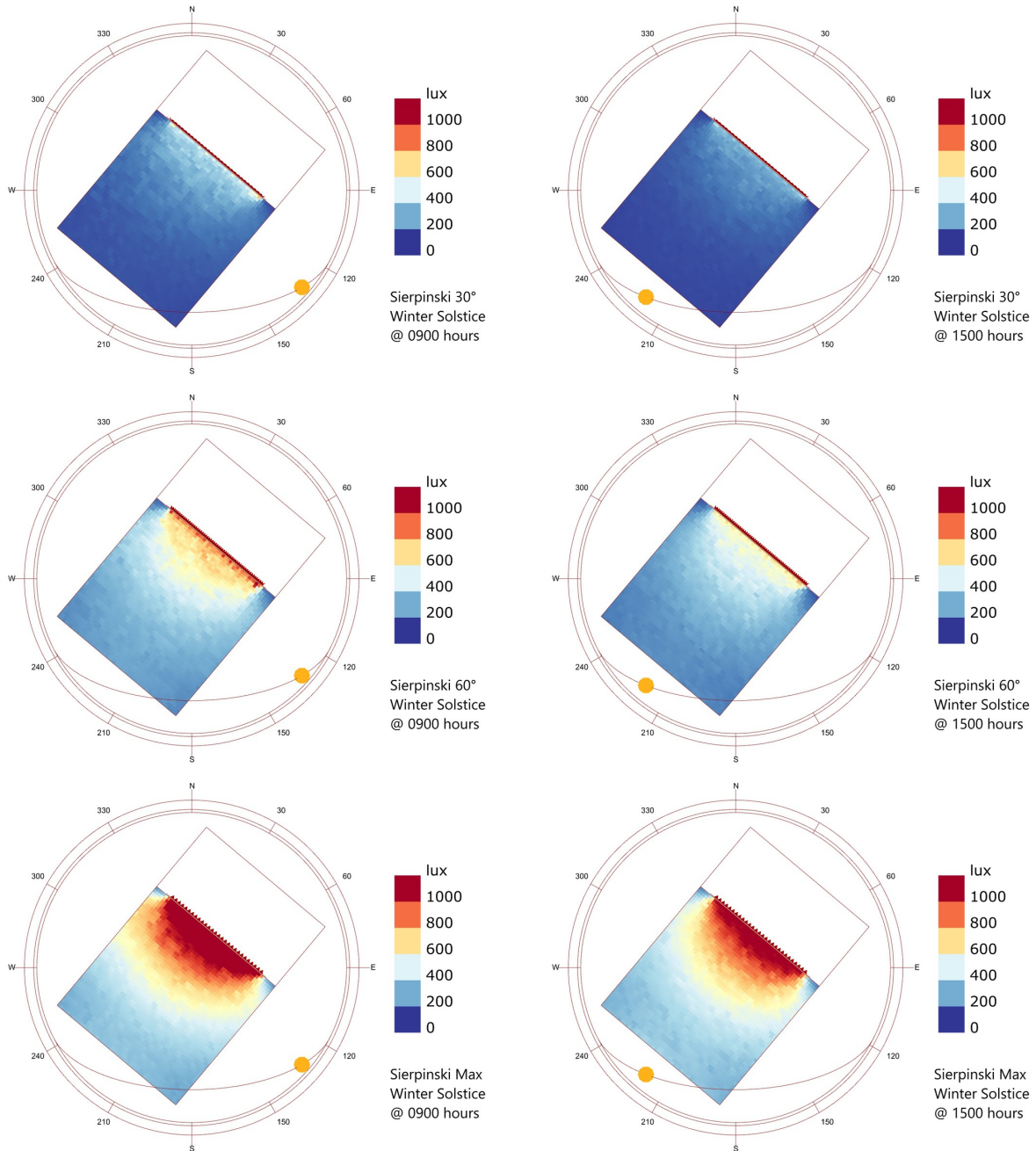
Daylighting analysis of Sierpinski design, 30°, 60°, and max actuation, during the fall equinox at 09:00 and 15:00.



Daylighting analysis of Sierpinski design, 30°, 60°, and max actuation, during the summer solstice at 09:00 and 1500.



Daylighting analysis of Sierpinski design, 30°, 60°, and max actuation, during the winter solstice at 09:00 and 15:00.



APPENDIX D: PUBLISHER PERMISSION LETTERS

Permission from SPIE to use content from publication [Del Rocco et al. \(2018\)](#).

Dear Joe,

Thank you for seeking permission from SPIE to reprint material from our publications. SPIE shares the copyright with you, so as author you retain the right to reproduce your paper in part or in whole.

Publisher's permission is hereby granted under the following conditions:

- (1) the material to be used has appeared in our publication without credit or acknowledgment to another source; and
- (2) you credit the original SPIE publication. Include the authors' names, title of paper, volume title, SPIE volume number, and year of publication in your credit statement.

Best wishes on your dissertation. Please let me know if I may be of any further assistance.

Best,

Katie Sinclair

Editorial Assistant, Publications

SPIE – the international society for optics and photonics

katies@spie.org

1 360 685 5436

SPIE.

Permission from Elsevier to use content from publication [Del Rocco et al. \(2020\)](#).



ELSEVIER

Dear Joseph Del Rocco,

Thank you for your query.

Please note that, as one of the authors of this article, you retain the right to reuse it in your thesis/dissertation. You do not require formal permission to do so. You are permitted to post this Elsevier article online if it is embedded within your thesis. You are also permitted to post your Author Accepted Manuscript online.

However posting of the final published article is prohibited.

*“As per our [Sharing Policy](#), authors are permitted to post the Accepted version of their article on their institutional repository – as long as it is for **internal institutional use only**.*

It can only be shared publicly on that site once the journal-specific embargo period has lapsed. For a list of embargo periods please see: [Embargo List](#).

You are not permitted to post the Published Journal Article (PJA) on the repository.”

Please feel free to contact me if you have any queries.

Kind regards,

Anita Mercy Vethakkan

Senior Copyrights Coordinator

ELSEVIER | HCM - Health Content Management

Permission from Advanced Building Skins to use content from publication [Moulton et al. \(2018\)](#).

You can use text, graphs and pictures from your paper/presentation as you wish.

Kind regards
Andreas Karweger

www.abs.green

Advanced Building Skins GmbH
Zentralstr. 44
CH-6003 Lucerne, Switzerland

Tel Lucerne: +41 41 508 70 36
Tel Munich: +49 89 20000-4161
Tel Bolzano: +39 0471 34 00 50

APPENDIX E: LIST OF RELEVANT PUBLICATIONS BY THE AUTHOR

Del Rocco, J. and Kider Jr., J. T. (2021). Radiant spectral energy for simulation in the built environment. In *Proceedings, Building Simulation 2021: 17th Conference of IBPSA*. IBPSA

Del Rocco, J., Bourke, P. D., Patterson, C. B., and Kider, J. T. (2020). Real-time spectral radiance estimation of hemispherical clear skies with machine learned regression models. *Solar Energy*, 204:48–63. <https://doi.org/10.1016/j.solener.2020.04.006>

Del Rocco, J., Patterson, C. B., Dhrif, H., and Kider, J. T. (2018). Learning and estimating whole sky visible, VNIR, SWIR radiance distributions from a commercial camera. In *Optics and Photonics for Information Processing XII*, volume 10751, page 107510F. SPIE. <https://doi.org/10.1117/12.2321295>

Moulton, N., Del Rocco, J., Kider Jr, J. T., and Fiore, S. M. (2018). An affective kinetic building façade system: Mood Swing. In *Proceedings, 13th Conference on Advanced Building Skins*, pages 417–426. Advanced Building Skins GmbH. ISBN: 978-3-9524883-4-8. <https://abs.green/files/pdf/content-2018.pdf>

LIST OF REFERENCES

- Adafruit Industries (2005). Adafruit Industries. <https://www.adafruit.com>. Accessed 2021-10-1.
- Afram, A., Janabi-Sharifi, F., Fung, A. S., and Raahemifar, K. (2017). Artificial neural network (ann) based model predictive control (mpc) and optimization of hvac systems: A state of the art review and case study of a residential hvac system. *Energy and Buildings*, 141:96–113.
- Ahmadi-Karvigh, S., Ghahramani, A., Becerik-Gerber, B., and Soibelman, L. (2017). One size does not fit all: Understanding user preferences for building automation systems. *Energy and Buildings*, 145:163–173.
- American Society of Heating, Refrigerating and Air-Conditioning Engineers (ASHRAE) (2021). ASHRAE Technical Committees: Section 7.0 Building Performance. <https://www.ashrae.org/technical-resources/technical-committees/section-7-0-building-performance>. Accessed: 2021-06-01.
- Anselmo, F. and Lauritano, A. (2003). Evaluation of the solar energy potential in urban settings by irradiation map production. In *2nd International Radiance Workshop*, pages 1–1, Berkeley, California. Radiance Community. <https://www.radiance-online.org/community/workshops/>.
- Antonanzas-Torres, F., Urraca, R., Polo, J., Perpiñán-Lamigueiro, O., and Escobar, R. (2019). Clear sky solar irradiance models: A review of seventy models. *Renewable and Sustainable Energy Reviews*, 107:374–387.
- Ardakan, A. M., Sok, E., and Niemasz, J. (2017). Electrochromic glass vs. fritted glass: an analysis of glare control performance. *Energy Procedia*, 122:343–348.
- Asadi, E., da Silva, M. G., Antunes, C. H., Dias, L., and Glicksman, L. (2014). Multi-objective optimization for building retrofit: A model using genetic algorithm and artificial neural network and an application. *Energy and Buildings*, 81:444–456.
- Aste, N., Manfren, M., and Marenzi, G. (2017). Building Automation and Control Systems and performance optimization: A framework for analysis. *Renewable and Sustainable Energy Reviews*, 75:313–330.
- Badescu, V., Gueymard, C. A., Cheval, S., Oprea, C., Baci, M., Dumitrescu, A., Iacobescu, F., Milos, I., and Rada, C. (2012). Computing global and diffuse solar hourly irradiation on clear sky. review and testing of 54 models. *Renewable and Sustainable Energy Reviews*, 16(3):1636–1656.
- Bainbridge, D. and Haggard, K. (2011). *Passive solar architecture: heating, cooling, ventilation, daylighting and more using natural flows*. Chelsea green publishing.

- Baker, N. V., Fanchiotti, A., and Steemers, K. (2013). *Daylighting in Architecture: A European Reference Book*. Routledge.
- Bakshi, A. and Jakubiec, J. A. (2011). A simple cost-benefit estimation for daylighting design and analysis during the design process. In *Building Simulation*.
- Balakrishnan, P. and Jakubiec, J. (2019). Spectral rendering with daylight: A comparison of two spectral daylight simulation platforms. In *Proceedings of the 16th IBPSA Conference*. Rome (Italy), 2-4 September 2019.
- Beausoleil-Morrison, I., Macdonald, F., Kummert, M., McDowell, T., and Jost, R. (2014). Co-simulation between esp-r and trnsys. *Journal of Building Performance Simulation*, 7(2):133–151.
- Beck, A. (2013). Spectrum of Solar Radiation. https://commons.wikimedia.org/wiki/File:Solar_spectrum_en.svg. CC BY-SA 3.0. Accessed 2020-11-5.
- Beckman, W. A., Broman, L., Fiksel, A., Klein, S. A., Lindberg, E., Schuler, M., and Thornton, J. (1994). Trnsys the most complete solar energy system modeling and simulation software. *Renewable energy*, 5(1-4):486–488.
- Bemporad, A. and Morari, M. (1999). Robust model predictive control: A survey. *Robustness in identification and control*, pages 207–226.
- Bennett, S. (1993). Development of the pid controller. *IEEE Control Systems Magazine*, 13(6):58–62.
- Berk, A., Conforti, P., Kennett, R., Perkins, T., Hawes, F., and Van Den Bosch, J. (2014). MODTRAN 6: A major upgrade of the MODTRAN radiative transfer code. In *2014 6th Workshop on Hyperspectral Image and Signal Processing: Evolution in Remote Sensing (WHISPERS)*, pages 1–4. IEEE. <https://doi.org/10.1109/WHISPERS.2014.8077573>.
- Berman, M. G., Jonides, J., and Kaplan, S. (2008). The cognitive benefits of interacting with nature. *Psychological science*, 19(12):1207–1212.
- Bertenshaw, D. (2020). The standardisation of light and photometry—a historical review. *Lighting Research & Technology*, 52(7):816–848.
- Birol, F. et al. (2020). World Energy Outlook 2020.
- Boltzmann, L. (1898). *Vorlesungen über Gastheorie: Th. Theorie van der Waals’; Gase mit zusammengesetzten Molekülen; Gasdissociation; Schlussbemerkungen*, volume 2. JA Barth.
- Boubekri, M. (2008). *Daylighting, architecture and health*. Routledge.
- Bouguer, P. (1729). *Essai d’optique sur la gradation de la lumière*. Claude Jombert.

- Bourgeois, D., Reinhart, C. F., and Ward, G. (2008). Standard daylight coefficient model for dynamic daylighting simulations. *Building Research & Information*, 36(1):68–82.
- Bourke, P. (2016). Lens correction and distortion. <http://paulbourke.net/dome/fisheycorrect>. Accessed: 2019-10-01.
- Boyce, P., Hunter, C., and Howlett, O. (2003). The benefits of daylight through windows. *Troy, New York: Rensselaer Polytechnic Institute*.
- Bruijn, P. and Verbruggen, H. (1984). Model algorithmic control using impulse response models. *Journal A*, 25(2):69–74.
- Bruneton, E. (2016). A qualitative and quantitative evaluation of 8 clear sky models. *IEEE transactions on visualization and computer graphics*, 23(12):2641–2655. <https://doi.org/10.1109/TVCG.2016.2622272>.
- Brunger, A. P. and Hooper, F. C. (1993). Anisotropic sky radiance model based on narrow field of view measurements of shortwave radiance. *Solar Energy*, 51(1):53–64.
- Burley, B., Adler, D., Chiang, M. J.-Y., Driskill, H., Habel, R., Kelly, P., Kutz, P., Li, Y. K., and Teece, D. (2018). The design and evolution of Disney’s Hyperion renderer. *ACM Transactions on Graphics (TOG)*, 37(3):33. <https://doi.org/10.1145/3182159>.
- Butler, D. (2008). Architects of a low-energy future: low-and zero-energy buildings could have a huge impact on energy use and carbon emissions. we have the technologies, but if they are to mitigate climate change, green-building design must hit the mass market. *Nature*, 452(7187):520–524.
- Camacho, E. F. and Bordons, C. (2015). Distributed model predictive control: Distributed model predictive control. *Optimal Control Applications and Methods*, 36(3):269–271.
- Campbell, M., Hoane Jr, A. J., and Hsu, F.-h. (2002). Deep blue. *Artificial intelligence*, 134(1-2):57–83.
- Capuano, L. et al. (2020). International Energy Outlook 2020.
- Carrascal-Lekunberri, E., Garrido, I., Heijde, B. V. d., Garrido, A. J., Sala, J. M., and Helsen, L. (2017). Energy conservation in an office building using an enhanced blind system control. *Energies*, 10(2):196.
- Cazorla, A., Olmo, F., and Alados-Arboledas, L. (2008a). Using a sky imager for aerosol characterization. *Atmospheric Environment*, 42(11):2739–2745.
- Cazorla, A., Olmo, F. J., and Alados-Arboledas, L. (2008b). Development of a sky imager for cloud cover assessment. *JOSA A*, 25(1):29–39.

- Chacon-Murguia, M. I. and Ramirez-Alonso, G. (2015). Fuzzy-neural self-adapting background modeling with automatic motion analysis for dynamic object detection. *Applied Soft Computing*, 36:570–577.
- Chandrasekhar, S. (1960). *Radiative Transfer*. Dover Publications Inc.
- Chauvin, R., Nou, J., Thil, S., and Grieu, S. (2015). Modelling the clear-sky intensity distribution using a sky imager. *Solar Energy*, 119:1–17. <https://doi.org/10.1016/j.solener.2015.06.026>.
- Chen, W. and Mied, R. P. (2013). Optical flow estimation for motion-compensated compression. *Image and Vision Computing*, 31(3):275–289.
- Christensen, C., Anderson, R., Horowitz, S., Courtney, A., and Spencer, J. (2006). BEopt (tm) software for building energy optimization: Features and capabilities. Technical report, National Renewable Energy Lab (NREL), Golden, CO (United States).
- Cordero, R. R., Damiani, A., Ferrer, J., Rayas, J., Jorquera, J., Tobar, M., Labbe, F., and Laroze, D. (2013). Downwelling and upwelling radiance distributions sampled under cloudless conditions in Antarctica. *Applied Optics*, 52(25):6287.
- Cornette, W. M. and Shanks, J. G. (1992). Physically reasonable analytic expression for the single-scattering phase function. *Applied optics*, 31(16):3152–3160. <https://doi.org/10.1364/AO.31.003152>.
- Crawley, D. B., Hand, J. W., Kummert, M., and Griffith, B. T. (2008). Contrasting the capabilities of building energy performance simulation programs. *Building and environment*, 43(4):661–673.
- Crawley, D. B., Lawrie, L. K., Pedersen, C. O., and Winkelmann, F. C. (2000). EnergyPlus: Energy Simulation Program. *ASHRAE Journal*, 42(4):49–56.
- Crawley, D. B., Lawrie, L. K., Winkelmann, F. C., Buhl, W. F., Huang, Y. J., Pedersen, C. O., Strand, R. K., Liesen, R. J., Fisher, D. E., Witte, M. J., et al. (2001). Energyplus: creating a new-generation building energy simulation program. *Energy and buildings*, 33(4):319–331. [https://doi.org/10.1016/S0378-7788\(00\)00114-6](https://doi.org/10.1016/S0378-7788(00)00114-6).
- Cutler, C. R. and Ramaker, B. L. (1980). Dynamic Matrix Control - A computer control algorithm. In *Joint Automatic Control Conference*, volume 17, page 72.
- Daysim (2019). Daysim software. <https://github.com/MITSustainableDesignLab/Daysim>.
- Del Rocco, J., Bourke, P. D., Patterson, C. B., and Kider, J. T. (2020). Real-time spectral radiance estimation of hemispherical clear skies with machine learned regression models. *Solar Energy*, 204:48–63. <https://doi.org/10.1016/j.solener.2020.04.006>.

- Del Rocco, J. and Kider Jr., J. T. (2021). Radiant spectral energy for simulation in the built environment. In *Proceedings, Building Simulation 2021: 17th Conference of IBPSA*. IBPSA.
- Del Rocco, J., Patterson, C. B., Dhrif, H., and Kider, J. T. (2018). Learning and estimating whole sky visible, VNIR, SWIR radiance distributions from a commercial camera. In *Optics and Photonics for Information Processing XII*, volume 10751, page 107510F. SPIE. <https://doi.org/10.1117/12.2321295>.
- Designing Buildings Ltd. (2020). Designing Buildings Wiki: Building Performance. https://www.designingbuildings.co.uk/wiki/Building_performance. Accessed: 2021-05-01.
- Dibdin, W. J. (1889). *Practical Photometry: a Guide to the Study of the Measurement of Light*. W. King.
- Domingos, P. (2012). A few useful things to know about machine learning. *Communications of the ACM*, 55(10):78–87. <https://doi.org/10.1145/2347736.2347755>.
- Drozdowski, Z. and Gupta, S. (2009). Adaptive fitting as case exploration for adaptivity in architecture. In *Building a Better Tomorrow [Proceedings of the 29th Annual Conference of the Association for Computer Aided Design in Architecture (ACADIA)]*, pages 105–109. IBPSA, CUMINCAD.
- Eltaweel, A. and Su, Y. (2017). Controlling venetian blinds based on parametric design; via implementing Grasshopper’s plugins: A case study of an office building in Cairo. *Energy and Buildings*, 139:31–43.
- Emde, C., Buras-Schnell, R., Kylling, A., Mayer, B., Gasteiger, J., Hamann, U., Kylling, J., Richter, B., Pause, C., Dowling, T., et al. (2016). The libRadtran software package for radiative transfer calculations (version 2.0.1). *Geoscientific Model Development*, 9(5):1647–1672. <http://doi.org/10.5194/gmd-9-1647-2016>.
- Faraday, M. (1832). Experimental researches in electricity. *Philosophical transactions of the Royal Society of London*, 5(122):125–162.
- Favoino, F., Jin, Q., and Overend, M. (2014). Towards an Ideal Adaptive Glazed Façade for Office Buildings. *Energy Procedia*, 62:289–298.
- Feigenbaum, E. A., Buchanan, B. G., and Lederberg, J. (1970). On generality and problem solving: A case study using the DENDRAL program.
- Ferreira, P., Ruano, A., Silva, S., and Conceicao, E. (2012). Neural networks based predictive control for thermal comfort and energy savings in public buildings. *Energy and buildings*, 55:238–251.

- Fisher, R., Perkins, S., Walker, A., and Wolfart, E. (1996). *Hypermedia image processing reference*. John Wiley & Sons Ltd. <https://www.worldcat.org/title/hypermedia-image-processing-reference/oclc/43115444>.
- Forgione, M., Piga, D., and Bemporad, A. (2020). Efficient calibration of embedded mpc. *IFAC-PapersOnLine*, 53(2):5189–5194.
- Foster, R., Gray, D., Bowles, J., Korwan, D., Slutsker, I., Sorokin, M., Roche, M., Smith, A., and Pezzaniti, L. (2020). Mantis: an all-sky visible-to-near-infrared hyper-angular spectropolarimeter. *Applied Optics*, 59(20):5896–5909.
- Garnier, A., Eynard, J., Caussanel, M., and Grieu, S. (2015). Predictive control of multizone heating, ventilation and air-conditioning systems in non-residential buildings. *Applied Soft Computing*, 37:847–862.
- Geurts, P., Ernst, D., and Wehenkel, L. (2006). Extremely randomized trees. *Machine learning*, 63(1):3–42.
- Ghosh, A. and Mallick, T. (2018). Evaluation of optical properties and protection factors of a pdlc switchable glazing for low energy building integration. *Solar Energy Materials and Solar Cells*, 176:391–396.
- Goral, C. M., Torrance, K. E., Greenberg, D. P., and Battaile, B. (1984). Modeling the interaction of light between diffuse surfaces. In *ACM SIGGRAPH computer graphics*, volume 18 Issue 3, pages 213–222. ACM.
- Greenberg, D., Pratt, K., Hancey, B., Jones, N., Schumann, L., Dobbs, J., Dong, Z., Bosworth, D., and Walter, B. (2013). Sustain: An experimental test bed for building energy simulation. *Energy and Buildings*, 58:44–57. <https://doi.org/10.1016/j.enbuild.2012.11.026>.
- Greenberg, D. P., Cohen, M. F., and Torrance, K. E. (1986). Radiosity: A method for computing global illumination. *The Visual Computer*, 2(5):291–297.
- Griffith, J. W. (1978). Benefits of daylighting: cost and energy savings. *ASHRAE J.:(United States)*, 20(1).
- Gueymard, C. et al. (1995). SMARTS2 A: simple model of the atmospheric radiative transfer of sunshine: algorithms and performance assessment. <https://www.nrel.gov/grid/solar-resource/smarts.html>.
- Gueymard, C. A. (2010). Spectral circumsolar radiation contribution to CPV. In *AIP Conference Proceedings*, volume 1277, pages 316–319. American Institute of Physics.
- Gueymard, C. A. (2018). Revised composite extraterrestrial spectrum based on recent solar irradiance observations. *Solar Energy*, 169:434–440.

- Gueymard, C. A. (2019). The smart's spectral irradiance model after 25 years: New developments and validation of reference spectra. *Solar Energy*, 187:233–253.
- Guglielmetti, R., Macumber, D., and Long, N. (2011). OpenStudio: an open source integrated analysis platform. <https://www.nrel.gov/docs/fy12osti/51836.pdf>. Accessed 2021-1-8.
- Gunay, H. B., O'Brien, W., Beausoleil-Morrison, I., and Gilani, S. (2017). Development and implementation of an adaptive lighting and blinds control algorithm. *Building and Environment*, 113:185–199.
- Guo, H., Shen, C., Zhang, H., Chen, H., and Jia, R. (2018). Simultaneous trajectory planning and tracking using an mpc method for cyber-physical systems: A case study of obstacle avoidance for an intelligent vehicle. *IEEE Transactions on Industrial Informatics*, 14(9):4273–4283.
- Gutjahr, B., Gröll, L., and Werling, M. (2016). Lateral vehicle trajectory optimization using constrained linear time-varying mpc. *IEEE Transactions on Intelligent Transportation Systems*, 18(6):1586–1595.
- Haber, J., Magnor, M., and Seidel, H.-P. (2005). Physically-based simulation of twilight phenomena. *ACM Transactions on Graphics (TOG)*, 24(4):1353–1373. <https://doi.org/10.1145/1095878.1095884>.
- Hall, M., Frank, E., Holmes, G., Pfahringer, B., Reutemann, P., and Witten, I. H. (2009). The weka data mining software: an update. *ACM SIGKDD explorations newsletter*, 11(1):10–18. <https://doi.org/10.1145/1656274.1656278>.
- Harrold, M. V. and Lush, D. M. (1988). Automatic controls in building services. In *IEE Proceedings B (Electric Power Applications)*, volume 135, pages 105–133. IET.
- Hensen, J. L. and Lamberts, R. (2012). *Building performance simulation for design and operation*. Routledge.
- Henyey, L. G. and Greenstein, J. L. (1941). Diffuse radiation in the galaxy. *The Astrophysical Journal*, 93:70–83.
- Hess, M., Koepke, P., and Schult, I. (1998). Optical properties of aerosols and clouds: The software package opac. *Bulletin of the American meteorological society*, 79(5):831–844.
- Hoerl, A. E. and Kennard, R. W. (1970). Ridge regression: Biased estimation for nonorthogonal problems. *Technometrics*, 12(1):55–67.
- Hoffmann, S., Lee, E. S., McNeil, A., Fernandes, L., Vidanovic, D., and Thanachareonkit, A. (2016). Balancing daylight, glare, and energy-efficiency goals: An evaluation of exterior coplanar shading systems using complex fenestration modeling tools. *Energy and Buildings*, 112:279–298.

- Holben, B. N., Eck, T. F., Slutsker, I., Tanre, D., Buis, J., Setzer, A., Vermote, E., Reagan, J. A., Kaufman, Y., Nakajima, T., et al. (1998). Aeronet—a federated instrument network and data archive for aerosol characterization. *Remote sensing of environment*, 66(1):1–16.
- Hong, T., Buhl, F., and Haves, P. (2008). EnergyPlus run time analysis. <https://www.osti.gov/biblio/951766>. Accessed 2020-12-20.
- Hosek, L. and Wilkie, A. (2012a). An analytic model for full spectral sky-dome radiance. *ACM Transactions on Graphics (TOG)*, 31(4):95. <https://doi.org/10.1145/2185520.2185591>.
- Hosek, L. and Wilkie, A. (2012b). An analytic model for full spectral sky-dome radiance. *ACM Transactions on Graphics (TOG)*, 31(4):95.
- Hraška, J., Hanuliak, P., Hartman, P., Zeman, M., and Stebelová, K. (2014). Comparative study of window glazing systems influence on melatonin secretion in patients in the hospital wards. In *Advanced Materials Research*, volume 899, pages 288–293. Trans Tech Publ.
- Hu, J., Zheng, W., Zhang, S., Li, H., Liu, Z., Zhang, G., and Yang, X. (2021). Thermal load prediction and operation optimization of office building with a zone-level artificial neural network and rule-based control. *Applied Energy*, 300:117429.
- Huang, H., Chen, L., and Hu, E. (2015). A new model predictive control scheme for energy and cost savings in commercial buildings: An airport terminal building case study. *Building and environment*, 89:203–216.
- Igawa, N., Koga, Y., Matsuzawa, T., and Nakamura, H. (2004). Models of sky radiance distribution and sky luminance distribution. *Solar Energy*, 77(2):137–157.
- Ihm, P., Nemri, A., and Krarti, M. (2009). Estimation of lighting energy savings from daylighting. *Building and Environment*, 44(3):509–514.
- Inanici, M. and ZGF Architects (2015). LARK Spectral Lighting plugin for Grasshopper. https://faculty.washington.edu/inanici/Lark/Lark_home_page.html. Accessed 2021-1-10.
- Iqbal, M. (1983). *An introduction to solar radiation*. Academic Press Canada.
- Ivanova, S. M. and Gueymard, C. A. (2019). Simulation and applications of cumulative anisotropic sky radiance patterns. *Solar Energy*, 178:278–294.
- Jahanbin, A. and Haghghi, M. S. (2021). On the possibility of creating smart contracts on bitcoin by mpc-based approaches. In *2021 26th International Computer Conference, Computer Society of Iran (CSICC)*, pages 1–7. IEEE.
- Jakica, N. (2017). State-of-the-art review of solar design tools and methods for assessing daylighting and solar potential for building-integrated photovoltaics. *Renewable and Sustainable Energy Reviews*.

- Jakubiec, J. A. and Reinhart, C. F. (2011). Diva 2.0: Integrating daylight and thermal simulations using rhinoceros 3d, daysim and energyplus. In *Proceedings of Building Simulation*, volume 20, pages 2202–2209. Citeseer.
- James J. Hirsch & Associates (JJH) (1999). Comparison of DOE-2.1E, DOE-2.2, eQUEST and PowerDOE. <https://www.doe2.com/compare.html>. Accessed: 2021-9-1.
- Janda, K. B. (2011). Buildings don't use energy: people do. *Architectural Science Review*, 54(1):15–22.
- Jarosz, W. (2008). *Efficient Monte Carlo methods for light transport in scattering media*. Citeseer.
- Joblove, G. H. and Greenberg, D. (1978). Color spaces for computer graphics. *ACM SIGGRAPH Computer Graphics*, 12(3):20–25. <https://doi.org/10.1145/965139.807362>.
- Jones, N. L., Greenberg, D. P., and Pratt, K. B. (2012). Fast computer graphics techniques for calculating direct solar radiation on complex building surfaces. *Journal of Building Performance Simulation*, 5(5):300–312.
- Jones, N. L., McCrone, C. J., Walter, B. J., Pratt, K. B., and Greenberg, D. P. (2013). Automated translation and thermal zoning of digital building models for energy analysis. Technical report, Cornell University, Ithaca, NY.
- Kajiya, J. T. (1986). The rendering equation. *ACM SIGGRAPH Computer Graphics*, 20(4):143–150. <https://doi.org/10.1145/15886.15902>.
- Kalman, R. E. (1960). A New Approach to Linear Filtering and Prediction Problems. *Journal of Basic Engineering*, 82(1):35–45.
- Kalman, R. E. et al. (1960). Contributions to the theory of optimal control. *Bol. soc. mat. mexicana*, 5(2):102–119.
- Kaplan, R. and Kaplan, S. (1989). *The experience of nature: A psychological perspective*. CUP Archive.
- Kaplan, S. (1995). The restorative benefits of nature: Toward an integrative framework. *Journal of environmental psychology*, 15(3):169–182.
- Kennel, F., Görges, D., and Liu, S. (2012). Energy management for smart grids with electric vehicles based on hierarchical mpc. *IEEE Transactions on industrial informatics*, 9(3):1528–1537.
- Kider, J. T. (2016). SENSEable Design Lab. <https://sdl.eecs.ucf.edu>.
- Kider, J. T., Knowlton, D., Newlin, J., Li, Y. K., and Greenberg, D. P. (2014). A framework for the experimental comparison of solar and skydome illumination. *ACM Transactions on Graphics (TOG)*, 33(6):180. <https://doi.org/10.1145/2661229.2661259>.

- Kider, J. T., Walter, B., Fang, S., Sekkin, E., and Greenberg, D. P. (2019). Transition portal for daylighting calculations in early phase design. *Energy and Buildings*, 198:353–363.
- Kim, J. T. and Todorovic, M. S. (2013). Tuning control of buildings glazing’s transmittance dependence on the solar radiation wavelength to optimize daylighting and building’s energy efficiency. *Energy and Buildings*, 63:108–118.
- Kim, W., Jeon, Y., and Kim, Y. (2016). Simulation-based optimization of an integrated daylighting and hvac system using the design of experiments method. *Applied energy*, 162:666–674.
- Kinney, J. A. S. (1958). Comparison of scotopic, mesopic, and photopic spectral sensitivity curves. *JOSA*, 48(3):185–190. <https://doi.org/10.1364/JOSA.48.000185>.
- Kittler, R. (1994). Some qualities of scattering functions defining sky radiance distributions. *Solar Energy*, 53(6):511–516. [https://doi.org/10.1016/0038-092X\(94\)90131-K](https://doi.org/10.1016/0038-092X(94)90131-K).
- Kocev, D., Vens, C., Struyf, J., and Džeroski, S. (2013). Tree ensembles for predicting structured outputs. *Pattern Recognition*, 46(3):817–833.
- Kocifaj, M. (2009). Sky luminance/radiance model with multiple scattering effect. *Solar Energy*, 83(10):1914–1922. <https://doi.org/10.1016/j.solener.2009.07.004>.
- Kocifaj, M. (2012). Angular distribution of scattered radiation under broken cloud arrays: an approximation of successive orders of scattering. *Solar Energy*, 86(12):3575–3586. <https://doi.org/10.1016/j.solener.2012.06.022>.
- Kocifaj, M. (2015). Unified model of radiance patterns under arbitrary sky conditions. *Solar Energy*, 115:40–51. <http://linkinghub.elsevier.com/retrieve/pii/S0038092X15000894>.
- Kocifaj, M. and Kómar, L. (2016). Modeling diffuse irradiance under arbitrary and homogeneous skies: Comparison and validation. *Applied Energy*, 166:117–127.
- Koenderink, J. J. (2010). *Color for the Sciences*. The MIT Press.
- Kohavi, R. et al. (1995). A study of cross-validation and bootstrap for accuracy estimation and model selection. In *Proceedings of the Fourteenth International Joint Conference on Artificial Intelligence*, pages 1137–1145. IJCAI. <https://www.ijcai.org/proceedings/1995-2>.
- Konis, K. (2019). A circadian design assist tool to evaluate daylight access in buildings for human biological lighting needs. *Solar Energy*, 191:449–458.
- Kusiak, A., Xu, G., and Zhang, Z. (2014). Minimization of energy consumption in hvac systems with data-driven models and an interior-point method. *Energy Conversion and Management*, 85:146–153.

- Lacis, A. A. and Hansen, J. (1974). A parameterization for the absorption of solar radiation in the earth's atmosphere. *Journal of the atmospheric sciences*, 31(1):118–133. [https://doi.org/10.1175/1520-0469\(1974\)031%3C0118:APFTA0%3E2.0.CO;2](https://doi.org/10.1175/1520-0469(1974)031%3C0118:APFTA0%3E2.0.CO;2).
- Lambert, J. H. (1760). *Photometria sive de mensura et gradibus luminis, colorum et umbrae*. sumptibus viduae E. Klett, typis CP Detleffsen.
- Larson, G. W. and Shakespeare, R. (1998). *Rendering with Radiance: The Art and Science of Lighting Visualization*. Morgan Kaufmann Publishers Inc., San Francisco, CA, USA.
- Lechner, N. (2014). *Heating, Cooling, Lighting: Sustainable Design Methods for Architects*. John Wiley & Sons.
- Lee Jr, R. L. (2008). Measuring overcast colors with all-sky imaging. *Applied optics*, 47(34):H106–H115.
- Li, D. H., Chau, T., and Wan, K. K. (2014). A review of the cie general sky classification approaches. *Renewable and Sustainable Energy Reviews*, 31:563–574.
- Li, D. H., Lou, S., Ghaffarianhoseini, A., Alshaibani, K. A., and Lam, J. C. (2017). A review of calculating procedures on daylight factor based metrics under various cie standard skies and obstructed environments. *Building and Environment*, 112:29–44.
- Li, Q., Lu, W., and Yang, J. (2011). A hybrid thresholding algorithm for cloud detection on ground-based color images. *Journal of atmospheric and oceanic technology*, 28(10):1286–1296.
- Liao, S.-H. (2005). Expert system methodologies and applications—a decade review from 1995 to 2004. *Expert systems with applications*, 28(1):93–103.
- LibRaw (2018). libraw, raw image decoder. <https://www.libraw.org>.
- Littlefair, P. J. (1981). The luminance distribution of an average sky. *Lighting Research & Technology*, 13(4):192–198. <https://doi.org/10.1177/096032718101300402>.
- López-Álvarez, M. A., Hernández-Andrés, J., Romero, J., Olmo, F. J., Cazorla, A., and Alados-Arboledas, L. (2008). Using a trichromatic CCD camera for spectral skylight estimation. *Applied optics*, 47(34):H31–H38.
- Macskassy, S. A. and Hirsh, H. (2003). Adding numbers to text classification. In *Proceedings of the twelfth international conference on Information and knowledge management*, pages 240–246. ACM. <https://doi.org/10.1145/956863.956910>.
- Mallory-Hill, S., Preiser, W. F., and Watson, C. G. (2012). *Enhancing Building Performance*. John Wiley & Sons.

- Malthus, T. and MacLellan, C. (2010). High performance fore optic accessories and tools for reflectance and radiometric measurements with the ASD FR3 spectroradiometer. In *ESA Hyperspectral Workshop 2010 “From Chris/Proba to PRISMA and EnMAP and beyond”*, page EP101432. European Space Agency. <http://hdl.handle.net/102.100.100/108223>.
- Marasov, S. (2019). Image Based Lights (IBL). <http://brabl.com/ibl/>. Accessed: 2019-11-20.
- Market Research Explore (2019). Global Electrochromic Materials Market Report 2019, Competitive Landscape, Trends and Opportunities. <https://www.marketresearchexplore.com>. Accessed 2021-1-18.
- Mayer, B. and Kylling, A. (2005). The libRadtran software package for radiative transfer calculations. *Atmospheric Chemistry and Physics*, 5(7):1855–1877.
- Mayhoub, M. and Carter, D. (2011). The costs and benefits of using daylight guidance to light office buildings. *Building and Environment*, 46(3):698–710.
- Mazria, E. and Kershner, K. (2008). Meeting the 2030 challenge through building codes. http://www.architecture2030.com/pdfs/2030Challenge_Codes_WP.pdf. Accessed: 2019-10-01.
- Meseguer, J., Pérez-Grande, I., and Sanz-Andrés, A. (2012). *Spacecraft Thermal Control*. Elsevier.
- Metro Performance Glass Ltd. (2021). Metro Performance Glass. <https://www.metroglass.co.nz>. Accessed: 2021-09-01.
- Mettanant, V. and Chaiwiwatworakul, P. (2014). Automated Vertical Blinds for Daylighting in Tropical Region. *Energy Procedia*, 52:278–286.
- Mie, G. (1908). Beiträge zur optik trüber medien, speziell kolloidaler metallösungen. *Annalen der physik*, 330(3):377–445.
- Moulton, N., Del Rocco, J., Kider Jr, J. T., and Fiore, S. M. (2018). An affective kinetic building façade system: Mood Swing. In *Proceedings, 13th Conference on Advanced Building Skins*, pages 417–426. Advanced Building Skins GmbH. ISBN: 978-3-9524883-4-8. <https://abs.green/files/pdf/content-2018.pdf>.
- Nagy, Z., Svetozarevic, B., Jayathissa, P., Begle, M., Hofer, J., Lydon, G., Willmann, A., and Schlueter, A. (2016). The adaptive solar facade: from concept to prototypes. *Frontiers of Architectural Research*, 5(2):143–156.
- Nakamura, H., Oki, M., and Hayashi, Y. (1985). A study on the estimation of the relative frequency of occurrences of the clear sky, the intermediate sky and the overcast sky in japan. *Journal of Light & Visual Environment*, 9(2):2_22–2_31. https://doi.org/10.2150/jlve.9.2_22.

- NCEI, N. (2019). National centers for environmental information. *Climate Data Online*. <https://www.ncdc.noaa.gov/cdo-web/>.
- Nesler, C. (1986). Adaptive control of thermal processes in buildings. *IEEE Control Systems Magazine*, 6(4):9–13.
- Nguyen, A.-T., Reiter, S., and Rigo, P. (2014). A review on simulation-based optimization methods applied to building performance analysis. *Applied Energy*, 113:1043–1058.
- Nimier-David, M., Vicini, D., Zeltner, T., and Jakob, W. (2019). Mitsuba 2: A retargetable forward and inverse renderer. *ACM Transactions on Graphics (TOG)*, 38(6):1–17.
- Nishita, T., Dobashi, Y., and Nakamae, E. (1996). Display of clouds taking into account multiple anisotropic scattering and sky light. In *Proceedings of the 23rd annual conference on Computer graphics and interactive techniques*, pages 379–386. ACM. <https://doi.org/10.1145/237170.237277>.
- Nishita, T., Sirai, T., Nakamae, E., and Tadamura, K. (1993). Display of the earth taking into account atmospheric scattering. In *SIGGRAPH*, volume 93, page 175. <https://doi.org/10.1145/166117.166140>.
- Nou, J., Chauvin, R., Eynard, J., Thil, S., and Grieu, S. (2018). Towards the intrahour forecasting of direct normal irradiance using sky-imaging data. *Heliyon*, 4(4):e00598. <https://doi.org/10.1016/j.heliyon.2018.e00598>.
- Office Of The Federal Coordinator For Meteorological Services And Supporting Research (2017). Chapter 9: Sky Condition. In *Federal Meteorological Handbook No. 1: Surface Weather Observations and Reports*, pages 45–50. National Oceanic and Atmospheric Administration, Washington, D.C., fcm-h1-2017 edition.
- Olbina, S. and Hu, J. (2012). Daylighting and thermal performance of automated split-controlled blinds. *Building and Environment*, 56:127–138.
- Parker, J. R. (2010). *Algorithms for image processing and computer vision*. John Wiley & Sons. <https://www.worldcat.org/title/algorithms-for-image-processing-and-computer-vision/oclc/813666888>.
- Pedregosa, F., Varoquaux, G., Gramfort, A., Michel, V., Thirion, B., Grisel, O., Blondel, M., Prettenhofer, P., Weiss, R., Dubourg, V., et al. (2011). Scikit-learn: Machine learning in python. *Journal of machine learning research*, 12(Oct):2825–2830.
- Perez, R., Seals, R., and Michalsky, J. (1993). All-weather model for sky luminance distribution—preliminary configuration and validation. *Solar energy*, 50(3):235–245. [https://doi.org/10.1016/0038-092X\(93\)90017-I](https://doi.org/10.1016/0038-092X(93)90017-I).
- Pharr, M., Jakob, W., and Humphreys, G. (2016). *Physically based rendering: From theory to implementation*. Morgan Kaufmann.

- Picard, R. R. and Cook, R. D. (1984). Cross-validation of regression models. *Journal of the American Statistical Association*, 79(387):575–583. <https://doi.org/10.1080/01621459.1984.10478083>.
- Planck, M. (1901). On the law of distribution of energy in the normal spectrum. *Annalen der physik*, 4(553):1.
- Pokrowski, G. (1929). Über einen scheinbaren mie-effekt und seine mögliche rolle in der atmosphärenoptik. *Zeitschrift für Physik*, 53(1-2):67–71.
- Potočnik, J., Cadena, J., Košir, M., and Poli, T. (2019). Occupant perception of spectral light content variations due to glazing type and internal finish. In *IOP Conference Series: Earth and Environmental Science*, volume 296 Issue 1. IOP Publishing.
- Poynton, C. A. (1995). A guided tour of colour space. In *New Foundation for Video Technology: The SMPTE Advanced Television and Electronic Imaging Conference*, pages 167–180. SMPTE. <https://doi.org/10.5594/M00840>.
- Preetham, A., Shirley, P., and Smits, B. (1999). A practical analytic model for daylight. In *Proceedings of the 26th Annual Conference on Computer Graphics and Interactive Techniques*, SIGGRAPH '99, pages 91–100. ACM, ACM Press/Addison-Wesley Publishing Co. <https://doi.org/10.1145/311535.311545>.
- Priya, S. S. and Iqbal, M. H. (2015). Solar radiation prediction using artificial neural network. *International Journal of Computer Applications*, 116(16).
- Qin, S. J. and Badgwell, T. A. (2003). A survey of industrial model predictive control technology. *Control engineering practice*, 11(7):733–764.
- Rawlings, J. B. (2000). Tutorial overview of model predictive control. *IEEE control systems magazine*, 20(3):38–52.
- Rea, M. S., Figueiro, M. G., and Bullough, J. D. (2002). Circadian photobiology: an emerging framework for lighting practice and research. *Lighting research & technology*, 34(3):177–187.
- Reda, I. and Andreas, A. (2004). Solar position algorithm for solar radiation applications. *Solar energy*, 76(5):577–589. <https://doi.org/10.1016/j.solener.2003.12.003>.
- Reinhart, C. F. (2004). Lightswitch-2002: a model for manual and automated control of electric lighting and blinds. *Solar Energy*, 77(1):15–28.
- Reinhart, C. F. and Davila, C. C. (2016). Urban building energy modeling—a review of a nascent field. *Building and Environment*, 97:196–202.
- Reinhart, C. F. and Walkenhorst, O. (2001). Validation of dynamic RADIANCE-based daylight simulations for a test office with external blinds. *Energy and buildings*, 33(7):683–697.

- Reinhart, C. F. and Wienold, J. (2011). The daylighting dashboard—A simulation-based design analysis for daylit spaces. *Building and environment*, 46(2):386–396.
- Ricchiazzi, P., Yang, S., Gautier, C., and Sowle, D. (1998). Sbdart: A research and teaching software tool for plane-parallel radiative transfer in the earth’s atmosphere. *Bulletin of the American Meteorological Society*, 79(10):2101–2114. [https://doi.org/10.1175/1520-0477\(1998\)079<2101:SARATS>2.0.CO;2](https://doi.org/10.1175/1520-0477(1998)079<2101:SARATS>2.0.CO;2).
- Richalet, J., Rault, A., Testud, J., and Papon, J. (1978). Model predictive heuristic control. *Automatica (journal of IFAC)*, 14(5):413–428.
- Riechert, M. (2018). rawpy (0.13.1), RAW image processing for Python. <https://pypi.org/project/rawpy>.
- Robert McNeel & Associates (1980). Rhinoceros 3D. <https://www.rhino3d.com>. Accessed 2021-1-3.
- Robertson, A. R. et al. (1977). The CIE 1976 color-difference formulae. *Color Research & Application*, 2(1):7–11. <https://doi.org/10.1002/j.1520-6378.1977.tb00104.x>.
- Robledo, J., Leloux, J., Sarr, B., Gueymard, C. A., and Darez, P. (2021). Dynamic simulation of the shading cast by a wind farm on an adjacent photovoltaic plant. In *Proceedings of EU PVSEC 2021*.
- Rosen, M. (1992). Investigation of the validity of the tdr model for the distribution of diffuse sky radiance. *Solar energy*, 48(2):123–131.
- Rossiter, J. A. (2017). *Model-based predictive control: a practical approach*. CRC press.
- Roudsari, M. S., Pak, M., Smith, A., et al. (2013). Ladybug: A parametric environmental plugin for Grasshopper to help designers create an environmentally-conscious design. In *Proceedings of the 13th international IBPSA conference held in Lyon, France Aug*, pages 3128–3135. https://www.ibpsa.org/proceedings/bs2013/p_2499.pdf.
- Saito, M. and Iwabuchi, H. (2016). Cloud Discrimination from Sky Images Using a Clear-Sky Index. *Journal of Atmospheric and Oceanic Technology*, 33(8):1583–1595.
- Saito, M., Iwabuchi, H., and Murata, I. (2016). Estimation of spectral distribution of sky radiance using a commercial digital camera. *Applied Optics*, 55(2):415. <https://doi.org/10.1364/AO.55.000415>.
- Salpakari, J. and Lund, P. (2016). Optimal and rule-based control strategies for energy flexibility in buildings with PV. *Applied Energy*, 161:425–436.
- Sapia, C. (2013). Daylighting in buildings: Developments of sunlight addressing by optical fiber. *Solar Energy*, 89:113–121.

- Satylmÿs, P., Bashford-Rogers, T., Chalmers, A., and Debattista, K. (2016). A machine-learning-driven sky model. *IEEE computer graphics and applications*, 37(1):80–91. <https://doi.org/10.1109/MCG.2016.67>.
- Saxena, M., Ward, G., Perry, T., Heschong, L., and Higa, R. (2010). Dynamic Radiance Predicting annual daylighting with variable fenestration optics using BSDFs. In *Proceedings of the Fourth National Conference of IBPSA-USA (SimBuild 2010)*, volume 4, pages 402–409.
- Schein, J., Bushby, S. T., and Schein, J. R. (2005). *A Simulation Study of a Hierarchical, Rule-Based Method for System-Level Fault Detection and Diagnostics in HVAC Systems*. US Department of Commerce, National Institute of Standards and Technology.
- Schumann, L. and Greenberg, D. P. (2012). Environment mapping for fast and robust calculation of indirect radiant energy. In *Proceedings of SimBuild 2012*, pages 263–269. International Building Performance Simulation Association (IBPSA).
- Sethi, M. and de Oliveira, J. P. (2015). From global ‘North–South’ to local ‘Urban–Rural’: A shifting paradigm in climate governance? *Urban Climate*, 14:529–543.
- Shortliffe, E. H., Davis, R., Axline, S. G., Buchanan, B. G., Green, C. C., and Cohen, S. N. (1975). Computer-based consultations in clinical therapeutics: explanation and rule acquisition capabilities of the mycin system. *Computers and biomedical research*, 8(4):303–320.
- Sierpinski, W. (1988). *Elementary Theory of Numbers (2nd)*, volume 31. Elsevier.
- Sigernes, F., Holmes, J. M., Dyrland, M., Lorentzen, D. A., Svenøe, T., Heia, K., Aso, T., Chernouss, S., and Deehr, C. S. (2008). Sensitivity calibration of digital colour cameras for auroral imaging. *Optics express*, 16(20):15623–15632.
- Skowronski, J. (1999). Pel recursive motion estimation and compensation in subbands. *Signal Processing: Image Communication*, 14(5):389–396.
- Skycraft Surplus Ltd. (1974). Skycraft Surplus. <https://skycraftsurplus.com>. Accessed: 2021-10-01.
- Smith, A. R. (1978). Color gamut transform pairs. *ACM SIGGRAPH Computer Graphics*, 12(3):12–19. <https://doi.org/10.1145/965139.807361>.
- Smith, C. J., Forster, P. M., and Crook, R. (2016). An all-sky radiative transfer method to predict optimal tilt and azimuth angle of a solar collector. *Solar Energy*, 123:88–101.
- Solemnia (2019). Adaptive Lighting for Alertness (ALFA) Software. <https://solemnia.com/Alfa.html>. Accessed 2021-1-10.
- Solomon, S., Portmann, R., Sanders, R., Daniel, J., Madsen, W., Bartram, B., and Dutton, E. (1999). On the role of nitrogen dioxide in the absorption of solar radiation. *Journal of Geophysical Research: Atmospheres*, 104(D10):12047–12058.

- Song, B. C. and Ra, J. B. (2000). A fast multi-resolution block matching algorithm for motion estimation. *Signal Processing: Image Communication*, 15(9):799–810.
- Stapleton, A. E. (1992). Ultraviolet radiation and plants: burning questions. *The Plant Cell*, 4(11):1353.
- Stazi, F., Naspi, F., and D’Orazio, M. (2017). A literature review on driving factors and contextual events influencing occupants’ behaviours in buildings. *Building and Environment*, 118:40–66.
- Stefan, J. (1891). Über die theorie der eisbildung, insbesondere über die eisbildung im polarmeere. *Annalen der Physik*, 278(2):269–286.
- Steven, M. D. and Unsworth, M. H. (1977). Standard distributions of clear sky radiance. *Quarterly Journal of the Royal Meteorological Society*, 103(437):457–465.
- Stoffel, T., Renne, D., Myers, D., Wilcox, S., Sengupta, M., George, R., and Turchi, C. (2010). Concentrating Solar Power: Best Practices Handbook for the Collection and Use of Solar Resource Data (CSP). *Technical Report*. <https://www.osti.gov/biblio/989017>.
- Stokes, M., Anderson, M., Chandrasekar, S., and Motta, R. (1996). A standard default color space for the internet-sRGB. *Microsoft and Hewlett-Packard Joint Report*. <https://www.w3.org/Graphics/Color/sRGB>.
- Stone, E. (2015). Completely painless programmer’s guide to XYZ, RGB, ICC, xyY, and TRCs. <https://ninedegreesbelow.com/photography/xyz-rgb.html>. Accessed: 2019-11-01.
- Strutt, J. W. (1871). On the light from the sky, its polarization and colour. *The London, Edinburgh, and Dublin Philosophical Magazine and Journal of Science*, 41(271):107–120.
- Stumpfel, J., Tchou, C., Jones, A., Hawkins, T., Wenger, A., and Debevec, P. (2004). Direct hdr capture of the sun and sky. In *Proceedings of the 3rd International Conference on Computer Graphics, Virtual Reality, Visualisation and Interaction in Africa, AFRIGRAPH ’04*, pages 145–149. ACM. <http://doi.acm.org/10.1145/1029949.1029977>.
- Sturzenegger, D., Gyalistras, D., Morari, M., and Smith, R. S. (2015). Model predictive climate control of a swiss office building: Implementation, results, and cost–benefit analysis. *IEEE Transactions on Control Systems Technology*, 24(1):1–12.
- Sun, K. and Hong, T. (2017). A framework for quantifying the impact of occupant behavior on energy savings of energy conservation measures. *Energy and Buildings*, 146:383–396.
- The American Institute of Architects (AIA) (2019). Architect’s Guide to Building Performance: Integrating Simulation into the Design Process. https://content.aia.org/sites/default/files/2019-06/AIA_BPSGuide_2019_FINAL.pdf.
- Thompson, E. D., Frolich, E., Bellows, J. C., Bassford, B. E., Skiko, E. J., and Fox, M. S. (2015). Process Diagnosis System (PDS)—A 30 Year History. In *Twenty-Seventh IAAI Conference*.

- Tibshirani, R. (1996). Regression shrinkage and selection via the lasso. *Journal of the Royal Statistical Society. Series B (Methodological)*, pages 267–288.
- Tohsing, K., Schrempf, M., Riechelmann, S., and Seckmeyer, G. (2014). Validation of spectral sky radiance derived from all-sky camera images-a case study. *Atmospheric Measurement Techniques* 7 (2014), Nr. 7. <https://doi.org/10.15488/5>.
- Treado, S., Gillette, G., and Kusuda, T. (1984). Daylighting with windows, skylights, and clerestories. *Energy and Buildings*, 6(4):319–330.
- Turnbull, T. L., Barlow, A. M., and Adams, M. A. (2013). Photosynthetic benefits of ultraviolet-a to pimelea ligustrina, a woody shrub of sub-alpine australia. *Oecologia*, 173(2):375–385.
- Tzempelikos, A. and Athienitis, A. K. (2007). The impact of shading design and control on building cooling and lighting demand. *Solar Energy*, 81(3):369–382.
- Ulrich, R. S. (1979). Visual landscapes and psychological well-being. *Landscape research*, 4(1):17–23.
- United Nations, D. o. E. and Social Affairs, P. D. (2018). World Urbanization Prospects: The 2018 Revision. *Data and Report Online*. <https://population.un.org/wup/>.
- U.S. DoE EERE (2013). Solar Radiation Basics. <https://www.energy.gov/eere/solar/solar-radiation-basics>. Accessed: 2021-9-1.
- U.S. DoE EERE (2014). Radiance. <https://www.energy.gov/eere/buildings/downloads/radiance>. Accessed: 2021-6-01.
- U.S. DoE EERE (2016a). About Building Energy Modeling. <https://www.energy.gov/eere/buildings/about-building-energy-modeling>. Accessed: 2021-9-1.
- U.S. DoE EERE (2016b). Building Energy Modeling. <https://www.energy.gov/eere/buildings/building-energy-modeling>. Accessed: 2019-11-01.
- USDOE Energy Information Administration (EIA) (2021). Use of electricity. <https://www.eia.gov/energyexplained/electricity/use-of-electricity.php>. Accessed 2021-9-5.
- van den Wymelenberg, K. (2012). Patterns of occupant interaction with window blinds: A literature review. *Energy and Buildings*, 51:165–176.
- Velasco, R., Brakke, A. P., and Chavarro, D. (2015). Dynamic façades and computation: Towards an inclusive categorization of high performance kinetic façade systems. In *International Conference on Computer-Aided Architectural Design Futures*, pages 172–191. Springer.
- Velux Foundations (2019). The Daylight Award. <http://thedaylightaward.com/award/>. Accessed: 2019-11-25.

- Vermote, E., Tanré, D., Deuzé, J., Herman, M., Morcrette, J., and Kotchenova, S. (2006). Second simulation of a satellite signal in the solar spectrum-vector (6SV). *6S User Guide Version*, 3:1–55.
- Versage, R., Melo, A. P., and Lamberts, R. (2010). Impact of different daylighting simulation results on the prediction of total energy consumption. In *Proceedings of the SimBuild 2010 Conference, New York, NY, USA*, volume 1113, page 17.
- Wang, J. J. and Shi, D. (2017). Spectral selective and photothermal nano structured thin films for energy efficient windows. *Applied Energy*, 208:83–96.
- Ward, G., Mistrick, R., Lee, E. S., McNeil, A., and Jonsson, J. (2011). Simulating the daylight performance of complex fenestration systems using bidirectional scattering distribution functions within radiance. *Leukos*, 7(4):241–261.
- Ward, G. J. (1994). The RADIANCE lighting simulation and rendering system. In *Proceedings of the 21st annual conference on Computer graphics and interactive techniques*, pages 459–472. ACM. <https://doi.org/10.1145/192161.192286>.
- Wien, W. (1894). Temperatur und entropie der strahlung. *Annalen der Physik*, 288(5):132–165.
- Willers, C. J. (2013). *Electro-optical system analysis and design: a radiometry perspective*. SPIE. <https://doi.org/10.1117/3.1001964>.
- Wong, K. V. and Chan, R. (2014). Smart glass and its potential in energy savings. *Journal of Energy Resources Technology*, 136(1).
- Wright, W. D. (1929). A re-determination of the trichromatic coefficients of the spectral colours. *Transactions of the Optical Society*, 30(4):141. <https://doi.org/10.1088/1475-4878/30/4/301>.
- Xie, Y., Sengupta, M., and Dudhia, J. (2016). A fast all-sky radiation model for solar applications (FARMS): Algorithm and performance evaluation. *Solar Energy*, 135:435–445.
- Yamashita, M., Yoshimura, M., and Nakashizuka, T. (2004). Cloud cover estimation using multitemporal hemisphere imageries. *International Archives of Photogrammetry Remote Sensing and Spatial Information Sciences*, 35(7):826–829.
- Yan, D., O’Brien, W., Hong, T., Feng, X., Burak Gunay, H., Tahmasebi, F., and Mahdavi, A. (2015). Occupant behavior modeling for building performance simulation: Current state and future challenges. *Energy and Buildings*, 107:264–278.
- Yao, W., Li, Z., Zhao, Q., Lu, Y., and Lu, R. (2015). A new anisotropic diffuse radiation model. *Energy Conversion and Management*, 95:304–313. <https://doi.org/10.1016/j.enconman.2015.01.016>.

- Yokoyama, S., Xing, J., Liu, Y., Faggionato, D., Altun, A., and Starmer, W. T. (2014). Epistatic adaptive evolution of human color vision. *PLoS Genet*, 10(12):e1004884.
- Young, T., Fresnel, A.-J., and Huygens, C. (1819). The wave theory of light. *Memoirs of Huygens, Young and Fresnel*, pages 145–156.
- Yu, C. H. (1977). Exploratory data analysis. *Methods*, 2:131–160. <https://dx.doi.org/10.1093/obo/9780199828340-0200>.
- Yuste, M., Galindo, R. E., Carvalho, S., Albella, J., and Sánchez, O. (2011). Improving the visible transmittance of low-e titanium nitride based coatings for solar thermal applications. *Applied Surface Science*, 258(5):1784–1788.
- Zadeh, L. A. (1973). Outline of a new approach to the analysis of complex systems and decision processes. *IEEE Transactions on systems, Man, and Cybernetics*, SMC-3(1):28–44.
- Zhao, B., Hu, M., Ao, X., Xuan, Q., and Pei, G. (2018). Comprehensive photonic approach for diurnal photovoltaic and nocturnal radiative cooling. *Solar Energy Materials and Solar Cells*, 178:266–272.
- Zhao, J., Lam, K. P., Ydstie, B. E., and Karaguzel, O. T. (2015). EnergyPlus model-based predictive control within design–build–operate energy information modelling infrastructure. *Journal of Building Performance Simulation*, 8(3):121–134.
- Zotti, G., Wilkie, A., and Purgathofer, W. (2007). A critical review of the preetham skylight model. In *WSCG '2007: Short Communications Proceedings*, pages 23–30. Václav Skala-UNION Agency. <http://hdl.handle.net/11025/11160>.
- Zou, H. and Hastie, T. (2005). Regularization and variable selection via the elastic net. *Journal of the Royal Statistical Society: Series B (Statistical Methodology)*, 67(2):301–320.